IDENTIFICATION OF A NOVEL SUBSTRATE OF IRE1 IN LIPOTOXIC STRESS RESPONSE

A DISSERTATION SUBMITTED TO

THE GRADUATE SCHOOL OF ENGINEERING AND SCIENCE

OF BILKENT UNIVERSITY

IN PARTIAL FULFILLMENT OF THE REQUIREMENTS FOR

THE DEGREE OF

DOCTOR OF PHILOSOPHY

IN

MOLECULAR BIOLOGY AND GENETICS

By

Zehra YILDIRIM

February 2022

IDENTIFICATION OF A NOVEL SUBSTRATE OF IRE1 IN LIPOTOXIC STRESS RESPONSE

By Zehra YILDIRIM
February 2022

We certify that we have read this dissertation and that in our opinion it is fully adequate, in scope and in quality, as a thesis for the degree of Doctor of Philosophy.

Ebru ERBAY (Advisor)

Hasan Tayfun ÖZÇELIK

Michelle Marie ADAMS

Erkan YILMAZ

Çağdaş Devrim SON

Approved for the Graduate School of Engineering and Science

Ezhan KARAŞAN
Director of the Graduate School

ABSTRACT

IDENTIFICATION OF A NOVEL SUBSTRATE OF IRE1 IN LIPOTOXIC STRESS RESPONSE

Zehra YILDIRIM

Ph.D. in Molecular Biology and Genetics

Advisor: Ebru ERBAY

February 2022

Fragile X Mental Retardation protein (FMRP), widely known for its role in hereditary intellectual disability, is a ribonucleic acid (RNA)-binding protein (RBP) that controls translation of select messenger RNAs (mRNAs). I discovered that endoplasmic reticulum (ER) stress induces phosphorylation of FMRP on a site that is known to enhance translation inhibition of FMRP-bound mRNAs. I show ER stress-induced activation of Inositol requiring enzyme-1 (IRE1), an ER-resident stress-sensing kinase/endoribonuclease, leads to FMRP phosphorylation and to suppression of macrophage cholesterol efflux and apoptotic cell clearance (efferocytosis). Conversely, FMRP-deficiency and pharmacological inhibition of IRE1 kinase activity enhances cholesterol efflux and efferocytosis, reducing atherosclerosis in mice. The results presented in my thesis provide mechanistic insights into how ER stress-induced IRE1 kinase activity contributes to macrophage cholesterol homeostasis and suggest IRE1 inhibition could be developed as a promising new therapeutic strategy to counteract atherosclerosis.

Keywords: ER stress, Kinase-substrate, Signaling, Cholesterol homeostasis, Efferocytosis, Atherosclerosis**.**

ÖZET

LİPOTOKSİK STRES YANITINDA IRE1'İN YENİ SUBSTRATININ TANIMLANMASI

Zehra YILDIRIM
Moleküler Biyoloji ve Genetik, Doktora
Tez Danışmanı: Ebru ERBAY
Şubat, 2022

Kalıtsal zihinsel engellilikteki rolüyle yaygın olarak bilinen Fragile X Mental Retardation proteini (FMRP), seçili mesajci ribonükleik asitlerin (mRNA) translasyonunu kontrol eden bir rıbonükleik asit (RNA) bağlanan proteindir (RNA binding protein; RBP). Bu çalışmada endoplazmik retikulum (ER) stresinin, FMRP'ye bağlı mRNA'ların translasyon inhibisyonunu arttırdığı bilinen bir bölgede FMRP'nin fosforilasyonunu indüklediğini keşfettim. ER'de yerleşik bir stres algılayıcı kinaz/endoribonükleaz olan İnositol Gerektiren Enzim 1 (IRE1)'in ER stres kaynaklı aktivasyonunun, FMRP fosforilasyonuna ve makrofaj kolesterol akışının ve apoptotik hücre temizlenmesinin (efferositoz) baskılanmasına yol açtığını gösterdim. Sonuç olarak, FMRP eksikliği ve IRE1 kinaz aktivitesinin farmakolojik inhibisyonu, farelerde aterosklerozu azaltarak kolesterolün hücreden atılımını ve eferositozu arttırdığını gösterdim. Bu çalışma, ER stresinin neden olduğu IRE1 kinaz aktivitesinin makrofaj kolesterol dengesine nasıl katkıda bulunduğuna dair mekanik bilgiler sağlarmakta ve aterosklerozu önlemenin umut verici yeni bir yolu olarak IRE1 inhibisyonunu önermektedir.

Anahtar sözcükler: ER stress, Kinaz-substrat, Sinyal yolaklari, Kolesterol dengesi, Eferositoz, Aterosikleroz

To my precious family…

Acknowledgements

I would like to thank first and foremost to my thesis advisor, Dr. Ebru Erbay for her mentorship and guidance. I am grateful for the freedom she has given in the lab and help me set my path to becoming an independent researcher.

I appreciate the help and scientific contribution of my thesis committee members Dr. Hasan Tayfun Özçelik and Dr. Michelle Marie Adams. I would like to thank Dr. Erkan Yılmaz and Dr. Çağdaş Devrim Son for guidance, support during my dissertation and for their contribution as members of my thesis jury.

I would like to thank to my ex- and current lab mates; Dr. Özlem Tufanlı, Dr. İnci Şimşek, Dr. Syed Hamid, Dr. İsmail Çimen, Dr. Begüm Kocatürk, Aslı Doğan, Aslı Dilber Yıldırım, Zehra Veli and Dr. Kikkie Poels for sharing their knowledge, support, and friendship.

I would like to express my appreciation to Dr. Peter Walter (University of California, San Francisco) for his valuable contribution to this project and WT-Ire1-pcDNA3, and Kinase-dead IRE1 mutant (K599A)-pcDNA3 plasmids. Dr. Jennifer C. Darnell (The Rockefeller University, New York) for providing and guiding with Fmr1 plasmid and to Dr. Roberta Gottlieb and Dr. Juliana Germano (Cedars-Sinai Medical Center) for their guidance with polysome profiling.

I would like thank Dr. Moshe Arditti, Dr. Roberta Gottlieb, and Dr. Honit Piplani for their help, support and encouragement in finding my post-doc position.

I would also like to thank Dr. Fotis Nicolos for sharing his knowledge and contributing to this thesis. I'm grateful for his support, friendship and jokes that cheer us up when we most need it!

I express my deepest appreciations to Aslı Doğan for her friendship and support in lab and in life. We came through the most difficult steps of PhD together and we made it together until the end…

I am eternally grateful to my big family; my husband Kadir, my parents Satı, Rıza, my sisters Nilgün, Ayşe and her husband Mehmet, my brother Engin and his wife Şennur for encouraging, supporting, and loving me unconditionally. I'm very lucky to have the best in love family, which are as valuable as my own family; my mother in love Halide, father in love Halil, sister in love Gökşen and her husband Kadir. I'm the luckiest aunty in the world to have four beautiful nieces: Zeynep Elif, Ela, Derin, and the most handsome nephew Ayaz. You are the suns and the moon of my life. You give me the joy and all the positive energy that I need to keep going.

There aren't any enough words to express my love and gratitude to my sister Ayşe and my parents. They are the foundation of my strength and success. I'm the luckiest person in the world to have all of you in my life. Mom; thank you for your endless love, support and giving me the best sister ever. My sole, best friend, and sister; thank you for being the best. Your love is all I need to get through any challenge. Thank you for always knowing what's in my heart. I never fell alone with you and your beautiful children Zeynep and Ayaz in my life.

And finally, I want to thank my truly amazing husband Kadir. He has always supported me as I followed my ambitions, even when it meant be away from each other for years. I can never thank him enough for always being there to encourage, love and cheer up.

This PhD. is dedicated to my husband, Kadir, for his never-ending support and love.

CONTENTS

LIST OF FIGURES

LIST OF TABLES

ABBREVIATIONS

ABCA1	ATP-Binding Cassette (ABC) Transporters Subfamily A Member-1
ABCG1	ATP-Binding Cassette (ABC) Transporters Subfamily G Member-1
AC	Apoptotic Cell
ACAT	Acetyl-Coa Acetyltransferases
acLDL	Acetylated Low-Density Lipoprotein
ADAR	Adenosine Deaminase
ag-LDL	Aggregated LDL
APOA-1	Apolipoprotein A1
Apoe	Apolipoprotein E-Deficient
ATF6	Activating Transcription Factor 6
ATP	Adenosine Triphosphate
BIP; KAR2	Binding Immunoglobulin Protein
BMDM	Bone Marrow-Derived Macrophages
CD36	Platelet Glycoprotein 4
CD47	Integrin-Associated Signal Transducer
cDNA	Complementary Deoxyribonucleic Acid
ChroM	Chromatin Modifying Enzymes
CVD	Cardiovascular Disease
DAPI	4',6-Diamidino-2-Phenylindole
DDR	DNA Damage Response
DMSO	Dimethyl Sulfoxide
ECL	Enhanced Chemiluminescence
EDTA	Ethylenediaminetetraacetic Acid
ELISA	The Enzyme-Linked Immunosorbent Assay
ER	Endoplasmic Reticulum
ERAD	Er Associated Degradation
ERP57	Endoplasmic Reticulum Resident Protein 57
FACS	Fluorescence-Activated Cell Sorting
FACS	Fluorescence-Activated Cell Sorting
FBS	Fetal Bovine Serum
FMRP	Fragile X Mental Retardation Protein
FXPOI	Fragile X-Associated Primary Ovarian Insufficiency
FXS	Fragile X Syndrome
FXTAS	Fragile X-Associated Tremor/Ataxia Syndrome
GAPDH	Glyceraldehyde-3-Phosphate Dehydrogenase
GLUT1	Glucose Transporter
HDL	High-Density Lipoprotein
HEPES	4-(2-Hydroxyethyl)-1-Piperazineethanesulfonic Acid
HILAQ	Heavy Isotope Labeled Azidohomoalanine Quantification
HMGCR	3-Hydroxy-3-Methylglutaryl Coenzyme A Reductase

HSP90	Heat Shock Protein 90kda Beta
IFN	Type I Interferon
IL	Interleukin
IP	Intraperitonel
IRE1	Inositol-Requiring Enzyme-1
ISR	Integrated Signal Response
KH1	K Homology 1
KH2	K Homology 2
LAL	Lysosomal Acid Lipase
LCAT	Lecithin-Cholesterol Acyltransferase
LDL	Low Density Lipoprotein
LDLR	Low Density Lipoprotein Receptor
LP	Lipoprotein
LPS	Lipopolysaccharide
LRP1	Ldl Receptor Related Protein 1
LXR	Liver X Receptor
MEF	Mouse Embryonic Fibroblasts
MerTK	Mer Proto-Oncogene Tyrosine Kinase
MFM	Methylated Full Mutation
MOMA	Monocyte/Macrophage Marker Antibody
mRNA	Messenger RNAs
MUFA	Mono-Unsaturated Fatty Acids
NADH	Nicotinamide Adenine Dinucleotide + Hydrogen
NADPH	Nicotinamide Adenine Dinucleotide Phosphate
NES	Nuclear Export Signal
NLS	Nuclear Localization Signal
oxLDL	Oxidized Low-Density Lipoprotein
PBS	Phosphate Buffer Saline
PDI	Protein Disulfide Isomerase
PEI	Polyethylemine
PERK	Protein Kinase Rna-Like Er Kinase
PI	Propidium Iodide Solution
PM	Peritoneal Macrophages
PNBM	P-Nitrobenzyl Mesylate
PPAR	Peroxisome Proliferator-Activated Receptor
PS	Phosphatidylserine
PUFA	Poly-Unsaturated Fatty Acids
RAC1	RAS-Related C3 Botulinum Toxin Substrate 1
RBM14	RNA-Binding Protein 14
RBP	RNA Binding Protein
RCT	Reverse Cholesterol Transport
RGG box	Arg-Gly-Gly Sequences

RNA	Ribonucleic Acid
RT-PCR	Reverse Transcriptase Pcr
SFA	Saturated Fatty Acid
SGK1	Serum/Glucocorticoid Regulated Kinase 1
siRNA	Small Interfering Rna
SM	Squalene Monooxygenase
SMC	Smooth Muscle Cell
SR-A	Scavenger Receptor Class A
SR-B1	Scavenger Receptor Class B Type 1
SREBP2	Sterol Regulatory Element- Binding Protein 2
sXBP1	Spliced X-Box Binding Protein 1
TBS	Tris-Buffered Saline
TF	Transcription Factors
TG	Thapsigargin
TM	Tunicamycin
TNF	Tumor Necrosis Factor
TUNEL	Terminal Deoxynucleotidyl Transferase Dutp Nick End
UFM	Unmethylated Full Mutation
UPR	Unfolded Protein Response
UTR	Untranslated Region
VSMC	Vascular Smooth Muscle Cell
WD	Western Diet
XBP1	X-Box Binding Protein 1
25HC	25-Hydroxycholesterol
4μ8c	7-Hydroxy-4-Methyl-2-Oxo-2H-1-Benzopyran-8-Carboxaldehyde

Chapter 1 Introduction

1.1 Cardiovascular Diseases

Cardiovascular diseases (CVDs), a group of disorders of the coronary artery diseases and heart failure, are the major health problem across the world [1-5]. Although its management is highly depended on the clinical status of the patients, cardiovascular diseases can be prevented by improving lifestyle and avoiding behavioral risk factors such as obesity, saturated and trans-fat consumption, inactivity, tobacco, and harmful use of alcohol [6, 7]. Replacement of saturated fatty acids with unsaturated fatty acids can help reduce CVD risk [8].

Among CVDs, one of the lead causes of mortality and morbidity is coronary artery diseases [9] with atherosclerosis as the main pathophysiological cause. Atherosclerosis is triggered by imbalanced lipid metabolism that leads to dysregulation and activation of endothelial cell wall, which then initiates the attraction, infiltration, and proliferation of vascular smooth muscle cells (VSMCs), monocytes, leukocytes, and other inflammatory cells. Further stress stimuli, apoptosis, necrosis, and autophagy play critical roles in the progression of atherosclerosis [10]. Despite the efforts towards discovering the factors behind initiation and progression of CVDs, molecular mechanisms of the process remain elusive.

1.1.1 Atherosclerosis

Atherosclerosis is a chronic inflammatory disease with characteristic of gradual accumulation of plaque deposits at the arterial tree [11, 12]. In atherosclerotic plaques, macrophages ingest lipoproteins and transform into lipid-laden foam cells. The foamy macrophages lose their ability to migrate away from the plaques, where they sustain a

local state of sterile inflammation, which occurs in the absence of pathogens and is typically associated with the release of immune-recognizable cellular content from damaged or dying cells [13]. Cholesterol efflux and efferocytosis (engulfment and clearance of apoptotic cells (AC)) by macrophages, on the other hand, help to resolve inflammation and contribute to plaque stability as counterbalancing mechanisms that oppose plaque rupture [14-19].

1.1.1.1 Molecular Mechanisms of Plaque Formation

Unhealthy lifestyle (such as physical inactivity, high fat diet, and obesity) [20, 21], environmental factors (such as solvents, pesticides, and air pollution) [22], disturbed blood flow, imbalanced cholesterol metabolism and oxidized low-density lipoprotein (oxLDL) accumulation or other factors cause intimal inflammation can trigger endothelium activation and/or dysfunction. Activated endothelial cells uptake oxLDL and express adhesion molecules that leads to recruitment of monocytes. These monocytes transmigrate into the sub-endothelium and differentiate into macrophages, to serve as lipid deposits by ingesting the excessive oxLDL and becoming foam cells. Moreover, VSMC migration into the sub-endothelium, where they gain expression of macrophage markers and macrophage like behaviors, also contribute significantly to the plaque formation. This process allows VSMCs to ingest lipids like macrophages and become foam cells. Ultimately, these heavily lipid-loaded cells undergo apoptosis and necroptosis, which are then cleared by macrophages via efferocytosis. Efficient efferocytosis is critical to reduce the apoptotic and primary necrotic cell burden in the plaque area to promote plaque stability. Any disturbance in this process can lead to necrotic core formation due to secondary necrosis of apoptotic foamy cells, contributing to plaque growth and instability. Unstable necrotic core growth can cause the thinning of the fibrous cap and leaving the plaque vulnerable to rupture, which result in thrombosis and trigger acute cardiovascular disease (Fig 1.1) [19, 23-25].

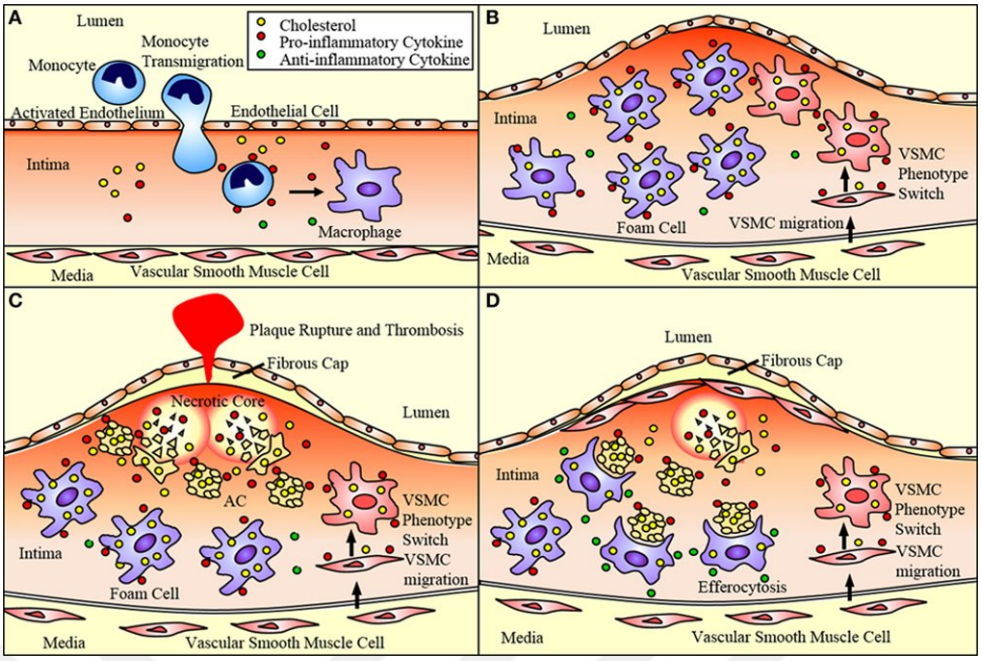

Figure 1.1. Schematic representation of plaque formation in arterial walls.

(A) Monocytes are recruited by the activated endothelial cells expressing adhesion molecules. These monocytes transmigrate into the intima, where they differentiate into macrophages. (B) Macrophages and differentiated macrophage-like VSMCs ingest oxLDL and become foam cells. (C) Lipid-laden foam cells ultimately undergo primary and secondary apoptosis, which needs to be cleared by M2 macrophages to avoid plaque rupture and thrombosis. (D) Extracellular matrix components secreted from VSMCs induce fibrous cap formation help maintain the plaque. Moreover, M2 macrophages secrete anti-inflammatory markers to resolve inflammation and clear dying cells to stabilize the plaque [19].

The connective tissue within the lesion gradually loses its arterial intimal thickening that leads to the replacement of fibrocellular tissue by collagen rich fibrous tissue, which often expends to become one of the major components of the advanced plaque. Inflammatory cytokines secreted from macrophages, increased cholesterol accumulation, lipotoxicity and apoptotic cells within the lesion area contribute to early stages of calcification progression. Spotty calcification caused by inflammation, increases inflammatory burden and result in a larger necrotic core with less collagen content. As calcification progresses, VSMCs differentiate into bone-like chondrocyte- and osteoblast-like cells, that release proteins to regulate calcification and matrix mineralization. Consequently, spotty micro-calcifications turn into late-stage macro-calcification, which contributes to plaque rupture [26-28].

There is a complex interaction between recruitment of inflammatory cells, foam cell formation, apoptosis, necrosis, calcification, fibrous cap rupture and thrombosis. Each process has its importance in the plaque progression leading to acute thrombosis that could result in acute coronary syndrome.

1.2 Cholesterol Homeostasis

Unbalanced cholesterol homeostasis can lead to numerous diseases, where cholesterol plays critical roles such as cancer, neurodegenerative and cardiovascular diseases. Increased plasma cholesterol is one of the major drivers of plaque formation and atherosclerosis, which is tightly regulated by series of pathways. Maintaining the cellular cholesterol level is a complex process, regulated by the balance between de novo biosynthesis, uptake, export, and esterification. (Fig 1.2) [29-31].

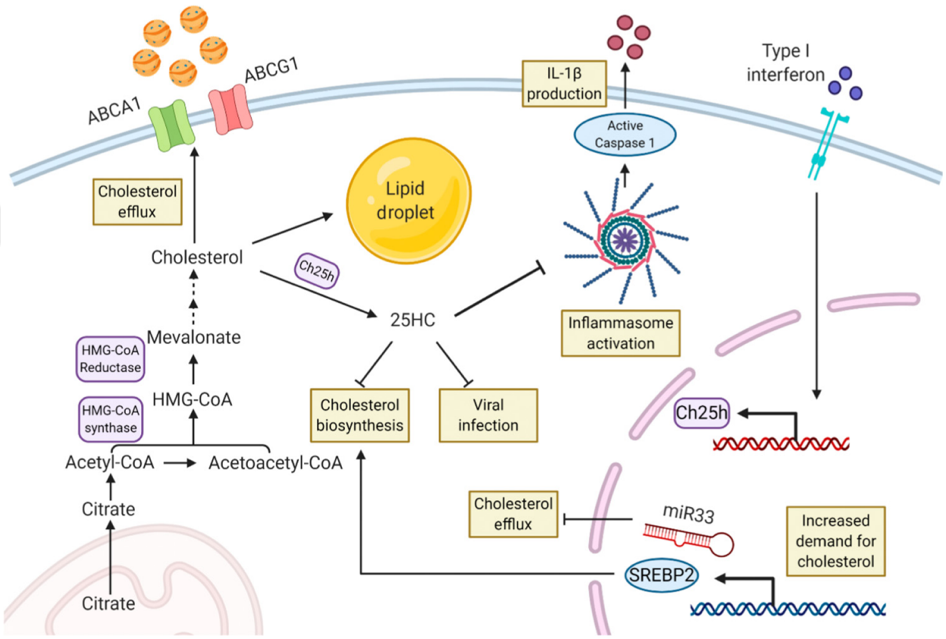

Figure 1.2. Cholesterol metabolism pathways in macrophages.

Increased cholesterol demand induces sterol regulatory element binding transcription factor 2 (SREBP2) and miR-33 to promote cholesterol biosynthesis and suppress efflux. Depending on metabolic needs of the cell, cholesterol synthesized from acetyl-CoA can either be stored in lipid droplets, esterified, or removed from the cell via reverse cholesterol transport (RCT) by transported mediated efflux through Adenosine triphosphate (ATP)-binding cassette transporters (ATP binding cassette subfamily A member 1, ABCA1 and ATP binding cassette subfamily G member 1, ABCG1). Type I interferon (IFN) signaling pathway produce 25-Hydroxycholesterol (25HC), that blocks cholesterol biosynthesis and inhibits inflammasome activation and viral infections [32].

1.2.1 Dietary Fat and Cholesterol

Plasma lipoprotein levels, as well as cellular cholesterol uptake and efflux mechanisms are modulated by the degree of dietary saturated fatty acid intake [33]. saturated dietary fatty acids (SFAs) have been suggested to regulate cholesterol homeostasis by inducing ER stress pathways, which induce cholesterol uptake, block cholesterol efflux, and activate inflammatory response [33, 34]. Moreover, excessive lipid accumulation in the ER membrane is sensed by transmembrane domains of the ER stress sensors, which determines the stress response [35, 36]. SFA has been shown to induce IRE1 oligomerization and activation [35].

Replacement of dietary SFA with mono-unsaturated (MUFA) or poly-unsaturated (PUFA) dietary fatty acids can help reduce CVD risk [8]. Unsaturated fatty acids shown to improve atherosclerosis by preventing most SAF-mediated deleterious effects associated with blocking inflammation, reducing foam cell formation and necrotic core formation in atherosclerotic plaques [35, 37, 38].

1.2.2 Cholesterol biosynthesis

Cholesterol is an essential constituent of mammalian cell membranes [39]. De novo cholesterol biosynthesis, namely mevalonate pathway, starts from acetyl-CoA through a series of around 30 reactions. The key regulator of the mevalonate pathway is SREBP2 and the rate limiting enzymes are 3-hydroxy-3-methylglutaryl coenzyme A reductase (HMGCR) and squalene monooxygenase (SM). This tightly regulated process requires acetyl-CoA, ATP, oxygen, and the reducing factors nicotinamide adenine dinucleotide phosphate (NADPH) and nicotinamide adenine dinucleotide + hydrogen (NADH) (Luo et al., 2020). Briefly, cholesterol synthesis is composed of the following steps (a) synthesis of mevalonate from acetyl-CoA (b) formation of isoprenoid units from mevalonate by loss of CO_2 (c) condensation of six isoprenoid units form squalene (d) cyclization of squalene give rise to the parent steroid, lanosterol and (e) formation of cholesterol from lanosterol [31, 40, 41]

1.2.3 Cholesterol Uptake

Cholesterol uptake is a biologic process, where modified low-density lipoproteins (LDLs) (such as acetylated low-density lipoprotein (acLDL) and oxLDL) are ingested by polarized cells via phagocytosis, pinocytosis (a receptor-independent endocytic pathway) or receptor mediated pathways [42]. Receptor-mediated cholesterol uptake from plasma lipoproteins is a less energy consuming alternative process to the de novo biosynthesis. Polarized cells (such as macrophages, enterocytes or hepatocytes) can carry cholesterol via low-density lipoprotein receptor (LDLR)-mediated uptake of cholesterol containing LDL particles, Scavenger receptor class B type 1 (SR-B1)-mediated selective uptake of cholesterol-rich high-density lipoproteins, HDL, scavenger receptor class A (SR-A), CD36 (also known as fatty acid translocase, FAT) and lectin-like oxLDL receptor-1 (LOX-1) mediated uptake of ox-LDL to meet their metabolic requirements [31, 43-45].

LDLR functions to internalize LDL at the cytosolic side of the cell membrane by endocytosis process followed by hydrolyzation of apoproteins and cholesteryl esters in the lysosomes. Upon the delivery of LDL particles, receptors are recycled to the cell surface. This cholesterol uptake process creates negative feedback to block the transcription of the genes (via the SREBP pathway) involved in cholesterol synthesis, including the LDLR itself, and ergo suppresses both cholesterol uptake and synthesis [46]. Recently, proprotein convertase subtilisin/kexin type 9 (PCSK9) has been shown to moderate LDLR recycling to the cell surface by targeting its degradation. LDLR activity and translocation is tightly regulated by the membrane cholesterol levels, steroid hormones, bile acid synthesis, and the cholesterol levels of the cell [40].

In macrophages, SR-A and CD36 perform nearly 75% to 90% of the lipoprotein-derived cholesterol uptake, which make them the most two important transporters in macrophages to regulate cholesterol uptake. Both receptors are highly expressed and therefore their transcription is tightly regulated in macrophages [44, 47]. Beside its major role in modified LDL binding, CD36 has multiple functions in efferocytosis, inflammation, lipid metabolism, fatty acid transport, immunity [48] and migration of macrophages upon oxLDL stimulation and contribute to macrophage recruitment to arterial lesions [49].

1.2.4 Cholesterol Efflux

HDLs provide protection against to the development of atherosclerosis via several activities, that are related to cholesterol transport, anti-inflammatory, endothelial and vascular functions. Cholesterol efflux by plaque macrophages is the first step in a multi-step process, referred to as “reverse cholesterol transport” (RCT), that reduces lipid accumulation in plaques [50, 51]. Macrophages efflux intracellular cholesterol using their plasma membrane cholesterol transporters; ABCA1, ABCG1 and as well as by SR-B1, in a bidirectional ATP-independent pathway. Lipid-poor Apolipoprotein A1 (Apo-A1) receive free cholesterol from ABCA1, whereas cholesterol efflux to high-density lipoprotein (HDL) particles is facilitated by ABCG1 and SR-B1 transporters. Lecithin-cholesterol acyltransferase (LCAT) esterifies the free cholesterol within the HDL particles and generate mature HDL and eventually mediate delivery of cholesterol to the liver for excretion. The liver takes up mature HDL through SR-B1 transporter and excretes HDL into the bile as free cholesterol or as bile acids. (Fig 1.3) [52-55].

The cholesterol efflux pathway is transcriptionally activated by the metabolic by-products of AC-derived cholesterol in the efferocytic macrophages. As such, efferocytosis and RCT synergize to reduce necrosis and resolve inflammation in plaques [56-60].

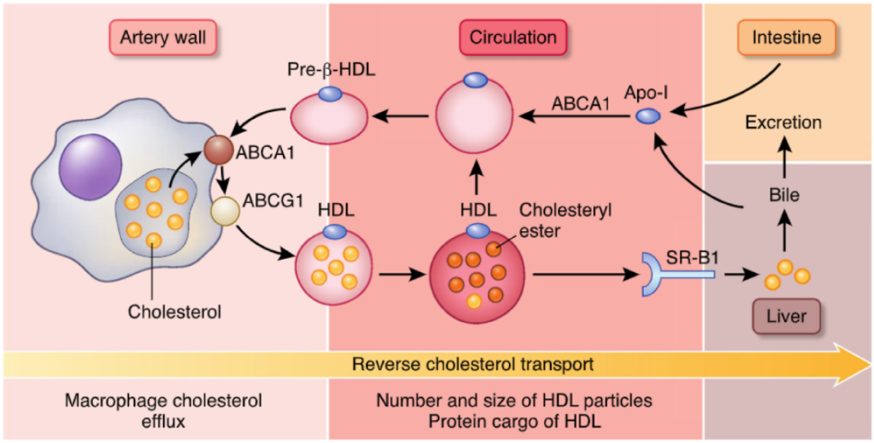

Figure 1.3. Cholesterol efflux by macrophage

ApoA-I receives cholesterol from macrophages on the artery wall, through ABCA1 receptor, forming the immature form of HDL (pre-β HDL). HDL then accepts cholesterol through ABCG1, esterifies the cholesterol and form mature HDL. By the reverse cholesterol mechanism HDL circles to liver and binds to SR-B1 receptor, where its converted back to cholesterol or bile acids for excretion [55].

1.2.5 Cholesterol Esterification and Foam Cell Formation

Cholesterol esterification is one of the main mechanisms to avoid the excessive cytotoxic free cholesterol accumulation. Regulation of cholesterol esterification is mediated by acetyl-CoA acetyltransferases (ACAT), which directs cholesterol for secretion or storage. Upon uptake, modified LDL is transported to the late endosome/lysosomes, where the cholesteryl esters are further hydrolyzed into free cholesterol and free fatty acids by lysosomal acid lipase (LAL) [61-64]. To prevent cytotoxicity, free cholesterol is either re-esterified by ACAT at the ER and stored in lipid droplets or released by transporter-mediated efflux. Excessive accumulation of cholesteryl esters in macrophages and VSMCs lead to foam cell formation [65]. Therefore, cholesterol esterification and transporter-mediated efflux are critical processes for maintaining the cholesterol homeostasis, representing promising therapeutic targets to prevent atherosclerosis progression and initiate regression pathway [64].

1.3 Efferocytosis

The efferocytosis process is a key step for the maintenance of tissue homeostasis. This process is performed by professional phagocytes, such as monocytes, macrophages, and dendritic cells, and by non-professional phagocytes such as epithelial cells [66].

During the early stages of atherogenesis, macrophages undergo apoptosis due to increased uptake of modified LDL and other cellular debris in the arterial wall. Atherosclerotic lesions contain professional phagocytes, which engulf these apoptotic cells to maintain plaque stability. Efficient efferocytosis is associated with reduced atherosclerosis progression, most likely due to reduced pro-inflammatory and induced anti-inflammatory mediators presented in the artery wall [67, 68]. However, excessive efferocytosis can induce ER stress and unfolded protein response (UPR) due to increased free-cholesterol and oxidized lipoproteins, which induces apoptosis in these stressed macrophages. Failure to remove apoptotic cells is one of the major causes in initiation of the atherosclerotic plaque formation. These cells may undergo ‘secondary necrosis’, where macrophages die and release their cellular contents. Oxidized lipids, pro-inflammatory mediators and cell debris, exaggerate the inflammatory response, eventually lead to the development of a necrotic core [69]. Thus, the critical balance

between apoptosis, efferocytosis, and secondary necrosis determines the faith of atherosclerosis progression and severity [17, 66].

Macrophages can bind to molecules such as phosphatidylserine (PS), that act as 'eat me' signal that are expressed on the dying cells. These molecules are recognized by the receptors like MER Proto-Oncogene Tyrosine Kinase (MerTK), Integrin, CD36 and SR-B1 on macrophages and initiate the engulfment of the apoptotic cell. This interaction result in activation of RAC1 and actin reorganization as well as peroxisome proliferator-activated receptors (PPARs) and liver X receptor (LXR) signaling, which result in the upregulation of efferocytosis receptors for continued efferocytosis and proteins involved in cholesterol efflux to promote an anti-inflammatory M2 macrophage phenotype (Fig 1.4) [19].

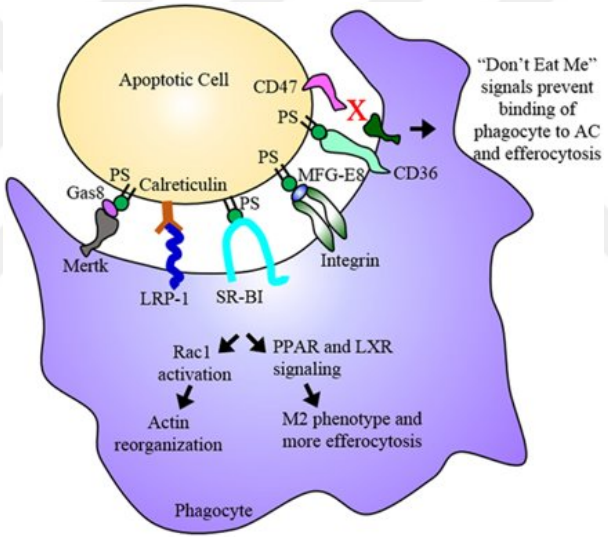

Figure 1.4. Apoptotic cell clearance by macrophages

'Eat me' signals (such as PS and calreticulin) expressed on apoptotic cells are recognized by efferocytosis receptors expressed on professional phagocytes. Upon binding to macrophages activate RAS-related C3 botulinum toxin substrate 1 (Rac1), PPAR and LXR pathways that initiate the engulfment and digestion of the apoptotic cell [19].

AC-derived cargo, including the free cholesterol, sterols, and other inflammatory cytokines, needs to be cleared to prevent cytotoxicity. Efflux of the free cholesterol is induced through LXR pathway that induce ABCA1-mediated transport to prevent its accumulation. The fatty acids are oxidated in mitochondria and upregulate the of

expression of pro-resolving Interleukin (IL)-10. Lastly PS lead to upregulation of glucose transporter (GLUT1) and serum/glucocorticoid regulated kinase 1 (SGK1). Upregulation of these genes accelerate intake of glucose that is required for dynamic actin rearrangement to engulf apoptotic cells [70-72].

1.4 Endoplasmic Reticulum Stress and Unfolded Protein response

Endoplasmic reticulum, a highly dynamic organelle, is composed of membrane networks responsible for various functions such as synthesis, quality check, repair, and transportation of proteins. ER is classified in two functionally distinct forms called smooth ER and rough ER (coated by ribosomes the surface of the ER). Ribosome-mRNA complexes positioned on ER membranes, engage protein synthesis simultaneously translocating them into the ER. The proteins synthesized by these ribosomes are mostly secrete molecules such as digestive enzymes, hormones, receptors and signaling molecules. Beside the ER membrane bound ribosomes, there are unattached/free ribosomes located in the cytoplasm, that synthesize proteins used within the cell. These proteins are folded by the mechanism called 'co-translational folding' and transported to other organelles such as nucleus, mitochondria, or peroxisomes (Fig 1.5) [73-75].

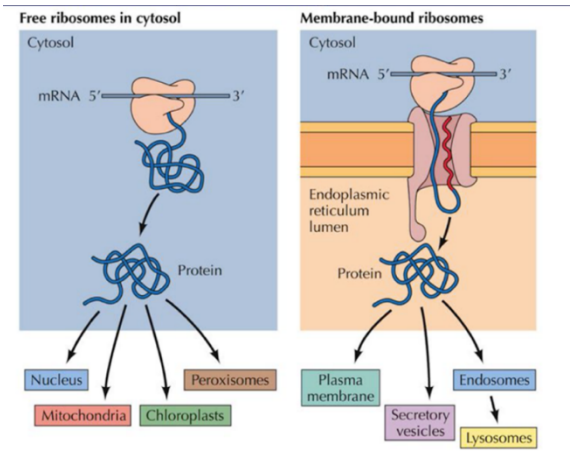

Figure 1.5. Free and membrane-bound ribosomes.

Proteins can be transported to ER by either post-translocation (via their ER-signal sequence) or co-translational translocation, where they are simultaneously translocated into the ER while being synthesized. Proteins synthesized in free ribosomes in the cytoplasm are usually transported to the organelles within the cells. On the other hand, proteins synthesized in the membrane bound ribosomes are usually secreted [73].

Chaperons are responsible for quality control and repair of unfolded and misfolded proteins within the ER due to variety of cell stress. Binding Immunoglobulin Protein (BIP; KAR2), Endoplasmic Reticulum Resident Protein 57 (ERP57), Heat Shock Protein 90kDa Beta (GRP94; GP96; HSP90), Protein Disulfide Isomerase (PDI), and Calreticulin are some of the mostly expressed ER resident chaperons [76-82].

Physiological and environmental factors such as genetic abnormalities, oxidative stress, viral infection, disturbed Ca^{2+} homeostasis, accumulation of free cholesterols or obesity or aging can lead to increased protein synthesis, which leads to accumulation of unfolded and misfolding proteins that exceed ER's folding capacity. This evet evokes a pathway called UPR, that is initiated at ER's membranes and aims to re-establish homeostasis. UPR is comprised of three branches; the activating transcription factor 6 (ATF6), protein kinase R- like ER kinase (PERK), and IRE1 [83]. UPR activation leads ER resident chaperones to dissociate from ER stressors to engage with unfolded proteins, which activate downstream UPR pathways (Fig 1.6) [84].

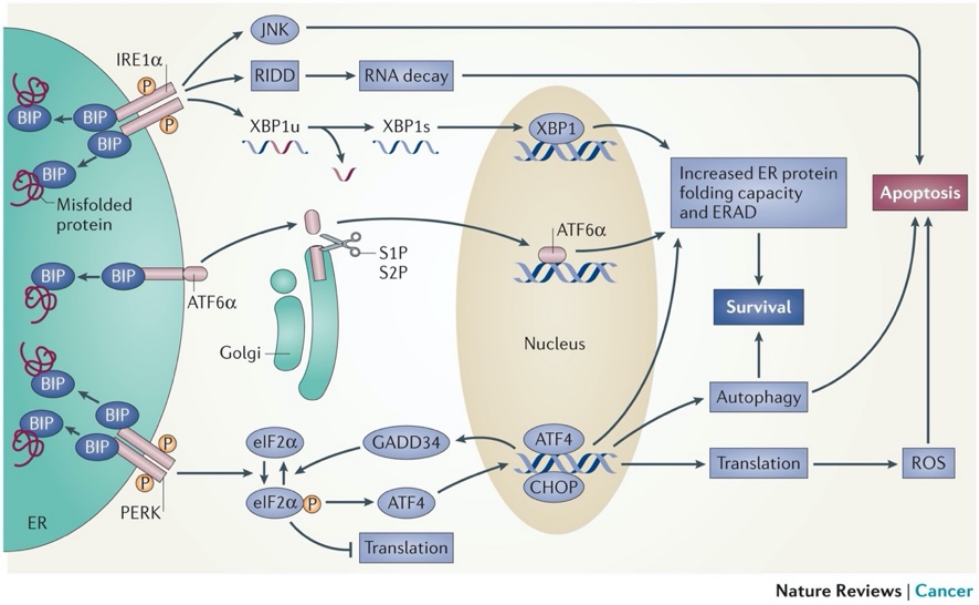

Figure 1.6. UPR signaling pathways.

UPR triggered by protein folding stress cause disassociation of BIP from the UPR signaling branches (IRE1- X box protein-1 (XBP1), PERK- Eukaryotic Initiation Factor 2 (EIF2α) and ATF6). Depending on the unfolded/misfolded protein load, UPR activation can lead to ER-associated protein degradation (ERAD) and attenuation of protein synthesis to promote cell survival or initiate apoptosis due to unresolved UPR signaling [84].

Accumulation of excessive free cholesterol in the ER membrane, pro-inflammatory cytokines, modified LDL and HDL may cause accumulation of unfolded proteins, where the key players are activated to launch pro-inflammatory response and disturb cholesterol homeostasis, which may in turn cause foam cell formation (Fig 1.7). Depending on the duration and dose of stress, ER activates transcriptional or translational processes via its stress sensors, determining the faith of the cell to either reestablish homeostasis or initiate apoptosis [85].

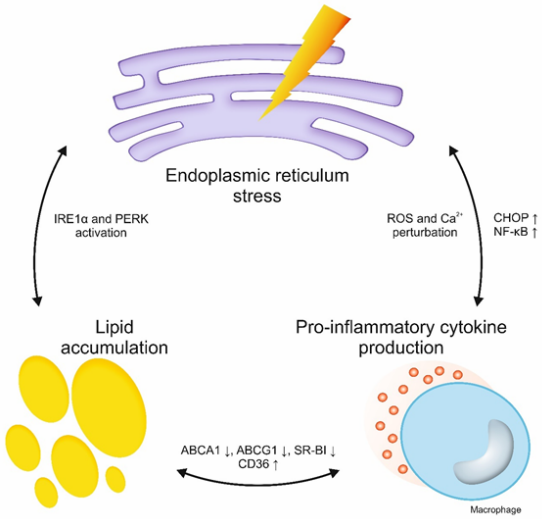

Figure 1.7. Relationship between lipid accumulation, pro-inflammatory response, and ER stress.

ER stress triggered by lipid accumulation triggers ER stress that leads to proinflammatory cytokine release. Cytokines can cause lipid accumulation through upregulation of CD36 and/or downregulation of ABCA1, ABCG1, and SR-B1, in return trigger further ER stress [85].

1.4.1 IRE1

As one of the major UPR regulator, IRE1 has dual protein kinase and endoribonuclease activities. Metazoans have two IRE1 paralogues, IRE1α (referred to as IRE1) and IRE1β. While IRE1α is ubiquitously expressed, IRE1β expression is restricted to gastrointestinal epithelium [86]. To date, IRE1 has been described to *trans*-autophosphorylate as a first step in the activation of its RNase modality, which initiates a non-conventional RNA splicing reaction and the production of the transcription

factor known as spliced X box protein-1 (XBP1s), which is one of the key drivers of the UPR [87-89].

IRE1 senses both folding stresses induced by unfolded protein accumulation and lipid bilayer stress on the ER membrane caused by accumulation of cholesterol or SFA. Lipid loading on the membrane bring IRE1 proteins in close proximity, where they can autophosphorylate each other (Fig 1.8) [85, 90]. While previous studies have shown that ER stress and subsequent IRE1 activation are causally associated with atherosclerosis progression, the mechanism by which IRE1 kinase domain contributes to the disease pathogenesis has remained elusive [91-93].

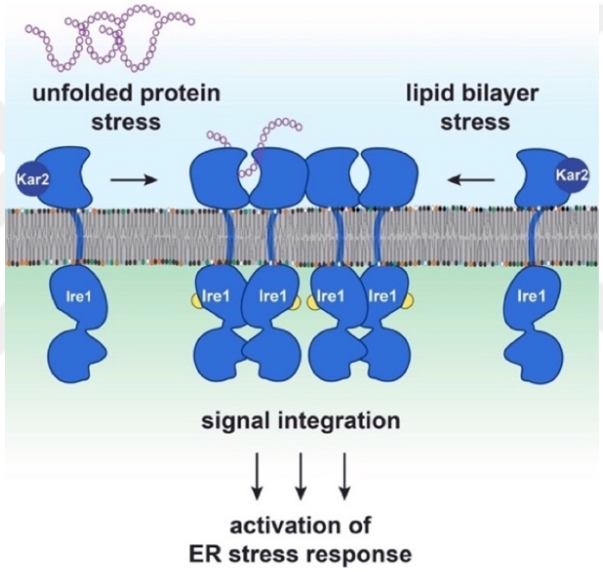

Figure 1.8. IRE1 activation.

Recent evidence has shown that lipid accumulation in ER membrane, can trigger lipid bilayer stress that activates UPR through its most conserved arm, IRE1 [94].

Despite its well characterized RNase domain, to date IRE kinase substrates remain unknown. The discovery of IRE1 kinase substrates will provide crucial information that can explain the contribution of this of this ancient transmembrane ER-stress sensor to many diseases where ER stress has been implicated [94].

1.5 Fragile X Mental Retardation Protein

FMRP is an RNA binding protein that its loss of function characterized by the Fragile X syndrome (FXS). FXS is the first genetic disorder that demonstrated RNA regulation in human cognitive function [95]. To date, FXS has been determined as the most common inherited form of intellectual disability, defined by developmental problems such as abnormal dendritic spines, childhood seizures and autistic behaviors [96, 97].

FMR1 gene contains 17 exons, that generate 12 different isoforms of FMRP protein through alternative splicing [98]. The FMR1 locus on Chromosome X, includes a methylated region, the promoter region, CGG stretch and the coding sequence [99]. Based on the expansion of polymorphic CGG repeat located in the 5′ UTR of exon 1, different classes of alleles are described as; (1) normal: 5–55 CGGs, (2) permutated (PM): 56–200 CGGs with a higher transcription, or decreased translation associated to the fragile X-associated tremor/ataxia syndrome (FXTAS) and fragile X-associated primary ovarian insufficiency (FXPOI) phenotypes; (3) full mutation: over 200 CGGs that result in unmethylated full mutation (UFM, similar to PM without an apparent phenotype or methylated full mutation (MFM) that leads to absence of both transcript and protein, and consequently cause FXS phenotype (Fig 1.9) [100].

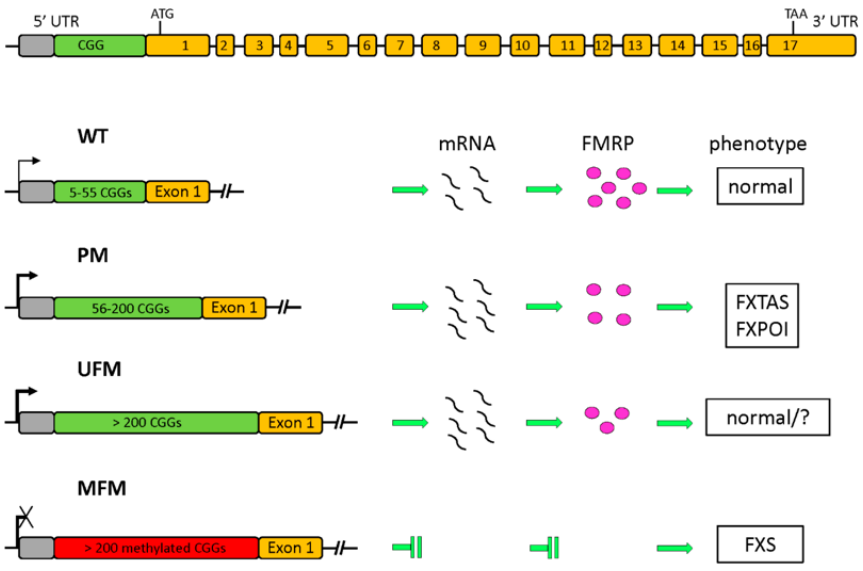

Figure 1.9. FMR1 gene and its allelic forms.

Structure of the Fmr1 gene. Polymorphic CGG sequence is located upstream in the 5′UTR. Different outcomes are displayed depending on the expansion of CGG repeat as normal, FXTAS/FXPOI, and FXS [100].

FMRP is a multifunctional polyribosome-associated RNA-binding protein, which presents four RNA binding domains, N-terminus, K homology 1 (KH1), K homology 1 (KH2), Arg-Gly-Gly sequences (RGG box) as well as a functional nuclear export signal (NES) and a nuclear localization signal (NLS) domain (Fig 1.10). FMRP can directly bind to a guanine (G)-rich sequence within the 3'-untranslated region (UTR) of mRNA to regulate mRNA stability [101, 102].

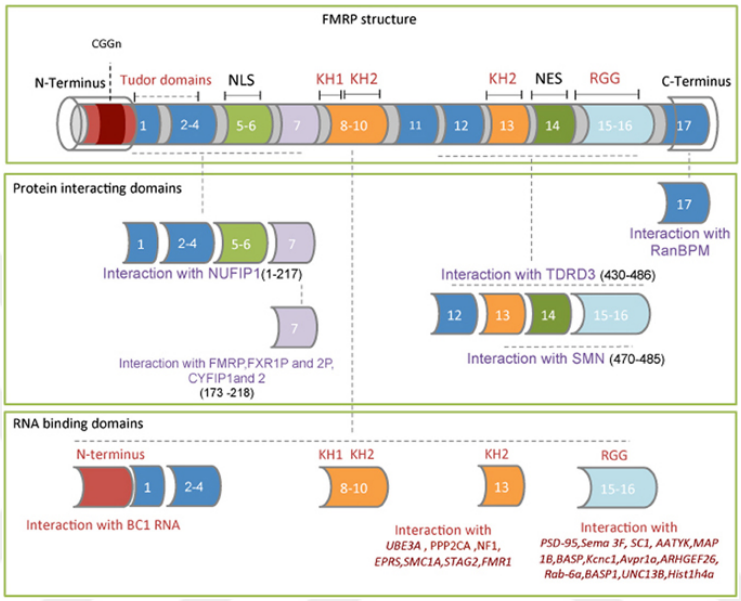

Figure 1.10. FMRP protein functional domains

FMRP has both RNA and protein binding domains. Direct RNA binding domains are well-defined as N-terminus, KH1, KH2 and RGG box, whereas protein binding domains (shown in the middle frame) are shown to bind NUFIP1, CYFIP1, CYFIP2, FXR1P, FXR2P, TDRD3, and SMN proteins [103].

FMRP functions to regulate neurodevelopment, synapse maturation, refinement, and plasticity [104]. Beside its essential role in translational repression by polysome stalling (Fig 1.11) [105, 106], FMRP has been identified to endure distinct roles in different compartments of the cell such as; in cytosol FMRP shuttle mRNAs to/from the nucleus with its nuclear export function [107], in nucleus FMRP binds chromatin during the DNA damage response (DDR) to regulate genome stability [108] and histone modification [109].

FMRP is proposed to regulate multiple RNA processes such as mRNA editing, pre-mRNA splicing, and in the microRNA pathways in association with RNA-editing

enzymes and RNA binding proteins like adenosine deaminase (ADAR) and RNA-binding protein 14 (RBM14) respectively [106, 110-114].

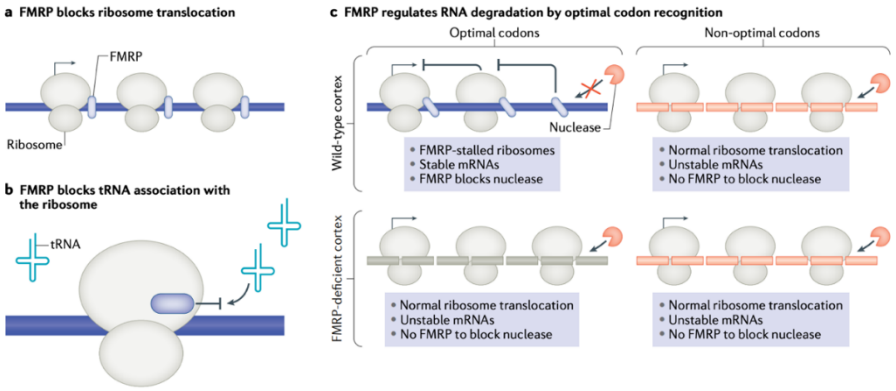

Figure 1.11. FMRP-mediated translational regulation by ribosome stalling.

Several mechanisms where FMRP is proposed to regulate translation in association with ribosomes. (a) blocking ribosome translocation, (b) transfer RNA (tRNA) association with ribosome, (c) blocking RNA degradation by blocking nuclease [106].

Transcriptional and post-transcriptional regulation play critical roles to set sterile inflammation in motion but also in its resolution and, eventually, plaque regression. Post-transcriptional regulatory steps often involve RBPs that interact with mRNA to alter its processing, transport, translation, and degradation. Several RBPs have been shown to alter the mRNA stability and translation of cytokines to turn-off the inflammatory response and key molecular regulators of cholesterol homeostasis and some have been linked to atherosclerosis development (atherogenesis) [115-120]. FMRP is an RBP that has been widely studied in neurons due to its causal role in the FXS [121-123]; however, its role in other cell types and pathways remain elusive.

1.6 Hypothesis and Aims

Atherosclerosis is a chronic inflammatory disease triggered by imbalanced lipid metabolism [11, 12]. In atherosclerotic plaques, macrophages ingest lipoproteins and transform into lipid-laden foam cells. The foamy macrophages lose their ability to migrate away from the plaques, where they sustain a local state of sterile inflammation caused by the release of immune-recognizable cellular content from damaged or dying

cells [13]. Cholesterol efflux and efferocytosis (the engulfment and clearance of AC) by macrophages, on the other hand, help to resolve inflammation and contribute to plaque stability as counterbalancing mechanisms that oppose plaque rupture [14-18]. Previous studies have shown that ER stress and subsequent IRE1 activation are causally associated with atherosclerosis progression [69, 91-93]. IRE1 senses both protein folding stress induced by an accumulation of unfolded proteins in the ER lumen and ER membrane lipid bilayer stress induced by an accumulation of cholesterol or SFA [85, 90]. To date, IRE1 has been described to *trans*-autophosphorylate as a first step in the activation of its RNase modality, which initiates a non-conventional RNA splicing reaction and the production of the transcription factor XBP1s, which is one of the key drivers of the UPR [87-89]. However, IRE1 kinase substrates have not been identified to date [124]. While the contribution of IRE1's RNase activity to atherosclerosis progression was demonstrated in an earlier study, the role of IRE1's kinase activity in atherosclerosis pathogenesis is unexplored [91].

The first aim of this thesis study was the discovery of an IRE1 kinase substrate that could potentially explain the wider role of IRE1 in inflammation and metabolism of immune cells. To this end, the published IRE1 interactome partners were analyzed [125] and due to IRE1's interaction with many FMRP-like proteins, FMRP was hypothesized to be a potential interactor and kinase target of IRE1. In this study, IRE1-FMRP kinase-substrate relationship was confirmed by showing physical interaction between them through co-immunoprecipitation technique and using in vitro and in cell kinase assays. Furthermore, IRE1-kinase dependent, specific phosphosites were discovered by phosphoproteomics analysis.

FMRP is widely studied in neurons for its role in hereditary intellectual disability, however its role in other cell and tissue types remain elusive. Considering FMRP's well known role in translational silencing, I hypothesized that ER stress-induced IRE1-mediated FMRP phosphorylation could target mRNAs involved in cholesterol homeostasis and efferocytosis, where ER stress plays major role. Polysome profiling followed by RNA-Sequencing analysis and Heavy Isotope Labeled Azidohomoalanine Quantification (HILAQ) methods were used to discover the FMRP mRNA targets in

ER stress induced macrophages, that revealed translational suppression of mRNAs involved in cholesterol homeostasis and efferocytosis. Cholesterol uptake, cholesterol efflux, foam cell formation, RCT and efferocytosis assays were performed using FMR1 knockout mouse models and small molecule IRE1 kinase inhibitor to investigate the consequences of disrupting IRE1 kinase-FMRP signaling axis on these processes.

Atherosclerosis progression was investigated using whole body and myeloid-specific Fmr1 knock out mice. In these mice and their appropriate control groups, hypercholesterolemia was induced by the administration of PCSK9-encoding adeno-associated virus (AAV_mPCSK9) followed by feeding with Western diet (WD) for 16 weeks. At the end of the experiment, the composition and size of the mouse aortic root plaques, the extent of atherosclerosis in *en face* aorta and immune cell and lipoprotein profiles (from blood and plasma) were analyzed.

Lastly, the effect of pharmacological inhibition of IRE1 kinase domain (by using AMG-18) was investigated in Apoe$^{-/-}$ mice that were fed with WD for 12 weeks. After 8 weeks, by which time plaque formation has initiated, AMG-18 was intraperitoneally injected into the mice (once or twice daily) to investigate its impact on atherosclerosis progression. Plaque composition of *en face* aorta and aortic root sections as well as immune cell and lipoprotein profiles of the blood samples were analyzed.

CHAPTER 2 MATERIAL AND METHODS

2.1 Materials

2.1.1 Reagents

Reagents used in this study are listed in Table 2.1. Neon transfection system kit (MPK10096) was from Thermo Scientific and used with the Neon electroporation system, also from Thermo Scientific, according to previously published protocols for Bone Marrow-Derived Macrophages (BMDM) [91, 126].

Table 2.1. Reagents.

Reagent	Company	Catalog No
Amersham Prime ECL Western Blotting Detection Reagent	GE Healthcare	RPN2236
Absolute Ethanol	Sigma-Aldrich	32221
Acrylamide %40 solution (acrylamidebisacrylamide)	Biorad	1610146
AMG-18	Tocris	6166
Ammonium Persulfate (APS)	Sigma	A3678
Ampicillin	Sigma	69-53-4
Aqua-Mount	VWR	41799-008
ATP-γ-S	Abcam	ab138911
Bovine Serum Albumin	Santa Cruz	sc23234
CC mount	Sigma	C9368
Cell Staining Buffer	Biolegend	420201
CellTrace™ CFSE cell proliferation kit	Thermo Scientific	C34554
CellTrace™ Violet Cell Proliferation Kit	Thermo Scientific	C34557
Chloroform	Sigma-Aldrich	24216
cholesterol efflux assay kit	Abcam	ab196985
Cholesterol Uptake Assay Kit	Abcam	ab236212
Control siRNA	Thermo Scientific	AM4611

Reagent	Company	Catalog No
Cremophor EL	EMD Millipore	238470
Cycloheximide	EMD Millipore	239763
DC Protein Assay Reagent	Biorad	5000116
Dil-labeled ac-LDL	Kalen Biomedical	770201-7
Dimethyl Sulfoxide (DMSO)	Sigma	D8418
Dulbecco's modified Eagle's Medium (DMEM)	Thermo Scientific	11965084
EDTA	Invitrogen	15575020
ERN1 human recombinant protein	Signalchem	E31-11G
Fatty Acid-Free Bovine Serum Albumin	Sigma	A6003
Fetal bovine serum (FBS)	Thermo Scientific	26140079
Fluoroshield mounting medium with DAPI	Abcam	ab104139
Fmr1 siRNA	Thermo Scientific	AM16708
FMRP human recombinant protein	Origine	TP322699
Formaldehyde	Thermo Scientific	31901
Glycine	Santa Cruz	sc-29096C
HBSS	Gibco	14175095
Hematoxylin	Sigma	HHS32
Hematoxylin and Eosin Stain Kit	Vector Laboratories	H-3502
Kapa 2G fast HS genotyping PCR	BiosystemsSupplier Diversity Partner	NC0597884
L-Glutamine	Thermo Scientific	25030081
Lambda phosphatase	Santu Cruz	sc-200312
Lipofectamine 3000	Invitrogen	L3000001
Lipoprotein-deficient serum	Sigma	S5519
Masson Trichrome	Abcam	04-010802
Methanol	Sigma-Aldrich	32213
Nitrocellulose Transfer Membrane	VWR	27376-991
Optimal cutting temperature compound (OCT compound)	Electron Microscopy Sciences	62550
Oil Red O solution	Sigma	O1391
p-Nitrobenzyl mesylate, PNBM	Abcam	ab138910
Page Ruler Prestained Protein Ladder	Thermo Fisher Scientific	26620
Palmitic Acid (PA)	Sigma	P0500
Penicillin/streptomycin (P/S)	Thermo Scientific	10378016
Phosphatase Inhibitor Cocktail 3	Sigma	P0044
Phosphate buffer saline (PBS)	Thermo Scientific	J67670.AP
Pierce protein G magnetic beads	Thermo Scintific	88848
Polyethylinimine (PEI)	Polysciences	23966
Power-Up-SYBR green	Applied Biosystems	A25742

Reagent	Company	Catalog No
Protease Inhibitor Cocktail EDTA Free	Sigma	P8340-5ML
PVDF Transfer Membrane	Pierce-Thermo Scientific	88518
Revert Aid First strand cDNA synthesis kit	Thermo Scientific	K1691
Roswell Park Memorial Institute (RPMI)-1640 medium	Thermo Scientific	11875093
Sucrose	Sigma	S0389
Thapsigargin (TG)	Santa Cruz	sc-24017A
Thioglycolate solution	Sigma	70157
Tris Base	Sigma	T1503
Trisure	Bioline Bio	38033
TRIsure	Bioline	BIO-38033
Triton X Molecular Biology Grade	Applichem	A1388,0500
Trypsin	Sigma	T4049-100ML
TUNEL	Roshe	11684795910
Tunicamycin	Santa Cruz	sc-3506
Wako Diagnostics total cholesterol E kit	Fujifilm Medical Systems	NC9138103
β-mercaptoethanol	Sigma	M3148-100ML
^{3}H-cholesterol	Perkin Elmer	NET139001MC
4μ8c	Calbiochem	412512
cis-9-Palmitoleic acid	Sigma	P9417
Trans-Palmitoleic acid	Nu-Chek-Prep	

2.1.2 Antibodies

Antibodies used in Immunofluorescence, Fluorescence-activated cell sorting (FACS) analysis and Western blot are listed in Table 2.2.

Table 2.2. Antibodies used in all procedures.

Antibody	Company	Catalog No	Working Conditions
Western Blotting			
anti-pIRE1 (phsopho-S724)	Abcam	ab124945	o/n 4°C
anti-FMRP	Abcam	ab17722	o/n 4°C
anti-LRP1	Abcam	ab92544	o/n 4°C
anti-Thiophosphate ester antibody	Abcam	ab133473	o/n 4°C
anti-β-Actin-horse radish peroxidase	Santa Cruz	47778	1 hr RT
anti-pFMRP, phosphor-S499	PhosphoSolutions	p1125-499	o/n 4°C

Antibody	Company	Catalog No	Working Conditions
anti-IRE1	Cell-Signaling	3294	o/n 4°C
anti-FMRP	Cell-Signaling	4317	o/n 4°C
anti-ABCA1	Novus Biologicals	NB400-105	o/n 4°C
anti-ABCG1	Novus Biologicals	NB400-132	o/n 4°C
anti-FMRP	Biolegend	834601	o/n 4°C
anti-MER	R&D	AF591-SP	o/n 4°C
Anti-pro Caspase1 + p10 + p12 antibody [EPR16883]	Abcam	ab179515	o/n 4°C
anti-IL-1-beta	Abcam	Ab9722	o/n 4°C
Secondary-IgG-Mouse	SeraCare	5220-0341	1 hr RT
Secondary-IgG-Rabbit	SeraCare	5220-0337	1 hr RT
Immunohistochemistry			
anti-MOMA-2	Bio-Rad	MCA519G	o/n 4°C
anti-α-SMA	Abcam	ab5694	o/n 4°C
anti-PE-F4/80	Biolegend	123110	o/n 4°C
TruStain FcX (anti-CD16/32)	Biolegend	101319	10 min 4°C
DAPI	Biolegend	422801	10 min 4°C
anti-pFMRP, phosphor-S499	PhosphoSolutions	p1125-499	o/n 4°C
anti-CD68	Santa Cruz	sc-20060	o/n 4°C
Flow Cytometry			
anti-PE-F4/80	Biolegend	123110	o/n 4°C
TruStain FcX (anti-CD16/32)	Biolegend	101319	10 min 4°C
Propidium iodide (PI)	Biolegend	421301	20 min 4°C
DAPI (4',6-Diamidino-2-Phenylindole, Dilactate)	Biolegend	422801	10 min 4°C
anti-CD45-Pac. Blue (clone 30-F11)	Biolegend	103101	20 min 4°C
anti-CD3e-PE (Clone 145-2C11)	Biolegend	100301	20 min 4°C
anti-CD11b-APC (Clone M1/70)	Biolegend	101211	20 min 4°C
anti-CD19-BV650 (Clone 6D5)	Biolegend	115541	20 min 4°C
anti-Ly6C-PE/Dazzle (Clone HK1.4)	Biolegend	128043	20 min 4°C
anti-Ly6G-PerCP Cy5.5 (1A8)	Biolegend	127615	20 min 4°C

2.1.3 Plasmids

WT-Ire1-pcDNA3, and Kinase-dead IRE1 mutant (K599A)-pcDNA3 plasmids were generated in Dr. Peter Walter's laboratory (University of California, San Francisco).

WT-Fmr1 plasmid was generated in Jennifer C. Darnell (The Rockefeller University, New York).

2.1.4 Cell Lines

Fmr1$^{-/-}$ mouse embryonic fibroblasts (MEF) were generated in Dr. David Nelson's laboratory (Baylor College of Medicine, Houston, Texas). HEK293T, Jurkat (human T lymphocytes) and L-929 (mouse fibroblasts) cells were obtained from ATCC. Cells were cultured in RPMI or DMEM supplemented with 10% heat-inactivated FBS and %1 P/S cocktail. Cells were cultured in a humidified CO2 incubator at 37°C.

2.1.5 Solutions

Buffer compositions are listed in Table 2.3.

Table 2.3. Buffer compositions.

Buffer	**Composition**
6X Laemmli SDS Loading Buffer (50 ml)	6 g SDS 23,5 ml glycerol 0.01% bromophenol blue 6 ml 0.5 M Tris HCl, pH: 6,8 10,5 ml dH2O 10% 2-mercaptoethanol
10X SDS Running Buffer	30g Tris-Base 144g Glycine 10gr SDS Adjust volume to 1 L with dH2O
10X Transfer Buffer	30g Tris-Base 144g Glycine Adjust volume to 1 L with dH2O
10X TBS	80 g NaCl 24.2 g Tris-Base adjust pH 7.6 with 1N HCl Adjust volume to 1 L with dH_2O
1X-TBS-T	450 ml ddH2O 50 ml TBS 500 µl Tween
Blocking solution (5%(w/v) milk/BSA)	2.5 g Bovine Serum Albumin 50 ml 1X TBS-T
10X PBS	80 g NaCl 2 g KCl 15.2 g sodium phosphate dibasic dehydrate

Buffer	Composition
	Adjust volume to 1 L with dH_2O pH to 7.4
0.5 M Tris-HCl (pH: 6.8)	30.3 g Tris Base 800 ml ddH_2O adjust pH to 6.8 with 1 N HCl Adjust volume to 500 ml with dH2O
1.5 M Tris-HCl (pH: 8.8)	90.8 g Tris Base 800 ml ddH_2O adjust pH to 8.8 with 1 N HCl Adjust volume to 500 ml with dH2O
15 % Resolving Gel	2.5 ml 1.5 M Tris-HCl, pH: 8.8 3.54 ml dH2O 3.75 ml 40% Acrylamide mix 100 ul 10% SDS 100 ul 10% Ammonium persulfate 10 ul TEMED
12 % Resolving Gel	2.5 ml 1.5 M Tris-HCl, pH: 8.8 4.29 ml dH2O 3 ml 40% Acrylamide mix 100 ul 10% SDS 100 ul 10% Ammonium persulfate 10 ul TEMED
10 % Resolving Gel	2.5 ml 1.5 M Tris-HCl, pH: 8.8 4.8 ml dH2O 2.5 ml 40% Acrylamide mix 100 ul 10% SDS 100 ul 10% Ammonium persulfate 10 ul TEMED
9 % Resolving Gel	2.5 ml 1.5 M Tris-HCl, pH: 8.8 5.3 ml dH2O 2 ml 40% Acrylamide mix 100 ul 10% SDS 100 ul 10% Ammonium persulfate 10 ul TEMED
8 % Resolving Gel	2 ml 1.5 M Tris-HCl, pH: 8.8 4.2 ml dH2O 1.6 ml 40% Acrylamide mix 80 ul 10% SDS 80 ul 10% Ammonium persulfate 8 ul TEMED
5 % Stacking Gel	2.5 ml 1.5 M Tris-HCl, pH: 8.8 6.29 ml dH2O 1 ml 40% Acrylamide mix 100 ul 10% SDS 100 ul 10% Ammonium persulfate 10 ul TEMED

Buffer	Composition
0.5 M Tris-HCl (pH: 6.8)	30.3 g Tris Base 800 ml ddH_2O adjust pH to 6.8 with 1 N HCl Adjust volume to 500 ml with dH_2O
1.5 M Tris-HCl (pH: 8.8)	90.8 g Tris Base 800 ml ddH_2O adjust pH to 8.8 with 1 N HCl Adjust volume to 500 ml with dH_2O
Phospholysis Buffer (250 ml)	50 mM HEPES, 12.5 ml from 1M stock 100 mM NaCl, 25 ml from 1M stock 4 mM Na4P2O7 (NaPP), 10 ml from 0.1 M stock 10 mM EDTA, 5 ml from 0.5 M stock 10 mM NaF, 2.5 ml from 1 M stock 1% Triton 2.5 ml Adjust volume to 250 ml (192.5 ml dH_2O) prior to use: 10 µM Phosphatase Inhibitor Cocktail 3 (1X last concentration from 1000X stock) 10 µM Protease Inhibitor Cocktail (1X last concentration from 1000X stock)
HBS solution (Instead of R buffer in Invitrogen Neon Transfection Kit)	21 mM commercial HEPES (pH; 7.05) 137 mM NaCl 5 mM KCl 0,7 mM Na2HPO4 6 mM Glucose Filter prior using keep at 4°C.
HBSS buffer	8 g NaCl 400 mg KCl 140 mg CaCl2 100 mg MgSO4-7H2O 100 mg MgCl2-6H2O 60 mg Na2HPO4-2H2O 60 mg KH2PO4 1g Glucose 350 mg NaHCO3
PA stock Solution	1.2821 g PA 10 ml absolute ethanol Heat to 55°C until dissolves Aliquot and store at -20°C
Alkaline Lysis Buffer	25 mM NaOH 0.2 mM $Na^2EDTA.2H_2O$ pH 12 (do not adjust)
Neutralization Buffer	40 mM Tris-HCL (242.28 g) pH 12 (do not adjust)
TAE buffer 50X	242 g tris base in double-distilled H2O 57.1 ml glacial acetic acid 100 ml 0.5 M EDTA solution (pH 8.0) Adjust volume to 1 L

2.2 Methods

2.2.1 General Study Design

Three or more independent replicates were performed for cell-based experiments. Mice were randomly assigned to independent cohorts, and data analysis was performed blind. The only elimination criteria used for mouse studies was based on health and as advised.

2.2.2 Mice Studies and Treatments

C57BL/6 (WT, $Fmr1^{+/+}$), $Fmr1^{-/-}$ and Apolipoprotein E-deficient ($Apoe^{-/-}$) mice were purchased from Jackson Laboratory. IRE1 conditional knock out ($Ire1\alpha^{flox/flox}$) mice were a kind gift from Dr. Takao Iwawaki (Kanazawa Medical University, Japan) and characterized before [127]. $Ire1\alpha^{flox/flox}$ mice were inter-crossed from with $LysM^{cre}$ mice purchased from Jackson Lab (004781) to obtain $Ire1\alpha^{flox/flox}$, $LysM^{cre}$ mice ($IRE1^{-/-}$), which had a myeloid-specific Ire1α gene deletion. Fmr1 conditional knock out ($Fmr1^{flox/flox}$) mice were a kind gift from Dr. David Nelson. $Fmr1^{flox/flox}$ mice were inter-crossed with $LysM^{cre}$ mice purchased from Jackson Lab (004781) to obtain myeloid Fmr1-deficient ($myFmr1^{-/-}$) mice.

Starting at 8 weeks of age, $Fmr1^{+/+}$, $Fmr1^{-/-}$, $myFmr1^{+/+}$ or $myFmr1^{-/-}$ mice were injected with $1x10^{10}$ AAV_PCSK9 (AAV8-D377Y-mPCSK9, Vector Biolabs AAV-268246) via tail vein, then fed with normal chow or high cholesterol/high fat atherosclerotic mouse diet from Envigo (TD.88137) for 6 to 16 weeks. $Apoe^{-/-}$ mice were fed with WD (12 weeks) and intraperitoneally injected with vehicle (DMSO) or AMG-18 (30 mg/kg) once or twice a day in the last 4 weeks of WD. C57BL/6 were injected with Tunicamycin (TM, 1 mg/kg) and with AMG-18 (30 mg/kg) or vehicle (DMSO) in 20% vol/vol Cremophor EL saline solution, as described in [91]. 8 hours later peritoneal macrophages were isolated by thioglycolate elicitation for further analysis. $Apoe^{-/-}$ mice were fed with WD for 12 weeks and treated by oral gavage with vehicle (1% BSA in PBS) or 1400 mg/ kg/day cis or trans-PAO dissolved in vehicle for 4 weeks while continuing WD.

Husbandry conditions and study approval: Mice were kept under specific pathogen-free conditions with food and water *ad libititum*. Both female and male mice were used for experiments. All animal experiments were performed according to protocols approved by the Experimental Animal Ethical Care Committees at Bilkent University, Ankara, Turkey or Cedars Sinai Medical Center, Los Angeles, USA or the University of Ottawa Animal Care Committee, Ottawa, ON K1N 6N5, Canada.

2.2.3 Genotyping of mice lines

Mice were numbered by toe cutting and samples were lysed in 60 µl alkaline lysis buffer for 1 hour followed by neutralization by addition of 60 µl of neutralization buffer. Run PCR products in 1.5 % agarose gel with SYBR safe stain (10000X) in TAE buffer. Primer sequences, Buffer compositions and PCR protocols of $Fmr1^{-/-}$, $myFmr1^{-/-}$, $Ire1^{-/-}$, $LysM^{cre}$ mice are listed in Table 2.4, Table 2.5 and Table 2.6 respectively.

Table 2.4. Genotyping primer list.

Primer	Sequence
Fmr1 flox 1F	5’ GCC TCA CAT CCT AGC CCT CTA C 3’
Fmr1 flox 2F	5’ GTT GAG CGG CCG AGT TTG TCA G 3’
Fmr1 flox 3R	5’ CCC ACT GGG AGA GGA TTA TTT GGG 3’
oIMR6734_WtFMRP	5’ TGT GAT AGA ATA TGC AGC ATG TGA 3’
oIMR2060_MutFMRP	5’ CAC GAG ACT AGT GAG ACG TG 3’
oIMR6735_Common	5’ CTT CTG GCA CCT CCA GCT T 3’
Cre IMR 3066	5’ CCC AGA AAT GCC AGA TTA CG 3’
Cre IMR 3067	5’ CTT GGG CTG CCA GAA TTT CTC 3’
Cre IMR 3068	5’ TTA CAG TCG GCC AGG CTG AC 3’

Table 2.5. PCR master mix compositions for genotyping.

myFmr1		**Fmr1 whole body KO**		**Cre**	
Kapa 2G 2X	5 µl	Kapa 2G 2X	5 µl	Kapa 2G 2X	5 µl
Fmr1 flox 1F	1 µl	oIMR6734_WtFMRP	0.5 µl	Cre IMR 3066	1 µl
Fmr1 flox 2f	1 µl	oIMR2060_MutFMRP	0.5 µl	Cre IMR 3067	0.5 µl
Fmr1 flox 3r	1 µl	oIMR6735_Common	0.5 µl	Cre IMR 3068	0.2 µl
DNA	2 µl	DNA	2 µl	DNA	2 µl
dH2O	-	dH2O	1.5 µl	dH2O	1.3 µl

Table 2.6. PCR cycles for genotyping.

Step	Temperature	Time
myFmr1		
Initial Denaturation	98°C	30 seconds
25-35 Cycles	98°C 45-72°C 72°C	5-10 seconds 10-30 seconds 15-30 seconds per kb
Final Extension	72°C	5-10 minutes
Fmr1 whole body KO		
Initial Denaturation	98°C	30 seconds
25-35 Cycles	98°C 45-72°C 72°C	5-10 seconds 10-30 seconds 15-30 seconds per kb
Final Extension	72°C	5-10 minutes
Fmr1 whole body KO		
Initial Denaturation	98°C	30 seconds
25-35 Cycles	98°C 45-72°C 72°C	5-10 seconds 10-30 seconds 15-30 seconds per kb
Final Extension	72°C	5-10 minutes

2.2.4 Macrophage Isolation and Differentiation from Bone Marrow

Peritoneal macrophages: 3% thioglycolate solution were injected to mice intraperitoneally and peritoneal macrophages were collected 4 days after by washing the peritoneal cavity with ice-cold PBS (10 ml) as described before [126, 128]. Cells were centrifuged at 500 x g for 5 min at 4°C and resuspended in RPMI medium in cell culture plates. Macrophages were incubated at 5% carbon dioxide incubator at 37°C for 30 minutes to attach and non-adherent cells were removed along with media. Cells were rinsed with PBS and used for protein isolation or RNA isolation.

BMDM: Bone marrows were collected form the tibia and femurs of mice into RPMI containing 1% Penicillin/streptomycin (P/S) cocktail as previously described [91]. After filtering through a cell strainer (BD, 352350), cells were centrifuged at 500 x g

for 5 minutes and re-suspended in RPMI enriched with 20% L929 cells conditioned medium, 10% heat-inactivated FBS and 1% P/S cocktail, followed by growth on petri dishes and differentiation to macrophages for 5-10 days.

Lipid-induced inflammasome activation of macrophages: After differentiation, DMSO/AMG-18 pre-treated (1 hour), Control/Fmr1 siRNA transfected (24 hours after transfection) or $Fmr1^{-/-}$ or $Fmr1^{+/+}$ BMDMs were primed with 200 ng ultrapure bacterial lipopolysaccharide (LPS) for 3 hours, followed by stimulation with 500 μM palmitate/1% bovine serum albumin (BSA) for additional 16 hours.

Palmitate (PA)/bovine serum albumin (BSA) complex preparation: PA was dissolved in absolute ethanol to yield a stock concentration of 500 mM and stored at −80°C. Stock PA was diluted to working concentration and suspended with %1 fatty acid free-BSA in serum free RPMI growth medium by mixing at 55°C for 15 minutes as described before [92].

2.2.5 Cell Culture and Transfection

$Fmr1^{-/-}$ MEF were generated in Dr. David Nelson's laboratory (Baylor College of Medicine, Houston, Texas). HEK293T, Jurkat (human T lymphocytes) and L-929 (mouse fibroblasts) cells were obtained from ATCC. Cells were cultured in RPMI or DMEM supplemented with 10% heat-inactivated FBS and %1 P/S cocktail. Cells were cultured in a humidified CO2 incubator at 37°C. All cells were regularly tested for mycoplasma contamination.

60-80% confluent HEK293T, WT or $Fmr1^{-/-}$ MEF cells were transfected using Lipofectamine 3000 or Polyethylemine (PEI). BMDM and HEK293T cells were electroporated either with IRE1-, Fmr1- or control-siRNA (100 nM) using Neon electroporator (Thermo Scientific) as per specific conditions provided by the manufacturer and as described earlier [91]. 24-36 hours after transfection, cells were treated with PA or TG to induce ER stress.

2.2.6 Western Blot

Cells were lysed in lysis buffer as described in [35]. After centrifugation at 8000 x g for 10 min., clear lysates were mixed with sodium dodecyl sulfate (SDS) loading dye and heated at 95°C for 5 minutes. Protein lysates were loaded to gels in appropriate concentrations according to their molecular weight and run at 80-100V. After separation, samples were transferred to polyvinylidene difluoride (PVDF) membrane at 100V for 60-90 min. Blocking and antibody incubation of the membranes were carried out in tris-buffered saline (TBS) buffer prepared with 0.1% Tween-20 (v/v) and 5% (w/v) dry milk or BSA. ECL prime reagent were used to develop the membranes and images were captured with ChemiDoc (BioRad). Buffer and gel commotions are listed in Table 2.3.

Lambda Protein Phosphatase (PPase) treatment of cell lysates: Protein lysates were treated with λ Phosphatase (Lambda phosphatase, PPase) at 30°C for 30 minutes in the PPase buffer mixture listed in Table 2.7, then lysates were mixed with sodium dodecyl sulfate (SDS) loading dye and heated at 95°C for 5 minutes.

Antibody dilutions: anti-pIRE1 1:2000, anti-FMRP 1:2000, anti-LRP1 1:5000, anti-IL-1 beta 1:500, Anti-pro Caspase1 + p10 + p12 1:2000, anti-Thiophosphate ester 1:5000, anti-pFMRP (phosphor-S499) 1:2000, anti-IRE1 1:2000, anti-ABCA1 1:1000, anti-ABCG1 1:1000, Anti-MERTK 1:1000, anti-β-Actin-horse radish peroxidase 1:5000, Secondary IgG-Goat 1:10000, Secondary IgG-Rabbit 1:10000, Secondary-IgG-Mouse 1:10000.

Table 2.7. PPase buffer mixture.

Component	**50 µl Reaction**
PPase Enzyme	1 µl
10X Buffer	5 µl
1X 10 mM MnCl2	5 µl
Protein lysate	40 µl

2.2.7 RNA Isolation and Quantitative Reverse Transcription Polymerase Chain Reaction (qRT-PCR)

Total RNA was isolated using TRIsure. RNA extractions were than reverse transcribed by using Revert Aid First strand complementary deoxyribonucleic acid (cDNA) synthesis kit to cDNA according to manufacturer's protocol. Master mix components were listed in Table 2.8. After reaction, cDNA mixture was diluted 10X by adding 90 µl of RNase-free water. Using specific primers listed in Table 2.9, cDNAs were amplified on Rotor Gene (Qiagen). Power-Up-SYBR green (Applied Biosystems, A25742) was used for qRT-PCR reaction.

Quantifications were performed using the ΔΔCt method and gene expression levels were normalized to GAPDH transcript levels following the Lifesciences-Roche website instructions. Briefly, fold-changes in expression were calculated as (Primer efficiency)-ΔΔCt where ΔΔCt means ΔCt (target gene) - ΔCt (reference gene) and Ct means (threshold cycle). Results were analysed from three or more independent experiments using the Student's t-test.

Table 2.8. cDNA conversion master mix.

Component	10 µl Reaction
Buffer	2 µl
Random Primer	1 µl
RT	0.5 µl
RI	0.5 µl
RNA (1000 ng)	1 µl
RNase-free water	4.5 µl

Table 2.9. PCR primers.

Name	Sequence
mmu-Fmr1-F	5' CCGAACAGATAATCGTCCACG 3'
mmu-Fmr1-R	5' ACGCTGTCTGGCTTTTCCTTC 3'
mmu-Abca1-F	5' AAAACCGCAGACATCCTTCAG 3'
mmu-Abca1-R	5' CATACCGAAACTCGTTCACCC 3'
mmu-Abcg1-F	5' GGTCCTGACACATCTGCGAA 3'
mmu-Abcg1-R	5' CAGGACCTTCTTGGCTTCGT 3'
mmu-Mertk-F	5' CAGGGCCTTTACCAGGGAGA 3'

Name	Sequence
mmu-Mertk-R	5’ TGTGTGCTGGATGTGATCTTC 3’
mmu-Lrp1-F	5’ GCCTACACCTGGAGAGATAGC 3’
mmu-Lrp1-R	5’ GGCAACTTACGAGCAGGCT 3’
mmu-Cd36-F	5’ GTGCTCTCCCTTGATTCTGC 3’
mmu-Cd36-R	5’ CTGCACCAATAACAGCTCCA 3’
mmu-Cd47-F	5’ TGGTGGGAAACTACACTTGCG 3’
mmu-Cd47-R	5’ CGTGCGGTTTTTCAGCTCTAT 3’
mmu-Calr-F	5’ GCAGACCCTGCCATCTATTTC 3’
mmu-Calr-R	5’ TCGGACTTATGTTTGGATTCGAC 3’
mmu-Rac1-F	5’ ATGCAGGCCATCAAGTGTG 3’
mmu-Rac1-R	5’ TAGGAGAGGGGACGCAATCT 3’
mmu-Gapdh-F	5’ ATTCAACGGCACAGTCAAGG 3’
mmu-Gapdh-R	5’ TGGATGCAGGGATGATGTTC 3’
mmu-IL-1β -F	5’ CAACCAACAAGTGATATTCTCCATG 3’
mmu-IL-1β -R	5’ GATCCACACTCTCCAGCTGCA 3’

2.2.8 Co-immunoprecipitation and Kinase Assay

Co-immunoprecipitation: HEK293T cells were co-transfected with IRE1 and FMRP plasmids for 24 hours followed by TG (600 nM) or TM (1 µg/ml) for 2 hours. Equal amounts of protein lysates were precipitated with specific antibodies (anti-IRE1 1:250 and anti-FMRP 1:250) at 4°C overnight on a rocker. Protein magnetic beads were added to each sample and incubated at 4°C for overnight. Immunoprecipitates were then analyzed by Western Blot.

Kinase assay: HEK293T cells were transfected with either with WT- or KD-IRE1 plasmids for 24 hours, followed by TG (600 nM) for 2 hours for IRE1 activation. Equal amounts of protein lysates were then precipitated with specific IRE1 antibody coated magnetic beads at 4°C overnight on a rocker. Immunoprecipitates were incubated at 30°C for 45 min in kinase assay buffer mix using IRE1 Kinase assay buffer as listed in Table 2.10, or commercial Kinase assay buffer from SignalChem K01-09 with specific ATP analogue (ATP-γ-S, 100 µM) and purified hFMRP protein. p-Nitrobenzyl mesylate (PNBM) and 0.5 M ETDA solution was added to reaction after 45 minutes and incubated for additional 2 hours at RT to alkylate the kinase substrate. Samples were boiled with SDS-PAGE loading dye at 95°C for 5 min to release the proteins from magnetic beads. Beads were separated using magnetic rack and supernatants were analyzed by Western Blot.

Table 2.10. IRE1 Kinase assay buffer.

Reagent	Stock	Final cons.
Hepes pH 7.4	1mM	20 mM
KoAC	1M	50mM
MnCl2	1M	1mM
MgCl2	1M	1mM
Na2Mao4	1M	1mM
NaF	500mM	2mM
H2O		
*Before starting the reaction add fresh phosphatase, protease inhibitors and ATP-γ-S.		

Kinase assay for phospho-proteomics: Recombinant active IRE1 (500 ng) and FMRP (500 ng) proteins were incubated in kinase buffer at 30°C for 45 minutes with ATP-γ-S (100 µM). Samples were then incubated at 24°C for 1 hour with PNBM (2.5 mM). Samples were boiled in SDS loading buffer at 95°C and loaded to SDS-polyacrylamide gel (SDS-PAGE) gels. Anti-Thiophosphate ester antibody was used to detect alkylated kinase substrate.

2.2.9 Identifying phosphorylation sites on hFMRP using Mass spectrometry

Two *in vitro* kinase reactions of hFMRP and ERN1, worth 4.5 µg protein each were methanol-chloroform precipitated [129]. Dried pellets were dissolved in either [1] 8 M urea/100 mM triethylammonium bicarbonate (TEAB, Thermo Scientific 90114), pH 8.5, or [2] 100 mM ammonium acetate (Sigma-Aldrich A1542), with or without 8 M urea. Proteins were reduced with 5 mM tris(2-carboxyethyl) phosphine hydrochloride (TCEP-HCl, Thermo Scientific C4709) and alkylated with 10 mM 2-chloroacetamide (Sigma-Aldrich 22790). Proteins dissolved in urea/TEAB were digested at 37°C in 0.8 M urea/100 mM TEAB, pH 8.5, sequentially with 500 ng Trypsin (Promega V5117) for 17 hours, followed by 500 ng Endoproteinase GluC (NEB P8100S) for 4.5 h and quenched with formic acid, 5 % final concentration, while proteins dissolved in urea/TEAB or urea/ammonium acetate were digested with 200 ng Proteinase K (Sigma-Aldrich P2308) at 37°C for 30 min and heat-quenched at 90°C for 15 min (similar reactions in ammonium acetate without urea were performed for 30 min or 15 min followed by 16 h digestion with trypsin) [130]. The digest was

injected directly onto a 20 cm, 100 µm ID column packed with BEH 1.7 µm C18 resin (Waters 186005225). Samples were separated at a flow rate of 400 nl/min on an nLC 1000 (Thermo LC120). Buffer A and B were 0.1% formic acid in 5% acetonitrile and 0.1% formic acid in 80% acetonitrile, respectively. A gradient of 1–25% B over 110 min, an increase to 40% B over next 20 min, an increase to 90% B over another 10 min and a hold at 90% B for the final 10 min was used for a total run time of 140 min. The column was re-equilibrated with 20 µl of buffer A prior to the injection of sample. Peptides were eluted directly from the tip of the column and nano-sprayed into the mass spectrometer by application of 2.8 kV voltage at back of the column. The Orbitrap Fusion Lumos (Thermo) was operated in data dependent mode. Full MS1 scans were collected in the Orbitrap at 120K resolution with a mass range of 400 to 1500 m/z and an AGC target of 4e5. The cycle time was set to 3 s, and within these 3 s, the most abundant ions per scan were selected for CID MS/MS in the ion trap with an AGC target of 2e4 and minimum intensity of 5000. Maximum fill times were set to 50 ms and 35 ms for MS and MS/MS scans, respectively. Quadrupole isolation at 1.6 m/z was used, monoisotopic precursor selection was enabled, charge states of 2–7 were selected, and dynamic exclusion was used with an exclusion duration of 5 s. Samples were also analyzed with HCD fragmentation (35 NCE) and detection at 7500 resolution.

Protein and peptide identification were done with Integrated Proteomics Pipeline – IP2 (Integrated Proteomics Applications). Tandem mass spectra were extracted from raw files using RawConverter [131] and searched with ProLuCID [132] against a concatenated database comprising of amino acid sequences from vendors for FMRP, hERN1 and Endoproteinase GluC, UniProt reference proteome of Escherichia coli K12 (UP000000625) Homo sapiens (UP000005640). The search space included all fully-tryptic and half-tryptic peptide candidates (no enzyme specificity for sample treated with Proteinase K). Carbamidomethylation (+57.02146) was considered a static modification on cysteine, and phosphorylation (+79.966331) was considered a differential modification on serine/threonine/tyrosine. Data was searched with 50 ppm precursor ion tolerance and 500 ppm fragment ion tolerance. Identified proteins were filtered to using DTASelect [133] and utilizing a target-decoy database search strategy to control the false discovery rate at 1%, at the spectrum level [134]. A minimum of 1 peptide per protein and 1 tryptic end per peptide (no tryptic ends in case of Proteinase K treatment) were required and precursor delta mass cut-off was fixed at 10 ppm.

Localization scores were assigned to identified sites of phosphorylation using A-Score [135].

2.2.10 Site Directed Mutagenesis

EGFP tagged FMRP plasmid was used as template to introduce site directed mutagenesis. Phusion High-Fidelity DNA Polymerase (M0530S) was used in the reaction with the primers listed in Table 2.11, reaction buffer Table 2.12 and in PCR conditions described in Table 2.13.

Table 2.11. Site-directed mutagenesis PCR primers.

Name	Sequence
S500A-F	5' GCATCAAATGCTGCTGAAGCAGAAGCTGACCACAGAGAC 3'
S500A-R	5' GTCTCTGTGGTCAGCTTCTGCTTCAGCAGCATTTGATGC 3'
S500-T502-S504A-F	5' GCATCAAATGCTGCTGAAGCAGAAGCTGACCACAGAGAC 3'
S500-T502-S504A-R	5' GTCTCTGTGGTCAGCTTCTGCTTCAGCAGCATTTGATGC 3'

Table 2.12. Site-directed mutagenesis PCR reaction mixture.

Component	50 µl Reaction	Final Concentration
Nuclease-free water	to 50 µl	
5X Phusion HF or GC Buffer	10 µl	1X
10 mM dNTPs	1 µl	200 µM
10 µM Forward Primer	2.5 µl	0.5 µM
10 µM Reverse Primer	2.5 µl	0.5 µM
Template DNA	variable	< 250 ng
DMSO (optional)	(1.5 µl)	3%
Phusion DNA Polymerase	0.5 µl	1.0 units/50 µl PCR

Table 2.13. Site-directed mutagenesis PCR cycles.

Step	Temperature	Time
Initial Denaturation	98°C	30 seconds
25-35 Cycles	98°C 45-72°C 72°C	5-10 seconds 10-30 seconds 15-30 seconds per kb
Final Extension	72°C	5-10 minutes
Hold	4-10°C	

2.2.11 Cholesterol Uptake, Cholesterol Efflux and Foam Cell Formation Assay

Cholesterol efflux assay: Efflux assay were performed according to manufacturer's instructions (ab196985). Briefly, macrophages were pre-loaded with fluorescently labeled cholesterol for 16 hours in RPMI media including ACAT inhibitor (5 mg/ml), followed by incubation in efflux medium including cholesterol acceptors apolipoprotein A1 (APOA1; 25 µg/ml) or high-density lipoprotein (HDL; 50 µg/ml) for 6 hours. % Efflux was calculated as cholesterol signal in medium/cholesterol signal in medium and cell using UV spectrophotometer.

Cholesterol uptake assay: Uptake assay were preformed according to manufacturer's instructions (ab236212). Briefly, macrophages were pre-loaded with fluorescently labeled cholesterol for 4 hours in RPMI media. % Cholesterol uptake was measured after washing with PBS 3X using UV spectrophotometer.

In vitro foam cell formation assay: BMDM were incubated with RPMI containing dil-labeled ac-LDL (25 µg/ml), 10% lipoprotein-deficient serum and 20% L-Glutamine for 24 hours. After cholesterol loading, cells were rinsed with PBS and collected in 2% BSA in PBS. Flow cytometry was performed on a BD Fortessa using FACSDiva software with single stain compensation controls acquired on the same day.

In vivo foam cell formation assay: $Fmr1^{+/+}$ and $Fmr1^{-/-}$ mice were injected with a gain-of-function mutant (D377Y) of proprotein convertase subtilisin kexin 9 (PCSK9)-

encoding adeno-associated virus (AAV_mPCSK9) and fed with 16 weeks of WD to induced hypercholesterolemia. Apoe$^{-/-}$ mice were fed with 12 weeks of WD with 4 weeks of AMG-18 (30 mg/kg, once a day) injection during the last 4 weeks of WD. The peritoneal macrophages collected and assessed for lipid accumulation by Oil-Red O and Hematoxylin staining.

2.2.12 Reverse Cholesterol Transport Assay

Preparation of radiolabel cholesterol: aggregated (ag)-LDL (50 µg/mL, made in house with endotoxin free LDL isolated from human plasma) and [^{3}H]-cholesterol (5 µCi/mL) were incubated for 1 hour at 37°C in a sterile endotoxin free bottle.

RCT assay: Fmr1$^{+/+}$ and Fmr1$^{-/-}$ BMDM were incubated with radiolabeled ag-LDL for 30 hours followed by warm HBSS wash and equilibration in 2mg/mL fatty-acid free BSA overnight. Cells were washed twice in ice cold HBSS and incubated with EDTA (5 mM) for 20 min at 4°C and spun down at 200 x g for 5 min. Cells were resuspended in ice cold DMEM and injected into C57BL/6 mice subcutaneously in the scruff of the neck. Blood was collected at 24 hours via the saphenous vein and at 48 hours via cardiac puncture of anesthetized mice. Plasma was used for liquid scintillation counting. At 48 hours livers were removed for scintillation counting. Feces were collected over a 48 hour period, and total feces radioactivity was measured. All [^{3}H]-tracer measurements are expressed relative to the injected amount.

2.2.13 *In vivo* and *in vitro* Efferocytosis Assay

Induction of apoptosis and labeling of Jurkat cells: Jurkat cells were fluorescently labeled with CellTrace CSFE or Violet (2 µM) in PBS for 20 min. Cells were then washed ones with PBS and seeded in conditioned DMEM medium followed by irradiation under a 254 nm UV lamp for 5 min. Cells were incubated under normal cell culture conditions for 3-4 hours. Apoptosis was confirmed by Anexin V$^+$ staining (minimum 85% Annexin V$^+$ cells). The apoptotic cells (ACs) were centrifuged at 500 x g for 5 min and resuspended in conditioned DMEM for experiments.

In vitro efferocytosis: Bone marrow-derived macrophages were plated in 6-well dishes at a density of $0.5x10^6$ cells per well. CSFE-labeled ACs were incubated with the macrophages for 2-4 min at a 5:1 AC:macrophage ratio followed by washing three times with PBS. Some groups of macrophages were then incubated for another 2 hours in normal cell culture media, followed by the addition of Violet-labeled ACs. After 2 hours, macrophages were washed three times with PBS to remove unbound ACs, and then the macrophages were fixed with 4% formaldehyde for 20 min, rinsed three times with PBS, blocked by TruStain FcX™ (anti-mouse CD16/32) for 10 min and then stained with PE-F4/80 o/n. The percentage of PE-F4/80$^+$ and CFSE$^+$ double positive cells to total PE-F4/80$^+$ cells were reported as % efferocytosis and PE-F4/80$^+$, CFSE$^+$ and Violet$^+$ triple positive cells to PE-F4/80$^+$ and CFSE$^+$ double positive cells were reported as % continuous efferocytosis.

In vivo efferocytosis: Fmr1$^{+/+}$ or Fmr1$^{-/-}$ mice were fed with WD for 16 weeks and injected with $1x10^6$ CFSE-labeled ACs and 1,5 hours later subsequently peritoneal lavages were collected and stained for PE-F4/80$^+$ resident macrophages. The percentage of PE-F4/80$^+$ and CFSE$^+$ double positive cells to total PE-F4/80$^+$ cells were reported as % efferocytosis. Another group of C57BL/6 were injected with AMG-18 (30 mg/kg) or vehicle (DMSO). After 8 hours both groups were interperitoneally injected with CFSE-labeled ACs and 1.5 hours later peritoneal lavages were collected and cultured for 30 minutes to allow cells to attach. Macrophages were washed three times with PBS to remove unbound ACs, and then the macrophages were fixed with 4% formaldehyde for 20 min, rinsed three times with PBS, blocked by TruStain FcX™ (anti-mouse CD16/32) for 10 minutes and then stained with PE-F4/80 o/n. The percentage of F4/80$^+$ and CFSE$^+$ double positive cells to total F4/80$^+$ cells were reported as % efferocytosis.

2.2.14 Polysome Fractionation and RNA-Seq

Polysome fractionation protocol was adapted from Stastna et al [136]. Briefly, Fmr1$^{+/+}$ and Fmr1$^{-/-}$ BMDM were treated with PA (500 µM) for 6 hours followed by cycloheximide (100 µg/mL) for 10 min prior to lysis with buffer (100 mM KCl, 20 mM Tris pH 7.5, 5 mM $MgCl_2$, 0.4% NP-40, 100 µg/mL cycloheximide, 0.1 U RNase inhibitor and protease inhibitor cocktail). Clear lysates were loaded to 10-50% sucrose

gradient (in Beckman Coulter Thinwall, Ultra-Clear tubes, 344059) and centrifuged (in Beckman LE-80K) for 120 min at 40,000 x rpm at 4°C in a swinging bucket rotor (Beckman SW41) with no-brake. Each gradient was collected as 17 fractions in microcentrifuge tubes with continuous monitoring of absorbance at 254 nm (Biologic LP (pump), Biorad 731-8300; BioFrac, Biorad 741-0002) and frozen immediately at -80°C for further analysis.

Total RNA was isolated using RNeasy RNA isolation kit (Qiagen, 74004) from polled fractions HMW (Heavy molecular weight), LMW (Light molecular weight) and NTR (Non translating region). RNA was quantified on Nanodrop 2000 (Invitrogen) and 3-6 µg of total RNA was used for polyA enriched RNA sequencing analysis. Services were purchased from LC Sciences (Texas, USA) for quality control, mRNA expression profiling and data analysis.

2.2.15 HILAQ (Heavy Isotope-Labeled Azidohomoalanine Quantification)

$Fmr1^{+/+}$ and $Fmr1^{-/-}$ BMDM cells were pre-treated with methionine-free RPMI medium for 30 min, then treated with PA (500 µM) together with AHA ($Fmr1^{+/+}$) or hAHA ($Fmr1^{-/-}$) for 6 hours. Whole cell lysate of azidohomoalanine (AHA) and heavy azidohomoalanine (hAHA) labeled samples were combined and proceeded with the protocol previously described by Ma et al [137]. All materials used in the reactions are listed in Table 2.14 and solutions in Table 2.15.

Table 2.14. Material list for HILAQ labeling.

Product	Brand	Cat no
hAHA, L-AZIDOHOMOALANINE:HCL (1,2,3,4-13C4, 99%; 2,4-15N2, 98%)	Cambridge Isotope Laboratories	CNLM-9461-0.1
AHA, L-AZIDOHOMOALANINE:HCL UNLABELED	Cambridge Isotope Laboratories	ULM-9460-0.1
Tert-Butanol	Sigma	360538-500ML
Tris [(1-benzyl-1H-1,2,3-triazol-4-yl) methyl]amine	Sigma	678937-50MG
Biotin-Alkyne	Invitrogen	B10185
Copper (II) sulfate	Sigma	451657-10G
Trichloroacetic acid solution	Sigma	T0699-100ML

Product	Brand	Cat no
Tris(2-carboxyethyl)phosphine hydrochloride	Sigma	C4706
Acetone (HPLC), Fisher Chemical™	Fisher Sci	A949SK-1
Urea	Sigma	U5378-100G
Cytiva (Formerly GE Healthcare Life Sciences) HyClone™ Fetal Bovine Serum (U.S.), Dialyzed	Fisher Sci	SH3007901HI
Gibco™ GlutaMAX™ Supplement	Fisher Sci	35-050-061
Gibco™ Sodium Pyruvate (100 mM)	Fisher Sci	11-360-070
Gibco™ HBSS, no calcium, no magnesium, no phenol red	Fisher Sci	14-175-095
Promega™ ProteaseMAX™ Surfactant, Trypsin Enhancer	Fisher Sci	PRV2071
2-Chloroacetamide	Sigma	22790-250G-F
Ammonium bicarbonate	Sigma	09830-500G
Promega Sequencing Grade Modified Trypsin	Fisher Sci	PRV5117
Thermo Scientific™ Pierce™ Fluorescence Biotin Quantitation Kit	Fisher Sci	PI46610
Thermo Scientific™ Pierce™ NeutrAvidin™ Agarose	Fisher Sci	PI29200
Acetonitrile, 99.9%, Extra Dry over Molecular Sieve, AcroSeal™, ACROS Organics	Fisher Sci	AC364315000
Trifluoroacetic acid (TFA)	Sigma	T6508-25ML
Thermo Scientific™ Pierce™ High Capacity NeutrAvidin™ Agarose, 5ml	Fisher Sci	PI29202

Table 2.15. Stock solutions used in HILAQ labeling.

Solution	Composition
hAHA 1 M stock solution (L-Azidohomoalanine-HCl, 13C4, 15N2)	Dissolve 18.655 mg of hAHA in 100 µl of molecular biology–grade water to make a 1 M stock. Store at −20 °C, protected from light, until precipitate can be seen.
AHA 1 M stock solution (L-Azidohomoalanine:HCL unlabeled ULM-9460-0.1)	Dissolve 18.095 mg of AHA in 100 µl of molecular biology–grade water to make a 1 M stock. Store at −20 °C, protected from light, until precipitate can be seen.
TBTA 50X stock solution	Dissolve 8.85 mg of TBTA in 200 µl of DMSO and vortex. Store at RT.
1.7 mM TBTA	Add 20 µl of 50X stock to a glass vial containing 180 µl of DMSO. Vortex and add 800 µl of tert-butanol. Store at RT until precipitate can be seen.

Solution	Composition
Biotin-alkyne 5 mM stock solution	Dissolve 25 mg of biotin-alkyne in 10.927 ml of DMSO to obtain a 5 mM stock solution. Make 500-µl aliquots and store them at −20 °C for up to 1 year. Protect the solution from light. Do not freeze–thaw.
TCEP 50 mM stock solution	Dissolve 14.3 mg of TCEP in 1 ml of molecular biology–grade water to make a 50 mM stock. Prepare fresh. Handle with caution, TCEP powder is corrosive.
Copper (III) sulfate 50 mM stock solution	Dissolve 7.98 mg of copper sulfate in 1 ml of molecular biology–grade water to make a 50 mM stock. Make 50-µl aliquots and store them at −20 °C for up to 6 months. Do not freeze–thaw.
Complete BMDM culture medium	RPMI high-glucose medium with 10% (vol/vol) FBS, 20% (vol/vol) FBS, 1% (vol/vol) L-glu and 1% (vol/vol) penicillin–streptomycin. This medium can be stored at 4°C, protected from light, until precipitate can be seen.
Pre-treatment medium	Dissolve 1% (wt/vol) Fatty acid-free BSA in RPMI and sterilize by 0.22(µm) filter. Heat the medium to 60°C and dissolve 500uM Palmitic acid.
Pre-Labeling medium	Dissolve 1% (wt/vol) Fatty acid-free BSA in Met-free RPMI and sterilize by 0.22(µm) filter.
Labeling medium	Dissolve 1% (wt/vol) Fatty acid-free BSA in Met-free RPMI and sterilize by 0.22(µm) filter. Heat the medium to 60°C and dissolve 500uM Palmitic acid. Add 4mM AHA or hAHA.
Lysis buffer	Add protease and phosphatase inhibitors to DPBS.

2.2.16 Bioinformatic analysis

IPA was performed to identify canonical pathways, diseases and functions, and gene networks that are most significant to microarray outcomes and to categorize differentially expressed genes in specific diseases and functions in RNA-Seq and AHA proteomics assays.

2.2.17 *En Face* Aorta and Macrophage Oil-Red O staining

Aortas opened longitudinally and foamy-macrophages were rinsed with PBS for 1 min then 60% isopropanol for 1 min and stained with Oil-Red O solution for 20 min and then distained in 60% isopropanol for 1 min and rinsed in PBS. The lesion area was quantified as percent of Oil-Red O staining area in total aorta area.

2.2.18 Immunohistochemistry

7 μm thick aortic root cryosections (from OCT embedded heart tissue) were stained with antibodies for: anti-MOMA-2 (1:500) and anti-α-SMA (1:500) and images were captured with fluorescent microscope. Cryosections were stained with Masson's Trichrome, TUNEL, Hematoxylin and Eosin (H&E) according to manufacturer's instructions. Cryosections were stained with H&E for morphometric lesion analysis. The total lesion area and necrotic area were quantified as previously described from 4 sequential sections (60 μM apart, beginning at the base of the aortic root) as previously described [35]. Foam cell area was calculated from Oil-Red O stained 4 sequential sections (60 μM apart, beginning at the base of the aortic root) and collagen content from Masson's Trichrome stained sections using ImageJ as previously described [35].

Fluorescent immunostainings were carried out on cryosections that were fixed in cold acetone for 10 minutes, blocked in goat serum/BSA/PBS as previously described. All stained sections were mounted with fluoroshield mounting reagent with DAPI. Fluorescent signal calculations: (a) TUNEL staining: the sections were double stained with MOMA-2 to mark the macrophage-enriched area. The Mean Fluorescent Intensity (MFI) corresponding to primary antibody signal was calculated from the MOMA-2 positive area. The background fluorescence of the non-stained area inside the lesion was subtracted from the total MFI corresponding to each signal (b) α-SMA staining: α-SMA positive area was calculated from the plaque area. The background fluorescence of the non-stained area inside the lesion was subtracted from the total MFI corresponding to each signal. Data were quantified as total MFI signal compared with baseline [35, 91].

Human plaque immunohistochemistry from parafilm embedded tissue sections: Incubate slides at 65°C for 60 min facing up. Deparaffinize twice in xylene for 5

minutes. Hydrate in 100%, 95%, 70% EtOH and H2O. Place in 10% Formalin for 30 minutes. Wash 2x in H2O. Place into TRIS EDTA 1x, 0.05% Tween20 with 10% glycerol for antigen retrieval for 20 min in steamer. Cool in ice bath for 20-30 min. Rinse with distilled water 3x, then leave in 1XTBST x 1 min. Circle sections with a hydrophobic pen. Block with blocking solution for 10 min at RT. Add primary antibody into blocking solution (1x) at a 1:50-1:200 ratio and close the slide box, incubate for 60-90 minutes at RT or overnight in cold-room. Wash in 1XTBST x 3. Add secondary antibody HRP polymer conjugated (Premixed anti-mouse, anti-rabbit, and rat in 4°C) and incubate for 15 minutes at RT. Wash in 1XTBST x 3 washes. Prepare Opal dyes (520, 570, 650) at desired conc. (usually 1:200-1:400) in 1X amplification buffer and incubate slides for 10 minutes. Wash immediately with TBST x 3. Proceed to antibody removal by submerging slides in citrate buffer (pH 6.0) with 10% glycerol and boiling for 20 min, cool down slides, and wash with DI H2O 3X and keep slides in TBST. Stain nuclei with DAPI at 4 ug/ml for 5 minutes and wash 3X with DI water. Mount slides using 1 drop of progold antifade solution and a glass cover slide.

2.2.19 Apoptosis Detection by Flow Cytometry

Apoptosis was induced after treatments by PA (500 µM) treatment for 12 hours. Fc receptors were blocked by pre-incubating cells with 0.25µg of TruStain FcX™ PLUS (anti-mouse CD16/32) Antibody per 10^6 cells for 5-10 minutes on ice. Cells were then incubated with PI on ice for 20 minutes in the dark followed by 2X with 2ml of cell staining buffer. Cells were resuspended in 500 µl of cell staining buffer and analyzed on a BD Fortessa using FACSDiva software with single stain compensation controls acquired on the same day. Data were analyzed using FlowJo analysis software (FlowJo, LLC).

2.2.20 Flow Cytometric analysis of Peripheral Blood

100 µl of blood was collected in EDTA-coated tubes and red blood cells were removed by incubation (3X) in Ammonium-Chloride-Potassium (ACK, Thermo Fisher A1049201) solution for 5 min at room temperature. Peripheral blood mononuclear

cells were then resuspended in FACS buffers (2% BSA in PBS) and incubated for 20 min on ice with the following antibodies: anti-CD45-Pac. Blue (clone 30-F11), CD3e-PE (Clone 145-2C11), CD11b-APC (Clone M1/70), CD19-BV650 (Clone 6D5), Ly6C-PE/Dazzle (Clone HK1.4) and Ly6G-PerCP Cy5.5 (1A8) in 1:100 dilution ratio. Stained samples were washed once and resuspended in FACS buffer containing DAPI (4 µg/ml). Flow cytometry was performed on a BD Fortessa using FACSDiva software with single stain compensation controls acquired on the same day. Data were analyzed using FlowJo analysis software (FlowJo, LLC). All antibodies were purchased from Biolegend (San Diego, CA) and used at the manufacturer's recommended concentrations.

2.2.21 Plasma Lipids and Lipoprotein Analysis

Plasma was analyzed by FPLC in the Department of Internal Medicine/Lipid Science, Wake Forest University School of Medicine Winston-Salem, NC 27019 as described [35]. The total cholesterol and triglyceride measurement were performed using WAKO Cholesterol E kit according to the manufacturer's instructions.

2.2.22 Statistics

Results are reported as mean ± SEM and statistical significance was determined with Unpaired t-test with Welch's or Mann-Whitney correction test by GraphPad Software, LLC. *P≤ 0.05, **P≤ 0.01, ***P≤ 0.001 was considered as * significan

CHAPTER 3 RESULTS

3.1 Lipids Induce FMRP Phosphorylation in IRE1 Kinase-dependent Manner

Previously published mass spectrometry-based IRE1 interactome data revealed multiple FMRP-interacting proteins potentially associating with IRE1 (Fig 3.1A) [125]. These proteins share significant sequence homology with FMRP and are usually found in homo/heteromeric complexes with FMRP [138]. Based on these observations, I reasoned that FMRP might also physically interact with IRE1. Indeed, FMRP co-immunoprecipitated with IRE1 in non-stress and ER stress conditions induced by thapsigargin (TG; an inhibitor of the ER Ca^{2+} pump) and tunicamycin (TM; an inhibitor of N-linked glycosylation) from human embryonic kidney cell line (HEK293T) cells that were transiently transfected with plasmids encoding both proteins (Fig 3.1B).

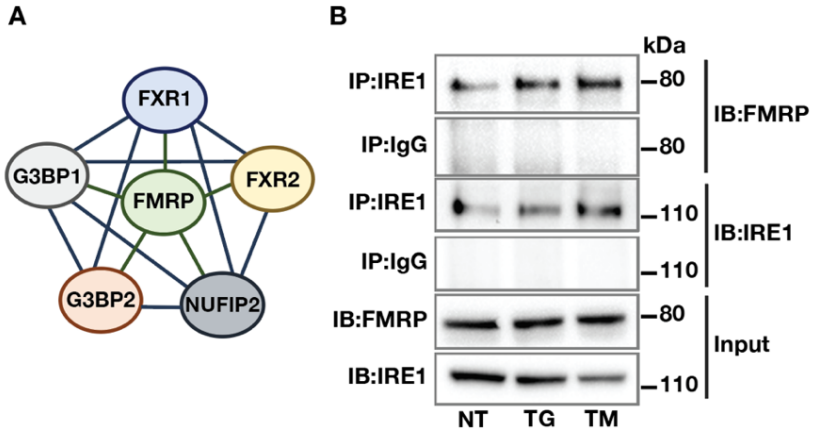

Figure 3.1. FMRP is a novel IRE1 kinase substrate.

(A) STING analysis of published IRE1 interactome proteins in relation to FMRP. **(B)** HEK293T cells were co-transfected with IRE1 and FMRP plasmids and stimulated with TG (600 nM) or TM (1 mg/ml) for 2 hours. Protein lysates were immunoprecipiated (IP) with anti-IRE1 or IgG (control) antibodies and analyzed by Western blotting using specific antibodies for FMRP and IRE1 (n=3). For all experiments, a representative blot is shown from at least (n=3) independent experiments. Data are mean ± SEM. Unpaired t-test with Welch's correction or paired t-test. *P≤ 0.05, **P≤ 0.01, ***P≤ 0.001.

Since FMRP phosphorylation is critical for translation suppression and the association with IRE1 juxtaposes it to a kinase whose substrate is unclear, I wondered whether ER stress alters FMRP phosphorylation state. To assess this possibility, I treated cultured macrophages with known ER stressors; TG and oxidized low density lipoprotein (oxLDL, another inducer of ER stress). Using specific antibodies that recognize S724 phosphorylation on IRE1 and S500 phosphorylation on FMRP [139, 140], I found that TG and oxLDL significantly induced IRE1 autophosphorylation and FMRP phosphorylation but did not affect levels of FMRP protein or Fmr1 mRNA (Fig 3.2A-C). Phosphatase treatment of the samples partially reversed the ER stress-induced increase in the pFMRP/FMRP ratio (Fig 3.2A and 3.2B), implying FMRP phosphorylation is enhanced by these ER stressors.

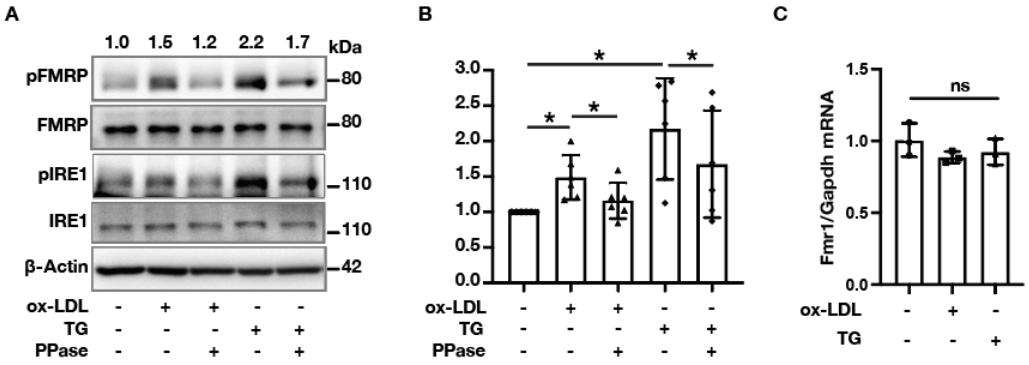

Figure 3.2. FMRP is phosphorylated by ER stress.

(A) RAW 264.7 mouse macrophages were treated with either oxLDL (50 μg/ml) or TG (300 nM) for 6 hours. Protein lysates were treated with λ Phosphatase (PPase) for 30 minutes and analyzed by western blotting using specific antibodies for pFMRP, FMRP, pIRE1, IRE1 and β-Actin. pFMRP/FMRP fold induction is depicted above the blots (n=6). **(B)** Western blot quantifications for pFMRP/FMRP ratio in Fig 3.1A. **(C)** qRT-PCR analysis of Fmr1 mRNA from the samples in Fig 3.1A (n=4). A representative blot is shown from at least (n=3) independent experiments. Data are mean ± SEM. Unpaired t-test with Welch's correction or paired t-test. *P≤ 0.05, **P≤ 0.01, ***P≤ 0.001.

Previous studies showed that hyperlipidemia induces ER stress in plaque macrophages *in vivo* [42, 141]. I next investigated whether hyperlipidemia also has an effect on FMRP phosphorylation on S499 (mouse S499 corresponds to human S500). To this end, I used mice deficient in apolipoprotein E ($Apoe^{-/-}$) as this a protein found in plasma lipoprotein particles and facilitates cholesterol clearance from the circulation

[142]. In agreement with previous reports, I observed that ER stress (as monitored by IRE1 autophosphorylation) was induced in the peritoneal macrophages (PM) obtained from hyperlipidemic, Apoe$^{-/-}$ mice that were fed with a WD for 16 weeks when compared to Apoe$^{-/-}$ mice fed with chow diet (CD) (Fig 3.3A). I found that FMRP S499 phosphorylation, which leads to FMRP-mediated translational suppression, was 1.4-fold elevated ($p \leq 0.01$) by a chronic exposure to hypercholesterolemia, whereas FMRP protein and Fmr1 mRNA expression levels remained unchanged (Fig 3.3A-C).

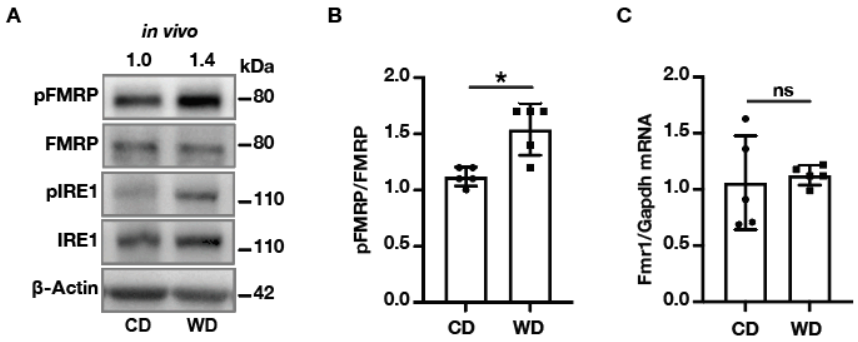

Figure 3.3. Lipid accumulation leads to FMRP phosphorylation.

(A) Apoe$^{-/-}$ mice were fed with CD or WD for 16 weeks followed by peritoneal macrophage (PM) isolation. Protein lysates were analyzed by western blotting using specific antibodies for pFMRP, FMRP, pIRE1, IRE1 and β-Actin. pFMRP/FMRP-fold induction is depicted above the blots (n=5). **(B)** Western blot quantifications for pFMRP/FMRP ratio in Fig 3.3A. **(C)** qRT-PCR analysis for Fmr1 mRNA from the samples in Fig 3.3A (n=3). For all experiments, a representative blot is shown from at least (n=3) independent experiments. Data are mean ± SEM. Unpaired *t*-test with Welch's correction or paired *t*-test. *P≤ 0.05, **P≤ 0.01, ***P≤ 0.001.

I further investigated FMRP phosphorylation in human atherosclerotic disease model, where macrophages are loaded with lipids and ER stress is activated with lipid accumulation. Co-staining of CD68 (a macrophage marker) pFMRP in human carotid artery sections showed that foamy macrophages located in plaque areas had significantly higher pFMRP (Fig 3.4).

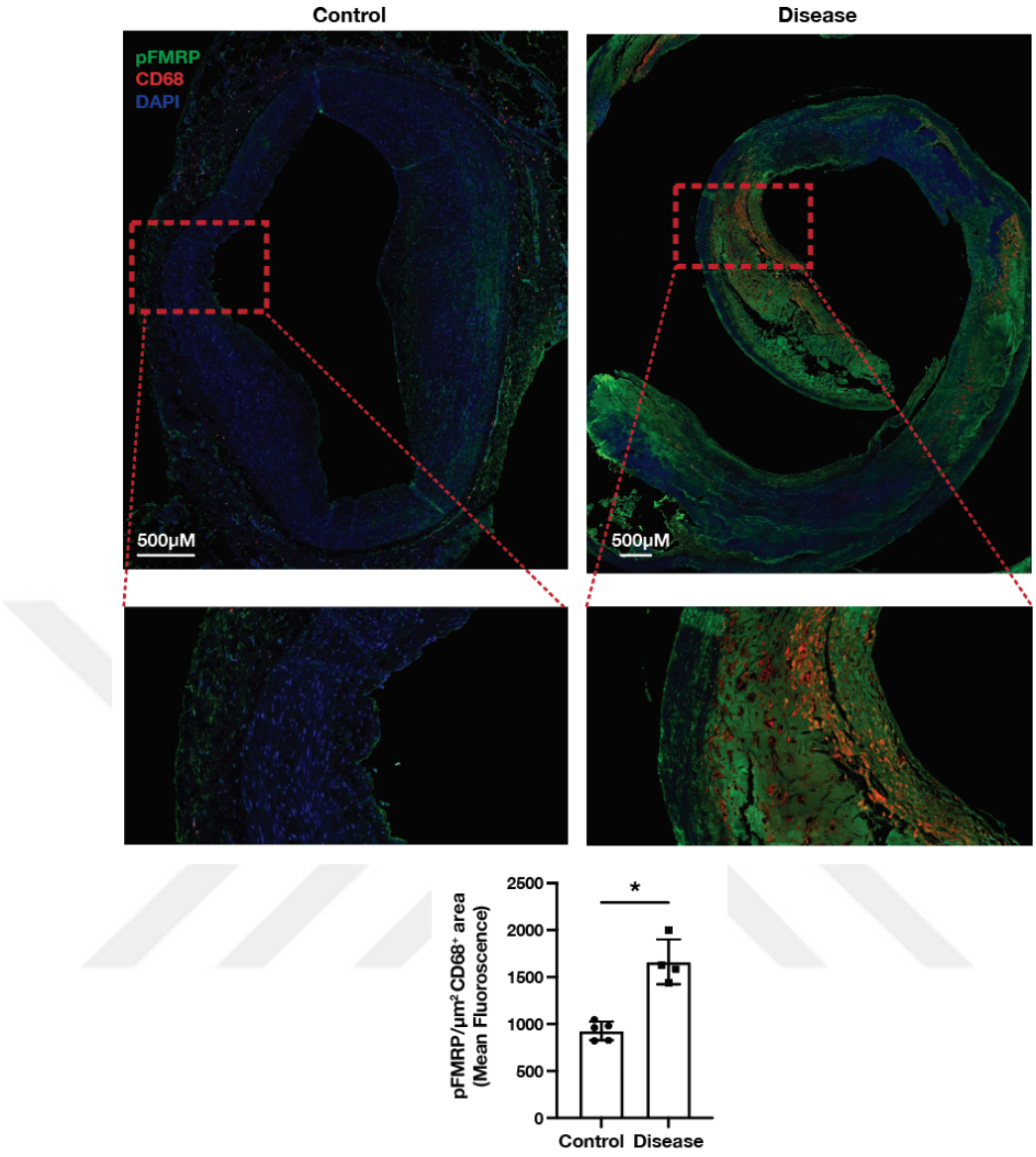

Figure 3.4. pFMRP is increased in foamy macrophages in human carotid artery plaques.

Parafilm sections from patients with atherosclerosis in carotid artery (disease) and no disease (control) groups were co-stained for CD68 (macrophages, red) and pFMRP (green) (n=5). pFMRP was quantified per μM2 $CD68^{+}$ area.

I next asked what role IRE1 plays in ER stress induced FMRP phosphorylation. To address this question, I transfected IRE1-specific siRNA to suppress IRE1 expression in a human cell line, followed by ER stress induction by a saturated fatty acid, palmitate (PA), that is known to induce ER stress, or TG. While both ER stressors induced the phosphorylation of IRE1 and FMRP, this was prevented in IRE1 knock-down cells (Fig 3.5A 3.5B).

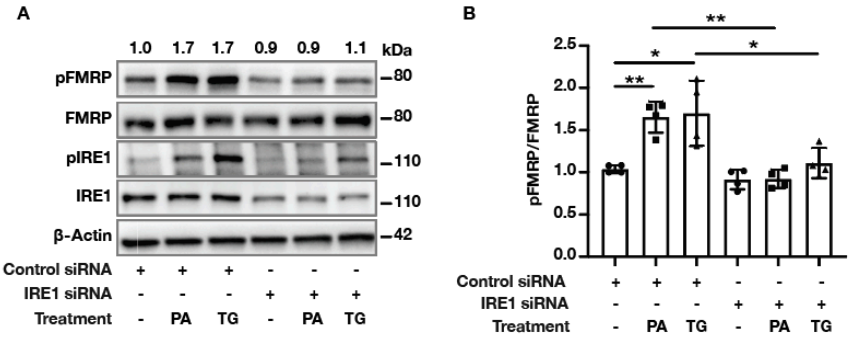

Figure 3.5. ER stress-induced FMRP phosphorylation is mediated by IRE1.

(A) Control- or IRE1-siRNA transfected HEK293T cells were stimulated by either PA (500 µM) or TG (600 nM) for 4 hours. Protein lysates were analyzed by western blotting using specific antibodies for pFMRP, FMRP, pIRE1, IRE1 and β-Actin. pFMRP/FMRP fold induction is depicted above the blots (n=4). **(B)** Western blot quantifications for pFMRP/FMRP ratio in Fig 3.5A.

In addition, I analyzed hypercholesterolemia-induced FMRP phosphorylation in PMs obtained from Apoe$^{-/-}$ mice with a genetic deletion of IRE1α in the myeloid lineage (IRE1$^{-/-}$) (see Methods) after feeding with CD or WD for 16 weeks. FMRP phosphorylation, but not FMRP protein or Fmr1 mRNA, was two-fold reduced ($p \leq 0.01$) in PM isolated from IRE1$^{-/-}$ mice when compared to those isolated from IRE1$^{+/+}$ mice (Fig 3.6A-C). While these results show a clear reduction of FMRP phosphorylation upon siRNA treatment or gene knock-out, I observed residual signal in both cases (Fig 3.5A and 3.6A).

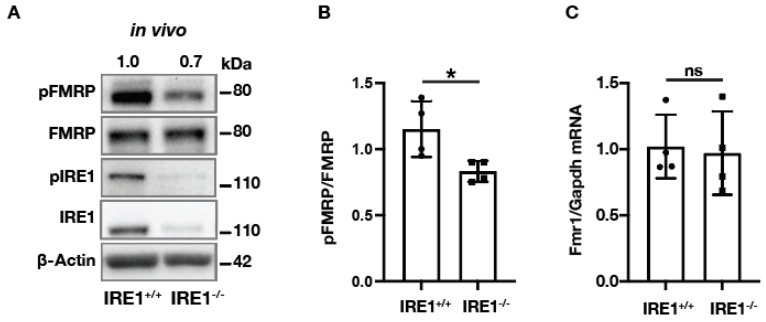

Figure 3.6. WD induced FMRP phosphorylation is regulated by IRE1.

(A) Protein lysates of thioglycolate-elicited PM from IRE1α$^{+/+}$ and IRE1α$^{-/-}$ mice (after 16 weeks on WD) were analyzed by western blotting using specific antibodies for

pFMRP, FMRP, pIRE1, IRE1 and β-Actin. pFMRP/FMRP fold induction is depicted above the blots (n=4). **(B)** Western blot quantifications for pFMRP/FMRP ratio in Fig1F. **(C)** qRT-PCR analysis for Fmr1 mRNA from the samples in Fig1F (n=6). For all experiments, a representative blot is shown from at least (n=3) independent experiments. Data are mean ± SEM. Unpaired *t*-test with Welch's correction or paired *t*-test. *P≤ 0.05, **P≤ 0.01, ***P≤ 0.001.

As I confirm below (Fig 3.9), the antibody used in these experiments is phosphorylation specific. I therefore surmise that partial phosphorylation on S500/S499 may also be mediated by the other kinases that are known to phosphorylate this residue on FMRP [143, 144], in addition to IRE1 as I show here. Collectively, my *in vitro* and *in vivo* results strongly support that ER stress-induced activation of IRE1 kinase leads to enhanced phosphorylation of FMRP on S500/S499.

3.2 IRE1 phosphorylates FMRP

To begin investigating the role of IRE1's kinase activity in ER stress-induced FMRP phosphorylation, I expressed a 3xFLAG-tagged IRE1 (FLAG-IRE1) and/or EGFP-FMRP in wild type MEFs. Tagged FMRP and IRE1 can be detected above endogenous FMRP and IRE1 as they are heavier due to the molecular weight of their tags. In all conditions, the MEFs were TG-treated (to stimulate IRE1 kinase activity) in the absence or presence of an IRE1 kinase-specific inhibitor (AMG-18) [91, 145-148]. In the absence of AMG-18, both IRE1 and FMRP were phosphorylated. AMG-18 treatment prevented IRE1 phosphorylation while clearly reducing FMRP phosphorylation (Fig 3.7A and 3.7B). While this data further supports the notion that IRE1 phosphorylates FMRP during ER stress, alternative kinase(s) appears to mediate the same reaction. This is consistent the published data that several kinases can phosphorylate the same residue on FMRP [143, 144]. Furthermore, in an in vivo setting where mice were injected with TM to induce IRE1 kinase activity, treatment with AMG-18 inhibited IRE1 kinase activity and reduced FMRP phosphorylation in PM (Fig 3.7C and 3.7D). Moreover, IRE1 RNase domain inhibition by specific inhibitor, 4μ8c, did not alter FMRP phosphorylation (Fig 3.7E, 3.7F and 3.7G). Taken together, my findings support the notion that IRE1 kinase activity makes an important contribution to ER stress-induced FMRP S499 phosphorylation in mouse macrophages and MEFs as well as S500 in HEK293T cells. My data also supports that other known

or unknown FMRP kinase(s) are responsible for basal FMRP phosphorylation that is observed in non-stress conditions.

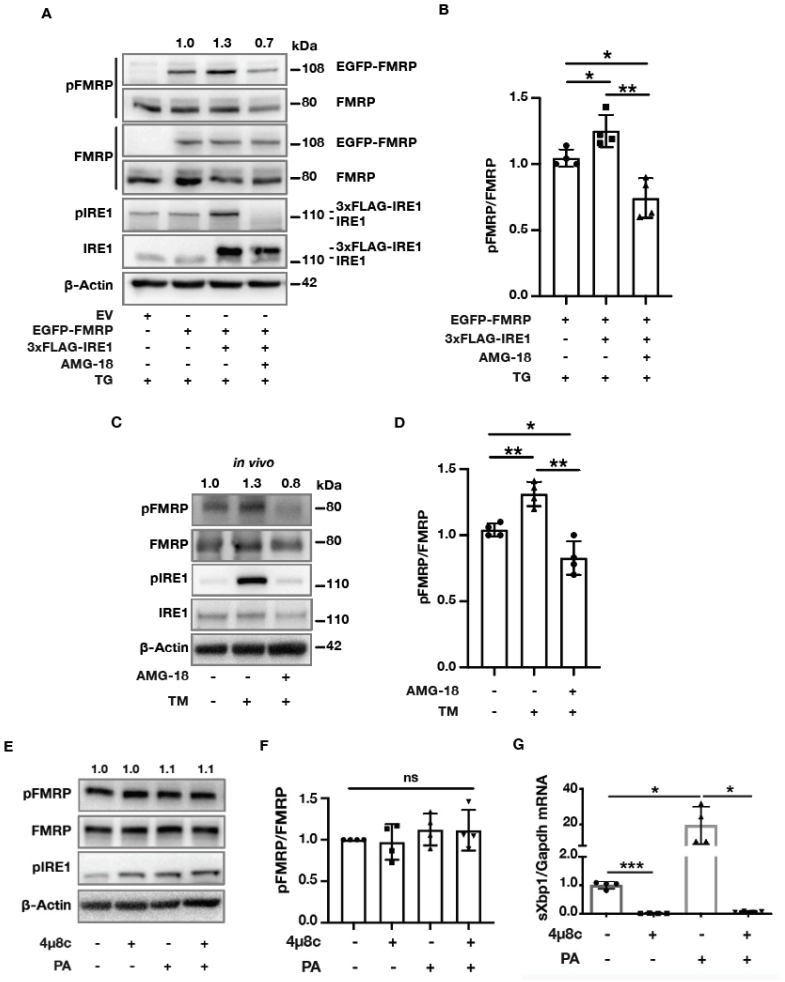

Figure 3.7. IRE1 Kinase domain dependent FMRP phosphorylation.

(A) MEF cells were transfected with either empty vector, EGFP-FMRP or 3xFLAG-IRE1 plasmids then pre-treated either with vehicle (DMSO) or AMG-18 (25 μM; 1 hour) followed by TG (600 nM) stimulation for 4 hours. Protein lysates were analyzed by western blotting using specific antibodies for pFMRP, FMRP, pIRE1, IRE1 and β-Actin. pFMRP/FMRP fold induction is depicted above the blots (n=4). **(B)** Western blot quantifications for pFMRP/FMRP ratio in Fig 3.7A. **(C)** C57BL/6 were injected either with DMSO or AMG-18 (30 mg/kg; 8 hours), followed by TM injection (1 mg/kg; 8 hours). Protein lysates of thioglycolate-elicited PM were analyzed by western blotting using antibodies for pFMRP, FMRP, pIRE1, IRE1 and β-Actin. pFMRP/FMRP fold induction is depicted above the blots (n=4). **(D)** Western blot quantifications for pFMRP/FMRP ratio in Fig 3.7C. **(E)** BMDM cells were collected from C57BL/6 mice and pre-treated with 4μ8c (100μM) followed by PA (500 μM) for 6 hours (n=4). **(F)** Western blot quantifications for pFMRP/FMRP ratio in Fig 3.7E. **(G)** qRT-PCR analysis for Xbp1s mRNA from the samples in Fig 3.7E (n=6). For all experiments, a representative blot is shown from at least (n=3) independent experiments. Data are mean ± SEM. Unpaired t-test with Welch's correction or paired t-test. *P≤ 0.05, **P≤ 0.01, ***P≤ 0.001.

To ask whether IRE1 can phosphorylate FMRP directly, I employed *in vitro* assays. To this end, I immunoprecipitated wild type (WT) or kinase dead (KD) mutant IRE1 from HEK293T cells (after treating with ER stressor) and incubated the immunoprecipitates with purified, recombinant human FMRP protein in a kinase reaction. The reaction included ATP-γ-S instead of ATP, which allows kinases to thio-phosphorylate their substrates. The resultant kinase reaction was analyzed by Western blotting using an anti-thiophosphate ester antibody. In the reaction containing IRE1-WT, both proteins were thio-phosphorylated, but not in the reaction containing the IRE1-KD mutant (Fig 3.8A). To determine the specific amino acids phosphorylated by IRE1, I performed the kinase reaction using purified, recombinant human IRE1-kinase/RNase domains (amino acids 468-977) and human FMRP proteins. Both IRE1 and FMRP were phosphorylated in this reaction in an AMG-18-sensitive manner (Fig 3.8B). Liquid chromatography-mass spectrometry (LC-MS/MS)-based analysis of the phosphorylated FMRP residues in this kinase reaction revealed eight IRE1-induced phosphorylation sites on FMRP at serine (S362, S494, S497, S500, S504) and threonine (T502, T592, T594) (Fig 3.8B, 3.8C and 3.8D) Data are available via ProteomeXchange with identifier PXD030594). Importantly, S500 in human FMRP) is the previously identified FMRP phosphorylation site that was shown to enhance FMRP-mediated translational suppression [143, 144, 149-153].

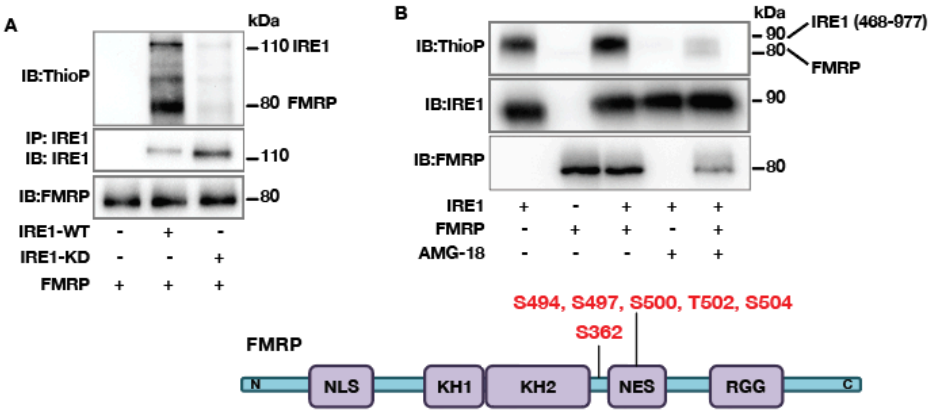

AA	Sequence	z	XCorr	DeltaCN	[M+H]+	A-Score
pS362	HLDIKEN*pS*THFSQPNSTK	3	2.8194	0.3306	2162.9890	14.23
	KHLDIKEN*pS*THFSQPNSTK	3	3.2526	0.3569	2291.0808	33.7
	KHLDIKEN*pS*THFSQPNSTK	4	3.4197	0.2304	2291.0813	34.46
pS494	RGPGYTSGTN*pS*EASNA	2	3.0995	0.4448	1648.6614	13.27
pS497	RGPGYTSGTNSEA*pS*NASETESDHRDELSDWSLAPTEEERE	4	3.457	0.3924	4476.8633	7.81
pS500	*pS*ETESDHRDELSDW	2	3.1722	0.3710	1785.6604	22.85
	NA*pS*ETESDHRDELSDW	2	3.1225	0.3763	1970.7406	30.93
>	**NA*pS*ETESDHRDELSDW**	**2**	**4.0257**	**0.4280**	**1970.7393**	**39.56**
	NA*pS*ETESDHRDELSDW	2	3.3907	0.3348	1970.7386	33.68
pT502	RGPGYTSGTNSEASNASE*pT*ESDHRDELSDWSLAPTEEERE	4	6.2067	0.5107	4476.8564	4.6
pS504	SETE*pS*DHRDELSDW	2	3.431	0.3944	1785.6588	15.5
pT592	SVH*pT*KTLQNTSSEGSR	3	3.996	0.2936	1811.8281	6.17
	SVH*pT*KTLQNTSSEGSR	3	4.4606	0.3795	1811.8282	7.53
	SVH*pT*KTLQNTSSEGSR	3	3.5417	0.3859	1811.8276	11.79
pT594	SVHTK*pT*LQNTSSEGSR	3	3.1378	0.3386	1811.8282	10.36

Figure 3.8. FMRP is phosphorylated by IRE1.

(A) HEK293T cells were transfected with either empty vector (EV), IRE1-WT or IRE1–KD plasmids and stimulated by TG (600 nM; 1 hour). Protein lysates from each transfection were separately immunoprecipitated (IP) with anti-IRE1 antibody and subjected to a kinase reaction with purified hFMRP protein and ATP-γ-S (100 μM) in kinase buffer. The IP protein were analyzed by western blotting using specific antibodies for thiophosphate esters (ThioP), IRE1 and FMRP (n=3). **(B)** Purified FMRP and IRE1 kinase (activated) proteins were subjected to kinase assay and analyzed by western blotting using specific antibodies for ThioP, IRE1 and FMRP (n=3) and with LC-MS/MS. Identified IRE1 kinase-mediated FMRP phosphorylation sites. **(C)** pFMRP sequence covered (83%) with two different digestion strategies – Proteinase K (red text) and Trypsin-GluC (highlighted yellow) using LC-MS/MS in samples from Fig 3.8B. **(D)** LC-MS/MS identified phosphorylated peptides from the samples in Fig 3.8B; with sites of phosphorylation (AA), charge state (*z*), identification parameters (XCorr and DeltaCN – greater values indicate higher confidence by peptide-spectrum match/PSM), measured precursor mass ($[M+H]^+$), and a confidence score for localization of phosphorylation on an amino acid (A-Score, value > 19 and > 13, represent > 99% and > 95% confidence, respectively); the peptide marked with (>) was evaluated further. For all experiments, a representative blot is shown from at least (n=3) independent experiments. Data are mean ± SEM. Unpaired *t*-test with Welch's correction or paired *t*-test. *P≤ 0.05, **P≤ 0.01, ***P≤ 0.001.

Using site-directed mutagenesis, I engineered two mutant versions of FMRP, in which I either changed S500 to alanine (SA mutant) or S500, T502, and S504 to alanine (STSA triple mutant) to block phosphorylation at S500 and amino acids in its proximity. I then induced ER stress with PA in $Fmr1^{-/-}$ MEFs transiently transfected with wild type (WT) FMRP and FMRP mutants (SA and STSA). PA induced FMRP phosphorylation in WT FMRP-reconstituted cells but failed to do so in cells expressing the SA and STSA mutants of FMRP (Fig 3.9). These data confirm the specificity of the FMRP antibody for phosphorylated S500 and is consistent with the notion that IRE1 kinase directly phosphorylates human FMRP protein on S500.

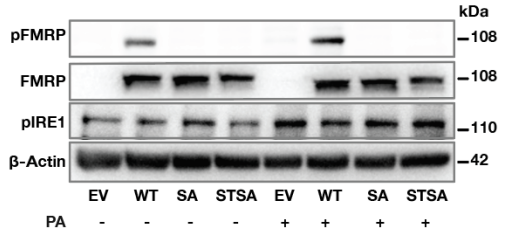

Figure 3.9. Site-directed mutagenesis of phospho-sites on FMRP.

$Fmr1^{-/-}$ MEF were transfected either with EV, WT-FMRP, SA-FMRP or STSA-FMRP plasmids followed by PA treatment (500 μM; 6 hours). Protein lysates were analyzed by western blotting using specific antibodies for FMRP, pFMRP, pIRE1 and β-Actin. pFMRP/FMRP fold induction is depicted above the blots (n=3). A representative blot is shown from at least (n=3) independent experiments.

3.3 IRE1-FMRP Signaling Induce Foam Cell formation

I next wondered what role FMRP plays in macrophage biology that is relevant to atherosclerotic plaque development. I performed an *in vivo* macrophage foam cell formation assay in the peritoneum of $Fmr1^{-/-}$ and $Fmr1^{+/+}$ mice, using a well-established method in which I induced hyperlipidemia using a combination of adenoviral-delivery of proprotein convertase subtilisin kexin 9 (AAV_PCSK9), a protein that directs hepatic low density lipoprotein (LDL) receptors for degradation, and feeding with WD for 16 weeks [154-156]. FMRP-deficiency significantly reduced foam cell formation *in vivo* (Fig 3.10A). Next, I fed $Apoe^{-/-}$ mice with a WD (12 weeks) and injected them daily? with the IRE1 kinase inhibitor, AMG-18, or vehicle for the last 4 weeks. AMG-18 reduced foam cell formation in the peritoneum *in vivo* (Fig

3.10B). This result indicates that IRE1-FMRP signaling axis enhances foam cell formation *in vivo*.

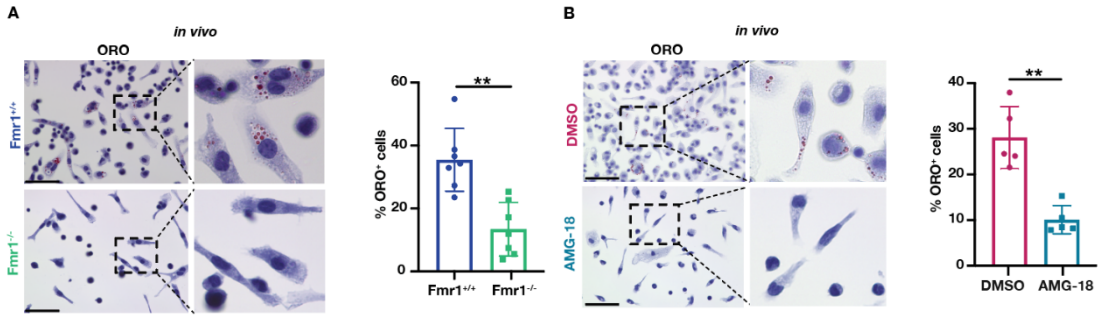

Figure 3.10. FMRP deficiency reduce foam cell formation *in vivo*.

(A) Fmr1$^{+/+}$ and Fmr1$^{-/-}$ mice were injected with AAV_PCSK9 and fed with 16 weeks of WD. Residential PM were stained with Oil Red O (ORO) and imaged (n=7; Scale bar = 50 µm). **(B)** Apoe-/- mice were fed with WD (12 weeks) and injected with vehicle (DMSO) or AMG-18 (30 mg/kg/day) in the last 4 weeks of WD. Residential PM were stained with ORO and imaged (n=5; Scale bar = 50 µm). Data are mean ± SEM. Unpaired t-test with Welch's correction. *P≤ 0.05, **P≤ 0.01, ***P≤ 0.001.

I further validated my *in vivo* results by transfecting wild type BMDMs with either Fmr1-specific or control siRNA and followed by loading the cells with 3,3'-dioctadecylindocarbocyanine (dil)-labeled acetylated LDL (Ac-LDL) [157]. Flow cytometry analysis revealed that Fmr1 silencing significantly reduced cholesterol accumulation in macrophages (Fig 3.11A and 3.11B). Likewise, Fmr1$^{-/-}$ BMDM displayed reduced foam cell formation when compared to Fmr1$^{+/+}$ BMDM (Fig 3.11C). A similar reduction in foam cell formation was observed with the IRE1 kinase inhibitor (Fig 3.11D).

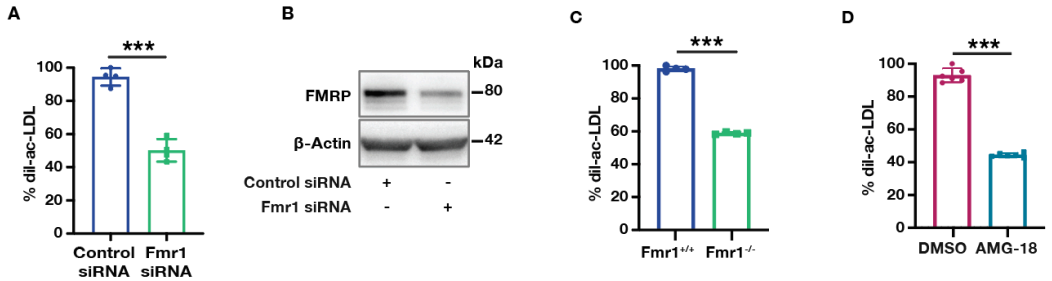

Figure 3.11. FMRP regulates foam cell formation *in vitro*.

(A) Flow cytometry analysis of control- or Fmr1-siRNA transfected BMDM after dil-ac-LDL (25 µg/ml) loading for 24 hours (n=4). **(B)** Protein lysates from macrophages

used in Fig 3.11A were analyzed by western blotting using specific antibodies for FMRP and β-Actin. **(C)** Flow cytometry analysis of $Fmr1^{+/+}$ and $Fmr1^{-/-}$ BMDM after dil-ac-LDL (25 µg/ml) loading for 24 hours (n=5). **(D)** Flow cytometry analysis of BMDMs pre-treated with either vehicle (DMSO) or AMG-18 (5 µM; 1 hour) after dil-ac-LDL (25 µg/ml) loading for 24 hours (n=6). Data are mean ± SEM. Unpaired *t*-test with Welch's correction. *P≤ 0.05, **P≤ 0.01, ***P≤ 0.001.

These results show that both the inhibition of IRE1 kinase activity and the genetic deletion of its proposed substrate, FMRP, reduce foam cell formation *in vitro* and *in vivo*. Reduced foam cell formation could be explained with less cholesterol uptake and/or increased cholesterol efflux. Both FMRP knock down and IRE1 kinase inhibition did not alter cholesterol uptake in macrophages (Fig 3.12A). I reasoned that this observation could be related to an increase in cholesterol export (RCT; due to increased translation of cholesterol exporters) from $Fmr1^{-/-}$ macrophages. Indeed, FMRP deficiency led to an increase in cholesterol efflux coupled to its loading onto the cholesterol carriers, apolipoprotein-A1 (APOA1) and HDL (Fig 3.12B), and, likewise, the IRE1 kinase inhibitor enhanced cholesterol efflux (Fig 3.12C). Thus, ER stress-associated reduction in cholesterol efflux is dependent on both IRE1 kinase activity and FMRP.

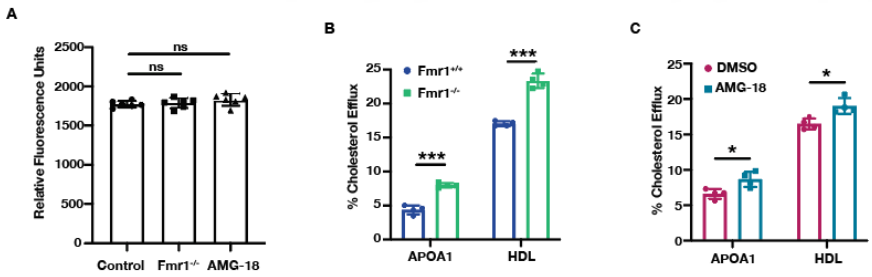

Figure 3.12. FMRP blocks cholesterol efflux.

(A) $Fmr1^{-/-}$ or AMG-18 pre-treated cells (10 µM, 1 hour) were treated with fluorescently labeled cholesterol for 4 hours (n=6). **(B-C)** Macrophages were pre-loaded with fluorescently labeled cholesterol (16 hours) followed by incubation in efflux medium including APOA1 (25 µg/ml) or HDL (50 µg/ml) as acceptors for 6 hours. % Efflux was calculated as cholesterol signal in medium/cholesterol signal in medium and cell: Cholesterol efflux in (B) $Fmr1^{+/+}$ and $Fmr1^{-/-}$ BMDM (n=4) and in **(C)** BMDM that were pre-treated either with DMSO or AMG-18 (5 µM; 1 hour) (n=4). Data are mean ± SEM. Unpaired *t*-test with Welch's correction. *P≤ 0.05, **P≤ 0.01, ***P≤ 0.001.

Next, I determined whether the absence of FMRP in BMDMs also enhances RCT in vivo. To this end, I pre-loaded Fmr1$^{+/+}$ and Fmr1$^{-/-}$ BMDMs with [^{3}H]-cholesterol and injected the cells subcutaneously into WT mice (Fig 3.13A). FMRP-deficiency in macrophages significantly increased radioactivity counts ([^{3}H]-cholesterol) in the plasma, liver, and feces of the recipient mice, when compared to recipient mice that received Fmr1$^{+/+}$ macrophages (Fig 3.13B-D), demonstrating that FMRP-deficiency in macrophages enhances RCT in mice.

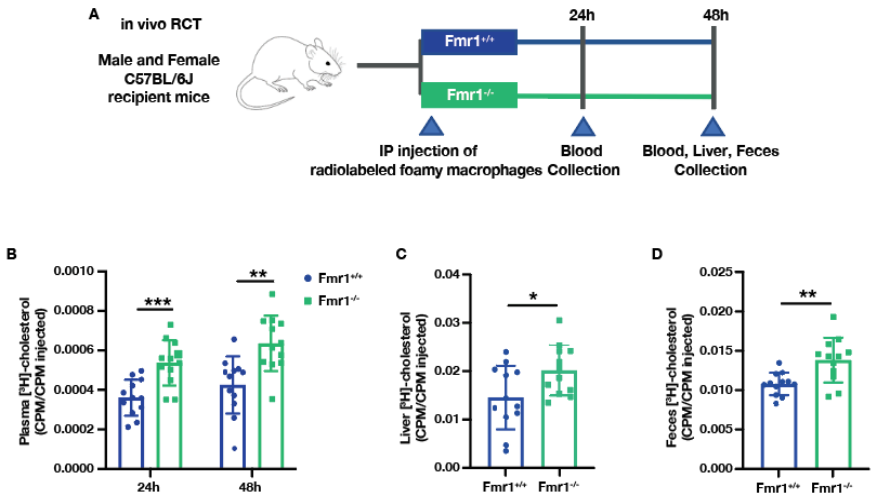

Figure 3.13. FMRP deficiency enhances RCT.

(A) Schematic representation of C57BL6 mice were injected with [^{3}H]-cholesterol-loaded foamy Fmr1$^{+/+}$ and Fmr1$^{-/-}$ BMDM, **(B)** plasma cholesterol levels after 24 and 48 hours, **(C)** liver cholesterol levels after 48 hours, and **(D)** feces cholesterol levels after 48 hours (n=12). Data are mean ± SEM. Unpaired *t*-test with Welch's correction. *P≤ 0.05, **P≤ 0.01, ***P≤ 0.001.

3.4 FMRP Regulates Macrophage Efferocytosis

I next investigated the impact of FMRP-deficiency on efferocytosis, a primary process that promotes atherosclerotic plaque regression by removing apoptotic macrophages in the lesion area. To this end, I transfected BMDM (red fluorescent-stained) with Fmr1-specific or control siRNA and incubated them with green fluorescent-labeled ACs, in which apoptosis was induced by ultraviolet (UV) irradiation. FMRP knock-down increased efferocytosis of ACs (as measured by colocalization of the fluorescent markers), when compared to control (Fig 3.14A). FMRP-deficient BMDMs also

increased efferocytosis when compared to wild type BMDMs under both no-stress and PA-induced ER stress conditions (Fig 3.14B).

Next, I induced hyperlipidemia in Fmr1$^{-/-}$ and Fmr1$^{+/+}$ mice as described above using a combination of AAV_PCSK9 injection and feeding with a WD. I then injected the mice intraperitoneally with green fluorescent-labeled ACs and harvested PM macrophages. FMRP-deficient PMs displayed enhanced efferocytosis compared to WT PMs (Fig 3.14C).

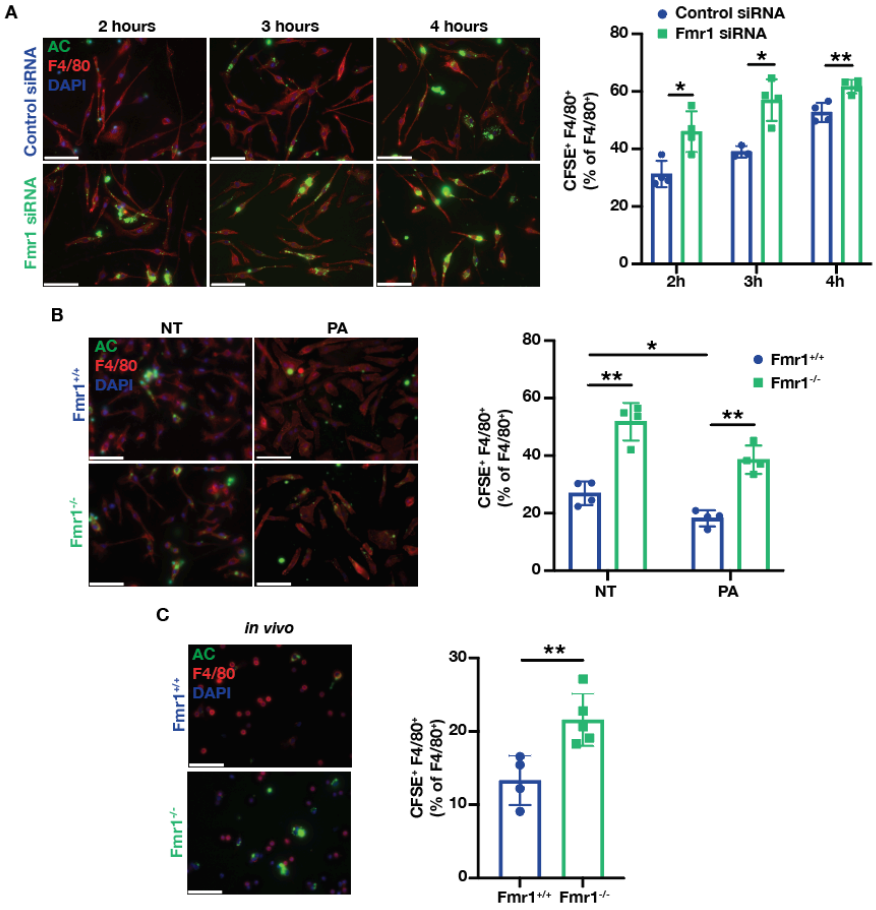

Figure 3.14. FMRP deficiency increases efferocytosis *in vivo*.

(A-C) *In vitro* and *in vivo* efferocytosis experiments, where percentage of macrophages F4/80^{+} (red) that ingested apoptotic cells (AC) labeled with carboxyfluorescein succinimidyl ester (CFSE)$^{+}$ (green) were reported as % efferocytosis: **(A)** BMDMs were transfected with Fmr1- or control-siRNA and incubated CFSE-labeled AC for the indicated hours (n=4), **(B)** Fmr1$^{+/+}$ and Fmr1$^{-/-}$ BMDMs were treated with PA (500 µM) for 6 hours and then incubated with CFSE-labeled ACs for 4 hours (n=4), **(C)** Fmr1$^{+/+}$ and Fmr1$^{-/-}$ mice were fed WD (16 weeks) and injected intraperitoneally with CFSE-labeled AC (1.5 hours), followed by PM elicitation (n=4-5). For all images scale bar = 50 µm; Red: Macrophages, Green: AC. Data are mean ± SEM. Unpaired *t*-test with Welch's correction. *P≤ 0.05, **P≤ 0.01, ***P≤ 0.001.

I next asked how IRE1 kinase activity impacts efferocytosis by macrophages. I observed that AMG-18 increased efferocytosis of ACs in BMDMs (Fig 3.15A). Next, I injected wild type mice with AMG-18 (for 8 hours) followed by injection of green fluorescent-labeled ACs. AMG-18 also induced efferocytosis of ACs by PM *in vivo* (Fig 3.15B).

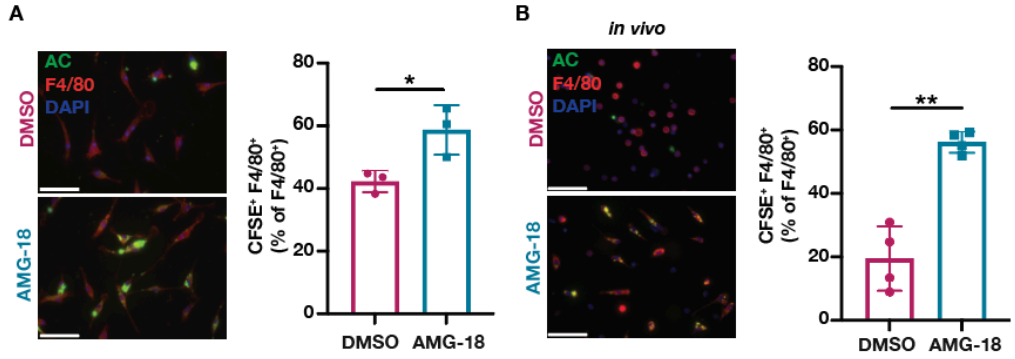

Figure 3.15. IRE1 kinase domain regulates efferocytosis.

(A-B) *In vitro* and *in vivo* efferocytosis experiments, where percentage of macrophages F4/80^{+} (red) that ingested apoptotic cells (AC) labeled with carboxyfluorescein succinimidyl ester (CFSE)$^{+}$ (green) were reported as % efferocytosis: **(A)** BMDM were pre-treated either with vehicle (DMSO) or AMG-18 (5 µM) for 1 hour then incubated with CFSE-labeled ACs for 4 hours (n=4), **(B)** C57BL/6 mice were injected with AMG-18 (30 mg/kg) or vehicle (DMSO) for 8 hours, followed by intraperitoneal injection with CFSE-labeled ACs for 1.5 hours and PM elicitation (n=4). For all images scale bar = 50 µm; Red: Macrophages, Green: AC. Data are mean ± SEM. Unpaired *t*-test with Welch's correction. *P≤ 0.05, **P≤ 0.01, ***P≤ 0.001.

Continued clearance of ACs by macrophages prevents the accumulation of necrotic cells and is an important process that promotes atherosclerosis regression [17]. To determine whether Fmr1$^{-/-}$ macrophages can efficiently internalize multiple ACs over consecutive rounds of engulfment, I incubated macrophages with green fluorescent-labeled AC for 2 hours, followed by second incubation with violet fluorescent-labeled AC for 2 more hours. FMRP-deficient BMDMs displayed an increase in continued efferocytosis when compared to wild type BMDMs (Fig 3.16A). Likewise, treatment of wild type BMDM with AMG-18 enhanced continued efferocytosis of ACs (Fig 3.16B). Collectively, these results demonstrate that the ablation of IRE1 kinase activity and its proposed substrate, FMRP, enhances efferocytosis *in vitro* and *in vivo*.

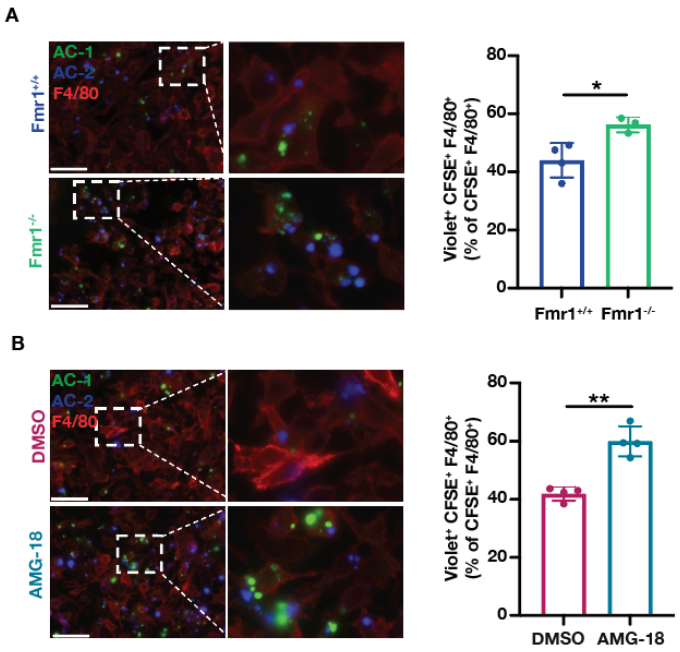

Figure 3.16. Both FMRP and IRE1 kinase inhibition enhances continuous clearance of apoptotic cells.

(A-B) *In vitro* continuous *efferocytosis experiments,* where macrophages were stained for F4/80^{+} (red), AC were labeled with CFSE (AC-1; green) or Violet (AC2; violet). % continuous efferocytosis was determined by the ratio of F4/80^{+}, CFSE^{+} and Violet^{+} (triple positive) cells to total F4/80^{+} and CFSE^{+} (double positive) cells: **(A)** Fmr1$^{+/+}$ and Fmr1$^{-/-}$ BMDM were incubated with AC-1 for 2 hours, and after 2 hours interval, incubated with AC-2 for 2 more hours (n=4-3); **(B)** BMDM were pre-treated either with vehicle (DMSO) or AMG-18 (5 µM) for 1 hour, incubated with CFSE-labeled AC-1 for 2 hours, followed by incubation with Violet-labeled AC-2 for 2 hours and PM collection (n=4). For all images scale bar = 50 µm; Red: Macrophages, Green: AC/AC-1, Violet: AC-2. Data are mean ± SEM. Unpaired *t*-test with Welch's correction. *P≤ 0.05, **P≤ 0.01, ***P≤ 0.001.

3.5 Translational Suppression of Cholesterol Transporters and Efferocytosis Regulators by FMRP during ER Stress

Consistent with my observations that macrophage FMRP plays a role in suppressing cholesterol efflux and efferocytosis, published data describing the FMRP-RNA interactome also suggest that FMRP interacts with mRNAs encoding proteins involved in cholesterol trafficking (such as Abca1 and Abcg1) and efferocytosis receptors (such as c-Mer tyrosine kinase (Mertk) and LDL Receptor-Related Protein 1 (Lrp1)), suggesting FMRP may impair their translation (Fig 3.17A) [105, 158].

I first sought to unravel the mechanism behind the FMRP regulated target mRNA expression. 3' untranslated region (UTR) analysis revealed that cholesterol transporters; Abca1, Abcg1 and efferocytosis receptors; Mertk, Lrp1 seed sequences contain multiple FMRP binding sites; ACUG and UGGA (Fig 3.17B).

In order to confirm that FMRP regulates 3'UTR of Abca1, Abcg1 and Mertk, luciferase reporters were co-transfected either with EV or FMRP. Overexpression of FMRP resulted in significant decrease in Abca1, Abcg1 and Mertk 3'UTR-controlled translation of the luciferase proteins in both no treatment and stress conditions. Additionally, TG treatment alone, which also promotes FMRP phosphorylation, decreased luciferase activity of target mRNAs (Fig 3.17C-3.17E).

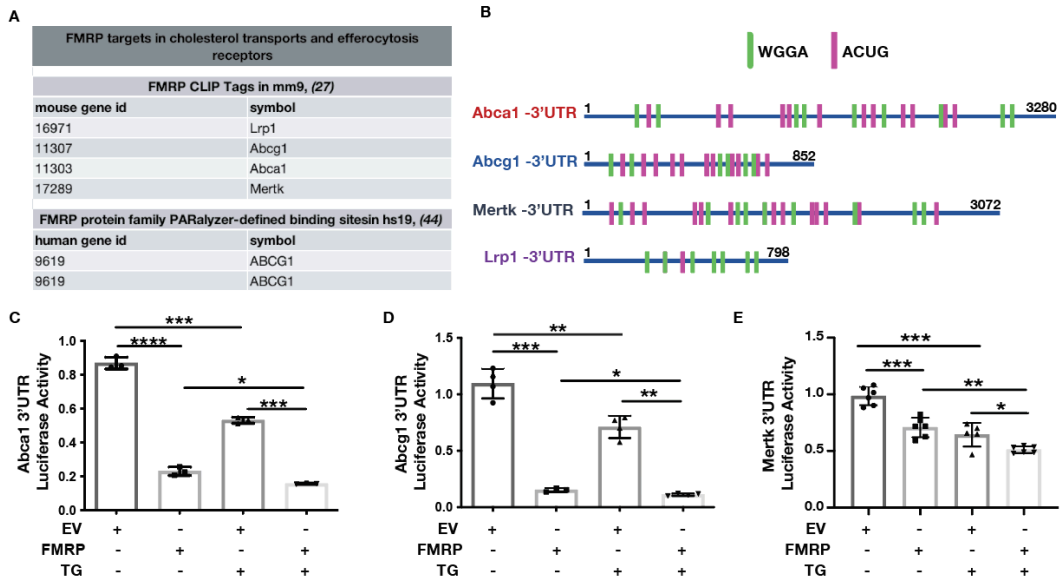

Figure 3.17. FMRP regulates translation of cholesterol transporters and efferocytosis regulators.

(A) FMRP mRNA targets determent from crosslinking-immunoprecipitation (CLIP) assay. **(B)** Schematic representation of FMRP binding motifs on target mRNA 3'UTRs. **(C-E)** HEK293TT cells were transfected with either EV or WT-FMRP plasmid, together with **(C)** Abca1 3′UTR (n=3), **(D)** Abcg1 3′UTR (n=4) or **(E)** Mertk 3′UTR (n=6). All conditions were co-transfected with firefly control plasmid. 24 hours later cells were treated either with TG (300 nM) or vehicle (DMSO) for 6 hours. Luciferase activity was normalized to Firefly activity. Results are representative of at least n=3 independent experiments. Data are mean ± SEM. Unpaired *t*-test with Welch's correction. *P≤ 0.05, **P≤ 0.01, ***P≤ 0.001.

3.6 Polysome Profiling and RNA Sequencing in Fmr1$^{-/-}$ Macrophages.

To assess the mRNA regulation by FMRP in ER stress induced macrophages, I performed polyribosome profiling in Fmr1$^{+/+}$ and Fmr1$^{-/-}$ BMDMs. I used PA as ER stressor, where FMRP is phosphorylated by IRE1 (Fig 3.18A). Overall mRNA distribution between the groups did not show any significant changes (Fig 3.18B).

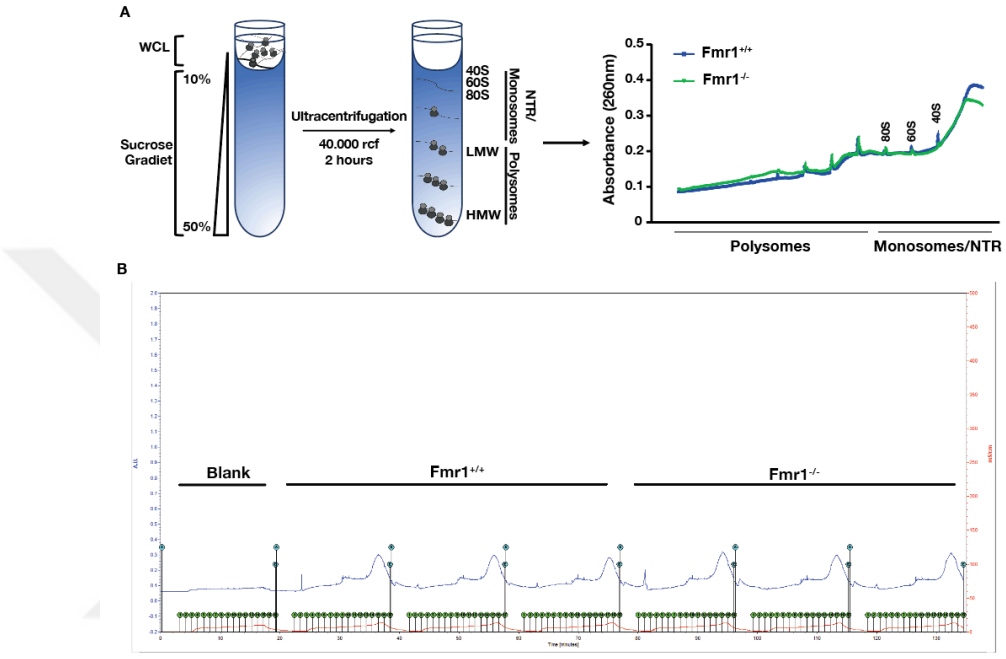

Figure 3.18. Polysome profiling in Fmr1$^{-/-}$ macrophages.

(A-B) RNA lysates from Fmr1$^{+/+}$ and Fmr1$^{-/-}$ BMDM that were treated with PA (500 µM) for 6 hours were fractionated using a 10%-50% sucrose gradient and separated to polysome, monosome/non-translating RNA (NTR). The absorbance (260 nm) of RNA was measured and plotted as a function of time (n=3). **(A)** Representative profile for RNA distribution from genotypes based on UV absorbance readings after sucrose gradient fractionation. **(B)** mRNA distribution after fractionation in Fmr1$^{+/+}$ and Fmr1$^{-/-}$ macrophages.

I analyzed the pooled fractions from each replicate as HMW, LMW and NTR by RNA-Sequencing. Supporting my previous findings, enrichment pilots revealed increased translation of mRNAs that are involved in fat-digestion and absorption, ABC-transporters, phagosome, and lysosome pathways that regulate cholesterol efflux and efferocytosis (Fig 3.19). Heat maps of individual proteins that are involved in these pathways show significant increase (Fig 3.20).

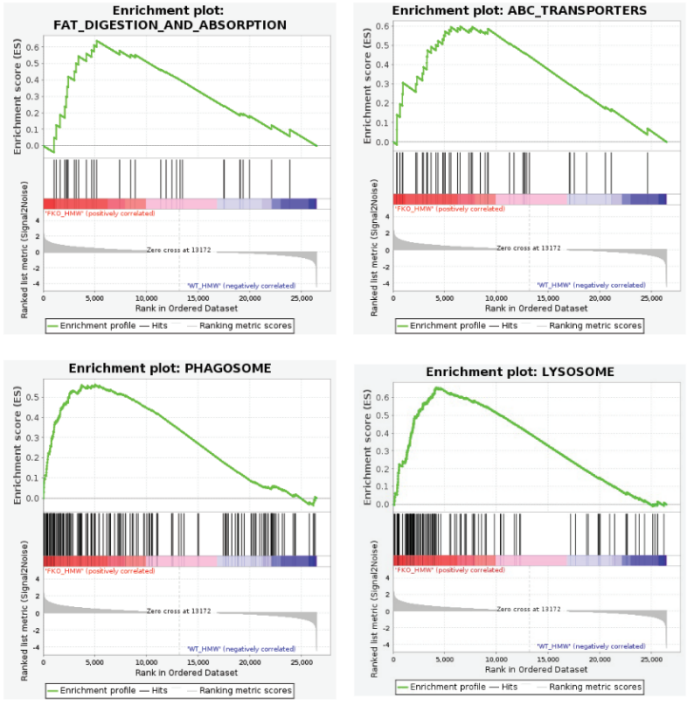

Figure 3.19. mRNA enrichment pilots from RNA-seq of HMW polysome fractions.

RNA lysates from Figure 3.18 pooled as HMW, LMW and NTR and analyzed by RNA sequencing. Enrichment pilots were prepared for HMW fractions from Fmr1$^{-/-}$ compared to Fmr1$^{+/+}$.

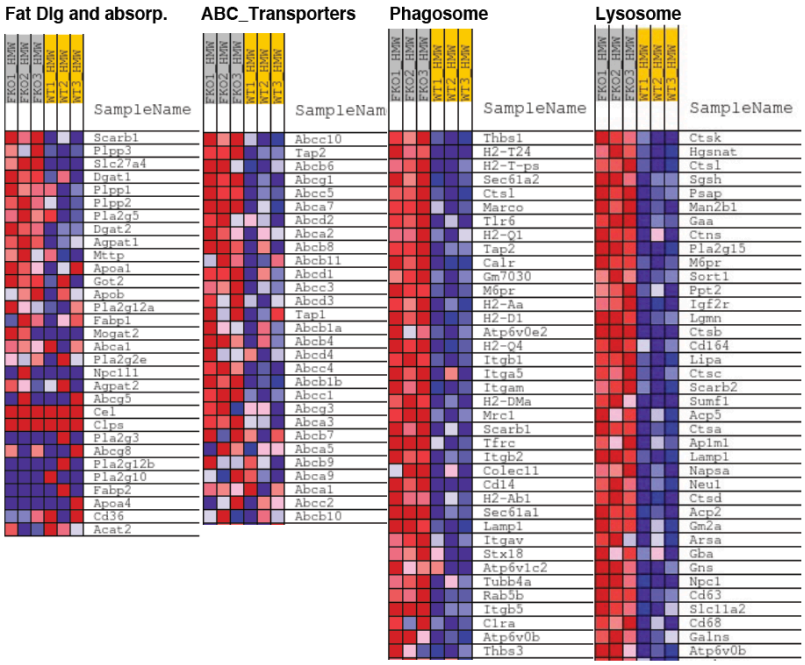

Figure 3.20. List of mRNAs enriched in HMW polysome fractions.

RNA lysates from Figure 3.18 pooled as HMW, LMW and NTR and analyzed by RNA sequencing. Heat maps of the mRNAs involved in enrichment pilots were prepared for HMW fractions from Fmr1$^{-/-}$ compared to Fmr1$^{+/+}$.

Next, ingenuity pathway analysis (IPA) was performed to identify canonical pathways, diseases, and bio functions in the polled fractions. Top enriched canonical pathways highlighted EIF2 signaling, mitochondrial dysfunction, oxidative phosphorylation, protein ubiquitination, EIF4 and p70S6K signaling pathways. Diseases and bio functions list revealed high number of molecules involved in cancer, organismal injury, endocrine system, infectious diseases, and gastrointestinal diseases (Fig 3.21). Other top enriched pathways are shown in Fig 3.22, where cholesterol biosynthesis, phagocytosis, inflammasome and ER stress pathways are enriched.

Top Canonical Pathways

Name	p-value	Overlap
EIF2 Signaling	4.77E-19	31.7 % 71/224
Mitochondrial Dysfunction	2.20E-15	32.2 % 55/171
Oxidative Phosphorylation	4.12E-14	36.9 % 41/111
Protein Ubiquitination Pathway	6.89E-13	25.1 % 69/275
Regulation of eIF4 and p70S6K Signaling	4.33E-12	28.5 % 51/179

Top Diseases and Bio Functions

Diseases and Disorders

Name	p-value range	# Molecules
Cancer	4.89E-09 - 2.35E-93	2285
Organismal Injury and Abnormalities	4.97E-09 - 2.35E-93	2325
Endocrine System Disorders	1.92E-11 - 2.65E-51	1808
Infectious Diseases	2.41E-10 - 2.68E-38	547
Gastrointestinal Disease	4.89E-09 - 6.92E-38	1960

Molecular and Cellular Functions

Name	p-value range	# Molecules
Protein Synthesis	1.47E-09 - 1.57E-42	446
Cell Death and Survival	4.36E-09 - 5.22E-41	913
Cellular Compromise	3.54E-09 - 2.29E-24	217
Cellular Movement	2.83E-09 - 2.77E-24	609
Cell Cycle	2.52E-09 - 1.51E-23	424

Physiological System Development and Function

Name	p-value range	# Molecules
Organismal Survival	8.37E-17 - 2.88E-36	711
Hematological System Development and Function	3.26E-09 - 9.90E-25	577
Tissue Morphology	8.64E-10 - 9.90E-25	528
Lymphoid Tissue Structure and Development	8.64E-10 - 1.33E-24	428
Immune Cell Trafficking	3.26E-09 - 2.77E-24	373

Figure 3.21. Top enriched canonical pathways and top enriched diseases and bio functions in Fmr1$^{-/-}$ macrophages.

RNA lysates from Fig 3.18 pooled as HMW, LMW and NTR and analyzed by RNA sequencing. Top canonical pathways, top disease and biological functions, determined by IPA analysis, are shown for mRNAs in HMW fractions from Fmr1$^{-/-}$ compared to Fmr1$^{+/+}$.

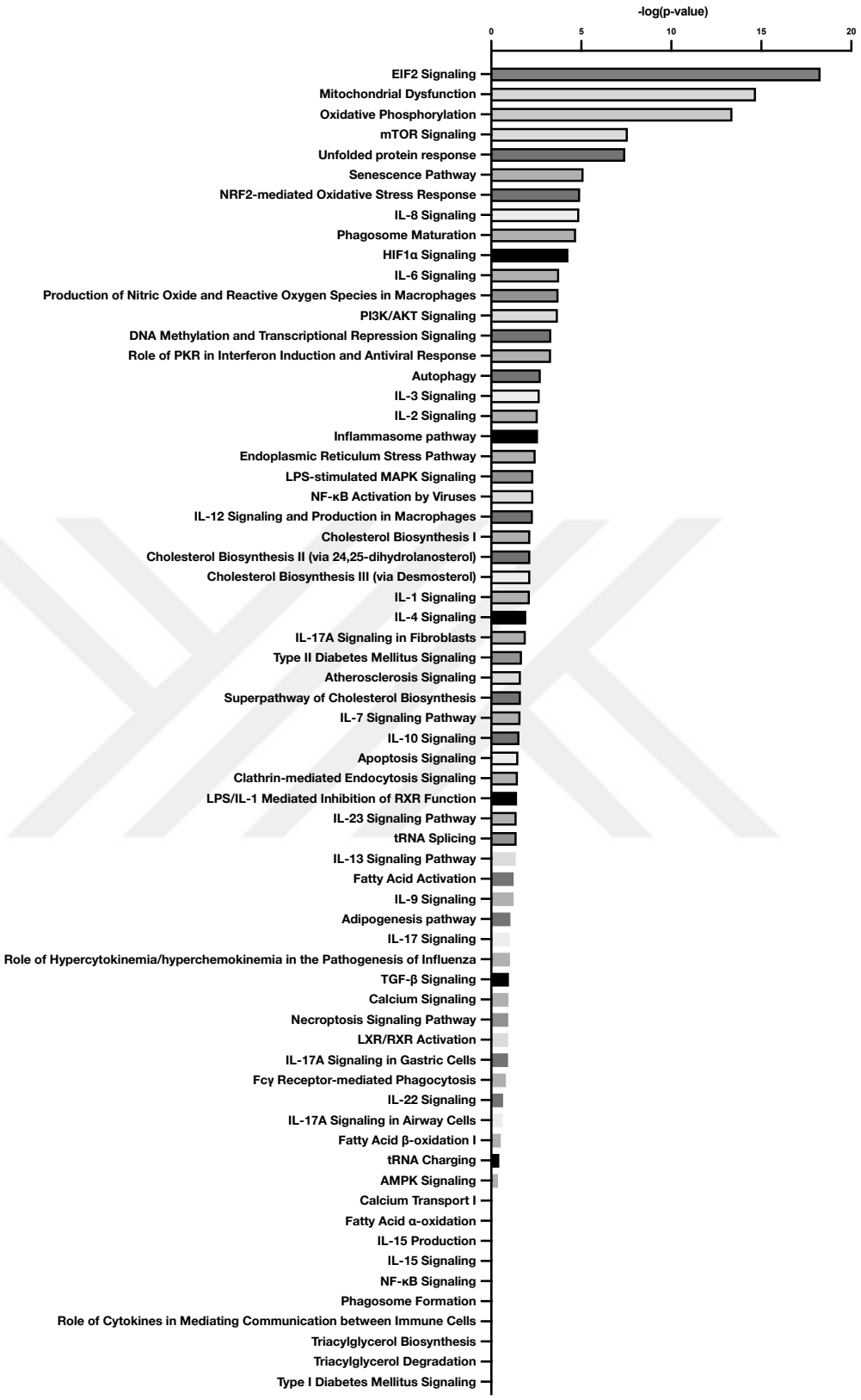

Figure 3.22. Eriched canonical pathways in Fmr1$^{-/-}$ macrophages.

RNA lysates from Fig 3.18 pooled as HMW, LMW and NTR and analyzed by RNA sequencing. Canonical pathways determined by IPA analysis are shown for mRNAs in HMW fractions from Fmr1$^{-/-}$ compared to Fmr1$^{+/+}$.

Next, I confirmed the FMRP targets involved in cholesterol transport and efferocytosis pathways from the same samples using RT-qPCR. Indeed, the mRNA distribution of Abca1, Abcg1, Mertk and Lrp1 were increased in the polysomes (Fig 3.23A) as well as the mRNA abundance for the cholesterol transporters, Abca1 and Abcg1, and the mRNA abundance for efferocytosis regulators, Mertk, Lrp1, and Cd36, were increased in translating polysome fractions and decreased in non-translating (NTR) fractions in the Fmr1$^{-/-}$ BMDMs when compared to Fmr1$^{+/+}$ BMDMs (Fig 3.23B), while the abundance of these mRNAs in the total cell lysate was unchanged (Fig 3.23C).

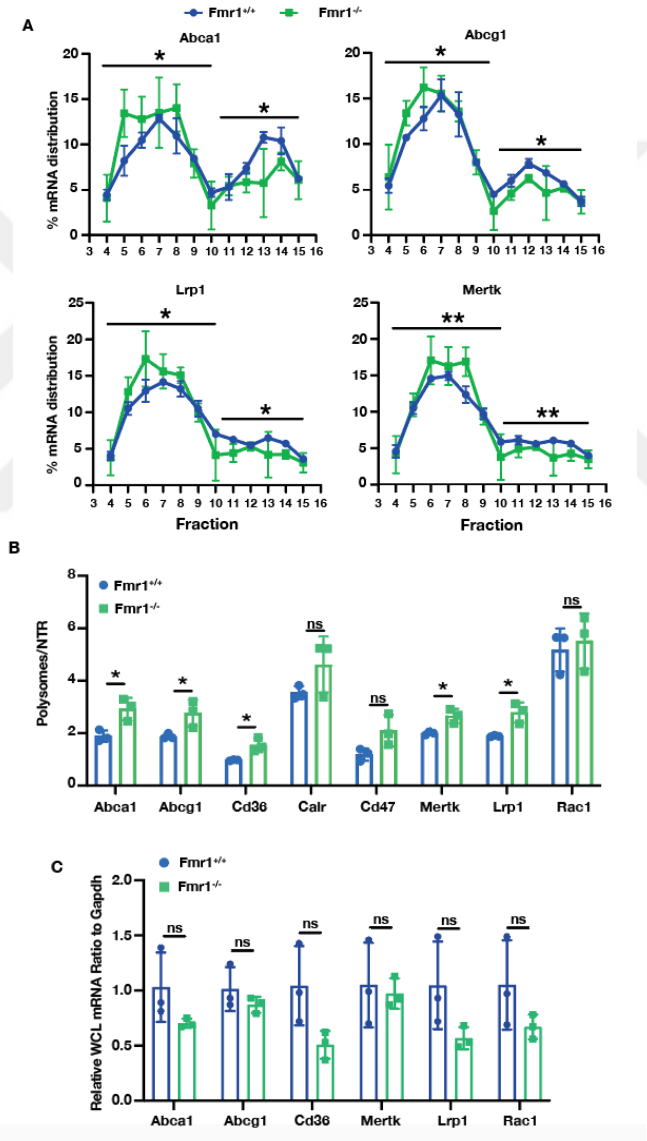

Figure 3.23. Translational regulation of FMRP mRNA targets.

(A) Total mRNA from 12 individual fractions that were subjected to real-time RT-PCR using specific primers for Abca1, Abcg1, Mertk and Lrp1 (n=3). **(B)** The ratio of the Abca1, Abcg1, Mertk, Lrp1, Cd36, Cd47 and Rac1 mRNA in polysome to NTR fraction (n=3). **(C)** Total mRNA qRT-PCR analysis of Abca1, Abcg1, Mertk, Lrp1,

Cd36 and Rac1 in total mRNA levels from same samples used in polysome fractions. Data are mean ± SEM. Unpaired *t*-test with Welch's correction. *P≤ 0.05, **P≤ 0.01, ***P≤ 0.001.

Further analysis of the corresponding protein expression changes for the FMRP-regulated mRNA targets showed that ABCA1, ABCG1, MerTK, and LRP1 protein expression levels were induced in Fmr1 siRNA treated BMDMs as well as in Fmr1$^{-/-}$ BMDMs (Fig 3.23A and 3.23B).

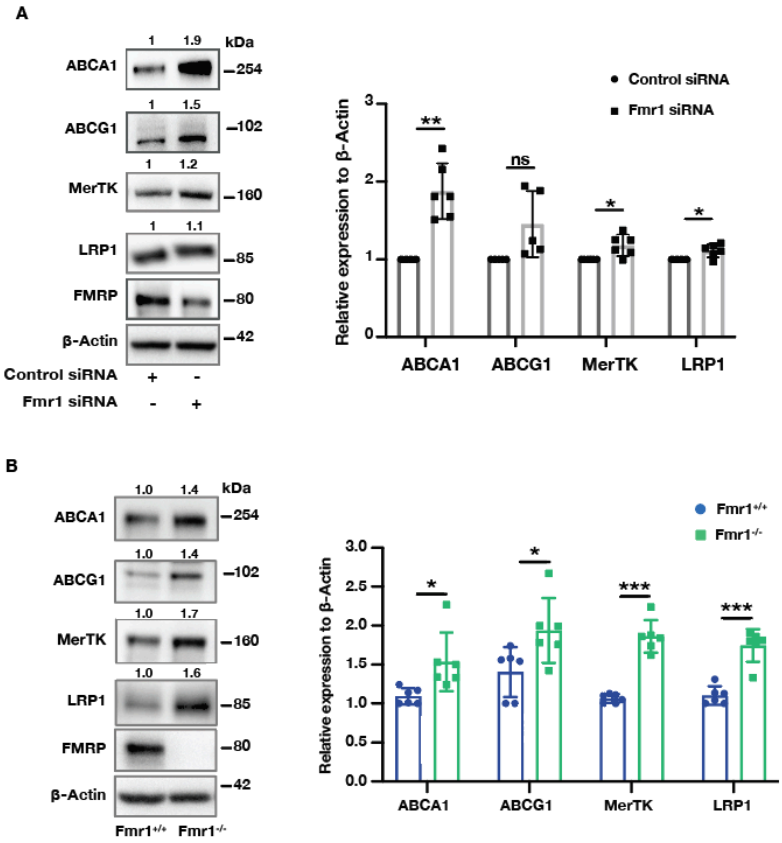

Figure 3.24. Protein expression of FMRP targets.

(A) BMDM were isolated from Fmr1$^{+/+}$ and Fmr1$^{-/-}$, and protein lysates were analyzed by western blotting using specific antibodies for ABCA1, ABCG1, MerTK, LRP1, FMRP and β-Actin antibodies (n=6). **(B)** BMDMs were transfected either with Control or FMR1 siRNA. Protein lysates were analyzed by western blotting using anti-ABCA1, anti-ABCG1, anti-MERTK, anti-LRP1, anti-RAC1, anti-FMRP and anti-β-Actin antibodies (n=5). For all experiments, a representative blot is shown from at least (n=3) independent experiments. Data are mean ± SEM. Unpaired *t*-test with Welch's correction or paired *t*-test. *P≤ 0.05, **P≤ 0.01, ***P≤ 0.001.

Similarly, FMRP targets were induced in IRE1 kinase inhibition by AMG-18 treated BMDMs macrophages, while IRE1 RNase inhibition by 4μ8c did not alter the translation of FMRP targets (Fig 3.25A and 3.25B). To further assess the impact of IRE1-mediated FMRP phosphorylation on the translation of FMRP's targets, I overexpressed the FMRP phosphorylation-deficient mutant (STSA) or WT-FMRP in $Fmr1^{-/-}$ MEFs and treated with PA to induce ER stress. ABCA1, LRP1 and MerTK expression levels were reduced in the $Fmr1^{-/-}$ MEF expressing WT-FMRP, but not in $Fmr1^{-/-}$ MEFs expressing STSA-FMRP (Fig 3.25C). Taken together, my data demonstrate that IRE1-mediated FMRP phosphorylation tunes cholesterol transporters and efferocytosis regulators expression in macrophages.

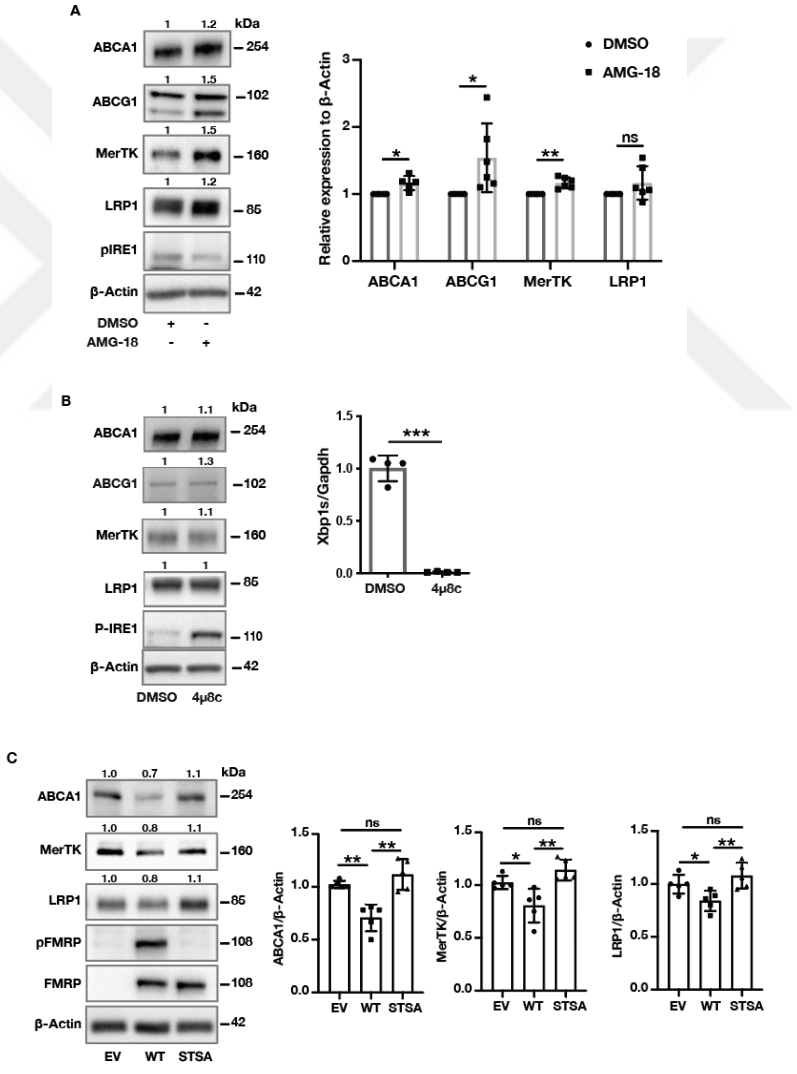

Figure 3.25. IRE1 Kinase domain regulates cholesterol transporters and efferocytosis regulators.

(A) BMDM were pre-treated either with vehicle (DMSO) or AMG-18 (5 μM) for 1

hour followed by vehicle or PA (500 µM) treatment for 6 hours. Protein lysates were analyzed by western blotting using anti-ABCA1, anti-ABCG1, anti-MERTK, anti-LRP1, anti-pIRE1 and anti-β-Actin antibodies (n=6). **(B)** BMDMs were pre-treated with 4µ8c (100µM) followed by PA (500 µM) for 6 hours. Protein lysates were analyzed by western blotting using specific antibodies for anti-ABCA1, anti-ABCG1, anti-MERTK, anti-LRP1, anti-pIRE1 and anti-β-Actin (n=3). **(C)** $Fmr1^{-/-}$ MEF cells were transfected with EV, WT-FMRP or STSA-FMRP plasmids followed by PA treatment (500 µM; 6 hours). Protein lysates were analyzed by western blotting using anti-ABCA1, anti-ABCG1, anti-MERTK, anti-LRP1, anti-FMRP, anti-pFMRP and anti-β-Actin antibodies (n=5). All results are from (n=3) independent experiments. In western blots, the fold protein expression change was calculated relative to β-Actin and depicted above the blots and a representative blot was shown. Data are mean ± SEM. Unpaired t-test with Welch's correction. *P≤ 0.05, **P≤ 0.01, ***P≤ 0.001.

3.7 Discovery of Novel FMRP Targets in ER Stress Induced Macrophages

I used HILAQ approach to discover newly synthesized proteins (NSPs) and related pathways involved in macrophage metabolism under PA stress, where FMRP is phosphorylated by IRE1. In this method bioorthogonal amino acids, Azidohomoalanine (AHA) and heavy Azidohomoalanine (hAHA), can be inserted into newly synthesized proteins and utilized for enrichment and measurement [159]. AHA and hAHA are methionine analogues that can be incorporated into proteins by adding to media for cultured cells or to food pellets for animals and these labeled proteins are then can be enriched using click chemistry (Figure 3.26) [160]. I first optimized AHA labeling duration in macrophages by treating cells for 1, 2.5 and 5.5 hours in the presence of PA treatment to induce FMRP phosphorylation (Figure 3.27). Streptavidin-HRP blot reveled that 5.5 hour of AHA treatment was the most efficient duration that yield the most protein labeling.

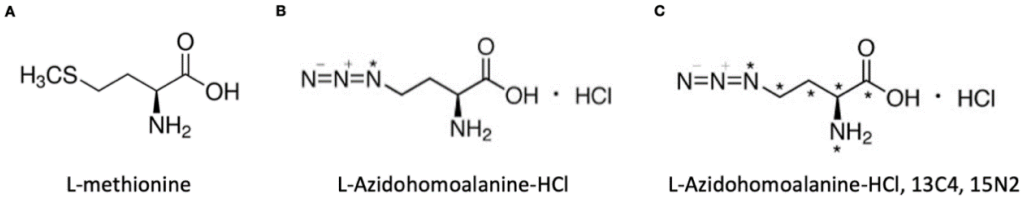

Figure 3.26. L-Methionine and its analogs.

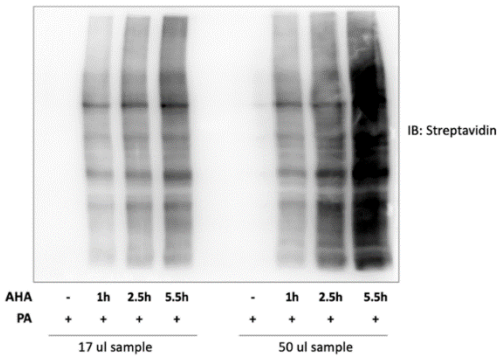

Figure 3.27. HILAQ optimization in macrophages.

BMDM were treated with PA (500 μM) and AHA (4 mM) for 1, 2.5 and 5.5 hours. Protein samples after labeling were analyzed by Western blot using anti-Streptavidin antibody.

I compared $Fmr1^{+/+}$ and $Fmr1^{-/-}$ samples that were treated with AHA and PA for 6 hours. I did not see any significant changes between the groups that suggest only selective group of mRNAs are regulated by FMRP rather than global translational regulation (Figure 3.28).

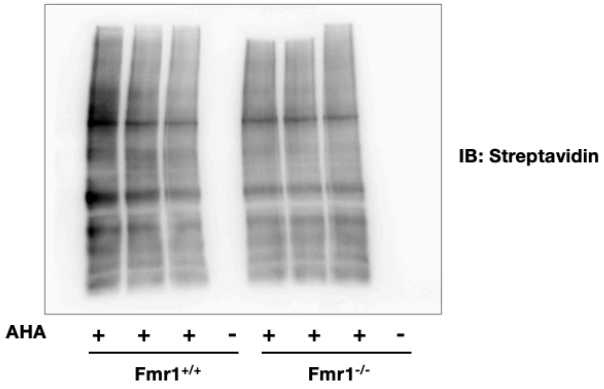

Figure 3.28. Comparison of $Fmr1^{+/+}$ and $Fmr1^{-/-}$ macrophages.

$Fmr1^{+/+}$ and $Fmr1^{-/-}$ BMDM were treated with PA (500 μM) and AHA (4 mM) for 6 hours (n=3). Protein samples after labeling were analyzed by Western blot using anti-Streptavidin antibody.

Next, I adapted HILAQ method to determine dynamic translational regulation in $Fmr1^{+/+}$ (labeled with AHA) and $Fmr1^{-/-}$ (labeled with hAHA) BMDMs that treated with PA and AHA/hAHA for 6 hours (Fig 3.29). After confirmation with western blot

(Fig 3.30), AHA labeled Fmr1$^{+/+}$ and hAHA labeled Fmr1$^{-/-}$ protein samples were then combined and proceeded with click reaction, digestion, enrichment, MS, and data analysis that revealed 151 differentially expressed proteins (Fig 3.31).

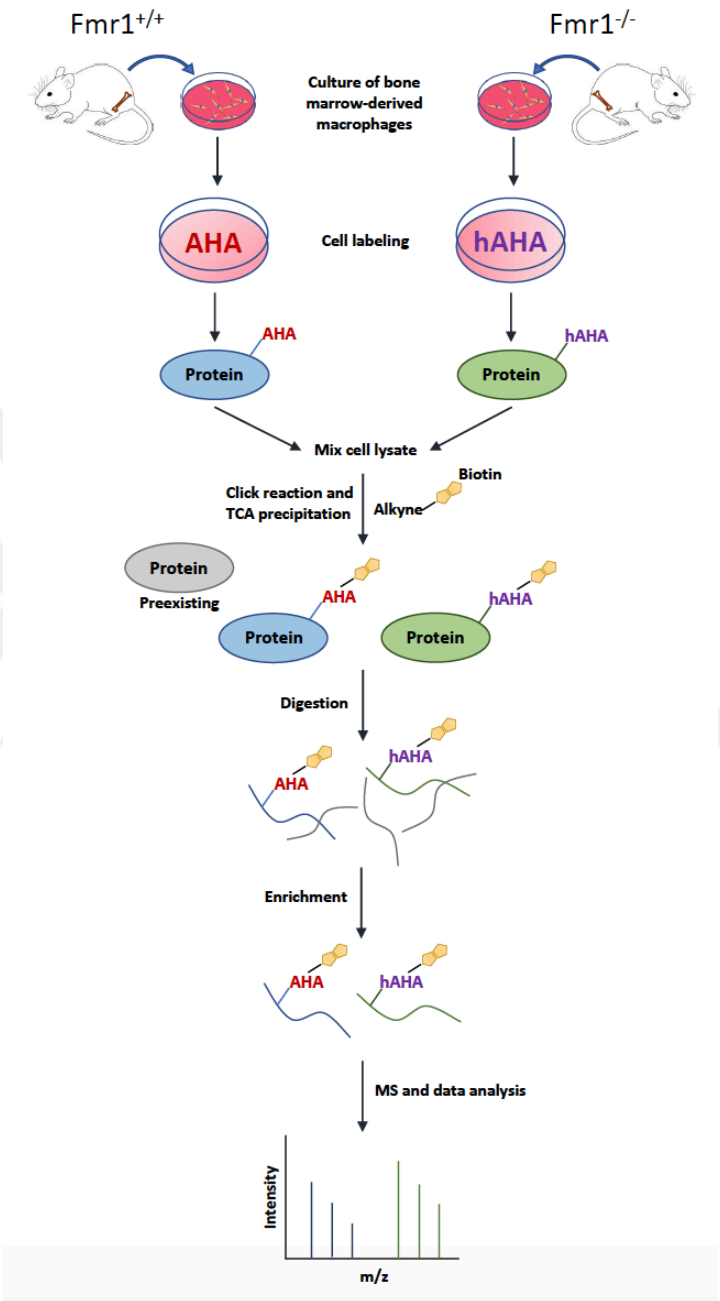

Figure 3.29. Schematic representation of HILAQ method.

Briefly, BMDM collected from Fmr1$^{+/+}$ and Fmr1$^{-/-}$ were treated either with AHA or hAHA in a PA-treatment medium for 6 hours. Followed by the labeling, protein lysates from both conditions were mixed and subjected to click reaction and precipitation. Samples were then digested, enriched, and prepared for MS analysis.

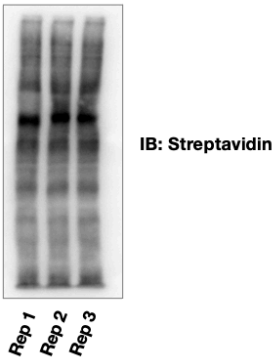

Figure 3.30. HILAQ in Fmr1$^{+/+}$ and Fmr1$^{-/-}$ macrophages.

Fmr1$^{+/+}$ and Fmr1$^{-/-}$ BMDM were treated with PA (500 µM) and AHA or hAHA (4 mM) for 6 hours respectively (n=3). AHA labeled Fmr1$^{+/+}$ and hAHA labeled Fmr1$^{-/-}$ protein samples were then combined and analyzed by Western blot using anti-Streptavidin-HRP antibody.

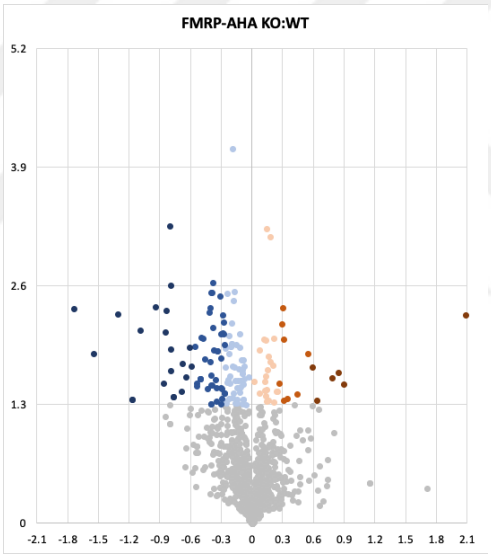

Figure 3.31. Differentially expressed proteins in macrophages.

Volcano pilot of the 151 differently expressed proteins in Fmr1$^{-/-}$ samples compared to Fmr1$^{+/+}$ after MS analysis. Blue indicates downregulation and red indicates upregulation.

IPA was performed to identify canonical pathways, diseases and bio functions that are enriched in Fmr1$^{-/-}$ macrophages (Fig 3.32). In line with my previous results, top enriched canonical pathways show FMRP's function in macrophage phagocytosis and endocytosis. Moreover, diseases and bio functions list reveal that 65 differentially

expressed proteins were involved in inflammatory response and 80 proteins were involved in cell death and survival. Other top enriched pathways are shown in Fig 3.33.

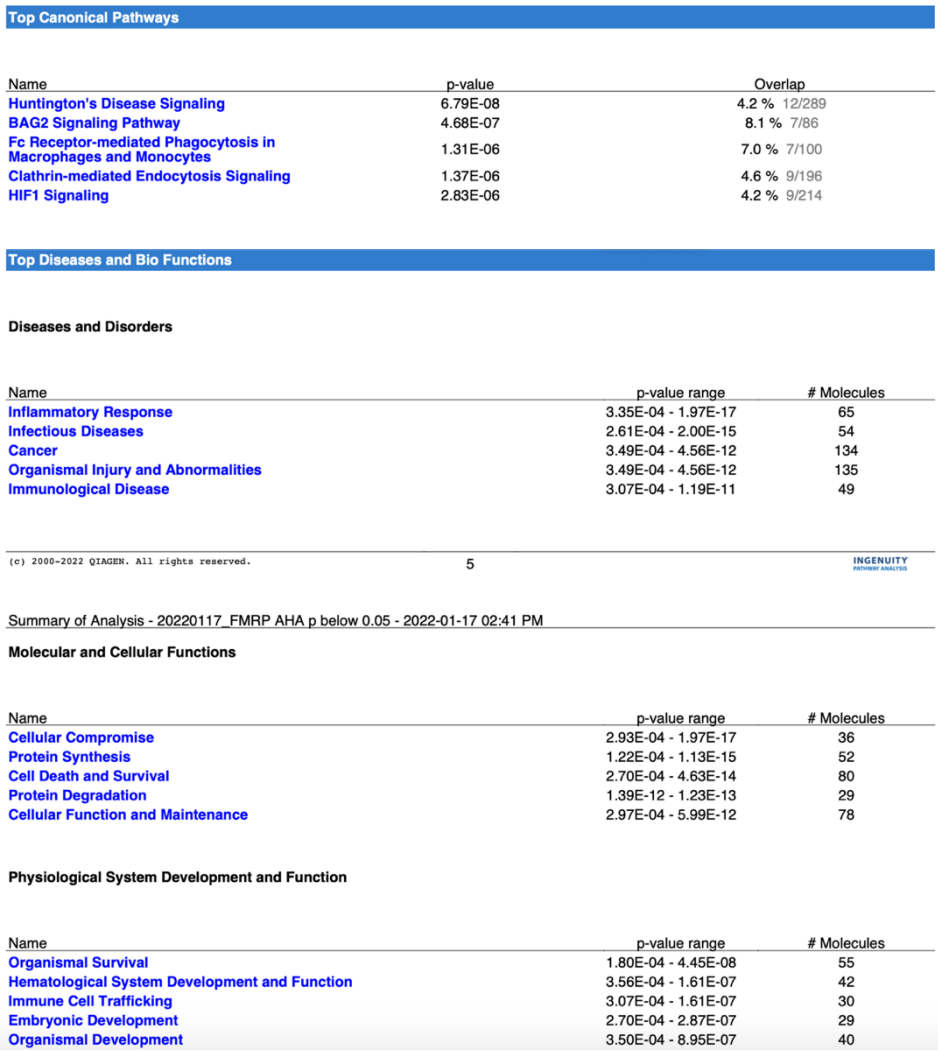

Top Canonical Pathways

Name	p-value	Overlap
Huntington's Disease Signaling	6.79E-08	4.2 % 12/289
BAG2 Signaling Pathway	4.68E-07	8.1 % 7/86
Fc Receptor-mediated Phagocytosis in Macrophages and Monocytes	1.31E-06	7.0 % 7/100
Clathrin-mediated Endocytosis Signaling	1.37E-06	4.6 % 9/196
HIF1 Signaling	2.83E-06	4.2 % 9/214

Top Diseases and Bio Functions

Diseases and Disorders

Name	p-value range	# Molecules
Inflammatory Response	3.35E-04 - 1.97E-17	65
Infectious Diseases	2.61E-04 - 2.00E-15	54
Cancer	3.49E-04 - 4.56E-12	134
Organismal Injury and Abnormalities	3.49E-04 - 4.56E-12	135
Immunological Disease	3.07E-04 - 1.19E-11	49

Summary of Analysis - 20220117_FMRP AHA p below 0.05 - 2022-01-17 02:41 PM

Molecular and Cellular Functions

Name	p-value range	# Molecules
Cellular Compromise	2.93E-04 - 1.97E-17	36
Protein Synthesis	1.22E-04 - 1.13E-15	52
Cell Death and Survival	2.70E-04 - 4.63E-14	80
Protein Degradation	1.39E-12 - 1.23E-13	29
Cellular Function and Maintenance	2.97E-04 - 5.99E-12	78

Physiological System Development and Function

Name	p-value range	# Molecules
Organismal Survival	1.80E-04 - 4.45E-08	55
Hematological System Development and Function	3.56E-04 - 1.61E-07	42
Immune Cell Trafficking	3.07E-04 - 1.61E-07	30
Embryonic Development	2.70E-04 - 2.87E-07	29
Organismal Development	3.50E-04 - 8.95E-07	40

Figure 3.32. Top enriched canonical pathways and top enriched diseases and bio functions in Fmr1$^{-/-}$ macrophages.

Protein samples in Fig 3.30 analyzed by MS after AHA and hAHA labeling. Top canonical pathways, top disease, and biological functions, determined by IPA analysis, are shown for Fmr1$^{-/-}$ compared to Fmr1$^{+/+}$ macrophages.

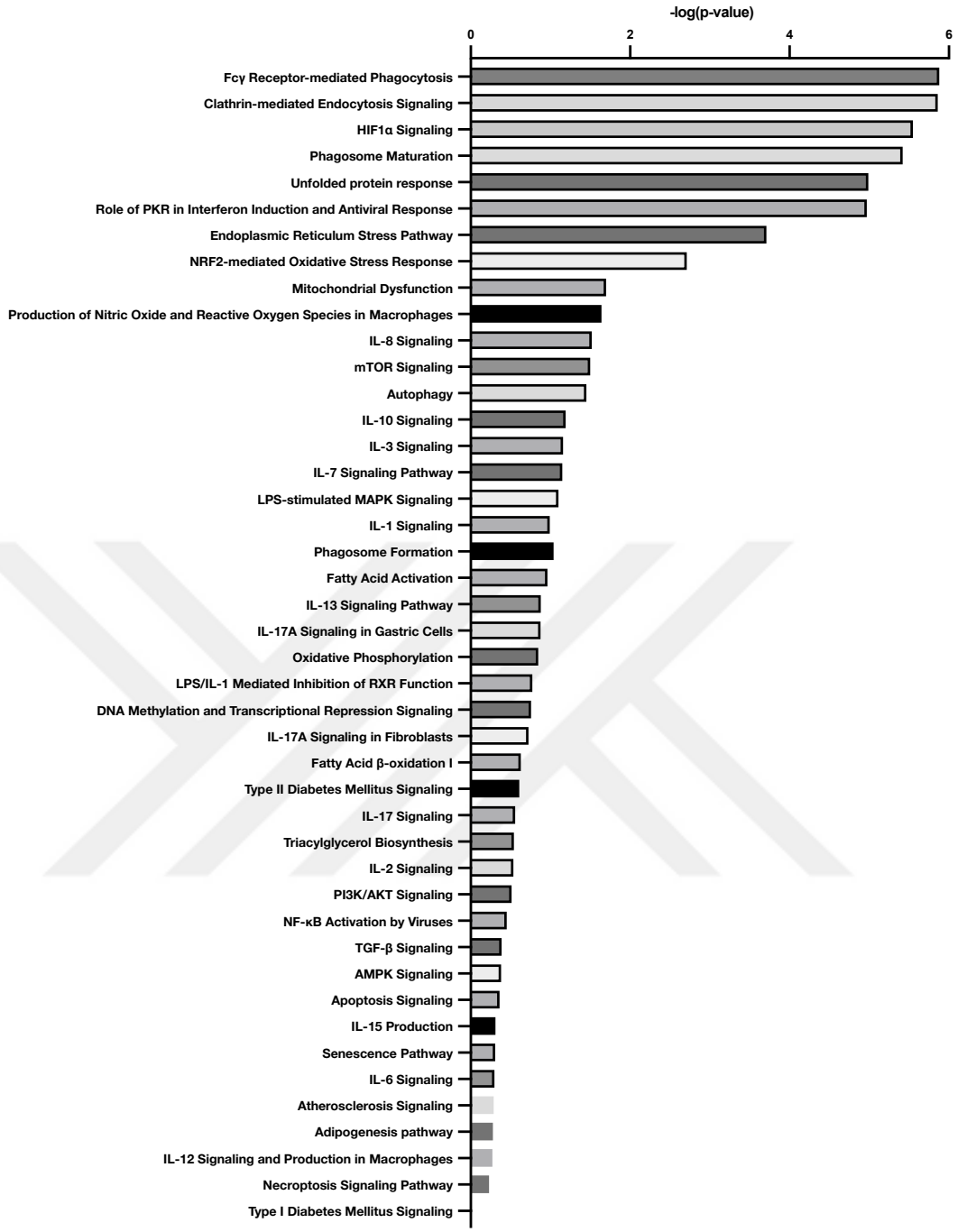

Figure 3.33. Enriched canonical pathways in Fmr1$^{-/-}$ macrophages.

Protein samples in Fig 3.30 analyzed by MS after AHA and hAHA labeling. Canonical pathways determined by IPA analysis are shown for mRNAs in HMW fractions from Fmr1$^{-/-}$ compared to Fmr1$^{+/+}$.

3.8 FMRP Knock-down Alleviates Atherosclerosis

My findings demonstrate that both IRE1 kinase inhibition and FMRP-deficiency result in increased RCT, reduced foam cell formation, and enhanced efferocytosis *in vivo*, suggesting that FMRP-deficiency in mice leads to protection from atherosclerosis. I tested this notion using $Fmr1^{-/-}$ and $Fmr1^{+/+}$ mice in which hyperlipidemia was induced by combining AAV_PCSK9 injection with a WD as described above (Fig 3.34A). Although there was a very slight decrease in body weight ratio; the plasma glucose, total plasma cholesterol (TPC), lipoprotein levels (Fig 3.34B-E), and the number of circulating, major type of immune cells were indistinguishable between the $Fmr1^{-/-}$ and $Fmr1^{+/+}$ genotypes (Fig 3.35A and 3.35B).

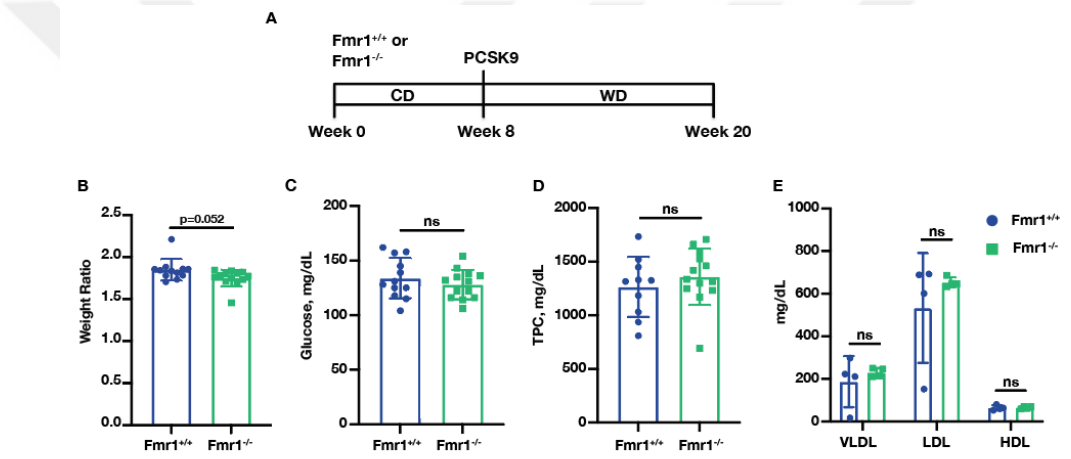

Figure 3.34. Atherosclerosis model in $Fmr1^{-/-}$ mice.

(A) Atherosclerosis experiment design in $Fmr1^{+/+}$ and $Fmr1^{-/-}$ mice that were injected with AAV_PCSK9 and fed WD (16 weeks). **(B)** The ratio of mouse weight at the beginning of the experiment over the weight at the end of the experiment in Fig 3.24A (n=12-13). **(C-E)** plasma measurements for **(C)** glucose (n=12-13), **(D)** cholesterol (n=12-13) and **(E)** lipoproteins (n=4) from mice in Fig 3.24A. **(F)** Gating strategy for the flow cytometry analysis of mouse peripheral blood. **(G)** Abundance of B cells, T cells and monocytes in the peripheral blood as % of total $CD45^{+}$ cells from the $Fmr1^{+/+}$ and $Fmr1^{-/-}$ mice in Fig5A (n=12-13). Data are mean ± SEM; Mann Whitney U test. *P≤ 0.05, **P≤ 0.01, ***P≤ 0.001.

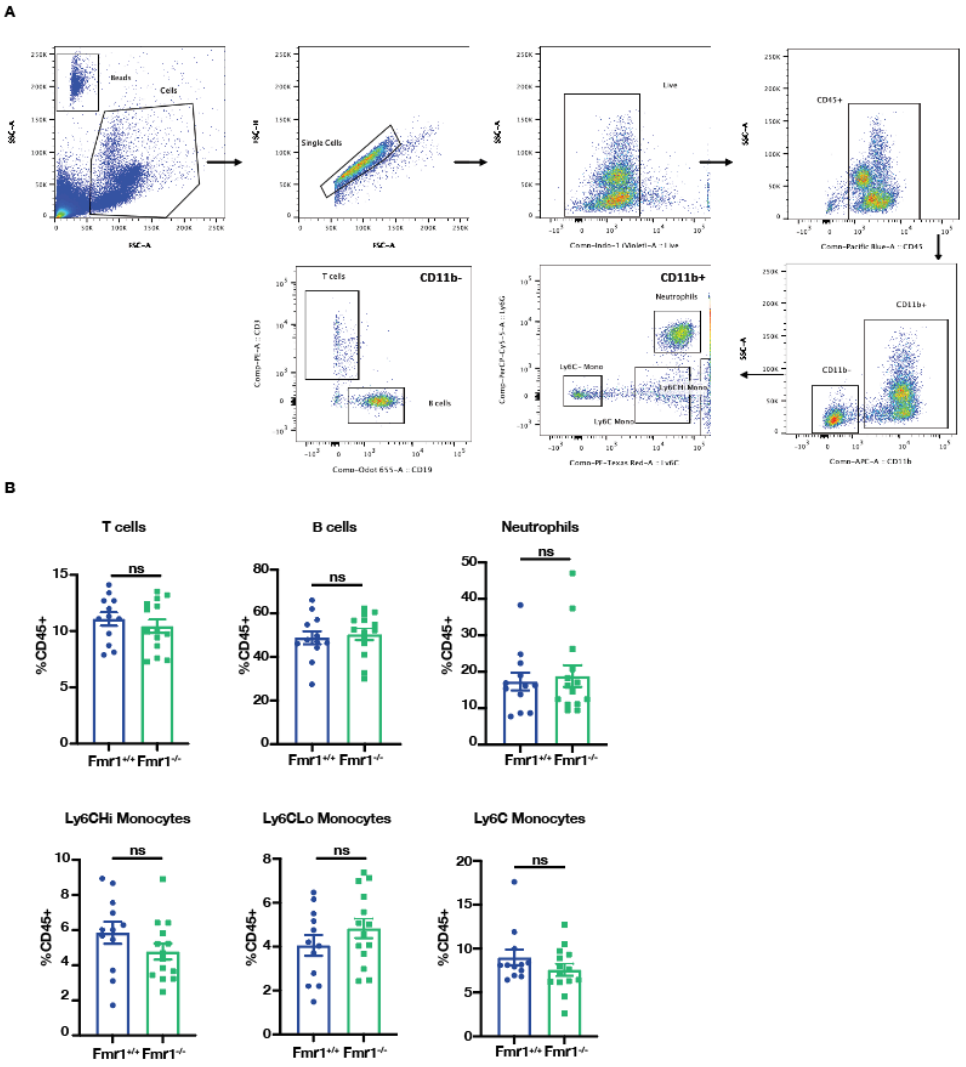

Figure 3.35. Blood cell counts in Fmr1$^{-/-}$ mice after 16 weeks of WD.

(A) Gating strategy for the flow cytometry analysis of mouse peripheral blood. **(B)** Abundance of B cells, T cells and monocytes in the peripheral blood as % of total CD45^{+} cells from the Fmr1$^{+/+}$ and Fmr1$^{-/-}$ mice in Fig5A (n=12-13). Data are mean ± SEM; Mann Whitney U test. *P≤ 0.05, **P≤ 0.01, ***P≤ 0.001.

Yet, FMRP-deficiency resulted in significant reduction in atherosclerotic lesions in *en face* aorta preparations (Fig 3.36A). FMRP-deficiency did not alter aortic root lesion area despite a significantly decreased foam cell area (as assessed by Oil Red O staining) (Fig 3.36B and 3.26C). I next asked what may be contributing to this phenotype. The necrotic core area in the lesions from Fmr1$^{-/-}$ mice was significantly less than in Fmr1$^{+/+}$ lesions (Fig3.36D), indicating improved AC clearance by Fmr1$^{-/-}$ macrophages in plaques.

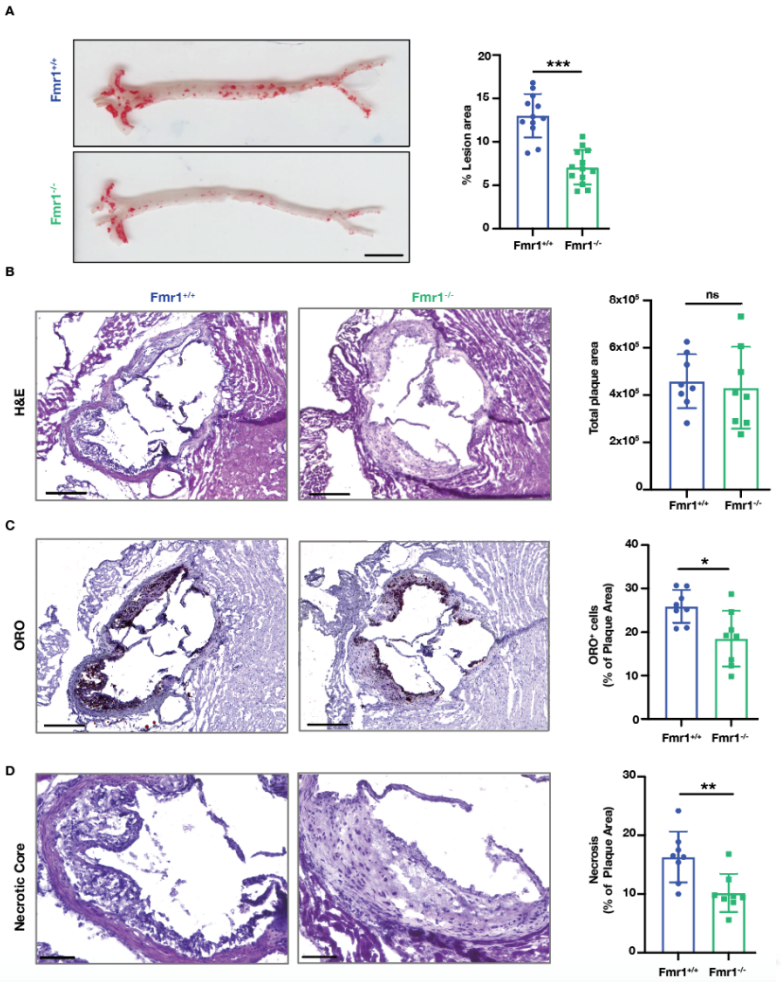

Figure 3.36. FMRP-deficiency block atherosclerosis progression.

(A) Lesion area calculated from *en face* aorta, stained with ORO (n=12-13; Scale bar = 5 mm). **(B)** Total plaque area was calculated from hematoxylin & eosin (H&E)-stained aortic root sections (n=8; Scale bar = 300 µm). **(C)** Foam cell area was calculated from ORO-stained aortic root sections (n=8; Scale bar = 300 µm). **(D)** Necrotic area was calculated from H&E-stained aortic root sections (n=8; Scale bar = 100 µm). Data are mean ± SEM; Mann Whitney U test. *P≤ 0.05, **P≤ 0.01, ***P≤ 0.001.

I also observed a significant reduction in lesion macrophages (as assessed by the anti-monocyte macrophage 2 (MOMA-2)-stained area) and the number of apoptotic cells (TUNEL-stained) per macrophage area (Fig 3.37A and 3.37B). I further investigated whether apoptosis is altered in Fmr1$^{-/-}$ and AMG-18 treated macrophages. There was no significant change between the groups (Fig 3.37C), supporting the notion that the primary target of IRE1-FMRP signaling is efficient clearance of apoptotic cells through increasing efferocytosis capacity. Additionally, I detected no change in

smooth muscle area (stained with smooth muscle actin (SMA)), but there was a significant increase in the collagen content of $Fmr1^{-/-}$ lesions when compared to $Fmr1^{+/+}$ lesions, suggesting this could be the reason why aortic root lesion area is not significantly altered (Fig 3.37D and 3.37E).

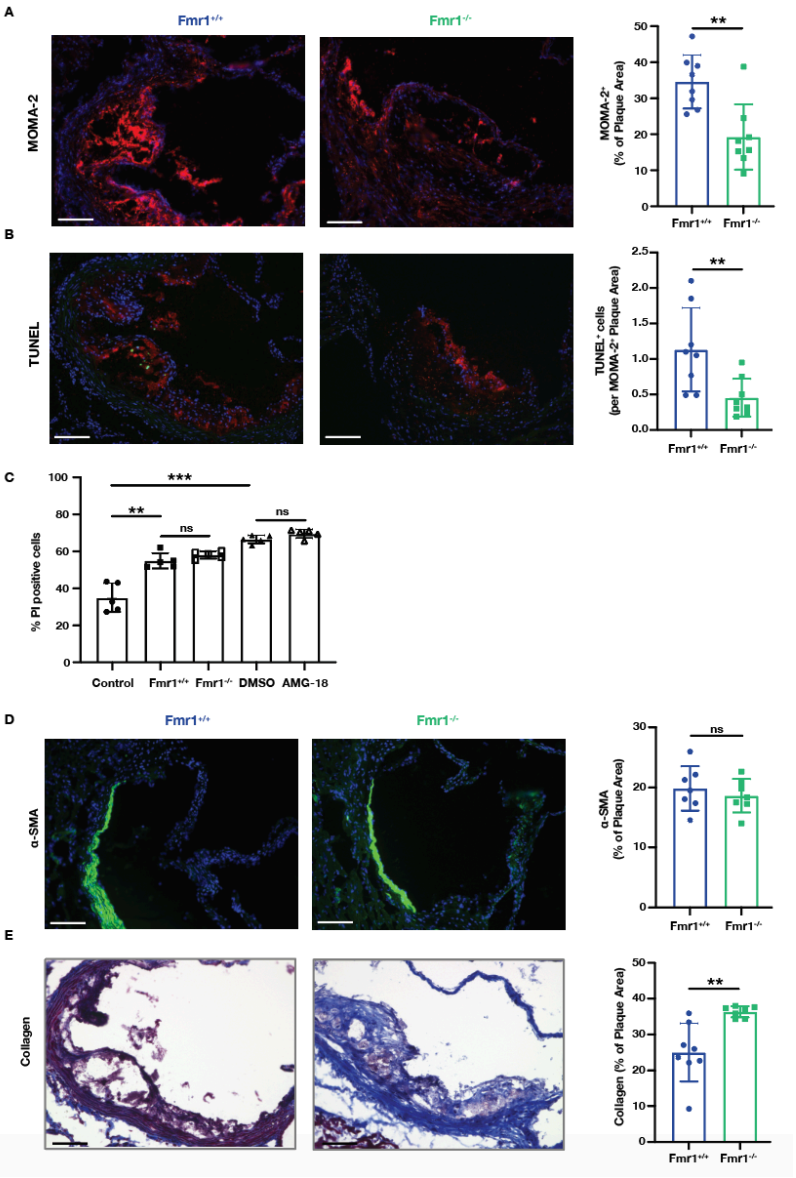

Figure 3.37. FMRP-deficiency reduce macrophage positive area and apoptosis in atherosclerotic plaques.

(A) Macrophage area was calculated from MOMA-2 (red)-stained aortic root sections as % of $MOMA2^{+}$ stained area to total plaque area (n=8; Scale bar = 100 µm). **(B)** Apoptosis was calculated from the number of $TUNEL^{+}$ cells (green) in the MOMA-2-stained (red) plaque area (n=8; Scale bar = 100 µm). **(C)** Apoptosis was measured in Fmr1+/+ and Fmr1-/- BMDMs or AMG-18 pre-treated cells (10 µM, 1 hour) were treated with PA (500 µM) treatment for 12 hours and then stained with Propidium iodide (PI) (n=5). **(D)** % α-SMA was calculated from aortic root sections stained with α-SMA (green) as % α-SMA^{+} area to the total plaque area (n=8, Scale bar 100 µm).

(E) % collagen area was calculated from Masson's Trichrome staining as the percentage of collagen (blue) area in total plaque area (n=8; Scale bar = 100 µm). Data are mean ± SEM; Mann Whitney U test. *P≤ 0.05, **P≤ 0.01, ***P≤ 0.001.

To approach the role of macrophage FMRP in atherosclerosis, I generated a myeloid Fmr1-deficient mouse model (myFmr1$^{-/-}$) and induced hyperlipidemia (Fig 3.38A). As expected from the systemic deletion data shown in Figure 5A, the body weight, plasma glucose and TPC were indistinguishable between the myFmr1$^{-/-}$ and myFmr1$^{+/+}$ genotypes (Fig 3.38C-D).

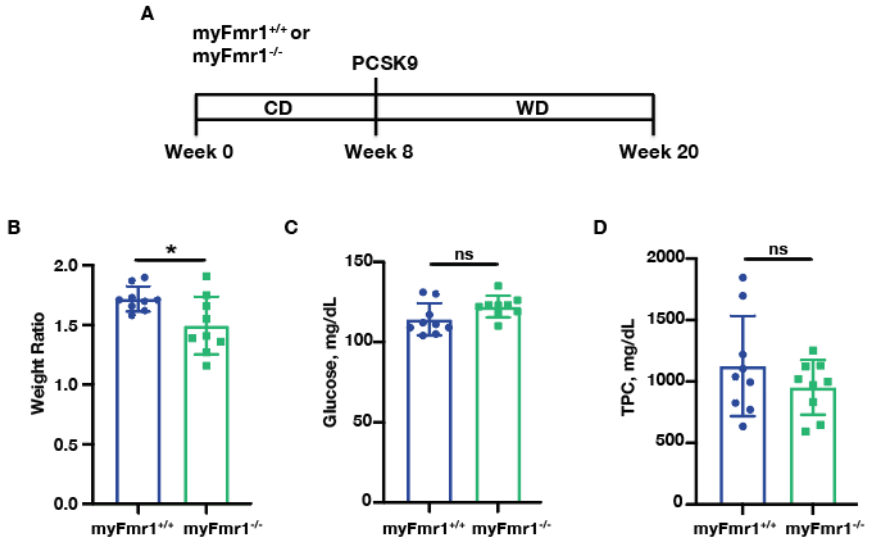

Figure 3.38. Atherosclerosis model in Fmr1$^{-/-}$ mice.

(A) Atherosclerosis experiment design in myFmr1$^{+/+}$ and myFmr1$^{-/-}$ mice that were injected with AAV_PCSK9 and fed WD (16 weeks). **(B)** The ratio of mouse weight at the beginning of the experiment over the weight at the end of the experiment in Fig 3.28 (n=9). **(C-D)** plasma measurements for **(C)** glucose (n=9) and **(D)** cholesterol (n=9) from mice in Fig 3.28A. Data are mean ± SEM; Mann Whitney U test. *P≤ 0.05, **P≤ 0.01, ***P≤ 0.001.

In general, myeloid-specific FMRP-deficiency paralleled the results obtained for Fmr1$^{-/-}$ mice: it resulted in significant reduction in atherosclerotic lesions in *en face* aorta preparations (Fig 3.39A). Myeloid specific FMRP-deficiency did not alter aortic root lesion area but significantly reduced foam cell area (Fig 3.39B and 3.39C). The necrotic core area in the lesions from myFmr1$^{-/-}$ mice was also significantly less than in myFmr1$^{+/+}$ lesions (Fig 3.39D), indicating improved AC clearance by Fmr1$^{-/-}$

macrophages in plaques and supporting my observations that FMRP deficiency increases macrophage efferocytosis *in vitro* and *in vivo* (Fig 3.14-3.16). Thus, comparing the data obtained with the Fmr1$^{-/-}$ mice with those obtained from the myFmr1$^{-/-}$ mice indicates that the atheroprotective effects observed in Fmr1$^{-/-}$ mice are mostly, if not exclusively, due to FMRP's role in myeloid cells such as macrophages.

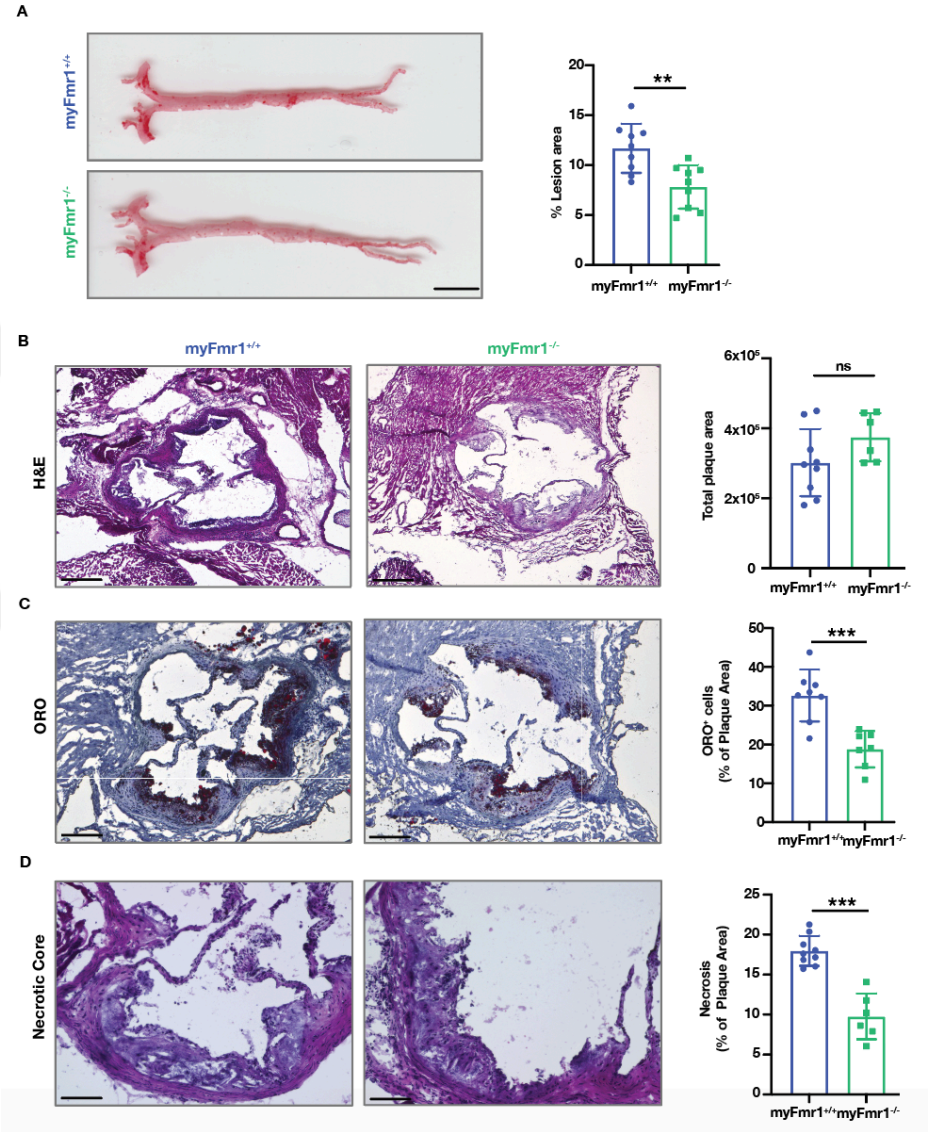

Figure 3.39. Myeloid specific FMRP deficiency block atherosclerosis progression.

(A) Lesion area calculated from *en face* aorta, stained with ORO (n=9; Scale bar = 5 mm). **(B)** Total plaque area was calculated from H&E-stained aortic root sections (n=9-6; Scale bar = 300 µm). **(C)** Foam cell area was calculated from ORO-stained aortic root sections (n=9-6; Scale bar = 300 µm). **(D)** Necrotic area was calculated from H&E-stained aortic root sections (n=9-6; Scale bar = 100 µm). Data are mean ± SEM; Mann Whitney U test. *P≤ 0.05, **P≤ 0.01, ***P≤ 0.001.

3.9 IRE1 Kinase-Domain Inhibition by Small Molecule Inhibitor Alleviates Atherosclerosis

To test the notion that IRE1 functions upstream of FMRP, I next investigated the impact of IRE1 kinase inhibition on atherosclerosis. To this end, I fed Apoe-/- mice with WD for 12 weeks and injected them with AMG-18 or vehicle once daily for the last 4 weeks of WD (Fig 3.40A). I observed no significant differences in body weight, plasma glucose or TPC, and the number of circulating immune cells between the groups (Fig 3.40B-F).

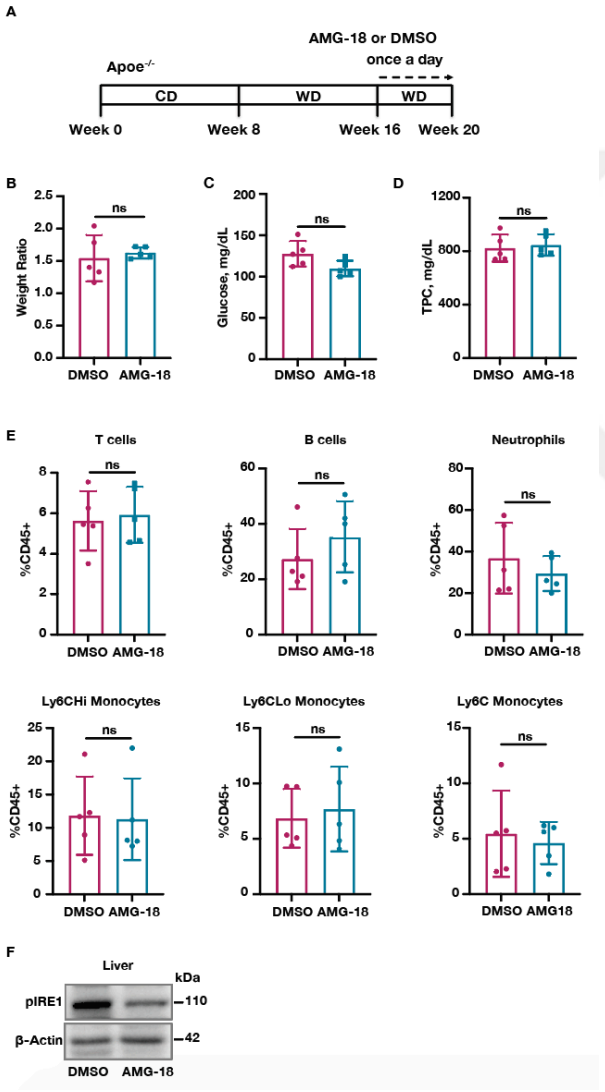

Figure 3.40. Atherosclerosis model in AMG-18 injected Apoe-/- mice.

(A) Atherosclerosis experiment design in Apoe$^{-/-}$ mice were fed with WD (12 weeks) and injected with vehicle (DMSO) or AMG-18 (30 mg/kg) once a day in the last 4 weeks of WD. **(B)** The ratio of mouse weight at the beginning of the experiment over the weight at the end of the experiment in Fig 6A (n=5). **(C-D)** Plasma measurements for **(C)** glucose (n=5) and **(D)** cholesterol (n=5) from mice in Fig 3.30A. **(E)**

Abundance of B cells, T cells and monocytes in the peripheral blood as % of total CD45^{+} cells from the vehicle (DMSO) or AMG-18 (30 mg/kg) once a day injected mice in Fig 6A (n=5). **(F)** Protein lysates of liver from mice in Fig 6A. Proteins were analyzed by western blotting using specific antibodies for pIRE1 and β-Actin (n=5). Data are mean ± SEM; Mann Whitney U test. *P≤ 0.05, **P≤ 0.01, ***P≤ 0.001.

Consistent with an earlier publication that determined the effective and non-toxic dose for AMG-18 in mice, the inhibitor engaged its molecular target effectively in the treatment group (as assessed by reduced IRE1 autophosphorylation) (Fig 3.40F). IRE1 kinase inhibition led to a decrease in atherosclerotic lesions in *en face* aorta preparations (Fig 3.41A). As shown above for the Fmr1$^{-/-}$ mice, the aortic root lesion area was not different between the groups (Fig 3.41B), but foam cell area as well as necrotic core area were significantly decreased (Fig3.41C and 3.41D).

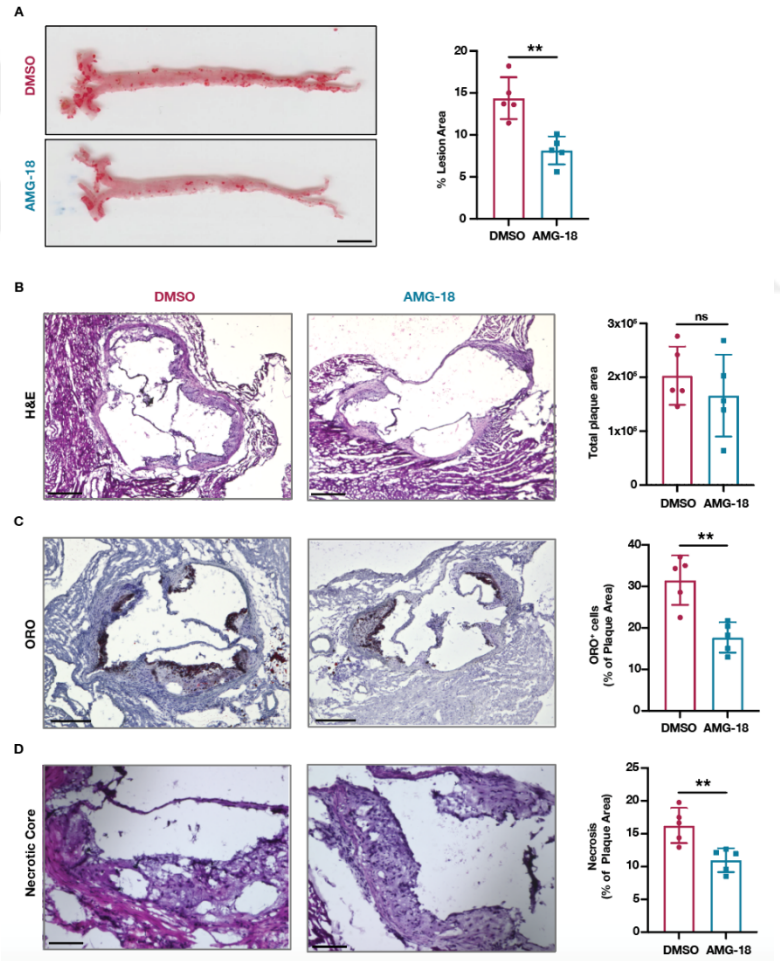

Figure 3.41. IRE1 Kinase inhibition alleviates atherosclerosis progression.

(A) Lesion area calculated from *en face* aorta, stained with ORO (n=5; Scale bar = 5 mm). **(B)** Total plaque area was calculated from H&E-stained aortic root sections (n=5; Scale bar = 300 µm). **(C)** Foam cell area was calculated from ORO-stained aortic

root sections (n=5; Scale bar = 300 µm). **(D)** Necrotic area was calculated from H&E-stained aortic root sections (n=5; Scale bar = 100 µm). Data are mean ± SEM; Mann Whitney U test. *P≤ 0.05, **P≤ 0.01, ***P≤ 0.001.

I also assessed the impact of twice daily injections of the same dose of AMG-18 on Apoe$^{-/-}$ mice that were fed with WD for 12 weeks (Fig 3.42A). While I noted a decrease in body weight ratio and TPC, there were no significant differences in plasma glucose levels similar to once daily injection (Fig 3.42B-3.42D), and the inhibitor engaged its molecular target effectively (as assessed by reduced IRE1 autophosphorylation) (Fig 3.42E and 3.42F).

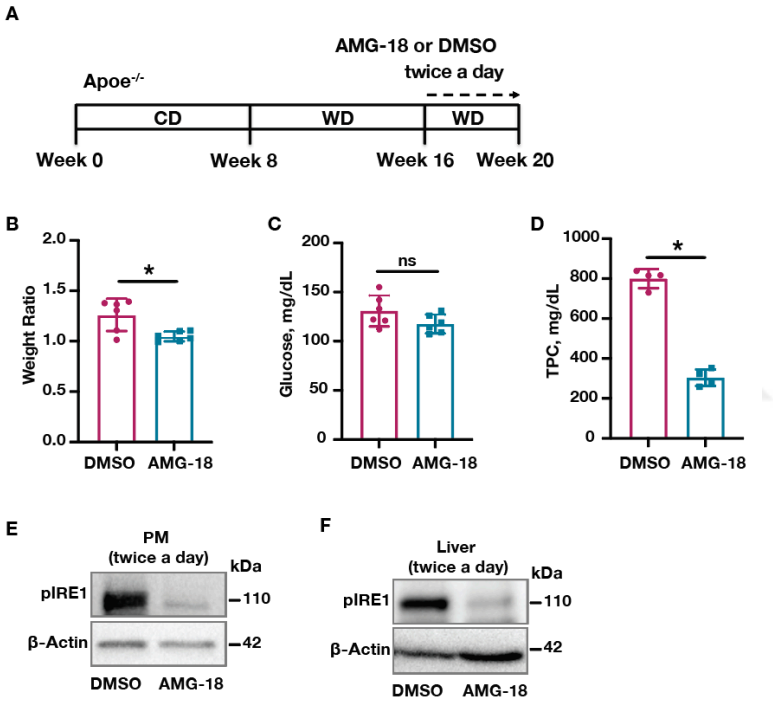

Figure 3.42. Atherosclerosis model in twice-a-day AMG-18 injected Apoe-/- mice.

(A) Atherosclerosis experiment design in Apoe$^{-/-}$ mice were fed with WD (12 weeks) and injected with vehicle (DMSO) or AMG-18 (30 mg/kg) twice a day in the last 4 weeks of WD. **(B)** The ratio of mouse weight at the beginning of the experiment over the weight at the end of the experiment in Fig 3.32A (n=6). **(C-D)** Plasma measurements for **(C)** glucose (n=6) and **(D)** cholesterol (n=6) from Fig 3.32A. Protein lysates of **(E)** thioglycolate-elicited PM and **(F)** liver from mice in Fig 3.32A. Proteins were analyzed by western blotting using specific antibodies for pIRE1 and β-Actin (n=6). Data are mean ± SEM; Mann Whitney U test. *P≤ 0.05, **P≤ 0.01, ***P≤ 0.001.

IRE1 kinase inhibition led to significant decrease in atherosclerotic lesions in *en face* aorta preparations (Fig 3.33A). AMG-18 injection did not alter aortic root lesion area but significantly decreased foam cell area and necrotic core area (Fig 3.33B-3.33D). Collectively, my findings thus demonstrate that the inhibition of IRE1 kinase activity by a small molecule inhibitor or genetic ablation of FMRP, its kinase substrate, in macrophages can reduce the progression of hypercholesterolemia-induced atherosclerosis.

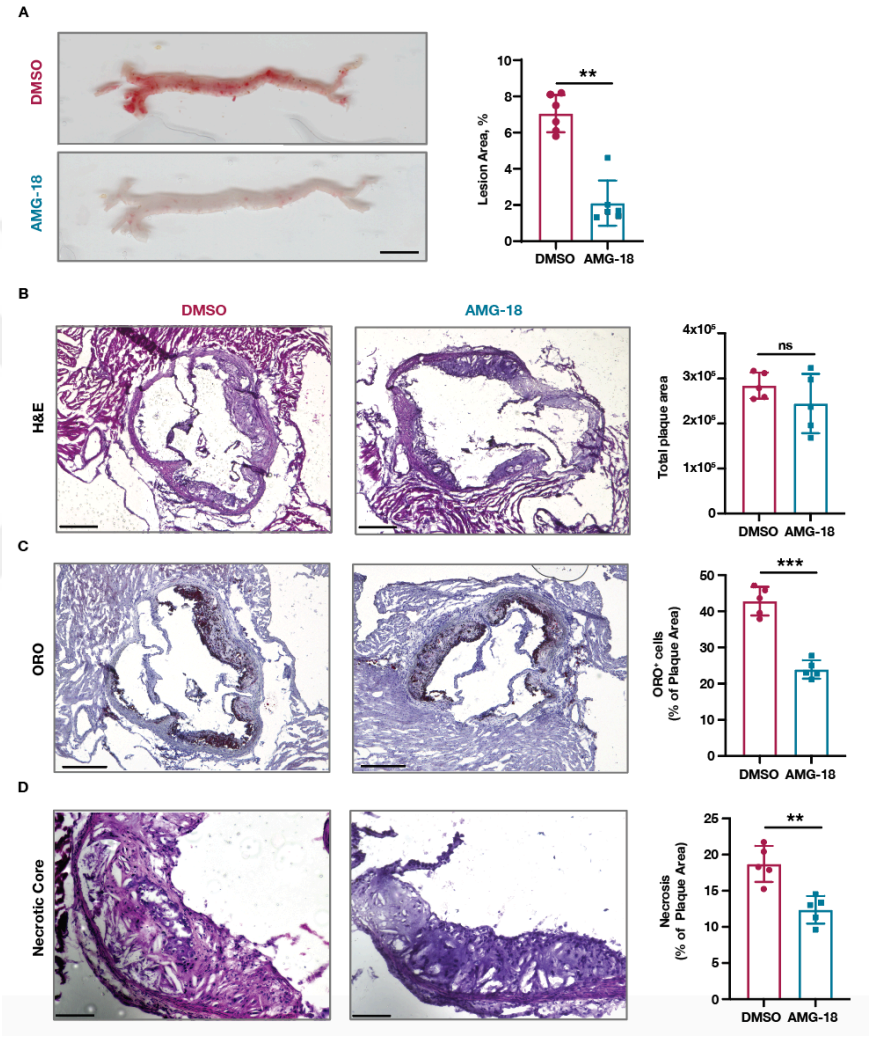

Figure 3.43. Twice a day injection of AMG-18 shows superior effect on preventing atherosclerosis progression.

(A) Lesion area calculated from *en face* aorta, stained with ORO (n=6; Scale bar = 5 mm). **(B)** Total plaque area was calculated from H&E-stained aortic root sections (n=5; Scale bar = 300 µm). **(C)** Foam cell area was calculated from ORO-stained aortic root sections (n=5; Scale bar = 300 µm). **(D)** Necrotic area was calculated from H&E-stained aortic root sections (n=5; Scale bar = 100 µm). Data are mean ± SEM; Mann Whitney U test. *P≤ 0.05, **P≤ 0.01, ***P≤ 0.001.

3.10 IRE1 Kinase Domain and FMRP Regulates m-IL-1β Secretion in Macrophages

In an earlier study, I had shown that small molecule inhibitors that are specific for IRE1's RNase activity prevented lipid-induced inflammasome activation and secretion of mature interleukin-1β (m-IL-1β) and interleukin-18 IL-18 in both mouse and human macrophages while reducing hyperlipidemia-induced m-IL-1β and IL-18 production and reducing atherosclerotic plaque size in mice [91]. FMRP suppression (by genetic knock down or via siRNA mediated knock down) also reduced m-IL-1β secreted from macrophages without altering inflammasome activation as determined by active caspase-1 in these macrophages (Fig 3.44A-F). However, knocking out FMRP from macrophages had no effect on IL-1β mRNA levels in the whole cell lysate or in the polysomes, suggesting against transcriptional or translational control over these cytokines' production (Fig 3.44G and 3.44H). Similarly, inhibition of IRE1 kinase also reduced m-IL-1β (Fig 3.44I-K). It has been shown that m-IL-1β can be secreted through ABCA1 and compete with cholesterol efflux through the same transporter [161]. Since IRE1 kinase-FMRP axis leads to marked upregulation of cholesterol efflux in macrophages (as shown in my study), it is plausible that increased demand for ABCA1 for cholesterol efflux could prevent m-IL-1β secretion through this route.

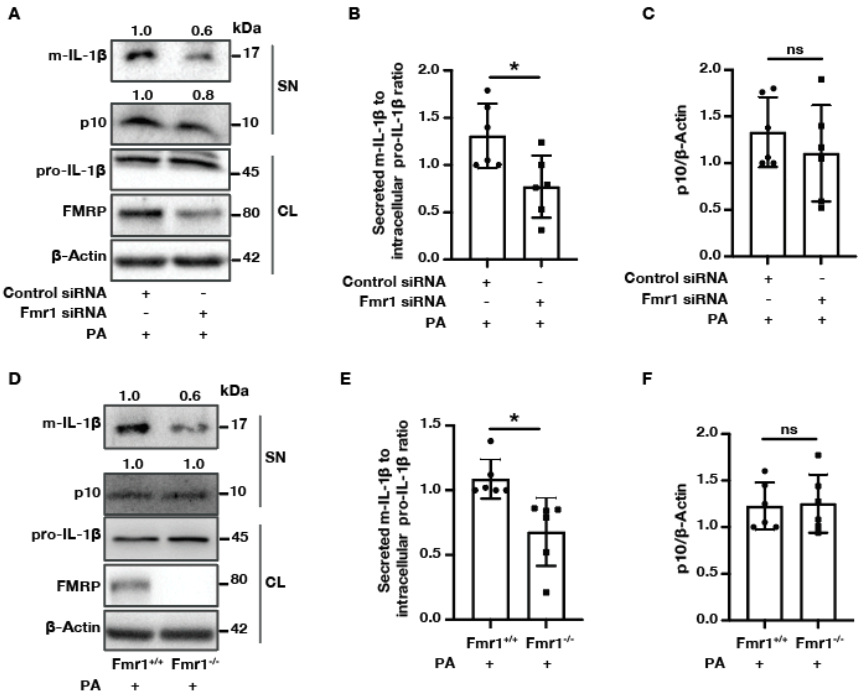

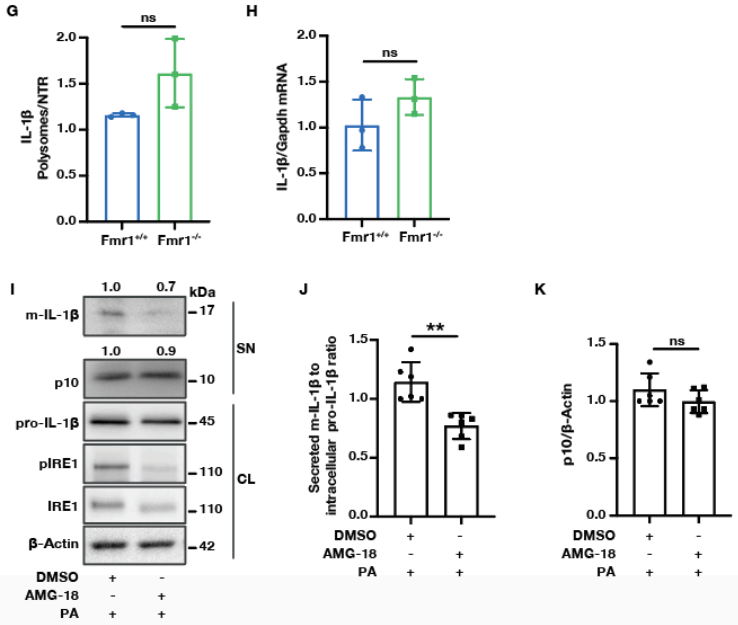

Figure 3.44. FMRP and IRE1 Kinase domain regulate IL-1β secretion.

(A) BMDMs were transfected with Fmr1- or control-siRNA and 24 hours after transfection cells were primed with LPS (200 µM) for 3 hours followed by PA (500 µM) treatment for 16 hours (n=6). **(B)** Quantification of secreted m-IL-1β to intracellular pro-IL-1β ratio normalized to β-Actin in Appendix Figure S6A. **(C)** Quantification of secreted p10 (caspase 1) to β-Actin in Appendix Figure S6A. **(D)** $Fmr1^{+/+}$ and $Fmr1^{-/-}$ BMDMs were primed with LPS (200 µM) for 3 hours followed by PA (500 µM) treatment for 16 hours (n=6). **(E)** Quantification of secreted m-IL-1β to intracellular pro-IL-1β ratio normalized to β-Actin in Appendix Figure S6D. **(F)** Quantification of secreted p10 (caspase 1) to β-Actin in Appendix Figure S6D. **(G)** The ratio of the pro-IL-1β mRNA in polysome to NTR fraction (n=3). (H) qRT-PCR analysis of pro-IL-1β in total mRNA levels from same samples used in polysome fractions (n=3). **(I)** BMDM cells were pre-treated with AMG-18 (10 µM) for 1 hour and the primed with LPS (200 µM) for 3 hours followed by PA (500 µM) treatment for 16 hours (n=6). **(J)** Quantification of secreted m-IL-1β to intracellular pro-IL-1β ratio normalized to β-Actin in Appendix Figure S6I. **(K)** Quantification of secreted p10 (caspase 1) to β-Actin in Appendix Figure S6I. Supernatants were analyzed by western blotting using specific antibody for IL-1β and caspase-1 and protein lysates were analyzed by western blotting using specific antibodies for FMRP, pIRE1, IRE1 and β-Actin. Data are mean ± SEM. Unpaired t-test with Welch's correction. *P≤ 0.05, **P≤ 0.01, ***P≤ 0.001.

3.11 Effect of dietary fat on macrophage ER stress and inflammasome activation

Unsaturated fatty acids shown to improve atherosclerosis by preventing most SAF-mediated deleterious effects. A bioactive lipid, Palmitoleate (PAO), regulates lipid

metabolism in liver and has been shown to evoke an overall lipidomic remodeling of the ER membranes in macrophages and mouse tissues. PAO can block lipid-induced inflammasome activation by preventing ER stress induction and chronic PAO supplementation lowers systemic IL-1β levels *in vivo* in hyperlipidemic mice resulting in reduction in plaque macrophages in mice [35]. To assess the impact of dietary unsaturated fatty acids on ER stress, in particular PAO, I treated BMDMs with palmitoleic acid (PAO) in its two forms trans- and cis-PAO. While cis-PAO blocked SFA-induced IRE1 kinase activation (as assessed by IRE1 auto-phosphorylation), trans-PAO treatment did not inhibit IRE1 activation in macrophages (Fig 3.45A). An earlier study had shown that cis-PAO prevents ER stress and IRE1 kinase activation, simultaneous to inflammasome activation by saturated fatty acids [35]. However, trans-PAO neither inhibited IRE1 kinase activation nor prevent PA-stimulated m-IL-1β production in macrophages (Fig 3.45B), suggesting that the cis configuration of PAO might have an important role on prevention of atherosclerosis.

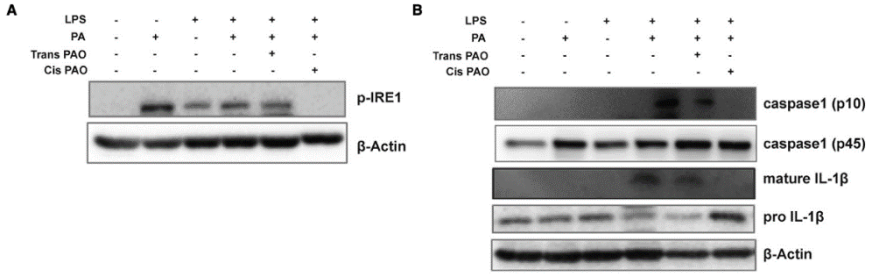

Figure 3.45. Trans-PAO treatment does not prevent lipid-induced IRE1 activation.

(A-B) BMDM **were** primed with LPS (200 μM) for 3 hours followed by co-treatment of PA (500 μM) with trans-PAO (500 μM) or cis-PAO (500 μM) treatment for 16 hours. **(A)** Protein lysates were analyzed by Western blotting using specific antibodies for p-IRE1 and β-Actin (n=3). **(B)** Supernatants and protein lysates were analyzed by western blotting using specific antibody for IL-1β, caspase-1 and β-Actin (n=3).

3.12 Impact of palmitoleic acid on atherosclerosis

Previous studies showed cis-PAO reduce atherosclerosis progression by blocking hyperlipidemia-induced organelle stress and inflammasome activation. Here I investigated trans-PAO's role in atherosclerotic plaque development in Apoe$^{-/-}$ mice model (Fig 3.46).

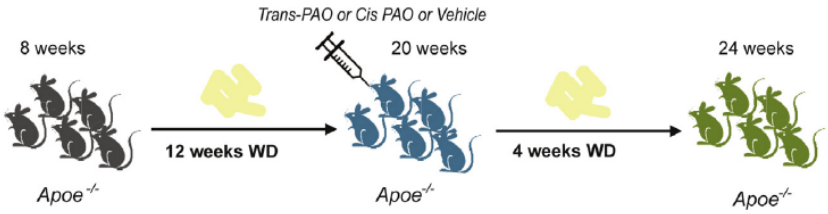

Figure 3.46. Atherosclerosis experiment design in Apoe$^{-/-}$ mice.

Apoe$^{-/-}$ mice were fed with WD for 12 weeks and treated by oral gavage with vehicle (1% BSA in PBS) or 1400 mg/kg/day cis or trans-PAO dissolved in vehicle for 4 weeks while continuing Western diet.

There were no significant changes in body weight, blood glucose levels, total plasma cholesterol, triglycerides, and the cholesterol content of lipoproteins between the trans-PAO-treated and control mice; however, there were a small but significant increase in the TG amount found in plasma high density lipoprotein in trans-PAO group (Fig. 3.47A).

A. Physical and biochemical characteristic of Apoe-/- mice in atherosclerosis studies

Variables	Treatment	Control	Trans-PAO	Cis PAO
n		12	9	6
Bodyweight (g)	Before	30.25±0.74	32.67±0.47	29±1.06
	After	30.92±0.82	31.89±061	28.67±061
Glucose (mg/dl)	Before	92.42±4.72	82.33±4.98	103.33±4.29
	After	88.00±4.51	91.78±6.36	93.67±7.29

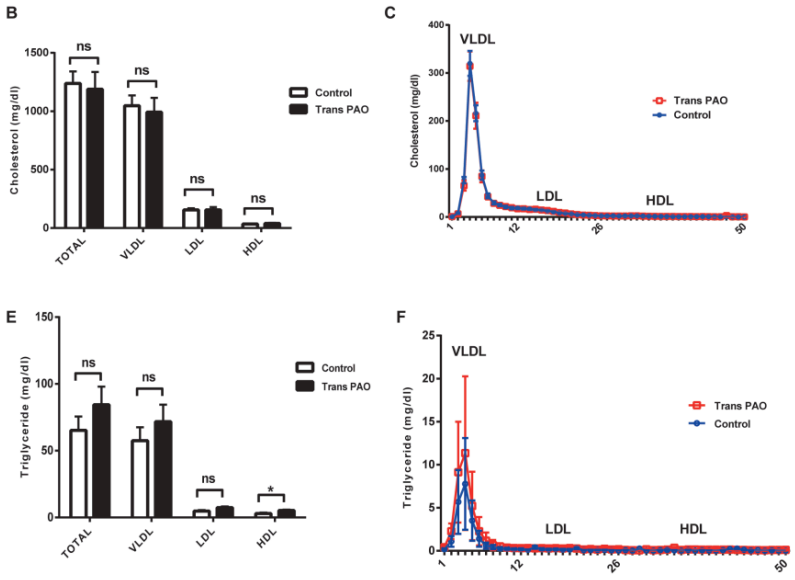

Figure 3.47. Characteristics of trans-PAO-treated Apoe-/- mice.

Measurements are from Apoe$^{-/-}$ mice on WD that received oral supplementation with PAO: **(A)** Total blood glucose and body weight changes, **(B)** Total plasma cholesterol

and lipoprotein (VLDL, LDL, HDL) cholesterol levels. **(C)** Lipoprotein profiles from control (blue) and trans-PAOtreated (red) Apoe-/- mice show an average percent distribution of total cholesterol for each group (n=5 per group). **(D)** Total plasma triglyceride and lipoprotein (VLDL, LDL, HDL) triglyceride levels. **(E)** Lipoprotein profiles from control (blue) and trans-PAO-treated (red) Apoe-/- mice show an average percent distribution of total triglyceride for each group (n=5 per group). Data are expressed as the mean ± SEM. VLDL, very low-density lipoprotein; LDL, low density lipoprotein; HDL, high density lipoprotein. Data are expressed as the mean ± SEM. ns = not significant *P < 0.05, (n=5 per group). Unpaired two-tailed Student's t test was used for statistical analysis.

Lastly, I evaluated the impact of trans-PAO on plaque development. *En face* aorta preparations showed that while cis-PAO treatment resulted in significant reduction, trans-PAO treatment did not alter lesion area (Fig 3.48A). Similarly, H&E, ORO and MOMA-2 stainings demonstrated that trans-PAO does not affect the lesion are, foam cell accumulation, necrotic core formation or macrophage content in the aortic sinus area, whereas cis-PAO significantly reduced foamy macrophage accumulation, necrotic core formation and MOMA-2 positive macrophage accumulation (Fig 3.48B-E), similar to IRE1 kinase inhibition (Fig 3.41 and 3.43). These results suggest that the cis configuration is critical for beneficial effects of cis-PAO, mostly thorough IRE1 activation.

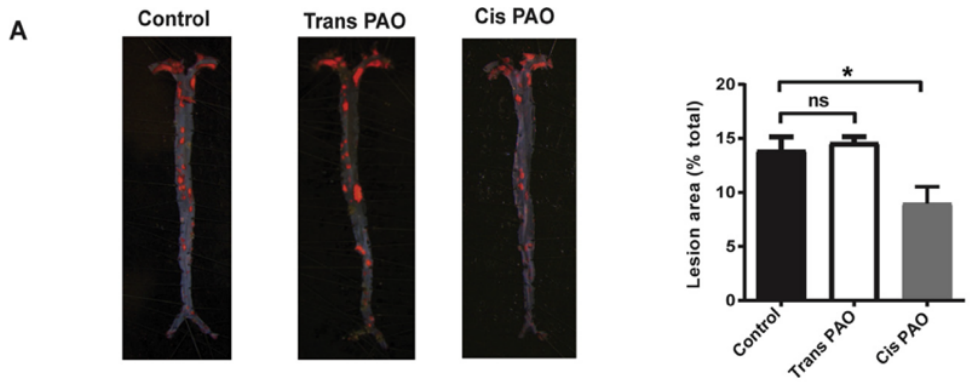

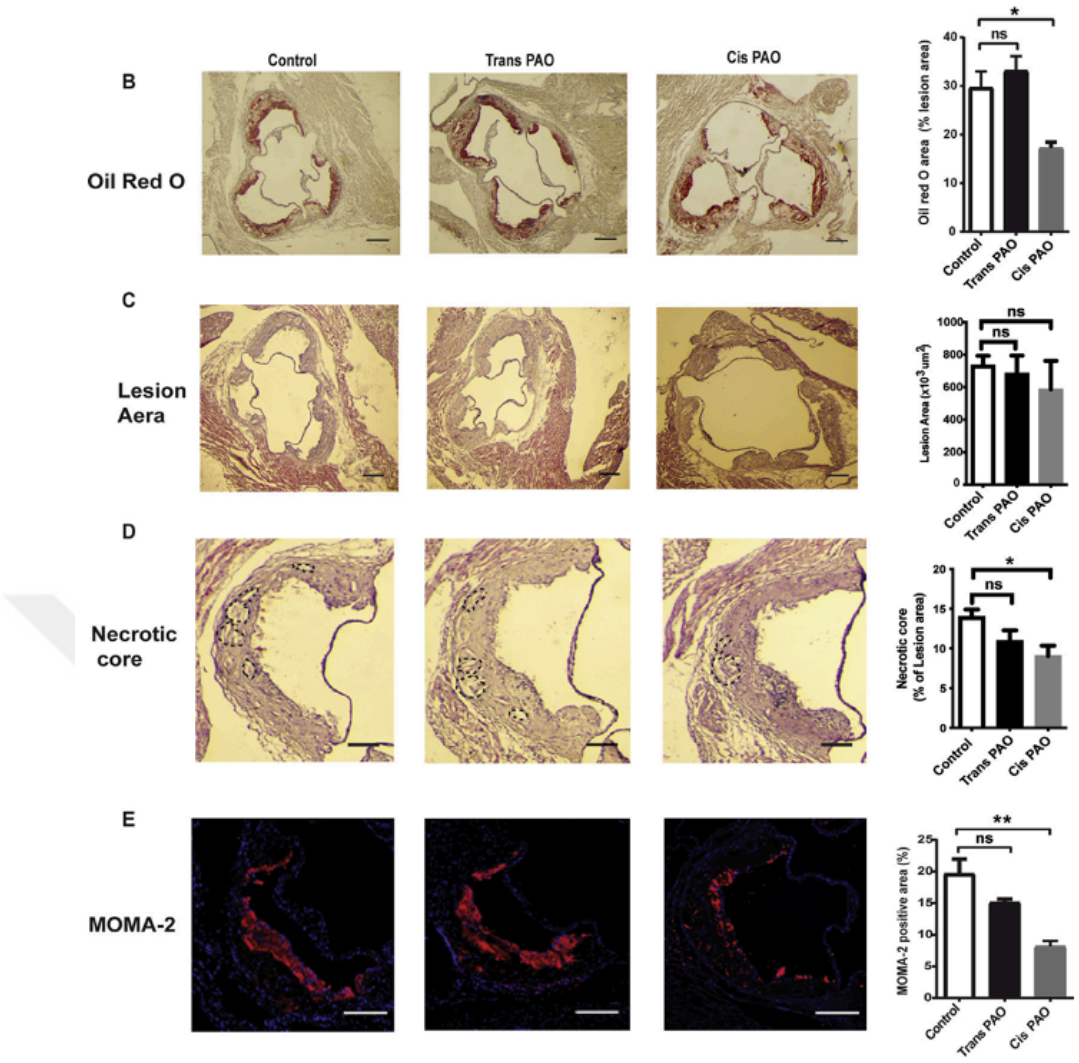

Figure 3.48. Trans-PAO does not prevent atherosclerosis in Apoe$^{-/-}$ mice.

(A) Lesion area was calculated from en face aorta preparations stained with Sudan IV (Control n=12, Trans-PAO n=9, Cis-PAO n=6). **(B)** Foam cell area was calculated from Oil Red O-stained aortic root sections (control n=9; Trans-PAO n=9, Cis-PAO n=5 scale bar: 300 mm). **(C)** Total plaque area and **(D)** necrotic area were calculated from hematoxylin and eosin (H&E)-stained aortic root lesions (control n=9, Trans-PAO n=9, Cis-PAO n=5, scale bar: 300 mm). **(E)** Macrophage content in aortic root lesions, as quantified after staining or MOMA-2 (green). (n=5 per group, scale bar: 150 mm). In each case, a representative image is shown in left and center, and the quantification of the data appears on the right. Control versus trans-PAO or cis-PAO; for statistical analysis.

Chapter 4 Discussion

Chronic lipid accumulation in the ER membranes (for example, during obesity and in hyperlipidemia) has been shown to impair ER functions and activate UPR signaling [35, 36, 162-164]. Numerous studies have shown that ER stress is an important primer for sterile inflammation that drives insulin resistance and atherogenesis [165]. Moreover, alleviating ER stress by inhibiting either PERK or IRE1 signaling was shown to prevent atherosclerosis progression [69, 91, 92, 126], but how chronic IRE1 kinase activation contributes to the atherosclerotic process remains unclear. My work revealed that in ER stressed induces the phosphorylation of FMRP, an RBP functioning as a translational suppressor, in an IRE1 kinase-dependent manner. This phosphorylation event results in a gain-of-function for FMRP, which leads to enhanced translational suppression of cholesterol transporters and efferocytosis receptors. Although ubiquitously expressed, prior work focused almost exclusively on FMRP's role in neurons in the context of its devastating role in FXS pathology [166-168]. My thesis work reveals a novel function for FMRP in regulating cholesterol trafficking in macrophages. Intriguingly, an earlier publication showed that FMRP protein expression is elevated in the macrophage-enriched area of human atherosclerotic plaques [169]. Moreover, lower cholesterol levels have been measured in a sub-population of the individuals afflicted with FXS, as well as in $Fmr1^{-/-}$ mice [170-172]. Although these findings foreshadowed a role of FMRP in the regulation of cholesterol homeostasis [105, 158, 169], FMRP's contribution to atherosclerosis was not investigated prior to this study, perhaps because Fmr1 gene lies on the X chromosome and most genome wide association studies in humans focus on variants on autosomal chromosomes excluding sex chromosomes. While characterizing the impact of IRE1 kinase activity and it's here proposed kinase substrate, FMRP, on macrophage functions, my thesis study revealed a role for an "IRE1-FMRP signaling axis" in the regulation of macrophage cholesterol trafficking and efferocytosis, which are among the primary cellular mechanisms that can regress atherosclerosis (Fig 4.1).

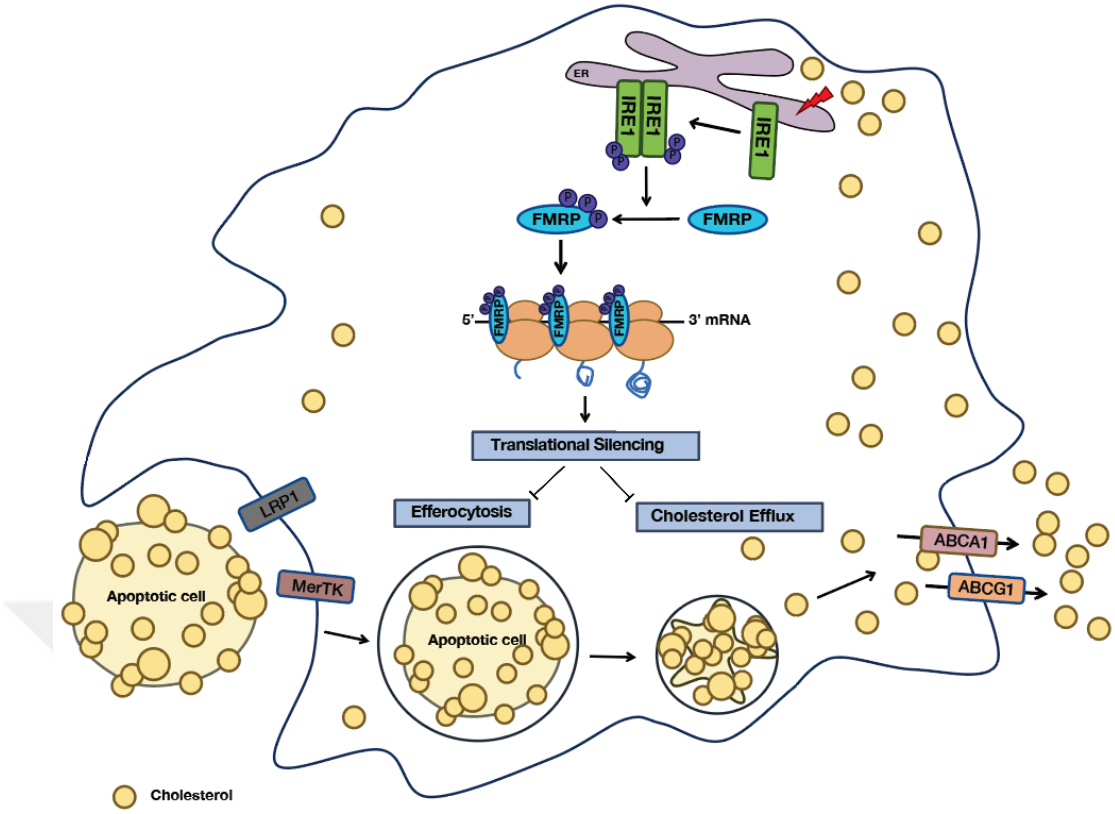

Figure 4.1. IRE1-FMRP signaling controls cholesterol efflux and efferocytosis pathways in macrophages.

IRE1-mediated FMRP phosphorylation suppresses translation of mRNA for key cholesterol transporters and efferocytosis receptors in macrophages and promotes atherosclerosis.

To gain insight into the physiological role of macrophage FMRP, I investigated the consequences of FMRP-deficiency on macrophage biology that are relevant to atherosclerosis development and plaque regression, such as foam cell formation, cholesterol efflux and efferocytosis. My findings show that FMRP has a prominent role in all three processes. Additionally, my observations are consistent with the finding that several mRNAs encoding cholesterol transporters and efferocytosis receptors interact with FMRP in prior RNA CLIP experiments [105, 158]. The data in my thesis study show that the absence of FMRP in macrophages increases the occupancy of these mRNAs in the polysome fraction, paralleling the increased expression of their corresponding protein products. In agreement with my observations *in cells*, FMRP-deficiency in macrophages increased RCT and efferocytosis in mice.

Moreover, system-wide and myeloid-specific Fmr1 knock-out mice were protected from hypercholesterolemia-induced atherosclerosis progression. In agreement with this notion, the IRE1 kinase-specific inhibitor, AMG-18, phenocopies the beneficial impact of FMRP deficiency (such as enhanced cholesterol efflux and efferocytosis) in macrophages. While my thesis study provides strong support for the role of macrophage FMRP in atherosclerosis progression, I did not examine the contribution of FMRP activity in other lesion cell types, such as endothelial or vascular smooth muscle cells, on atherosclerosis. The impairment of RCT and efferocytosis by IRE1-FMRP signaling implies that interventions to ablate FMRP in a macrophage-specific manner and in the adult organism could promote atherosclerotic plaque stabilization and hinder plaque progression, while escaping adverse impact of FMRP-deficiency on neuronal development.

FXS inheritance is depended on the CGG repeats, rather than Mendelian pattern [173]. Moreover, due to X-inactivation mechanism in females, FXS does not follow standard X-linked dominant inheritance. This mechanism result in significant difference in the occurrence of FXS as 1 in 7000 males and 1 in 11000 females, with milder phenotype in female compared to males [123]. In this study, I did not observe any aberrant difference in phenotype or the experimental results of the male and female $Fmr1^{-/-}$ mice. This might be due to the complexity of the human disease and limitations of mice models in studying disease models.

FMRP has been widely studied in neurons for its important roles in RNA metabolism. As an RNA binding protein, FMRP has been proposed to form ribonucleoprotein particle (RNP) complexes that might play different roles depending on the developmental stage of the brain [103, 174]. These studies highlight the negative effects of the FMRP loss of function; however, in this thesis I propose a beneficiary effect of FMRP knock-down or inhibition of its phosphorylation in atherosclerosis development. Atherosclerosis is classified as disease of aging that mostly occurs in adult life, presenting FMRP as a therapeutic target possibly without having the risk of developmental impact of FMRP.

Two recent studies show that FMRP plays a metabolic role in the liver. For example, systemic FMRP-deficiency in mice led to enhanced glucose tolerance and insulin sensitivity, while lowering plasma triglyceride and cholesterol content [172]. Another

study showed combined deficiency of FMRP and its paralog FXR2 (Fragile X mental retardation autosomal homolog 2) resulted in lower body fat and increased sensitivity to insulin [175]. Intriguingly, the FMRP loss-of-function in liver resulted in increased translation of hepatic mRNA involved in lipid metabolism [172]. In contrast to this previous work, I did not find Fmr1-deficiency associated changes in plasma cholesterol or lipoprotein levels in my atherosclerosis mouse models, perhaps due to the severe hypercholesterolemia induced by both genetic and dietary interventions.

In an earlier study, small molecule inhibitors that are specific for IRE1's RNase activity prevented lipid-induced inflammasome activation and secretion of mature interleukin- 1β (mIL-1β) and m-IL-18 in both mouse and human macrophages while reducing hyperlipidemia-induced m-IL-1β and m-IL-18 production and reducing atherosclerotic plaque size in mice [91]. FMRP suppression (by genetic knock down or via siRNA mediated knock down) also reduced m-IL-1β secreted from macrophages without altering inflammasome activation as determined by active caspase-1 in these macrophages (Appendix Fig S6A-S6F). However, knocking out FMRP from macrophages had no effect on IL-1β mRNA levels in the whole cell lysate or in the polysomes, suggesting against transcriptional or translational control over these cytokines' production (Appendix Fig S6G and S6H). Similarly, inhibition of IRE1 kinase also reduced m-IL-1β (Appendix Fig S6I-S6K). It has been shown that m-IL-1β can be secreted through ABCA1 and compete with cholesterol efflux through the same transporter [161]. Since IRE1 kinase-FMRP axis leads to marked upregulation of cholesterol efflux in macrophages (as shown in this study), it is plausible that increased demand for ABCA1 for cholesterol efflux could prevent m-IL-1β secretion through this route.

My finding that IRE1 phosphorylates FMRP leads to an important question: Why does the UPR signaling impinge on FMRP-mediated translational suppression? While intensely debated, multiple mechanisms have been proposed for translational suppression by FMRP including polyribosome stalling, miRNA-mediated translational silencing, and impairing translational initiation [105, 176-178]. Recently, phosphorylation-dependent FMRP-RNA phase separation has been suggested as a concept underlying these diverse regulatory mechanisms [179]. It is plausible that during ER stress, IRE1-induced FMRP phosphorylation, licensed by S500

phosphorylation and then spreading to adjacent serines and threonines, enhances phase-separation of FMRP and leads to the redistribution of FMRP-bound RNA into cytoplasmic granules, where they will not be translated. This would, in effect, reduce the protein folding stress and improve ER homeostasis. Indeed, ER stress induces stress granule formation, which contain mRNAs, RBPs (including FMRP), 40S ribosomal subunits and translational pre-initiation factors [180].

Finally, I demonstrated that IRE1 kinase-specific inhibitor, AMG-18, can phenocopy the beneficial impact of FMRP deficiency (such as enhanced cholesterol efflux and efferocytosis) in macrophages. Although I cannot definitively show that FMRP is the only mediator downstream of IRE1 kinase activity in regulating the proposed mechanisms, my data strongly supports that the novel IRE1 kinase target, FMRP's, expression in macrophages plays an important role in cholesterol efflux and apoptotic cell clearance and is an important contributor to atheroprotection offered by IRE1 kinase inhibition.

My thesis study provides mechanistic insight into the translational regulation of cholesterol efflux and efferocytosis by macrophages during ER stress, highlighting IRE1 and its effector FMRP as a promising molecular target for regulating atherosclerosis. The small molecule inhibitors of IRE1 kinase activity represent a translational opportunity in combating atherosclerosis.

Chapter 5 Future Perspectives

A maladaptive immune response to lipid imbalance drives atherosclerosis. Lipid accumulation in plaque-infiltrating macrophages stresses the ER and promotes atherosclerosis progression. Various studies have shown that ER stress is an important primer of sterile inflammation [165] and alleviating ER stress by inhibiting IRE1 signaling prevents atherosclerosis progression [69, 91, 92, 126]. However, whether IRE1 kinase activity contributes to the atherosclerosis progression has remained elusive prior to my thesis study. Targeting chronic ER stress in atherosclerosis is challenging due to the essential cellular homeostatic functions governed by IRE1. My thesis work revealed that in ER-stressed macrophages phosphorylation of FMRP, an RBP functioning as a translational suppressor, is enhanced in an IRE1 kinase-dependent manner. This phosphorylation event results in a gain-of-function for FMRP, which leads to enhanced translational suppression of cholesterol transporters and efferocytosis receptors that contribute to atherosclerosis progression.

I described a novel, promising mechanistic target for regulating atherosclerosis by inhibition of IRE1 kinase activity or through targeting IRE1 kinase's substrate FMRP. My findings show that targeting FMRP-regulated translational control over macrophage cholesterol trafficking and efferocytosis by targeting IRE1-FMRP signaling axis represent a novel therapeutic approach to cardiovascular disease. In this study, I showed that targeting IRE1 by small molecule inhibitor, AMG-18, is a potential therapeutic approach to prevent and/or initiate the regression of atherosclerosis. Moreover, proposed pathway can be targeted by RNA-based therapeutic strategies like antisense oligo (ASO) against either IRE1 or FMR1 RNA present a translational opportunity in combating atherosclerosis.

My RNA-Seq and AHA-proteomics analysis in this thesis study revealed many potential and novel FMRP targets in ER stress induced macrophages. These targets can be further investigated to discover novel pathways downstream of IRE1-FMRP axis. For example, although I did not study the cholesterol synthesis pathway in this

work, my RNA-Seq and AHA-proteomics analysis revealed proteins involved in the cholesterol biogenesis. Moreover, investigating this signaling axis in other metabolically active organs targeted by hyperlipidemia (such as liver) could lead to discovery and validation of novel targets that play role in cholesterol synthesis pathway. In summary, The RNA-Seq and AHA-proteomics analysis reported in the study has great potential to develop into numerous studies that could represent novel targets and provide better understanding to how IRE1-FMRP interaction contribute to disease pathogenesis.

Beside polysome stalling, IRE1-mediated phosphorylation of FMRP could lead to the redistribution of FMRP-bound RNAs into cytoplasmic granules, where they will not be translated. I discovered that ER stress pathway is further enhanced in FMRP knockout macrophages in fatty acid stressed macrophages. Further analysis is required to profile stress granule and associated mRNA regulation by IRE1-mediated FMRP phosphorylation. This pathway would have the potential to reduce the protein folding stress and improve ER homeostasis

Bibliography

1. Low Wang, C.C., et al., *Clinical Update: Cardiovascular Disease in Diabetes Mellitus: Atherosclerotic Cardiovascular Disease and Heart Failure in Type 2 Diabetes Mellitus - Mechanisms, Management, and Clinical Considerations.* Circulation, 2016. **133**(24): p. 2459-502.
2. Ormazabal, V., et al., *Association between insulin resistance and the development of cardiovascular disease.* Cardiovascular Diabetology, 2018. **17**(1): p. 122.
3. Sowers, J.R., M. Epstein, and E.D. Frohlich, *Diabetes, hypertension, and cardiovascular disease: an update.* Hypertension, 2001. **37**(4): p. 1053-9.
4. Martín-Timón, I., et al., *Type 2 diabetes and cardiovascular disease: Have all risk factors the same strength?* World J Diabetes, 2014. **5**(4): p. 444-70.
5. Roth, G.A., et al., *Global Burden of Cardiovascular Diseases and Risk Factors, 1990-2019: Update From the GBD 2019 Study.* J Am Coll Cardiol, 2020. **76**(25): p. 2982-3021.
6. Olvera Lopez E, B.B., Jan A., *Cardiovascular Disease*. 2022, Treasure Island (FL): StatPearls Publishing.
7. Stewart, J., G. Manmathan, and P. Wilkinson, *Primary prevention of cardiovascular disease: A review of contemporary guidance and literature.* JRSM Cardiovasc Dis, 2017. **6**: p. 2048004016687211.
8. Wang, D.D. and F.B. Hu, *Dietary Fat and Risk of Cardiovascular Disease: Recent Controversies and Advances.* Annu Rev Nutr, 2017. **37**: p. 423-446.
9. Virani, S.S., et al., *Heart Disease and Stroke Statistics-2021 Update: A Report From the American Heart Association.* Circulation, 2021. **143**(8): p. e254-e743.
10. Robbins, C.S., et al., *Local proliferation dominates lesional macrophage accumulation in atherosclerosis.* Nat Med, 2013. **19**(9): p. 1166-72.
11. Weber, C. and H. Noels, *Atherosclerosis: current pathogenesis and therapeutic options.* Nat Med, 2011. **17**(11): p. 1410-22.
12. Rocha, V.Z. and P. Libby, *Obesity, inflammation, and atherosclerosis.* Nat Rev Cardiol, 2009. **6**(6): p. 399-409.
13. Randolph, G.J., *Mechanisms that regulate macrophage burden in atherosclerosis.* Circ Res, 2014. **114**(11): p. 1757-71.
14. Westerterp, M., et al., *Deficiency of ATP-binding cassette transporters A1 and G1 in macrophages increases inflammation and accelerates atherosclerosis in mice.* Circ Res, 2013. **112**(11): p. 1456-65.
15. Westerterp, M., et al., *Cholesterol Efflux Pathways Suppress Inflammasome Activation, NETosis, and Atherogenesis.* Circulation, 2018. **138**(9): p. 898-912.
16. Khera, A.V., et al., *Cholesterol efflux capacity, high-density lipoprotein function, and atherosclerosis.* N Engl J Med, 2011. **364**(2): p. 127-35.
17. Yurdagul, A., Jr., et al., *Mechanisms and Consequences of Defective Efferocytosis in Atherosclerosis.* Front Cardiovasc Med, 2017. **4**: p. 86.
18. Kojima, Y., I.L. Weissman, and N.J. Leeper, *The Role of Efferocytosis in Atherosclerosis.* Circulation, 2017. **135**(5): p. 476-489.
19. Brophy, M.L., et al., *Eating the Dead to Keep Atherosclerosis at Bay.* Front Cardiovasc Med, 2017. **4**: p. 2.

20. Laufs, U., et al., *Physical inactivity increases oxidative stress, endothelial dysfunction, and atherosclerosis.* Arterioscler Thromb Vasc Biol, 2005. **25**(4): p. 809-14.
21. Lechner, K., et al., *Lifestyle factors and high-risk atherosclerosis: Pathways and mechanisms beyond traditional risk factors.* Eur J Prev Cardiol, 2020. **27**(4): p. 394-406.
22. Cosselman, K.E., A. Navas-Acien, and J.D. Kaufman, *Environmental factors in cardiovascular disease.* Nat Rev Cardiol, 2015. **12**(11): p. 627-42.
23. Bentzon, J.F., et al., *Mechanisms of plaque formation and rupture.* Circ Res, 2014. **114**(12): p. 1852-66.
24. Mehta, V. and E. Tzima, *A turbulent path to plaque formation.* Nature, 2016. **540**(7634): p. 531-532.
25. Wang, L., et al., *Integrin-YAP/TAZ-JNK cascade mediates atheroprotective effect of unidirectional shear flow.* Nature, 2016. **540**(7634): p. 579-582.
26. Akers, E.J., S.J. Nicholls, and B.A. Di Bartolo, *Plaque Calcification: Do Lipoproteins Have a Role?* Arterioscler Thromb Vasc Biol, 2019. **39**(10): p. 1902-1910.
27. Shi, X., et al., *Calcification in Atherosclerotic Plaque Vulnerability: Friend or Foe?* Frontiers in Physiology, 2020. **11**.
28. Hoshino, T., et al., *Mechanical stress analysis of a rigid inclusion in distensible material: a model of atherosclerotic calcification and plaque vulnerability.* Am J Physiol Heart Circ Physiol, 2009. **297**(2): p. H802-10.
29. Qiu, C., et al., *High-density lipoprotein cholesterol efflux capacity is inversely associated with cardiovascular risk: a systematic review and meta-analysis.* Lipids Health Dis, 2017. **16**(1): p. 212.
30. Ikonen, E., *Cellular cholesterol trafficking and compartmentalization.* Nat Rev Mol Cell Biol, 2008. **9**(2): p. 125-38.
31. Luo, J., H. Yang, and B.L. Song, *Mechanisms and regulation of cholesterol homeostasis.* Nat Rev Mol Cell Biol, 2020. **21**(4): p. 225-245.
32. Yan, J. and T. Horng, *Lipid Metabolism in Regulation of Macrophage Functions.* Trends Cell Biol, 2020. **30**(12): p. 979-989.
33. Afonso Mda, S., et al., *The impact of dietary fatty acids on macrophage cholesterol homeostasis.* J Nutr Biochem, 2014. **25**(2): p. 95-103.
34. Sukhorukov, V.N., et al., *Endoplasmic Reticulum Stress in Macrophages: The Vicious Circle of Lipid Accumulation and Pro-Inflammatory Response.* Biomedicines, 2020. **8**(7).
35. Çimen, I., et al., *Prevention of atherosclerosis by bioactive palmitoleate through suppression of organelle stress and inflammasome activation.* Sci Transl Med, 2016. **8**(358): p. 358ra126.
36. Volmer, R., K. van der Ploeg, and D. Ron, *Membrane lipid saturation activates endoplasmic reticulum unfolded protein response transducers through their transmembrane domains.* Proc Natl Acad Sci U S A, 2013. **110**(12): p. 4628-33.
37. Lian, Z., et al., *Replacing Saturated Fat With Unsaturated Fat in Western Diet Reduces Foamy Monocytes and Atherosclerosis in Male Ldlr(-/-) Mice.* Arterioscler Thromb Vasc Biol, 2020. **40**(1): p. 72-85.
38. de Oliveira, P.A., et al., *Unsaturated Fatty Acids Improve Atherosclerosis Markers in Obese and Overweight Non-diabetic Elderly Patients.* Obes Surg, 2017. **27**(10): p. 2663-2671.

39. Solomon, K.R. and M.R. Freeman, *The complex interplay between cholesterol and prostate malignancy.* Urol Clin North Am, 2011. **38**(3): p. 243-59.
40. Botham, K.M. and P.A. Mayes, *Cholesterol Synthesis, Transport, & Excretion*, in *Harper's Illustrated Biochemistry, 30e*, V.W. Rodwell, et al., Editors. 2016, McGraw-Hill Education: New York, NY.
41. Cerqueira, N.M.F.S.A., et al., *Cholesterol Biosynthesis: A Mechanistic Overview.* Biochemistry, 2016. **55**(39): p. 5483-5506.
42. Moore, K.J., F.J. Sheedy, and E.A. Fisher, *Macrophages in atherosclerosis: a dynamic balance.* Nat Rev Immunol, 2013. **13**(10): p. 709-21.
43. Go, G.W. and A. Mani, *Low-density lipoprotein receptor (LDLR) family orchestrates cholesterol homeostasis.* Yale J Biol Med, 2012. **85**(1): p. 19-28.
44. Yu, X.H., et al., *Foam cells in atherosclerosis.* Clin Chim Acta, 2013. **424**: p. 245-52.
45. Xu, S., et al., *LOX-1 in atherosclerosis: biological functions and pharmacological modifiers.* Cell Mol Life Sci, 2013. **70**(16): p. 2859-72.
46. Herijgers, N., et al., *Low density lipoprotein receptor of macrophages facilitates atherosclerotic lesion formation in C57Bl/6 mice.* Arterioscler Thromb Vasc Biol, 2000. **20**(8): p. 1961-7.
47. Kunjathoor, V.V., et al., *Scavenger receptors class A-I/II and CD36 are the principal receptors responsible for the uptake of modified low density lipoprotein leading to lipid loading in macrophages.* J Biol Chem, 2002. **277**(51): p. 49982-8.
48. Febbraio, M., D.P. Hajjar, and R.L. Silverstein, *CD36: a class B scavenger receptor involved in angiogenesis, atherosclerosis, inflammation, and lipid metabolism.* J Clin Invest, 2001. **108**(6): p. 785-91.
49. Park, Y.M., *CD36, a scavenger receptor implicated in atherosclerosis.* Exp Mol Med, 2014. **46**(6): p. e99.
50. Afonso, M.S., et al., *Molecular Pathways Underlying Cholesterol Homeostasis.* Nutrients, 2018. **10**(6).
51. Duong, M., et al., *Induction of obesity impairs reverse cholesterol transport in ob/ob mice.* PLoS One, 2018. **13**(9): p. e0202102.
52. Oram, J.F., et al., *ABCA1 is the cAMP-inducible apolipoprotein receptor that mediates cholesterol secretion from macrophages.* J Biol Chem, 2000. **275**(44): p. 34508-11.
53. Costet, P., et al., *Sterol-dependent transactivation of the ABC1 promoter by the liver X receptor/retinoid X receptor.* J Biol Chem, 2000. **275**(36): p. 28240-5.
54. Liao, S. and C.S. McLachlan, *Cholesterol Efflux: Does It Contribute to Aortic Stiffening?* Journal of Cardiovascular Development and Disease, 2018. **5**(2): p. 23.
55. Heinecke, J.W., *A new era for quantifying HDL and cardiovascular risk?* Nature Medicine, 2012. **18**(9): p. 1346-1347.
56. Guo, Y., et al., *Synthetic High-Density Lipoprotein-Mediated Targeted Delivery of Liver X Receptors Agonist Promotes Atherosclerosis Regression.* EBioMedicine, 2018. **28**: p. 225-233.
57. Zimmer, S., et al., *Cyclodextrin promotes atherosclerosis regression via macrophage reprogramming.* Sci Transl Med, 2016. **8**(333): p. 333ra50.
58. Joyce, C.W., et al., *The ATP binding cassette transporter A1 (ABCA1) modulates the development of aortic atherosclerosis in C57BL/6 and apoE-knockout mice.* Proc Natl Acad Sci U S A, 2002. **99**(1): p. 407-12.

59. Klucken, J., et al., *ABCG1 (ABC8), the human homolog of the Drosophila white gene, is a regulator of macrophage cholesterol and phospholipid transport.* Proc Natl Acad Sci U S A, 2000. **97**(2): p. 817-22.
60. Tall, A.R. and L. Yvan-Charvet, *Cholesterol, inflammation and innate immunity.* Nat Rev Immunol, 2015. **15**(2): p. 104-16.
61. Du, H., et al., *Reduction of atherosclerotic plaques by lysosomal acid lipase supplementation.* Arterioscler Thromb Vasc Biol, 2004. **24**(1): p. 147-54.
62. Ouimet, M., et al., *Autophagy regulates cholesterol efflux from macrophage foam cells via lysosomal acid lipase.* Cell Metab, 2011. **13**(6): p. 655-67.
63. Dubland, J.A. and G.A. Francis, *Lysosomal acid lipase: at the crossroads of normal and atherogenic cholesterol metabolism.* Front Cell Dev Biol, 2015. **3**: p. 3.
64. Wang, D., et al., *Targeting Foam Cell Formation in Atherosclerosis: Therapeutic Potential of Natural Products.* Pharmacol Rev, 2019. **71**(4): p. 596-670.
65. Sekiya, M., et al., *The role of neutral cholesterol ester hydrolysis in macrophage foam cells.* J Atheroscler Thromb, 2011. **18**(5): p. 359-64.
66. Boada-Romero, E., et al., *The clearance of dead cells by efferocytosis.* Nat Rev Mol Cell Biol, 2020. **21**(7): p. 398-414.
67. Henson, P.M., D.L. Bratton, and V.A. Fadok, *Apoptotic cell removal.* Curr Biol, 2001. **11**(19): p. R795-805.
68. Bhatia, V.K., et al., *Complement C1q reduces early atherosclerosis in low-density lipoprotein receptor-deficient mice.* Am J Pathol, 2007. **170**(1): p. 416-26.
69. Tabas, I., *The role of endoplasmic reticulum stress in the progression of atherosclerosis.* Circ Res, 2010. **107**(7): p. 839-50.
70. Bird, L., *Transporters help clear cell corpses.* Nature Reviews Immunology, 2019. **19**(1): p. 5-5.
71. Morioka, S., et al., *Efferocytosis induces a novel SLC program to promote glucose uptake and lactate release.* Nature, 2018. **563**(7733): p. 714-718.
72. Doran, A.C., A. Yurdagul, and I. Tabas, *Efferocytosis in health and disease.* Nature Reviews Immunology, 2020. **20**(4): p. 254-267.
73. Johnson Chavarria, E.M., *The Cell: A Molecular Approach, Seventh Edition.* The Yale Journal of Biology and Medicine, 2016. **89**(3): p. 424-424.
74. Alberts, B.W.J.H.T., *Molecular biology of the cell*. 2008, New York: Garland Science.
75. Waudby, C.A., C.M. Dobson, and J. Christodoulou, *Nature and Regulation of Protein Folding on the Ribosome.* Trends Biochem Sci, 2019. **44**(11): p. 914-926.
76. Alberts, B., et al., *The Endoplasmic Reticulum*, in *Molecular Biology of the Cell. .* 2002, New York: Garland Science.
77. Wiersma, V.R., et al., *Mechanisms of Translocation of ER Chaperones to the Cell Surface and Immunomodulatory Roles in Cancer and Autoimmunity.* Front Oncol, 2015. **5**: p. 7.
78. Zhang, Y., E. Baig, and D.B. Williams, *Functions of ERp57 in the folding and assembly of major histocompatibility complex class I molecules.* J Biol Chem, 2006. **281**(21): p. 14622-31.
79. Nagata, K., *Expression and function of heat shock protein 47: a collagen-specific molecular chaperone in the endoplasmic reticulum.* Matrix Biol, 1998. **16**(7): p. 379-86.

80. Gruber, C.W., et al., *Protein disulfide isomerase: the structure of oxidative folding.* Trends Biochem Sci, 2006. **31**(8): p. 455-64.
81. Schopf, F.H., M.M. Biebl, and J. Buchner, *The HSP90 chaperone machinery.* Nat Rev Mol Cell Biol, 2017. **18**(6): p. 345-360.
82. Peterson, J.R., et al., *Transient, lectin-like association of calreticulin with folding intermediates of cellular and viral glycoproteins.* Mol Biol Cell, 1995. **6**(9): p. 1173-84.
83. Ron, D. and P. Walter, *Signal integration in the endoplasmic reticulum unfolded protein response.* Nature Reviews Molecular Cell Biology, 2007. **8**(7): p. 519-529.
84. Wang, M. and R.J. Kaufman, *The impact of the endoplasmic reticulum protein-folding environment on cancer development.* Nature Reviews Cancer, 2014. **14**(9): p. 581-597.
85. Sukhorukov, V.N., et al., *Endoplasmic Reticulum Stress in Macrophages: The Vicious Circle of Lipid Accumulation and Pro-Inflammatory Response.* Biomedicines, 2020. **8**(7): p. 210.
86. Cloots, E., et al., *Evolution and function of the epithelial cell-specific ER stress sensor IRE1β.* Mucosal Immunology, 2021.
87. Walter, P. and D. Ron, *The unfolded protein response: from stress pathway to homeostatic regulation.* Science, 2011. **334**(6059): p. 1081-6.
88. Robblee, M.M., et al., *Saturated Fatty Acids Engage an IRE1α-Dependent Pathway to Activate the NLRP3 Inflammasome in Myeloid Cells.* Cell Rep, 2016. **14**(11): p. 2611-23.
89. Çimen, I., et al., *Prevention of atherosclerosis by bioactive palmitoleate through suppression of organelle stress and inflammasome activation.* Science Translational Medicine, 2016. **8**(358): p. 358ra126-358ra126.
90. Seimon, T.A., et al., *Atherogenic lipids and lipoproteins trigger CD36-TLR2-dependent apoptosis in macrophages undergoing endoplasmic reticulum stress.* Cell Metab, 2010. **12**(5): p. 467-82.
91. Tufanli, O., et al., *Targeting IRE1 with small molecules counteracts progression of atherosclerosis.* Proc Natl Acad Sci U S A, 2017. **114**(8): p. E1395-e1404.
92. Erbay, E., et al., *Reducing endoplasmic reticulum stress through a macrophage lipid chaperone alleviates atherosclerosis.* Nat Med, 2009. **15**(12): p. 1383-91.
93. Zhou, A.X. and I. Tabas, *The UPR in atherosclerosis.* Semin Immunopathol, 2013. **35**(3): p. 321-32.
94. Halbleib, K., et al., *Activation of the Unfolded Protein Response by Lipid Bilayer Stress.* Mol Cell, 2017. **67**(4): p. 673-684.e8.
95. Verkerk, A.J., et al., *Identification of a gene (FMR-1) containing a CGG repeat coincident with a breakpoint cluster region exhibiting length variation in fragile X syndrome.* Cell, 1991. **65**(5): p. 905-14.
96. Hernandez, R.N., et al., *Autism spectrum disorder in fragile X syndrome: a longitudinal evaluation.* Am J Med Genet A, 2009. **149a**(6): p. 1125-37.
97. Hagerman, R.J., et al., *Advances in the treatment of fragile X syndrome.* Pediatrics, 2009. **123**(1): p. 378-90.
98. Brackett, D.M., et al., *FMR1 transcript isoforms: association with polyribosomes; regional and developmental expression in mouse brain.* PLoS One, 2013. **8**(3): p. e58296.

99. Naumann, A., et al., *A distinct DNA-methylation boundary in the 5'- upstream sequence of the FMR1 promoter binds nuclear proteins and is lost in fragile X syndrome.* Am J Hum Genet, 2009. **85**(5): p. 606-16.
100. Tabolacci, E., et al., *Transcriptional Reactivation of the FMR1 Gene. A Possible Approach to the Treatment of the Fragile X Syndrome.* Genes (Basel), 2016. **7**(8).
101. Siomi, H., et al., *Essential role for KH domains in RNA binding: impaired RNA binding by a mutation in the KH domain of FMR1 that causes fragile X syndrome.* Cell, 1994. **77**(1): p. 33-9.
102. Bardoni, B., et al., *Analysis of domains affecting intracellular localization of the FMRP protein.* Neurobiol Dis, 1997. **4**(5): p. 329-36.
103. Fernandez, E., N. Rajan, and C. Bagni, *The FMRP regulon: from targets to disease convergence.* Frontiers in Neuroscience, 2013. **7**.
104. Doll, C.A. and K. Broadie, *Neuron class-specific requirements for Fragile X Mental Retardation Protein in critical period development of calcium signaling in learning and memory circuitry.* Neurobiol Dis, 2016. **89**: p. 76-87.
105. Darnell, J.C., et al., *FMRP stalls ribosomal translocation on mRNAs linked to synaptic function and autism.* Cell, 2011. **146**(2): p. 247-61.
106. Richter, J.D. and X. Zhao, *The molecular biology of FMRP: new insights into fragile X syndrome.* Nature Reviews Neuroscience, 2021. **22**(4): p. 209-222.
107. Okray, Z., et al., *A novel fragile X syndrome mutation reveals a conserved role for the carboxy-terminus in FMRP localization and function.* EMBO Mol Med, 2015. **7**(4): p. 423-37.
108. Alpatov, R., et al., *A chromatin-dependent role of the fragile X mental retardation protein FMRP in the DNA damage response.* Cell, 2014. **157**(4): p. 869-81.
109. He, Q. and W. Ge, *FMRP: a new chapter with chromatin.* Protein Cell, 2014. **5**(12): p. 885-8.
110. Majumder, P., et al., *Co-regulation of mRNA translation by TDP-43 and Fragile X Syndrome protein FMRP.* Acta Neuropathol, 2016. **132**(5): p. 721-738.
111. Shamay-Ramot, A., et al., *Fmrp Interacts with Adar and Regulates RNA Editing, Synaptic Density and Locomotor Activity in Zebrafish.* PLoS Genet, 2015. **11**(12): p. e1005702.
112. Filippini, A., et al., *Absence of the Fragile X Mental Retardation Protein results in defects of RNA editing of neuronal mRNAs in mouse.* RNA Biol, 2017. **14**(11): p. 1580-1591.
113. Zhou, L.T., et al., *A novel role of fragile X mental retardation protein in pre-mRNA alternative splicing through RNA-binding protein 14.* Neuroscience, 2017. **349**: p. 64-75.
114. Sudhakaran, I.P., et al., *FMRP and Ataxin-2 function together in long-term olfactory habituation and neuronal translational control.* Proc Natl Acad Sci U S A, 2014. **111**(1): p. E99-e108.
115. Haneklaus, M., et al., *The RNA-binding protein Tristetraprolin (TTP) is a critical negative regulator of the NLRP3 inflammasome.* J Biol Chem, 2017. **292**(17): p. 6869-6881.
116. Kang, J.G., et al., *Zinc finger protein tristetraprolin interacts with CCL3 mRNA and regulates tissue inflammation.* J Immunol, 2011. **187**(5): p. 2696-701.

117. Zhang, H., et al., *mRNA-binding protein ZFP36 is expressed in atherosclerotic lesions and reduces inflammation in aortic endothelial cells.* Arterioscler Thromb Vasc Biol, 2013. **33**(6): p. 1212-20.
118. Chiu, D.S., et al., *High-density lipoprotein-binding protein (HBP)/vigilin is expressed in human atherosclerotic lesions and colocalizes with apolipoprotein E.* Arterioscler Thromb Vasc Biol, 1997. **17**(11): p. 2350-8.
119. Mobin, M.B., et al., *The RNA-binding protein vigilin regulates VLDL secretion through modulation of Apob mRNA translation.* Nat Commun, 2016. **7**: p. 12848.
120. Ramírez, C.M., et al., *RNA binding protein HuR regulates the expression of ABCA1.* J Lipid Res, 2014. **55**(6): p. 1066-76.
121. Hersh, J.H. and R.A. Saul, *Health supervision for children with fragile X syndrome.* Pediatrics, 2011. **127**(5): p. 994-1006.
122. Bagni, C., et al., *Fragile X syndrome: causes, diagnosis, mechanisms, and therapeutics.* J Clin Invest, 2012. **122**(12): p. 4314-22.
123. Hunter, J., et al., *Epidemiology of fragile X syndrome: a systematic review and meta-analysis.* Am J Med Genet A, 2014. **164a**(7): p. 1648-58.
124. Shamu, C.E. and P. Walter, *Oligomerization and phosphorylation of the Ire1p kinase during intracellular signaling from the endoplasmic reticulum to the nucleus.* Embo j, 1996. **15**(12): p. 3028-39.
125. Acosta-Alvear, D., et al., *The unfolded protein response and endoplasmic reticulum protein targeting machineries converge on the stress sensor IRE1.* Elife, 2018. **7**.
126. Onat, U.I., et al., *Intercepting the Lipid-Induced Integrated Stress Response Reduces Atherosclerosis.* J Am Coll Cardiol, 2019. **73**(10): p. 1149-1169.
127. Iwawaki, T., et al., *Function of IRE1 alpha in the placenta is essential for placental development and embryonic viability.* Proc Natl Acad Sci U S A, 2009. **106**(39): p. 16657-62.
128. Zhang, X., R. Goncalves, and D.M. Mosser, *The isolation and characterization of murine macrophages.* Curr Protoc Immunol, 2008. **Chapter 14**: p. Unit 14.1.
129. Wessel, D. and U.I. Flügge, *A method for the quantitative recovery of protein in dilute solution in the presence of detergents and lipids.* Anal Biochem, 1984. **138**(1): p. 141-3.
130. Baboo, S., et al., *DeGlyPHER: An Ultrasensitive Method for the Analysis of Viral Spike N-Glycoforms.* Anal Chem, 2021. **93**(40): p. 13651-13657.
131. He, L., et al., *Extracting Accurate Precursor Information for Tandem Mass Spectra by RawConverter.* Anal Chem, 2015. **87**(22): p. 11361-7.
132. Xu, T., et al., *ProLuCID: An improved SEQUEST-like algorithm with enhanced sensitivity and specificity.* J Proteomics, 2015. **129**: p. 16-24.
133. Tabb, D.L., W.H. McDonald, and J.R. Yates, 3rd, *DTASelect and Contrast: tools for assembling and comparing protein identifications from shotgun proteomics.* J Proteome Res, 2002. **1**(1): p. 21-6.
134. Peng, J., et al., *Evaluation of multidimensional chromatography coupled with tandem mass spectrometry (LC/LC-MS/MS) for large-scale protein analysis: the yeast proteome.* J Proteome Res, 2003. **2**(1): p. 43-50.
135. Beausoleil, S.A., et al., *A probability-based approach for high-throughput protein phosphorylation analysis and site localization.* Nat Biotechnol, 2006. **24**(10): p. 1285-92.

136. Stastna, M., et al., *Dynamic Proteomic and miRNA Analysis of Polysomes from Isolated Mouse Heart After Langendorff Perfusion.* J Vis Exp, 2018(138).
137. Ma, Y., et al., *Quantitative analysis of newly synthesized proteins.* Nat Protoc, 2018. **13**(8): p. 1744-1762.
138. Zhang, Y., et al., *The fragile X mental retardation syndrome protein interacts with novel homologs FXR1 and FXR2.* Embo j, 1995. **14**(21): p. 5358-66.
139. Wang, Y., et al., *Discovery of LAMP-2A as potential biomarkers for glioblastoma development by modulating apoptosis through N-CoR degradation.* Cell Commun Signal, 2021. **19**(1): p. 40.
140. Reynolds, C.D., et al., *Comparison of Equivalence between Two Commercially Available S499-Phosphorylated FMRP Antibodies in Mice.* PLoS One, 2015. **10**(11): p. e0143134.
141. Kim, J., et al., *Allomyrina Dichotoma Larvae Regulate Food Intake and Body Weight in High Fat Diet-Induced Obese Mice Through mTOR and Mapk Signaling Pathways.* Nutrients, 2016. **8**(2): p. 100.
142. Davignon, J., et al., *Apolipoprotein E and atherosclerosis: insight from animal and human studies.* Clin Chim Acta, 1999. **286**(1-2): p. 115-43.
143. Narayanan, U., et al., *S6K1 phosphorylates and regulates fragile X mental retardation protein (FMRP) with the neuronal protein synthesis-dependent mammalian target of rapamycin (mTOR) signaling cascade.* J Biol Chem, 2008. **283**(27): p. 18478-82.
144. Bartley, C.M., et al., *Mammalian FMRP S499 Is Phosphorylated by CK2 and Promotes Secondary Phosphorylation of FMRP.* eNeuro, 2016. **3**(6).
145. Harnoss, J.M., et al., *Disruption of IRE1α through its kinase domain attenuates multiple myeloma.* Proc Natl Acad Sci U S A, 2019. **116**(33): p. 16420-16429.
146. Ghosh, R., et al., *Allosteric inhibition of the IRE1α RNase preserves cell viability and function during endoplasmic reticulum stress.* Cell, 2014. **158**(3): p. 534-48.
147. Papandreou, I., et al., *Identification of an Ire1alpha endonuclease specific inhibitor with cytotoxic activity against human multiple myeloma.* Blood, 2011. **117**(4): p. 1311-4.
148. Harnoss, J.M., et al., *Disruption of IRE1α through its Kinase Domain Attenuates Multiple Myeloma.* bioRxiv, 2018: p. 495242.
149. Bartley, C.M., R.A. O'Keefe, and A. Bordey, *FMRP S499 is phosphorylated independent of mTORC1-S6K1 activity.* PLoS One, 2014. **9**(5): p. e96956.
150. Ceman, S., et al., *Phosphorylation influences the translation state of FMRP-associated polyribosomes.* Hum Mol Genet, 2003. **12**(24): p. 3295-305.
151. Prieto, M., A. Folci, and S. Martin, *Post-translational modifications of the Fragile X Mental Retardation Protein in neuronal function and dysfunction.* Mol Psychiatry, 2020. **25**(8): p. 1688-1703.
152. Coffee, R.L., Jr., et al., *In vivo neuronal function of the fragile X mental retardation protein is regulated by phosphorylation.* Hum Mol Genet, 2012. **21**(4): p. 900-15.
153. Niere, F., J.R. Wilkerson, and K.M. Huber, *Evidence for a fragile X mental retardation protein-mediated translational switch in metabotropic glutamate receptor-triggered Arc translation and long-term depression.* J Neurosci, 2012. **32**(17): p. 5924-36.
154. Peled, M., et al., *A wild-type mouse-based model for the regression of inflammation in atherosclerosis.* PLoS One, 2017. **12**(3): p. e0173975.

155. Li, J., et al., *Secreted PCSK9 promotes LDL receptor degradation independently of proteolytic activity.* Biochem J, 2007. **406**(2): p. 203-7.
156. Tsimikas, S., et al., *Human oxidation-specific antibodies reduce foam cell formation and atherosclerosis progression.* J Am Coll Cardiol, 2011. **58**(16): p. 1715-27.
157. Carotti, S., et al., *Fragile X mental retardation protein in intrahepatic cholangiocarcinoma: regulating the cancer cell behavior plasticity at the leading edge.* Oncogene, 2021. **40**(23): p. 4033-4049.
158. Ascano, M., Jr., et al., *FMRP targets distinct mRNA sequence elements to regulate protein expression.* Nature, 2012. **492**(7429): p. 382-6.
159. McClatchy, D.B., et al., *Pulsed Azidohomoalanine Labeling in Mammals (PALM) Detects Changes in Liver-Specific LKB1 Knockout Mice.* J Proteome Res, 2015. **14**(11): p. 4815-22.
160. Kolb, H.C., M.G. Finn, and K.B. Sharpless, *Click Chemistry: Diverse Chemical Function from a Few Good Reactions.* Angew Chem Int Ed Engl, 2001. **40**(11): p. 2004-2021.
161. Tumurkhuu, G., et al., *Chlamydia pneumoniae Hijacks a Host Autoregulatory IL-1β Loop to Drive Foam Cell Formation and Accelerate Atherosclerosis.* Cell Metab, 2018. **28**(3): p. 432-448.e4.
162. Li, Y., et al., *Enrichment of endoplasmic reticulum with cholesterol inhibits sarcoplasmic-endoplasmic reticulum calcium ATPase-2b activity in parallel with increased order of membrane lipids: implications for depletion of endoplasmic reticulum calcium stores and apoptosis in cholesterol-loaded macrophages.* J Biol Chem, 2004. **279**(35): p. 37030-9.
163. Borradaile, N.M., et al., *Disruption of endoplasmic reticulum structure and integrity in lipotoxic cell death.* J Lipid Res, 2006. **47**(12): p. 2726-37.
164. Fu, S., et al., *Aberrant lipid metabolism disrupts calcium homeostasis causing liver endoplasmic reticulum stress in obesity.* Nature, 2011. **473**(7348): p. 528-31.
165. Hotamisligil, G.S., *Inflammation, metaflammation and immunometabolic disorders.* Nature Reviews, 2017. **542**(7640): p. 177-185.
166. Davis, J.K. and K. Broadie, *Multifarious Functions of the Fragile X Mental Retardation Protein.* Trends Genet, 2017. **33**(10): p. 703-714.
167. Sethna, F., C. Moon, and H. Wang, *From FMRP function to potential therapies for fragile X syndrome.* Neurochem Res, 2014. **39**(6): p. 1016-31.
168. Leboucher, A., et al., *Fmr1-Deficiency Impacts Body Composition, Skeleton, and Bone Microstructure in a Mouse Model of Fragile X Syndrome.* Front Endocrinol (Lausanne), 2019. **10**: p. 678.
169. Tuomisto, T.T., et al., *Gene expression in macrophage-rich inflammatory cell infiltrates in human atherosclerotic lesions as studied by laser microdissection and DNA array: overexpression of HMG-CoA reductase, colony stimulating factor receptors, CD11A/CD18 integrins, and interleukin receptors.* Arterioscler Thromb Vasc Biol, 2003. **23**(12): p. 2235-40.
170. Berry-Kravis, E., et al., *Cholesterol levels in fragile X syndrome.* Am J Med Genet A, 2015. **167a**(2): p. 379-84.
171. Lisik, M.Z., E. Gutmajster, and A.L. Sieroń, *Low Levels of HDL in Fragile X Syndrome Patients.* Lipids, 2016. **51**(2): p. 189-92.
172. Leboucher, A., et al., *The translational regulator FMRP controls lipid and glucose metabolism in mice and humans.* Mol Metab, 2019. **21**: p. 22-35.

173. Stone, W.L., H. Basit, and E. Los, *Fragile X Syndrome*, in *StatPearls*. 2022, StatPearls Publishing

174. Razak, K.A., K.C. Dominick, and C.A. Erickson, *Developmental studies in fragile X syndrome.* J Neurodev Disord, 2020. **12**(1): p. 13.
175. Lumaban, J.G. and D.L. Nelson, *The Fragile X proteins Fmrp and Fxr2p cooperate to regulate glucose metabolism in mice.* Hum Mol Genet, 2015. **24**(8): p. 2175-84.
176. Napoli, I., et al., *The fragile X syndrome protein represses activity-dependent translation through CYFIP1, a new 4E-BP.* Cell, 2008. **134**(6): p. 1042-54.
177. Chen, E., et al., *Fragile X mental retardation protein regulates translation by binding directly to the ribosome.* Mol Cell, 2014. **54**(3): p. 407-417.
178. Edbauer, D., et al., *Regulation of synaptic structure and function by FMRP-associated microRNAs miR-125b and miR-132.* Neuron, 2010. **65**(3): p. 373-84.
179. Tsang, B., et al., *Phosphoregulated FMRP phase separation models activity-dependent translation through bidirectional control of mRNA granule formation.* Proc Natl Acad Sci U S A, 2019. **116**(10): p. 4218-4227.
180. Buchan, J.R. and R. Parker, *Eukaryotic stress granules: the ins and outs of translation.* Mol Cell, 2009. **36**(6): p. 932-41.

Copy Right Permissions

Figure 1.1, Figure 1.4, Figure 1.5, Figure 1.7, Figure 1.9, Figure 1.10

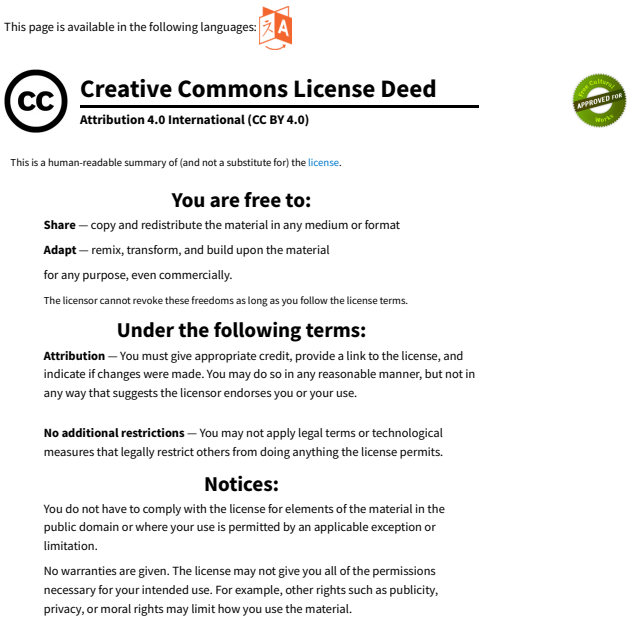

This page is available in the following languages:

Creative Commons License Deed

Attribution 4.0 International (CC BY 4.0)

This is a human-readable summary of (and not a substitute for) the license.

You are free to:

Share — copy and redistribute the material in any medium or format

Adapt — remix, transform, and build upon the material

for any purpose, even commercially.

The licensor cannot revoke these freedoms as long as you follow the license terms.

Under the following terms:

Attribution — You must give appropriate credit, provide a link to the license, and indicate if changes were made. You may do so in any reasonable manner, but not in any way that suggests the licensor endorses you or your use.

No additional restrictions — You may not apply legal terms or technological measures that legally restrict others from doing anything the license permits.

Notices:

You do not have to comply with the license for elements of the material in the public domain or where your use is permitted by an applicable exception or limitation.

No warranties are given. The license may not give you all of the permissions necessary for your intended use. For example, other rights such as publicity, privacy, or moral rights may limit how you use the material.

Figure 1.2

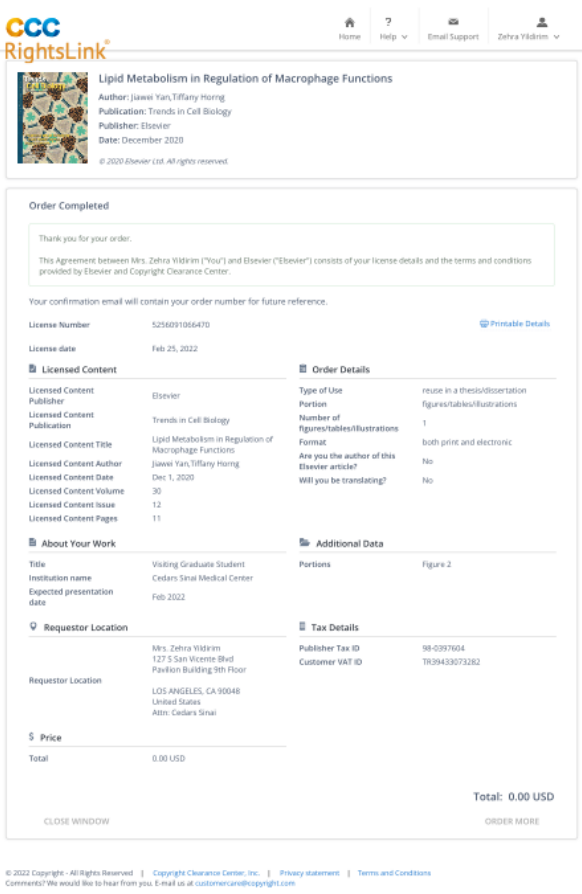

CCC RightsLink

Home | Help | Email Support | Zehra Yildirim

Lipid Metabolism in Regulation of Macrophage Functions

Author: Jiawei Yan,Tiffany Horng
Publication: Trends in Cell Biology
Publisher: Elsevier
Date: December 2020

© 2020 Elsevier Ltd. All rights reserved.

Order Completed

Thank you for your order.

This Agreement between Mrs. Zehra Yildirim ("You") and Elsevier ("Elsevier") consists of your license details and the terms and conditions provided by Elsevier and Copyright Clearance Center.

Your confirmation email will contain your order number for future reference.

License Number	5256091066470
License date	Feb 25, 2022

Printable Details

Licensed Content

Licensed Content Publisher	Elsevier
Licensed Content Publication	Trends in Cell Biology
Licensed Content Title	Lipid Metabolism in Regulation of Macrophage Functions
Licensed Content Author	Jiawei Yan,Tiffany Horng
Licensed Content Date	Dec 1, 2020
Licensed Content Volume	30
Licensed Content Issue	12
Licensed Content Pages	11

Order Details

Type of Use	reuse in a thesis/dissertation
Portion	figures/tables/illustrations
Number of figures/tables/illustrations	1
Format	both print and electronic
Are you the author of this Elsevier article?	No
Will you be translating?	No

About Your Work

Title	Visiting Graduate Student
Institution name	Cedars Sinai Medical Center
Expected presentation date	Feb 2022

Additional Data

Portions	Figure 2

Requestor Location

Requestor Location	Mrs. Zehra Yildirim 127 S San Vicente Blvd Pavilion Building 9th Floor LOS ANGELES, CA 90048 United States Attn: Cedars Sinai

Tax Details

Publisher Tax ID	98-0397604
Customer VAT ID	TR3943073282

Price

Total	0.00 USD

Total: 0.00 USD

CLOSE WINDOW ORDER MORE

Figure 1.3

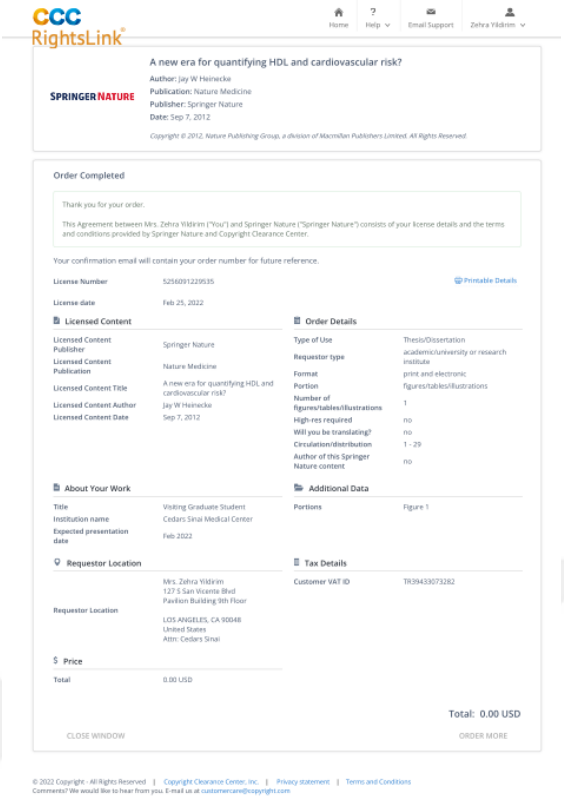

Figure 1.6

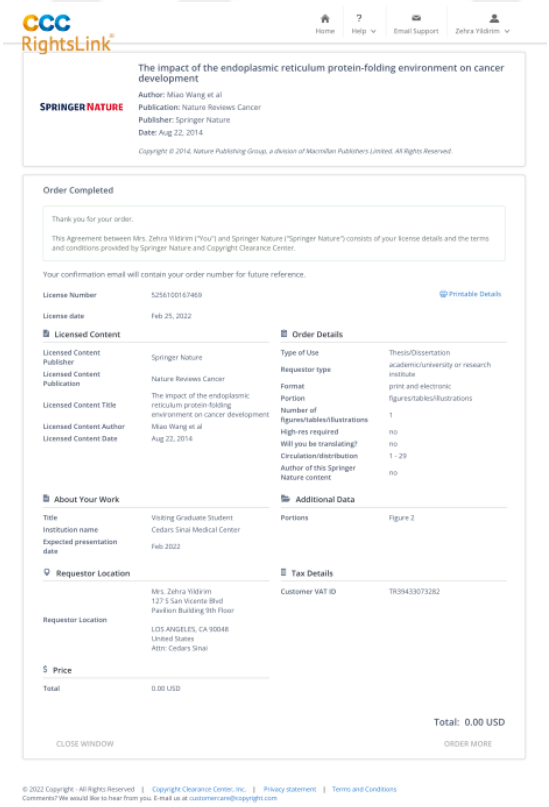

Figure 1.8

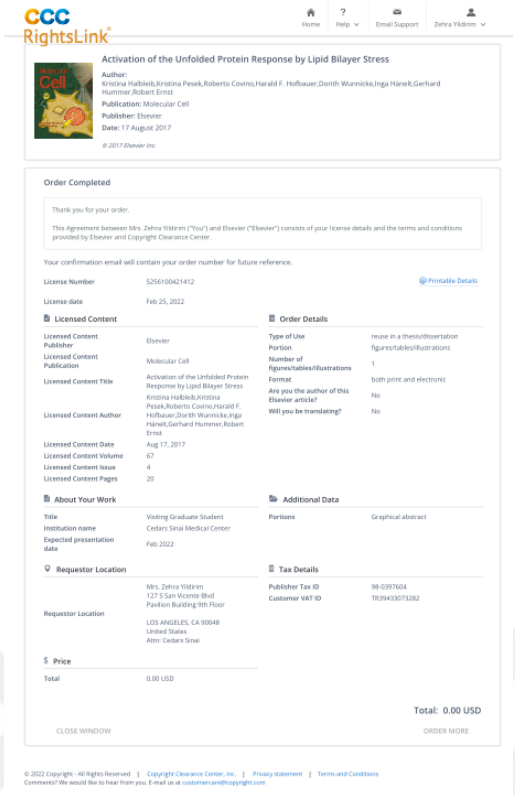

Figure 1.11

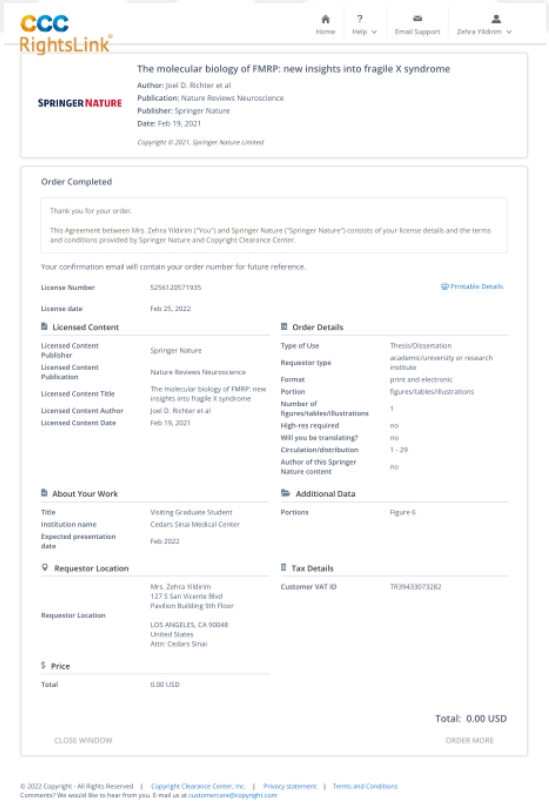

Figure 1.12

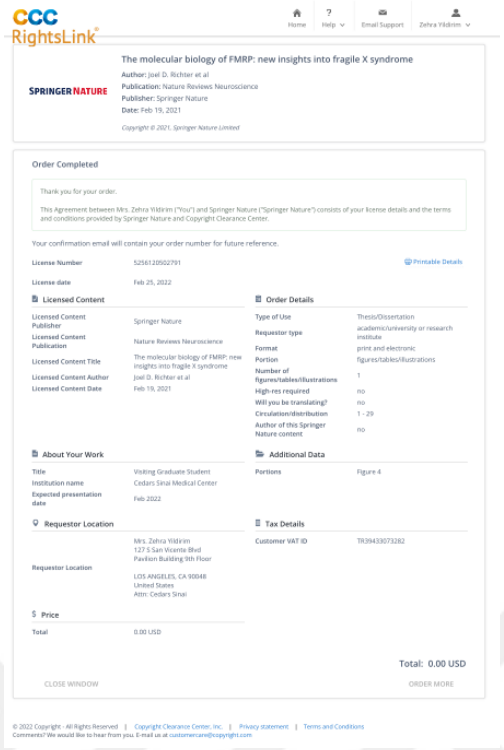

CCC RightsLink

Home | Help | Email Support | Zehra Yildirim

SPRINGER NATURE

The molecular biology of FMRP: new insights into fragile X syndrome

Author: Joel D. Richter et al
Publication: Nature Reviews Neuroscience
Publisher: Springer Nature
Date: Feb 19, 2021

Copyright © 2021, Springer Nature Limited

Order Completed

Thank you for your order.

This Agreement between Mrs. Zehra Yildirim ("You") and Springer Nature ("Springer Nature") consists of your license details and the terms and conditions provided by Springer Nature and Copyright Clearance Center.

Your confirmation email will contain your order number for future reference.

Printable Details

License Number	5256120502791
License date	Feb 25, 2022

Licensed Content

Licensed Content Publisher	Springer Nature
Licensed Content Publication	Nature Reviews Neuroscience
Licensed Content Title	The molecular biology of FMRP: new insights into fragile X syndrome
Licensed Content Author	Joel D. Richter et al
Licensed Content Date	Feb 19, 2021

Order Details

Type of Use	Thesis/Dissertation
Requestor type	academic/university or research institute
Format	print and electronic
Portion	figures/tables/illustrations
Number of figures/tables/illustrations	1
High-res required	no
Will you be translating?	no
Circulation/distribution	1 - 29
Author of this Springer Nature content	no

About Your Work

Title	Visiting Graduate Student
Institution name	Cedars Sinai Medical Center
Expected presentation date	Feb 2022

Additional Data

Portions	Figure 4

Requestor Location

Requestor Location	Mrs. Zehra Yildirim 127 S San Vicente Blvd Pavilion Building 9th Floor LOS ANGELES, CA 90048 United States Attn: Cedars Sinai

Tax Details

Customer VAT ID	TR394338073282

Price

Total	0.00 USD

Total: 0.00 USD

CLOSE WINDOW ORDER MORE

CV

SMIDT HEART INSTITUTE • CEDARS SINAI MEDICAL CENTER •
127 S. San Vincente Blvd • Advanced Health Sciences Pavilion A9104 • Los Angeles • CA 90048 •
PHONE: +1 310 729 1227 •
E-MAIL: ZEHRA.YILDIRIM@CSHS.ORG

ZEHRA YILDIRIM

EDUCATION

Visiting Grad Student **Feb. 2019 – Mar. 2022**
Smidt Heart Institute,
Cedars Sinai Medical Center

PhD Candidate **Jan. 2016 – Mar. 2022**
Department of Molecular Biology and Genetics
Ihsan Dogramaci Bilkent University, Ankara, Turkey

Master of Science **Feb. 2013 - Jan. 2015**
Bioengineering Department,
Hacettepe University, Ankara, Turkey

Bachelor of Science **Sep. 2006 - Jun. 2010**
Biology Department,
Kirikkkale University, Kirikkale, Turkey

ACADEMIC TRAINING

PhD Research **Jan. 2016 – Mar. 2022**

Thesis: Identification of a Novel Substrate of IRE1 in Lipotoxic Stress Response

Thesis advisor: Associate Prof. Dr. Ebru Erbay

Thesis project is based on a novel concept that interlinks endoplasmic reticulum stress response with post-transcriptional modifications and RNA processing. Chemical inhibitors of ER stress pathway as well as genetic knock out mouse models were used to discover novel kinase substate of a major ER stress player IRE1, and how ER stress modulates RNA processing and affects cholesterol homeostasis and efferocytosis both *in vitro* and *in vivo*.

Techniques used in this study; Atherosclerosis study (handling mice colony, delivery of drugs and virus (intraperitoneal or retroorbital), mouse dissection, tissue collection and processing), Radioactive Reverse Cholesterol Transport assay, Lipid extraction, Cholesterol Efflux and Influx assays, Foam cell formation assay, Efferocytosis and Phagocytosis assays, Kinase assay, Protein/RNA immunoprecipitation, Luciferase assay, Polysome profiling and RNA-Seq, Pulse azidohomoalanine (AHA) labeling and Proteomics (HILAQ), Western Blotting, ELISA, Cell

culture, Electroporation, Bone marrow derived macrophage isolation and differentiation, Thioglycolate stimulated peritoneal macrophage isolation, Flow cytometry, IHC, Cryo-sectioning of tissues, Mitochondrial oxygen consumption analysis, mtDNA quantification, Mitotracker and mtROS staining, RNA isolation and RT-qPCR, Cloning, Site directed mutagenesis, PPase treatment and protein analysis.

MSc. Research **Feb. 2013 - Jan. 2015**

Thesis: Novel Cellulase Enzyme Production Towards Biofuels Sector by Recombinant Bacterium *Escherichia coli*

Academic adviser: Assoc. Prof. Dr. Eda Çelik

Project supported by The Scientific and Technological Research Council of Turkey (Grant #: 114M133) that is based on this thesis study.

This study was based on secretory production of glycosylated recombinant enzymes in *E. coli*. An endoglucanase Cel5A and its glycosylated form was investigated for extracellular production in *E. coli* as a fusion to the carrier protein and compared to periplasmic production enabled by fusing the periplasmic signal peptide.
Techniques used in this study; SDS-PAGE and Western Blotting, PCR, Cloning, DNA analysis and Enzyme activity assay techniques.

BSc. Research **Sep. 2006 - Jun. 2010**

Senior Project: Evaluation of the effect of Propionic Acid and Phosphoric Acid on *Drosophila melanogaster* larvae

Academic adviser: Prof. Dr. Şükran Çakır-Arıca

In this study, the effect of propionic acid and phosphoric acid on induced mutations in trans-heterozygous *Drosophila melanogaster* larvae were investigated using somatic mutation and recombination test (SMART).

Internships

- Intergen Genetics Centre, Ankara, Turkey**,** 2013

  Techniques observed and practiced during this internship; how to analyse the structures and numbers of the chromosomes from patient samples, fluorescence in situ hybridization (FISH), DNA extraction, PCR, electrophoresis techniques.

- Memorial Hospital, International Hospital and Jinepol Women's Health Clinic Istanbul, Turkey, 2009

  Techniques observed and practiced during these three internships; how to evaluate sperms in terms of quantity, mobility and structure; vitality and function tests; fast freezing of sperm, embryo and ovarian tissue; *in vitro* oocyte maturation; pre-implementation genetic diagnosis; testicular sperm retrieval through a surgical procedure and testicular sperm aspiration; genetic evaluation of the sperms in severe male infertility (sperm FISH); analysis of the structures and numbers of the chromosomes; PCR, DNA electrophoresis and blastomere fixation.

- Gazi Public Hospital, Ankara, Turkey, 2008

  During this internship Microbiology, Biochemistry and Pathology laboratories were observed and patient sample processing were practiced.

TEACHING EXPERIENCE

Teaching Assistant, Ihsan Dogramaci Bilkent University **2016-2018**

Molecular Biology of The Gene (1 semester)

Biology II (MBG102) Laboratory (1 semester)

Molecular Genetics (MBG223) Laboratory (2 semesters)

Science and Ethics (MBG416) (2 semesters)

Trained undergraduate and MSc students **2016-2020**

An undergrad student from UCLA, Cedars Sinai Medical Center

Two undergrad students and two MSc students, Ihsan Dogramaci Bilkent University

Private Tutor **2007-2016**

Biology and Mathematics

SEMINARS, CONFERENCES AND POSTER PRESENTATIONS

- Weekly Smidt Heart Institute Research Seminar Series, Cedars Sinai Medical Center, CA, USA
- Weekly Cardiometabolism Virtual Seminar Series
- NanoDay, UNAM, Bilkent University, Ankara, Turkey 2017
- 4th Nanomedicine World Congress and 2nd International NanoBioTechnology Symposium, Ankara, Turkey 2015
- Poster presentation at 1st International Conference on Synthetic Biology, Houston, USA, 2015, OMICS International Conferences
- Zehra Tatli, Matthew DeLisa and Eda Celik, Comparison of Intracellular and Extracellular Cellulase Production by Recombinant Bacterium *Escherichia coli*, Curr Synthetic Sys Biol 2015, 3:3, DOI: 10.4172/2332-0737.C1.003
- Poster presentation at 4th Nanomed/Nanobiotech Conference, Mugla, Turkey, 2015
- Zehra Tatli, Matthew DeLisa and Eda Celik, Enhanced Production of Novel Cellulase Enzyme Towards Biofuels Sector by Recombinant Bacterium *Escherichia coli*.
- Poster presentation at 11th Research Projects Exhibition, 2014, Hacettepe University, Ankara, Turkey
- Oral Presentation at XVI. National Biology Students' Conference, Nigde, Turkey 2009
- Oral Presentation at Genetically Modified Organisms, 4th Biology Day, Alanya Turkey 2008
- Renewable Energy and Environmental Technologies Cluster, 2014, Hacettepe University, Ankara, Turkey.
- Obtaining Accurate and Reliable Test Results and Modes of Administration Results, 2013, Union of Chambers of Turkish Engineers and Architects, Chambers of Chemical Engineering, Hacettepe University, Ankara, Turkey

PUBLICATIONS

***Yildirim Z**, Baboo S, Hamid SM, Dogan AE, Tufanli O, Robichaud S, Emerton C, Diedrich JK, Vatandaslar H, Nikolos F, Gu Y, Iwawaki T, Tarling E, Ouimet M, Nelson DL, Yates III JR, Walter P, Erbay E. "Intercepting IRE1 kinase-FMRP signaling prevents atherosclerosis progression" EMBO Mol. Med. 2022 Feb;e15344. doi: 10.15252/emmm.202115344

*Dogan AE, Baboo S, Hamid MS, Yildirim AD, **Yildirim Z**, Tufanli O, Diedrich JK, Sen G, Riera C, Yates III JR, Walter P, Gottlieb R, Erbay E. "Regulation of Mitochondrial Biogenesis through RNA-mediated Interorganelle Communication" in revision at JBC.

*Yildirim AD, Citir M, Dogan AE, Veli Z, **Yildirim Z**, Tufanli O, Rettel M, Kaplan AT, Schultz C, Erbay E. "Endoplasmic Reticulum Stress-Induced Sphingosine-1 Phosphate Lyase Phosphorylation Potentiates the Mitochondrial Unfolded Protein Response" in revision at JLR.

*Ramani K, Robinson AE, Berlind J, Fan W, Abeynayake A, Binek A, Barbier-Torres L, Noureddin M, Nissen NN, **Yildirim Z**, Erbay E, Mato JM, Van Eyk JE, Lu SC. S-Adenosylmethionine Inhibits La Ribonucleoprotein Domain Family Member 1 in Murine Liver and Human Liver Cancer Cells. Hepatology. 2021 Aug 27. doi: 10.1002/hep.32130. Epub ahead of print. PMID: 34449924.

*Hamid SM, Citir M, Terzi EM, Cimen I, **Yildirim Z**, Dogan AE, Kocaturk B, Onat UI, Arditi M, Weber C, Traynor-Kaplan A, Schultz C, Erbay E. Inositol-requiring enzyme-1 regulates phosphoinositide signaling lipids and macrophage growth. EMBO Rep. 2020 Dec 3;21(12): e51462. doi: 10.15252/embr.202051462. Epub 2020 Nov 2. PMID: 33140520; PMCID: PMC7726810.

*Cimen I, **Yildirim Z**, Dogan AE, Yildirim AD, Tufanli O, Onat UI, Nguyen U, Watkins SM, Weber C, Erbay E. Double bond configuration of palmitoleate is critical for atheroprotection. Mol Metab. 2019 Oct; 28:58-72. doi: 10.1016/j.molmet.2019.08.004.

***Yildirim Z** and Çelik E, Periplasmic and extracellular production of cellulase from recombinant *Escherichia coli* cells. J. Chem. Technol. Biotechnol. 2016, DOI: 10.1002/jctb.5008.

REFERENCES

Assoc. Professor Ebru Erbay, MD, PhD
Department of Cardiology
& Department of Biomedical Sciences
Smidt Heart Institute
Cedars Sinai Medical Center
127 S. San Vincente Blvd
Advanced Health Sciences Pavilion, A9104
Los Angeles, CA 90048
ebru.erbay@cshs.org
310-423-7483, 617-909-8887

Professor Moshe Arditi, MD
Executive vice chair of the Department of Pediatrics
for Research, Director of the Pediatric Infectious
Diseases and Immunology Division, Director of
the Infectious and Immunological Diseases Research Center in the Department of the Biomedical Sciences, Smidt Heart Institute.
Cedars Sinai Medical Center
8700 Beverly Blvd.
Davis Building, Rooms D4024, D4025, D4027
Los Angeles, CA 90048
moshe.arditi@cshs.org
310-423-0806, 310-423-2593

Professor Roberta Gottlieb, MD
Vice Chair of Translational Medicine,
Department of Biomedical Sciences,
Director of Molecular Cardiobiology,
Dorothy and E. Phillip Lyon Chair in Molecular
Cardiology, Smidt Heart Institute.
Cedars Sinai Medical Center
127 S. San Vicente Blvd.
Advanced Health Sciences Pavilion, A9100
Los Angeles, CA 90048
roberta.gottlieb@cshs.org
424-315-2556

Professor Tayfun Ozcelik, MD
Dean of Faculty of Science and Chair
Department of Molecular biology and Genetics
Bilkent University, Ankara, Turkey
tozcelik@bilkent.edu.tr
+90 312-290-2139

PUBLICATIONS

Article

SOURCE DATA | TRANSPARENT PROCESS | OPEN ACCESS

EMBO Molecular Medicine

Intercepting IRE1 kinase-FMRP signaling prevents atherosclerosis progression

Zehra Yildirim[1,2], Sabyasachi Baboo[3], Syed M Hamid[1], Asli E Dogan[1,2], Ozlem Tufanli[4], Sabrina Robichaud[5], Christina Emerton[5], Jolene K Diedrich[3], Hasan Vatandaslar[6], Fotis Nikolos[7], Yanghong Gu[8], Takao Iwawaki[9], Elizabeth Tarling[10], Mireille Ouimet[5], David L Nelson[8], John R Yates III[3], Peter Walter[10] & Ebru Erbay[1,11,*]

Abstract

Fragile X Mental Retardation protein (FMRP), widely known for its role in hereditary intellectual disability, is an RNA-binding protein (RBP) that controls translation of select mRNAs. We discovered that endoplasmic reticulum (ER) stress induces phosphorylation of FMRP on a site that is known to enhance translation inhibition of FMRP-bound mRNAs. We show ER stress-induced activation of Inositol requiring enzyme-1 (IRE1), an ER-resident stress-sensing kinase/endoribonuclease, leads to FMRP phosphorylation and to suppression of macrophage cholesterol efflux and apoptotic cell clearance (efferocytosis). Conversely, FMRP deficiency and pharmacological inhibition of IRE1 kinase activity enhances cholesterol efflux and efferocytosis, reducing atherosclerosis in mice. Our results provide mechanistic insights into how ER stress-induced IRE1 kinase activity contributes to macrophage cholesterol homeostasis and suggests IRE1 inhibition as a promising new way to counteract atherosclerosis.

Keywords atherosclerosis; cholesterol homeostasis; efferocytosis; ER stress; translational regulation

Subject Categories Cardiovascular System; Immunology; Metabolism

DOI 10.15252/emmm.202115344 | Received 27 October 2021 | Revised 2 February 2022 | Accepted 4 February 2022

EMBO Mol Med (2022) e15344

Introduction

Atherosclerosis is a chronic inflammatory disease triggered by imbalanced lipid metabolism (Rocha & Libby, 2009; Weber & Noels, 2011). In atherosclerotic plaques, macrophages ingest lipoproteins and transform into lipid-laden foam cells. The foamy macrophages lose their ability to migrate away from the plaques, where they sustain a local state of sterile inflammation, which occurs in the absence of pathogens and is typically associated with the release of immune-recognizable cellular content from damaged or dying cells (Randolph, 2014). Cholesterol efflux and efferocytosis (the engulfment and clearance of apoptotic cells (AC)) by macrophages, on the other hand, help to resolve inflammation and contribute to plaque stability as counterbalancing mechanisms that oppose plaque rupture (Khera *et al*, 2011; Westerterp *et al*, 2013, 2018; Kojima *et al*, 2017; Yurdagul *et al*, 2017). Cholesterol efflux by plaque macrophages is the first step in a multistep process, referred to as "reverse cholesterol transport" (RCT), that reduces lipid accumulation in plaques. Macrophages efflux intracellular cholesterol using their plasma membrane cholesterol transporters (such as the ATP-binding cassette (ABC) transporters subfamily A member-1 (ABCA1) and subfamily G member-1 (ABCG1)), which in turn hand the exported cholesterol over to lipid-poor apolipoproteins, forming high-density lipoprotein (HDL) particles (Costet *et al*, 2000; Oram *et al*, 2000). The cholesterol efflux pathway is transcriptionally activated by the metabolic by-products of AC-derived cholesterol in the efferocytic macrophages. As such, efferocytosis and RCT synergize to reduce necrosis and resolve inflammation in plaques (Klucken *et al*, 2000; Joyce *et al*, 2002; Tall & Yvan-Charvet, 2015; Zimmer *et al*, 2016; Guo *et al*, 2018).

1 Department of Cardiology, Smidt Heart Institute, Cedars-Sinai Medical Center, Los Angeles, CA, USA
2 Department of Molecular Biology and Genetics, National Nanotechnology Center, Bilkent University, Ankara, Turkey
3 Department of Molecular Medicine, The Scripps Research Institute, La Jolla, CA, USA
4 Lagone Medical Center, New York University, New York, NY, USA
5 Department of Biochemistry, Microbiology and Immunology, Heart Institute, University of Ottawa, Ottawa, ON, Canada
6 Institute of Molecular Health Sciences, Swiss Federal Institute of Technology (ETH), Zürich, Switzerland
7 Samuel Oschin Cancer Center, Cedars-Sinai Medical Center, Los Angeles, CA, USA
8 Department of Molecular and Human Genetics, Baylor College of Medicine, Houston, TX, USA
9 Department of Life Science, Medical Research Institute, Kanazawa Medical University, Ishikawa, Japan
10 Department of Biochemistry and Biophysics, Howard Hughes Medical Institute, University of California at San Francisco, San Francisco, CA, USA
11 David Geffen School of Medicine, University of California at Los Angeles, Los Angeles, CA, USA
*Corresponding author. Tel: +1 310 4237483; E-mail: ebru.erbay@cshs.org; ebru.erbay@ucla.edu

Transcriptional and post-transcriptional regulation play critical roles to set sterile inflammation in motion but also in its resolution and, eventually, plaque regression. Post-transcriptional regulatory steps often involve RNA-binding proteins (RBPs) that interact with mRNA to alter its processing, transport, translation, and degradation. Several RBPs have been shown to alter the mRNA stability and translation of cytokines to turn-off the inflammatory response and key molecular regulators of cholesterol homeostasis and some have been linked to atherosclerosis development (atherogenesis) (Chiu *et al*, 1997; Kang *et al*, 2011; Zhang *et al*, 2013; Ramírez *et al*, 2014; Mobin *et al*, 2016; Haneklaus *et al*, 2017). Fragile X Mental Retardation Protein (FMRP) is an RBP that has been widely studied in neurons due to its causal role in the Fragile X Mental Retardation Syndrome (FXS) (Hersh & Saul, 2011; Bagni *et al*, 2012; Hunter *et al*, 2014). In FXS, a hypermethylated CGG repeat expansion in the 5′ untranslated region (5′ UTR) of the *FMR1* mRNA results in its transcriptional silencing. A subpopulation of the individuals afflicted with FXS and FMRP-deficient (Fmr1 $^{/}$) mice have lower cholesterol levels (Leboucher *et al*, 2019b). While a prior study has shown FMRP protein expression is induced in macrophage-enriched areas of the human atherosclerotic plaque (Hansmeier *et al*, 2018), FMRP's contribution to the atherosclerotic process has not been investigated directly, and our knowledge of FMRP function has remained largely limited to studies in neurons (Darnell *et al*, 2011). A key serine phosphorylation (S500 in human; S499 in mouse) on FMRP triggers hierarchical phosphorylation of surrounding serines and threonines, while enhancing FMRP's translation-repressing activity on many synaptic function-linked mRNAs bound by it. The identity of the kinase(s) that phosphorylates FMRP has remained subject to intense discussion (Ceman *et al*, 2003; Narayanan *et al*, 2008; Coffee *et al*, 2012; Niere *et al*, 2012; Bartley *et al*, 2014, 2016; Prieto *et al*, 2020).

In this study, we present evidence that ER stress and hypercholesterolemia in mice induces the phosphorylation of macrophage FMRP on S500 by the inositol-requiring enzyme-1 (IRE1), a conserved endoplasmic reticulum (ER) stress-sensing kinase/endoribonuclease (RNase). Metazoans have two IRE1 paralogues, IRE1α (referred to as IRE1 in this paper) and IRE1β. While IRE1α is ubiquitously expressed, IRE1β expression is restricted to gastrointestinal epithelium (Cloots *et al*, 2021). To date, IRE1 has been described to *trans*-autophosphorylate as a first step in the activation of its RNase modality, which initiates a nonconventional RNA-splicing reaction and the production of the transcription factor known as spliced X box protein-1 (XBP1s), which is one of the key drivers of the unfolded protein response (UPR) (Walter & Ron, 2011; Çimen *et al*, 2016a; Robblee *et al*, 2016). IRE1 senses both protein folding stress induced by an accumulation of unfolded proteins in the ER lumen and ER membrane lipid bilayer stress induced by an accumulation of cholesterol or saturated fatty acids (SFA) (Seimon *et al*, 2010; Sukhorukov *et al*, 2020). While previous studies by us and others have shown that ER stress and subsequent IRE1 activation are causally associated with atherosclerosis progression, the mechanism by which IRE1 contributes to the disease pathogenesis has remained elusive (Erbay *et al*, 2009; Zhou & Tabas, 2013; Tufanli *et al*, 2017). Here, we show that IRE1 phosphorylates FMRP on S500, which in turn leads to post-transcriptional suppression of cholesterol efflux and efferocytosis by macrophages. FMRP deficiency and IRE1 kinase inhibition both enhance RCT and efferocytosis *in vivo*, reducing foam cell formation and atherosclerosis progression in mice. These findings reveal a novel role for FMRP in macrophages in the regulation of cholesterol homeostasis and efferocytosis and provide mechanistic insight into IRE1-driven atherosclerotic processes during hypercholesterolemia.

Results

Lipids induce FMRP phosphorylation in IRE1 kinase-dependent manner

Previously published mass spectrometry-based IRE1 interactome data revealed multiple FMRP-interacting proteins potentially associating with IRE1 (Fig 1A) (Acosta-Alvear *et al*, 2018). These proteins share significant sequence homology with FMRP and are usually found in homo/heteromeric complexes with FMRP (Zhang *et al*, 1995). Based on these observations, we reasoned that FMRP might also physically interact with IRE1. Indeed, FMRP co-immunoprecipitated with IRE1 in non-stress and ER stress conditions induced by thapsigargin (TG; an inhibitor of the ER Ca^{2+} pump) and tunicamycin (TM; an inhibitor of N-linked glycosylation) from human embryonic kidney cell line (HEK293T) cells that were transiently transfected with plasmids encoding both proteins (Fig 1B).

Since FMRP phosphorylation is critical for translation suppression and the association with IRE1 juxtaposes it to a kinase whose substrate is unclear, we wondered whether ER stress alters FMRP phosphorylation state. To assess this possibility, we treated cultured macrophages with known ER stressors, such as TG and oxidized low-density lipoprotein (oxLDL, another inducer of ER stress). Using specific antibodies that recognize S724 phosphorylation on IRE1 and S500 phosphorylation on FMRP (Reynolds *et al*, 2015; Wang *et al*, 2021), we found that TG and oxLDL significantly induced IRE1 autophosphorylation and FMRP phosphorylation but did not affect levels of FMRP protein or Fmr1 mRNA (Fig 1C and Appendix Fig S1A and B). Phosphatase treatment of the samples partially reversed the ER stress-induced increase in the pFMRP/FMRP ratio (Fig 1C, Appendix Fig S1B), implying FMRP phosphorylation is enhanced by these ER stressors.

Previous studies showed that hyperlipidemia induces ER stress in plaque macrophages *in vivo* (Moore *et al*, 2013; Kim *et al*, 2016). We next investigated whether hyperlipidemia also has an effect on FMRP phosphorylation on S499 (mouse S499 corresponds to human S500). To this end, we used mice deficient in apolipoprotein E (Apoe $^{/}$) as this is a protein found in plasma lipoprotein particles and facilitates cholesterol clearance from the circulation (Davignon *et al*, 1999). In agreement with previous reports, we observed that ER stress (as monitored by IRE1 autophosphorylation) was induced in the peritoneal macrophages (PM) obtained from hyperlipidemic, Apoe $^{/}$ mice that were fed with a Western diet (WD) for 16 weeks when compared to Apoe $^{/}$ mice fed with chow diet (CD) (Fig 1D). We found that FMRP S499 phosphorylation, which leads to FMRP-mediated translational suppression, was 1.4-fold elevated by a chronic exposure to hypercholesterolemia, whereas FMRP protein and Fmr1 mRNA expression levels remained unchanged (Fig 1D; Appendix Fig S1C and D).

We next asked what role IRE1 plays in ER stress-induced FMRP phosphorylation. To address this question, we transfected IRE1-

specific siRNA to suppress IRE1 expression in a human cell line, followed by ER stress induction by a saturated fatty acid, palmitate (PA), that is known to induce ER stress, or TG. While both ER stressors induced the phosphorylation of IRE1 and FMRP, this was prevented in IRE1 knock-down cells (Fig 1E and Appendix Fig S1E). In addition, we analyzed hypercholesterolemia-induced FMRP phosphorylation in PMs obtained from Apoe$^{-/-}$ mice with a genetic deletion of IRE1α in the myeloid lineage (IRE1$^{-/-}$) (see Methods) after feeding with WD for 16 weeks. FMRP phosphorylation, but not FMRP protein or Fmr1 mRNA, was reduced in PM isolated from IRE1$^{-/-}$ mice when compared to those isolated from IRE1$^{+/+}$ mice (Fig 1F, Appendix Fig S1F and G). While these results show a clear

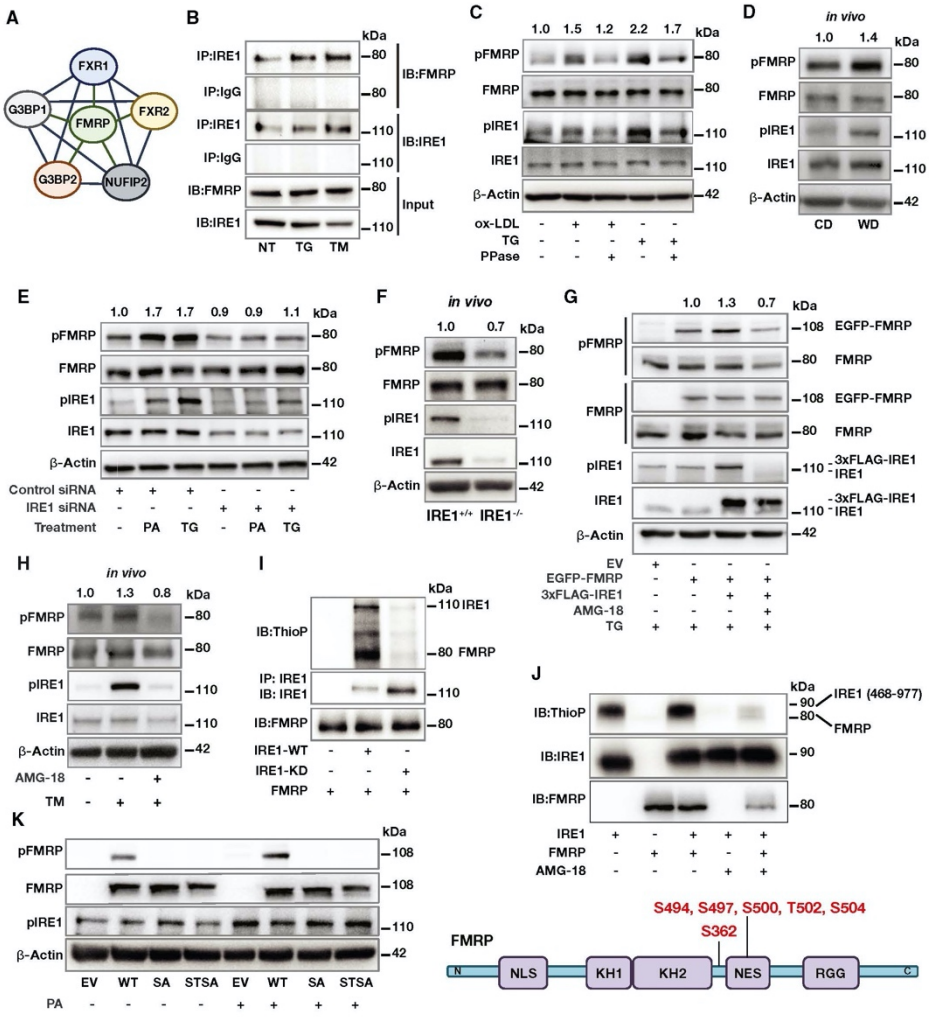

Figure 1.

Figure 1. FMRP is a novel IRE1 kinase substrate.

A STING analysis of published IRE1 interactome proteins in relation to FMRP (Acosta-Alvear *et al*, 2018).

B HEK293T cells were co-transfected with IRE1 and FMRP plasmids and stimulated with TG (600 nM) or TM (1 mg/ml) for 2 h. Protein lysates were immunoprecipitated (IP) with anti-IRE1 or IgG (control) antibodies and analyzed by Western blotting using specific antibodies for FMRP and IRE1 ($n = 3$ biological replicates).

C RAW 264.7 mouse macrophages were treated with either oxLDL (50 μg/ml) or TG (300 nM) for 6 h. Protein lysates were treated with λ Phosphatase (PPase) for 30 min and analyzed by Western blotting using specific antibodies for pFMRP, FMRP, pIRE1, IRE1, and β-Actin. pFMRP/FMRP fold induction is depicted above the blots ($n = 6$ biological replicates).

D Apoe$^{-/-}$ mice were fed with chow diet (CD) or western diet (WD) for 16 weeks followed by peritoneal macrophage (PM) isolation. Protein lysates were analyzed by Western blotting using specific antibodies for pFMRP, FMRP, pIRE1, IRE1, and β-Actin. pFMRP/FMRP-fold induction is depicted above the blots ($n = 5$ mice per group).

E Control- or IRE1-siRNA transfected HEK293T cells were stimulated by either PA (500 μM) or TG (600 nM) for 4 h. Protein lysates were analyzed by Western blotting using specific antibodies for pFMRP, FMRP, pIRE1, IRE1, and β-Actin. pFMRP/FMRP fold induction is depicted above the blots ($n = 4$ biological replicates).

F Protein lysates of thioglycolate-elicited PM from IRE1α$^{+/+}$ and IRE1α$^{-/-}$ mice (after 16 weeks on WD) were analyzed by Western blotting using specific antibodies for pFMRP, FMRP, pIRE1, IRE1, and β-Actin. pFMRP/FMRP fold induction is depicted above the blots ($n = 4$ mice per group).

G MEF cells were transfected with either empty vector, EGFP-FMRP or 3xFLAG-IRE1 plasmids then pre-treated either with vehicle (dimethyl sulfoxide, DMSO) or AMG-18 (25 μM; 1 h) followed by TG (600 nM) stimulation for 4 h. Protein lysates were analyzed by Western blotting using specific antibodies for pFMRP, FMRP, pIRE1, IRE1, and β-Actin. pFMRP/FMRP fold induction is depicted above the blots ($n = 4$ biological replicates).

H C57BL/6 were injected either with DMSO or AMG-18 (30 mg/kg; 8 h), followed by TM injection (1 mg/kg; 8 h). Protein lysates of thioglycolate-elicited PM were analyzed by Western blotting using antibodies for pFMRP, FMRP, pIRE1, IRE1, and β-Actin. pFMRP/FMRP fold induction is depicted above the blots ($n = 4$ mice per group).

I HEK293T cells were transfected with either empty vector (EV), IRE1-WT, or IRE1–KD plasmids and stimulated by TG (600 nM; 1 h). Protein lysates from each transfection were separately immunoprecipitated (IP) with anti-IRE1 antibody and subjected to a kinase reaction with purified hFMRP protein and ATP-γ-S (100 μM) in kinase buffer. The IP protein were analyzed by Western blotting using specific antibodies for thiophosphate esters (ThioP), IRE1, and FMRP ($n = 3$ biological replicates).

J Purified FMRP and IRE1 kinase (activated) proteins were subjected to kinase assay and analyzed by Western blotting using specific antibodies for ThioP, IRE1, and FMRP ($n = 3$ biological replicates) and with LC-MS/MS. Identified IRE1 kinase-mediated FMRP phosphorylation sites (bottom).

K Fmr1$^{-/-}$ mouse embryonic fibroblasts (MEF) were transfected either with EV, WT-FMRP, SA-FMRP, or STSA-FMRP plasmids followed by PA treatment (500 μM; 6 h). Protein lysates were analyzed by Western blotting using specific antibodies for FMRP, pFMRP, pIRE1, and β-Actin ($n = 3$ biological replicates).

Data information: A representative blot is shown. In D, E, G, and H data are cumulative results of two independent experiments. Data are mean ± SEM. Unpaired *t*-test with Welch's correction or paired *t*-test.
Source data are available online for this figure.

reduction in FMRP phosphorylation upon siRNA treatment or gene knock-out, we observed residual signal in both cases (Fig 1E and F). As we confirm below (Fig 1K), the antibody used in these experiments is phosphorylation specific. We, therefore, surmise that partial phosphorylation on S500/S499 may also be mediated by the other kinases that are known to phosphorylate this residue on FMRP (Narayanan *et al*, 2008; Bartley *et al*, 2016), in addition to IRE1 as we show here. Collectively, our *in vitro* and *in vivo* results strongly support that ER stress-induced activation of IRE1 kinase leads to enhanced phosphorylation of FMRP on S500/S499.

IRE1 phosphorylates FMRP

To begin investigating the role of IRE1's kinase activity in ER stress-induced FMRP phosphorylation, we expressed a 3xFLAG-tagged IRE1 (FLAG-IRE1) and/or EGFP-FMRP in wild-type mouse embryonic fibroblasts (MEFs). Endogenous FMRP and IRE1 migrated faster in SDS–PAGE gel than the epitope tagged EGFP-FMRP and FLAG-IRE1, respectively. In all conditions, the MEFs were TG-treated (to stimulate IRE1 kinase activity) in the absence or presence of an IRE1 kinase-specific inhibitor (AMG-18) (Papandreou *et al*, 2011; Ghosh *et al*, 2014; Tufanli *et al*, 2017; Harnoss *et al*, 2019). In the absence of AMG-18, both IRE1 and FMRP were phosphorylated. AMG-18 treatment prevented IRE1 phosphorylation while clearly reducing FMRP phosphorylation (Fig 1G and Appendix Fig S1H). While these data further support the notion that IRE1 phosphorylates FMRP during ER stress, alternative kinase(s) appears to mediate the same reaction. This is consistent the published data that several kinases can phosphorylate the same residue on FMRP (Narayanan *et al*, 2008; Bartley *et al*, 2016). Furthermore, in an *in vivo* setting where mice were injected with TM to induce IRE1 kinase activity, treatment with AMG-18 inhibited IRE1 kinase activity and reduced FMRP phosphorylation in PM (Fig 1H and Appendix Fig S1I). Taken together, our findings support the notion that IRE1 kinase activity makes an important contribution to ER stress-induced FMRP S499 phosphorylation in mouse macrophages and MEFs as well as S500 in HEK293T cells. Our data also support that other known or unknown FMRP kinase(s) are responsible for basal FMRP phosphorylation that is observed in non-stress conditions.

To ask whether IRE1 can phosphorylate FMRP directly, we employed *in vitro* assays. To this end, we immunoprecipitated wild type (WT) or kinase dead (KD) mutant IRE1 from HEK293T cells (after treating with ER stressor) and incubated the immunoprecipitates with purified, recombinant human FMRP protein in a kinase reaction. The reaction included ATP-γ-S instead of ATP, which allows kinases to thio-phosphorylate their substrates. The resultant kinase reaction was analyzed by Western blotting using an anti-thiophosphate ester antibody. In the reaction containing IRE1-WT, both proteins were thio-phosphorylated, but not in the reaction containing the IRE1-KD mutant (Fig 1I).

To determine the specific amino acids phosphorylated by IRE1, we performed the kinase reaction using purified, recombinant human IRE1-kinase/RNase domains (amino acids 468–977) and human FMRP proteins. Both IRE1 and FMRP were phosphorylated in this reaction in an AMG-18-sensitive manner (Fig 1J). Liquid chromatography-mass spectrometry (LC-MS/MS)-based analysis of the phosphorylated FMRP residues in this kinase reaction revealed eight IRE1-induced phosphorylation sites on FMRP at serine (S362,

S494, S497, S500, S504) and threonine (T502, T592, T594) (Fig 1J, Appendix Fig S1J and K). Importantly, S500 in human FMRP is the previously identified FMRP phosphorylation site that was shown to enhance FMRP-mediated translational suppression (Ceman *et al*, 2003; Narayanan *et al*, 2008; Coffee *et al*, 2012; Niere *et al*, 2012; Bartley *et al*, 2014, 2016; Prieto *et al*, 2020).

Using site-directed mutagenesis, we engineered two mutant versions of FMRP, in which we either changed S500 to alanine (SA mutant) or S500, T502, and S504 to alanine (STSA triple mutant) to block phosphorylation at S500 and amino acids in its proximity. We then induced ER stress with PA in Fmr1 $^{/}$ MEFs transiently transfected with WT FMRP and FMRP mutants (SA and STSA). PA induced FMRP phosphorylation in WT FMRP-reconstituted cells but failed to do so in cells expressing the SA and STSA mutants of FMRP (Fig 1J). These data confirm the specificity of the FMRP antibody for phosphorylated S500 and is consistent with the notion that IRE1 kinase directly phosphorylates human FMRP protein on S500.

IRE1-FMRP signaling induces foam cell formation while suppressing RCT

We next wondered what role FMRP plays in macrophage biology that is relevant to atherosclerotic plaque development. We performed an *in vivo* macrophage foam cell formation assay in the peritoneum of Fmr1 $^{/}$ and Fmr1$^{+/+}$ mice, using a well-established method in which we induced hyperlipidemia using a combination of adenoviral-delivery of proprotein convertase subtilisin kexin 9 (AAV_PCSK9), a protein that directs hepatic low-density lipoprotein (LDL) receptors for degradation, and feeding with WD for 16 weeks (Li *et al*, 2007; Tsimikas *et al*, 2011; Peled *et al*, 2017). FMRP deficiency significantly reduced foam cell formation *in vivo* (Fig 2A). Next, we fed Apoe $^{/}$ mice with a WD (12 weeks) and injected them daily with the IRE1 kinase inhibitor, AMG-18, or vehicle for the last 4 weeks. AMG-18 reduced foam cell formation in the peritoneum *in vivo* (Fig 2B). This result indicates that IRE1-FMRP signaling axis enhances foam cell formation.

We also transfected wild type BMDMs with either Fmr1-specific or control siRNA and followed by loading the cells with 3,3′-dioctadecylindocarbocyanine (dil)-labeled acetylated LDL (Ac-LDL) (Carotti *et al*, 2021). Flow cytometry analysis revealed that Fmr1 silencing significantly reduced % dil-acLDL internalized in macrophages (Fig 2C, Appendix Fig S2A). Likewise, Fmr1 $^{/}$ BMDM displayed reduced % dil-acLDL internalization when compared to Fmr1$^{+/+}$ BMDM (Fig 2D). A similar reduction in foam cell formation was observed with the IRE1 kinase inhibitor (Fig 2E). These results indicate that both the inhibition of IRE1 kinase activity and the genetic deletion of its proposed substrate, FMRP, reduce foam cell formation *in vitro* and *in vivo*. Reduced foam cell formation could be explained with less cholesterol uptake, however, neither FMRP knock down nor IRE1 kinase inhibition altered cholesterol uptake in macrophages (Appendix Fig S2B). We reasoned that this observation is most likely related to an increase in cholesterol export (RCT; due to increased translation of cholesterol exporters) from Fmr1 $^{/}$ macrophages. Indeed, FMRP deficiency led to an increase in cholesterol efflux coupled with its loading onto the cholesterol carriers, apolipoprotein-A1 (APOA1) and HDL (Fig 2F), and, likewise, the IRE1 kinase inhibitor enhanced cholesterol efflux (Fig 2G). Thus, ER stress-associated reduction in cholesterol efflux is dependent on both IRE1 kinase activity and FMRP.

Next, we determined whether the absence of FMRP in BMDMs also enhances RCT *in vivo*. To this end, we pre-loaded Fmr1$^{+/+}$ and Fmr1 $^{/}$ BMDMs with [^{3}H]-cholesterol and injected the cells subcutaneously into WT mice (Fig 2H). FMRP deficiency in macrophages significantly increased radioactivity counts ([^{3}H]-cholesterol) in the plasma, liver, and feces of the recipient mice, when compared to recipient mice that received Fmr1$^{+/+}$ macrophages (Fig 2I–K), demonstrating that FMRP deficiency in macrophages enhances RCT in mice.

FMRP regulates macrophage efferocytosis

We next investigated the impact of FMRP deficiency on efferocytosis, a primary process that promotes atherosclerotic plaque regression by removing apoptotic macrophages in the lesion area. To this end, we transfected BMDM (red fluorescent stained) with Fmr1-specific or control siRNA and incubated them with green fluorescent-labeled apoptotic cells (ACs), in which apoptosis was induced by ultraviolet (UV) irradiation. FMRP knock-down increased efferocytosis of ACs (as measured by colocalization of the fluorescent markers), when compared to control (Fig 3A). FMRP-deficient BMDMs also increased efferocytosis when compared to wild type BMDMs under both no-stress and PA-induced ER stress conditions (Fig 3B). Next, we induced hyperlipidemia in Fmr1 $^{/}$ and Fmr1$^{+/+}$ mice as described above using a combination of AAV_PCSK9 injection and feeding with a WD. We then injected the mice intraperitoneally with green fluorescent-labeled ACs and harvested PM macrophages. FMRP-deficient PMs displayed enhanced efferocytosis compared to WT PMs (Fig 3C).

We next asked how IRE1 kinase activity impacts efferocytosis by macrophages. We observed that AMG-18 increased efferocytosis of ACs in BMDMs (Fig 3D). Next, we injected wild type mice with AMG-18 (for 8 h) followed by injection of green fluorescent-labeled ACs. AMG-18 also induced efferocytosis of ACs by PM *in vivo* (Fig 3E).

Continued clearance of ACs by macrophages prevents the accumulation of necrotic cells and is an important process that promotes atherosclerosis regression (Yurdagul *et al*, 2017). To determine whether Fmr1 $^{/}$ macrophages can efficiently internalize multiple ACs over consecutive rounds of engulfment, we incubated macrophages with green fluorescent-labeled AC for 2 h, followed by second incubation with violet fluorescent-labeled AC for 2 more hours. FMRP-deficient BMDMs displayed an increase in continued efferocytosis when compared to wild type BMDMs (Fig 3F). Likewise, treatment of wild type BMDM with AMG-18 enhanced continued efferocytosis of ACs (Fig 3G). Collectively, these results demonstrate that the ablation of IRE1 kinase activity and its proposed substrate, FMRP, enhances efferocytosis *in vitro* and *in vivo*.

Translational suppression of cholesterol transporters and efferocytosis regulators by FMRP during ER stress

Consistent with our observations that macrophage FMRP plays a role in suppressing cholesterol efflux and efferocytosis, published data describing the FMRP-RNA interactome also suggest that FMRP interacts with mRNA-encoding proteins involved in cholesterol trafficking (such as Abca1 and Abcg1) and efferocytosis receptors (such

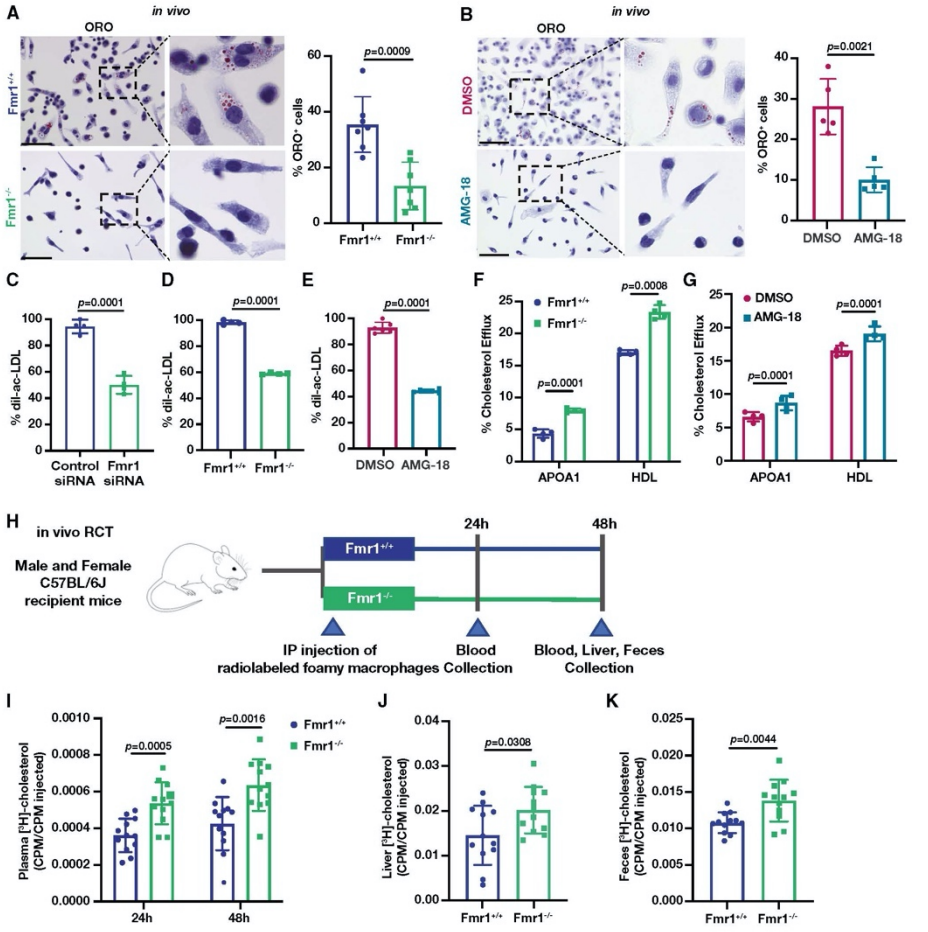

Figure 2. FMRP deficiency enhances RCT while reducing foam cell formation *in vivo*.

A $Fmr1^{+/+}$ and $Fmr1^{-/-}$ mice were injected with AAV_PCSK9 and fed with 16 weeks of WD. Residential PM were stained with Oil Red O (ORO) and imaged (n = 7 mice per group; Scale bar = 50 μm).

B $Apoe^{-/-}$ mice were fed with WD (12 weeks) and injected with vehicle (DMSO) or AMG-18 (30 mg/kg/day) in the last 4 weeks of WD. Residential PM were stained with ORO and imaged (n = 5 mice per group; Scale bar = 50 μm).

C–E Flow cytometry analysis of BMDMs after dil-ac-LDL (25 μg/ml) loading for 24 h; (C) control- or Fmr1-siRNA transfected BMDM (n = 4 biological replicates), (D) $Fmr1^{+/+}$ and $Fmr1^{-/-}$ BMDM (n = 4 biological replicates), (E) BMDM pre-treated with either vehicle (DMSO) or AMG-18 (5 μM; 1 h) (n = 6 biological replicates).

F, G Macrophages were pre-loaded with fluorescently labeled cholesterol (16 h) followed by incubation in efflux medium including APOA1 (25 μg/ml) or HDL (50 μg/ml) as acceptors for 6 h. % Efflux was calculated as cholesterol signal in medium/cholesterol signal in medium and cell: Cholesterol efflux in (F) $Fmr1^{+/+}$ and $Fmr1^{-/-}$ BMDM (n = 4 biological replicates) and in (G) BMDM that were pre-treated either with DMSO or AMG-18 (5 μM; 1 h) (n = 4 biological replicates).

H–K RCT experiment: (H) Schematic representation of C57BL6 mice were injected with $[^3H]$-cholesterol-loaded foamy $Fmr1^{+/+}$ and $Fmr1^{-/-}$ BMDM, (I) plasma cholesterol levels after 24 and 48 h, (J) liver cholesterol levels after 48 h, and (K) feces cholesterol levels after 48 h (n = 12 mice per group).

Data information: Data are mean ± SEM. Unpaired t-test with Welch's correction.
Source data are available online for this figure.

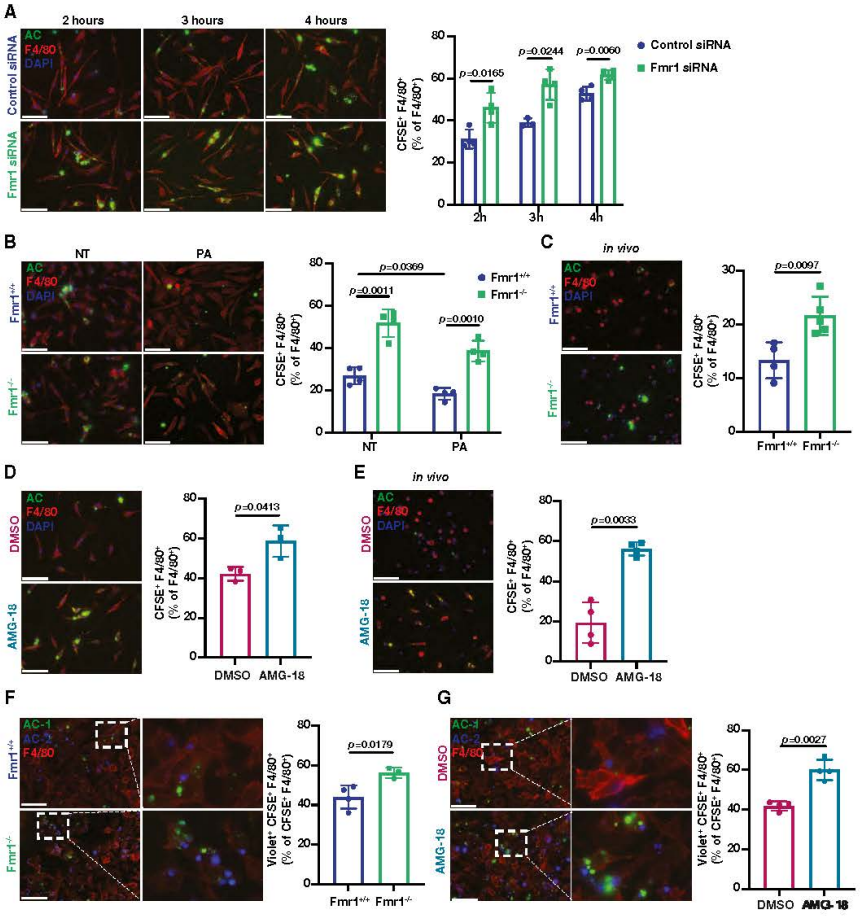

Figure 3. FMRP deficiency increases efferocytosis *in vivo*.

A–E *In vitro* and *in vivo* efferocytosis experiments, where percentage of macrophages F4/80$^+$ (red) that ingested apoptotic cells (AC) labeled with carboxyfluorescein succinimidyl ester (CFSE)$^+$ (green) were reported as % efferocytosis. (A) BMDMs were transfected with Fmr1- or control-siRNA and incubated CFSE-labeled AC for the indicated hours ($n = 4$ biological replicates). (B) Fmr1$^{+/+}$ and Fmr1$^{-/-}$ BMDMs were treated with PA (500 μM) for 6 h and then incubated with CFSE-labeled ACs for 4 h ($n = 4$ biological replicates). (C) Fmr1$^{+/+}$ and Fmr1$^{-/-}$ mice were fed WD (16 weeks) and injected intraperitoneally with CFSE-labeled AC (1.5 h), followed by PM elicitation ($n = 4$–5 mice per group). (D) BMDM were pre-treated either with vehicle (DMSO) or AMG-18 (5 μM) for 1 h then incubated with CFSE-labeled Acs for 4 h ($n = 3$ biological replicates). (E) C57BL/6 mice were injected with AMG-18 (30 mg/kg) or vehicle (DMSO) for 8 h, followed by intraperitoneal injection with CFSE-labeled ACs for 1.5 h and PM elicitation ($n = 4$ mice per group).

F, G *In vitro* continuous *efferocytosis experiments*, where macrophages were stained for F4/80$^+$ (red), AC were labeled with CFSE (AC-1; green) or Violet (AC2; violet). % continuous efferocytosis was determined by the ratio of F4/80$^+$, CFSE$^+$, and Violet$^+$ (triple positive) cells to total F4/80$^+$ and CFSE$^+$ (double positive) cells. (F) Fmr1$^{+/+}$ and Fmr1$^{-/-}$ BMDM were incubated with AC-1 for 2 h, and after 2 h interval, incubated with AC-2 for 2 more hours ($n = 4$–3 biological replicates). (G) BMDM were pre-treated either with vehicle (DMSO) or AMG-18 (5 μM) for 1 h, incubated with CFSE-labeled AC-1 for 2 h, followed by incubation with Violet-labeled AC-2 for 2 h and PM collection ($n = 4$ biological replicates).

Data information: For all images scale bar = 50 μm; Red: Macrophages, Green: AC/AC-1, Violet: AC-2. Data are mean ± SEM. Unpaired *t*-test with Welch's correction. Source data are available online for this figure.

as c-Mer tyrosine kinase (Mertk) and LDL receptor-related protein 1 (Lrp1)), suggesting FMRP may impair their translation (Darnell *et al*, 2011; Ascano *et al*, 2012). To assess this notion in macrophages, we next performed polyribosome profiling in $Fmr1^{+/+}$ and $Fmr1^{-/-}$ BMDMs under PA-induced ER stress conditions (Fig 4A and B, Appendix Fig S3A). Indeed, the mRNA abundance for the cholesterol transporters, Abca1 and Abcg1, and the mRNA abundance for efferocytosis regulators, Mertk, Lrp1, and Cd36, were increased in translating polysome fractions and decreased in non-translating (NTR) fractions in the $Fmr1^{-/-}$ BMDMs when compared to $Fmr1^{+/+}$ BMDMs (Fig 4B), while the abundance of these mRNAs in the total cell lysate was unchanged (Appendix Fig S3B).

We next analyzed the corresponding protein expression changes for the FMRP-regulated mRNA targets from the same experiment in Fig 4A and B. As expected, ABCA1, ABCG1, MerTK, and LRP1 protein expression levels were induced in $Fmr1^{-/-}$ BMDMs (Fig 4C and Appendix Fig S3C). To further assess the impact of IRE1-mediated FMRP phosphorylation on the translation of FMRP's targets, we overexpressed the FMRP phosphorylation-deficient mutant (STSA) or WT-FMRP in $Fmr1^{-/-}$ MEFs and treated with PA to induce ER stress. ABCA1, LRP1, and MerTK expression levels were reduced in the $Fmr1^{-/-}$ MEF expressing WT-FMRP, but not in $Fmr1^{-/-}$ MEFs expressing STSA-FMRP (Fig 4D and Appendix Fig S3D). Taken together, our data demonstrate that IRE1-mediated

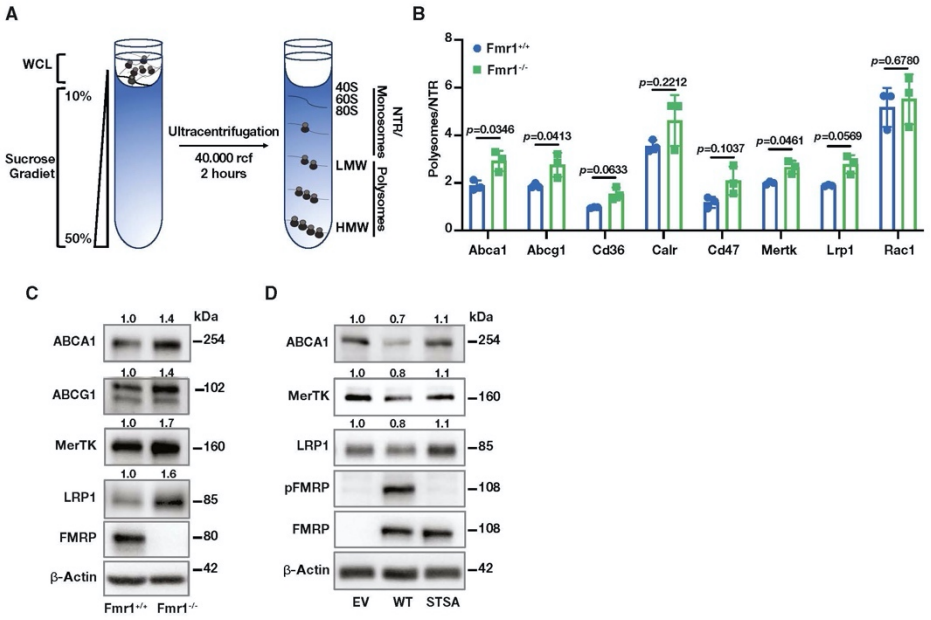

Figure 4. FMRP targets in macrophages.

A, B RNA lysates from $Fmr1^{+/+}$ and $Fmr1^{-/-}$ BMDM that were treated with PA (500 μM; 6 h) were fractionated using a 10–50% sucrose gradient and separated to polysome, monosome/NTR fractions. The absorbance (260 nm) of RNA was measured and plotted as a function of time (n = 3 biological replicates). (A) Representative profile for RNA distribution from genotypes based on UV absorbance readings after sucrose gradient fractionation. (B) The ratio of the Abca1, Abcg1, Mertk, Lrp1, Cd36, Cd47, and Rac1 mRNA in polysome to NTR fraction (n = 3 biological replicates).

C BMDM were isolated from $Fmr1^{+/+}$ and $Fmr1^{-/-}$, and protein lysates were analyzed by Western blotting using specific antibodies for ABCA1, ABCG1, MerTK, LRP1, FMRP, and β-Actin antibodies and fold inductions relative to β-Actin are depicted above the blots (n = 6 biological replicates).

D $Fmr1^{-/-}$ MEF cells were transfected with EV, WT-FMRP, or STSA-FMRP plasmids followed by PA treatment (500 μM; 6 h). Protein lysates were analyzed by Western blotting using specific antibodies for ABCA1, MerTK, LRP1, pFMRP, FMRP, and β-Actin and fold inductions relative to β-Actin are depicted above the blots (n = 5 biological replicates).

Data information: A representative blot is shown. In C and D, data are cumulative results of 2 and 3 independent experiments, respectively. In Western blots, the protein expression fold change was calculated relative to β-Actin and depicted above the blots and a representative blot was shown. Data are mean ± SEM. Unpaired t-test with Welch's correction.
Source data are available online for this figure.

FMRP phosphorylation tunes cholesterol transporters and efferocytosis regulators expression in macrophages.

FMRP knock-down and IRE1 kinase inhibition alleviates atherosclerosis

Our findings demonstrate that both IRE1 kinase inhibition and FMRP deficiency result in increased RCT, reduced foam cell formation, and enhanced efferocytosis *in vivo*, suggesting that FMRP deficiency in mice leads to protection from atherosclerosis. We tested this notion using Fmr1 $^{/}$ and Fmr1$^{+/+}$ mice in which hyperlipidemia was induced by combining AAV_PCSK9 injection with a WD as described above (Fig 5A). Although there was a very slight decrease in body weight ratio; the plasma glucose, total plasma cholesterol (TPC), lipoprotein levels, and the number of circulating, major type of immune cells were indistinguishable between the Fmr1 $^{/}$ and Fmr1$^{+/+}$ genotypes (Appendix Fig S4A–F). Yet, FMRP deficiency resulted in a significant reduction in atherosclerotic lesions in *en face* aorta preparations (Fig 5B). FMRP deficiency did not alter aortic root lesion area despite a significantly decreased foam cell area (as assessed by Oil Red O staining) (Fig 5C and D). We next asked what may be contributing to this phenotype. The necrotic core area in the lesions from Fmr1 $^{/}$ mice was significantly less than in Fmr1$^{+/+}$ lesions (Fig 5E), indicating improved AC clearance by Fmr1 $^{/}$ macrophages in plaques. We also observed a significant reduction in lesion macrophages (as assessed by the anti-monocyte macrophage 2 (MOMA-2)-stained area) and the number of apoptotic cells (TUNEL-stained) per macrophage area (Appendix Fig S4G and H). We further investigated whether apoptosis is altered in Fmr1 $^{/}$ and AMG-18-treated macrophages. There was no significant change between the groups (Appendix Fig S4I), supporting the notion that the primary consequence of inhibiting IRE1-FMRP signaling is efficient clearance of apoptotic cells through increasing efferocytosis capacity. Additionally, we detected no change in smooth muscle area (stained with smooth muscle actin (SMA)), but there was a significant increase in the collagen content of Fmr1 $^{/}$ lesions when compared to Fmr1$^{+/+}$ lesions, suggesting this could be the reason why aortic root lesion area is not significantly altered (Appendix Fig S4J and K).

To approach the role of macrophage FMRP in atherosclerosis, we generated a myeloid Fmr1-deficient mouse model (myFmr1 $^{/}$) and induced hyperlipidemia (Fig 5F). As expected from the systemic deletion data shown in Fig 5A, the body weight, plasma glucose and TPC were indistinguishable between the myFmr1 $^{/}$ and myFmr1$^{+/+}$ genotypes (Appendix Fig S4L–N). in general, myeloid-specific FMRP deficiency paralleled the results obtained for Fmr1 $^{/}$ mice: it resulted in a significant reduction in atherosclerotic lesions in *en face* aorta preparations (Fig 5G). Myeloid-specific FMRP deficiency did not alter aortic root lesion area but significantly reduced foam cell area (Fig 5H and I). The necrotic core area in the lesions from myFmr1 $^{/}$ mice was also significantly less than in myFmr1$^{+/+}$ lesions (Fig 5J), indicating improved AC clearance by Fmr1 $^{/}$ macrophages in plaques and supporting our observations that FMRP deficiency increases macrophage efferocytosis *in vitro* and *in vivo* (Fig 3). Thus, comparing the data obtained with the Fmr1 $^{/}$ mice with those obtained from the myFmr1 $^{/}$ mice indicates that the atheroprotective effects observed in Fmr1 $^{/}$ mice are mostly, if not exclusively, due to FMRP's role in myeloid cells such as macrophages.

To test the notion that IRE1 functions upstream of FMRP, we next investigated the impact of IRE1 kinase inhibition on atherosclerosis. To this end, we fed Apoe $^{/}$ mice with WD for 12 weeks and injected them with AMG-18 or vehicle once daily for the last 4 weeks of WD (Fig 6A). We observed no significant differences in body weight, plasma glucose or TPC, and the number of circulating immune cells between the groups (Appendix Fig S5A–D). Consistent with an earlier publication that determined the effective and non-toxic dose for AMG-18 in mice, the inhibitor engaged its molecular target effectively in the treatment group (as assessed by reduced IRE1 autophosphorylation) (Appendix Fig S5E). IRE1 kinase inhibition led to a decrease in atherosclerotic lesions in *en face* aorta preparations (Fig 6B). As shown above for the Fmr1 $^{/}$ mice, the aortic root lesion area was not different between the groups (Fig 6C), but foam cell area as well as necrotic core area were significantly decreased (Fig 6D and E).

We also assessed the impact of twice daily injections of the same dose of AMG-18 on Apoe $^{/}$ mice that were fed with WD for 12 weeks (Fig 6F). While we noted a decrease in body weight ratio and TPC, there were no significant differences in plasma glucose levels similar to once daily injection (Appendix Fig S5F–H), and the inhibitor engaged its molecular target effectively (as assessed by reduced IRE1 autophosphorylation) (Appendix Fig S5I and J). IRE1 kinase inhibition led to a significant decrease in atherosclerotic lesions in *en face* aorta preparations (Fig 6G). AMG-18 injection did not alter aortic root lesion area but significantly decreased foam cell area and necrotic core area (Fig 6H–J). Collectively, our findings

Figure 5. FMRP-deficiency alleviates atherosclerosis.

A Atherosclerosis experiment design in Fmr1$^{+/+}$ and Fmr1$^{-/-}$ mice that were injected with AAV_PCSK9 and fed WD (16 weeks).
B Lesion area calculated from *en face* aorta, stained with ORO (n – 12–13 mice per group; Scale bar – 5 mm).
C Total plaque area was calculated from hematoxylin & eosin (H&E)-stained aortic root sections (n – 8 mice per group; Scale bar – 300 μm).
D Foam cell area was calculated from ORO-stained aortic root sections (n – 8 mice per group; Scale bar – 300 μm).
E Necrotic area was calculated from H&E-stained aortic root sections (n – 8 mice per group; Scale bar – 100 μm).
F Atherosclerosis experiment design in myFmr1$^{+/+}$ and myFmr1$^{-/-}$ mice that were injected with AAV_PCSK9 and fed WD (16 weeks).
G Lesion area calculated from *en face* aorta, stained with ORO (n – 9 mice per group; Scale bar – 5 mm).
H Total plaque area was calculated from H&E-stained aortic root sections (n – 9–6 mice per group; Scale bar – 300 μm).
I Foam cell area was calculated from ORO-stained aortic root sections (n – 9–6 mice per group; Scale bar – 300 μm).
J Necrotic area was calculated from H&E-stained aortic root sections (n – 9–6 mice per group; Scale bar – 100 μm).

Data information: Data are mean ± SEM; Mann Whitney U test.
Source data are available online for this figure.

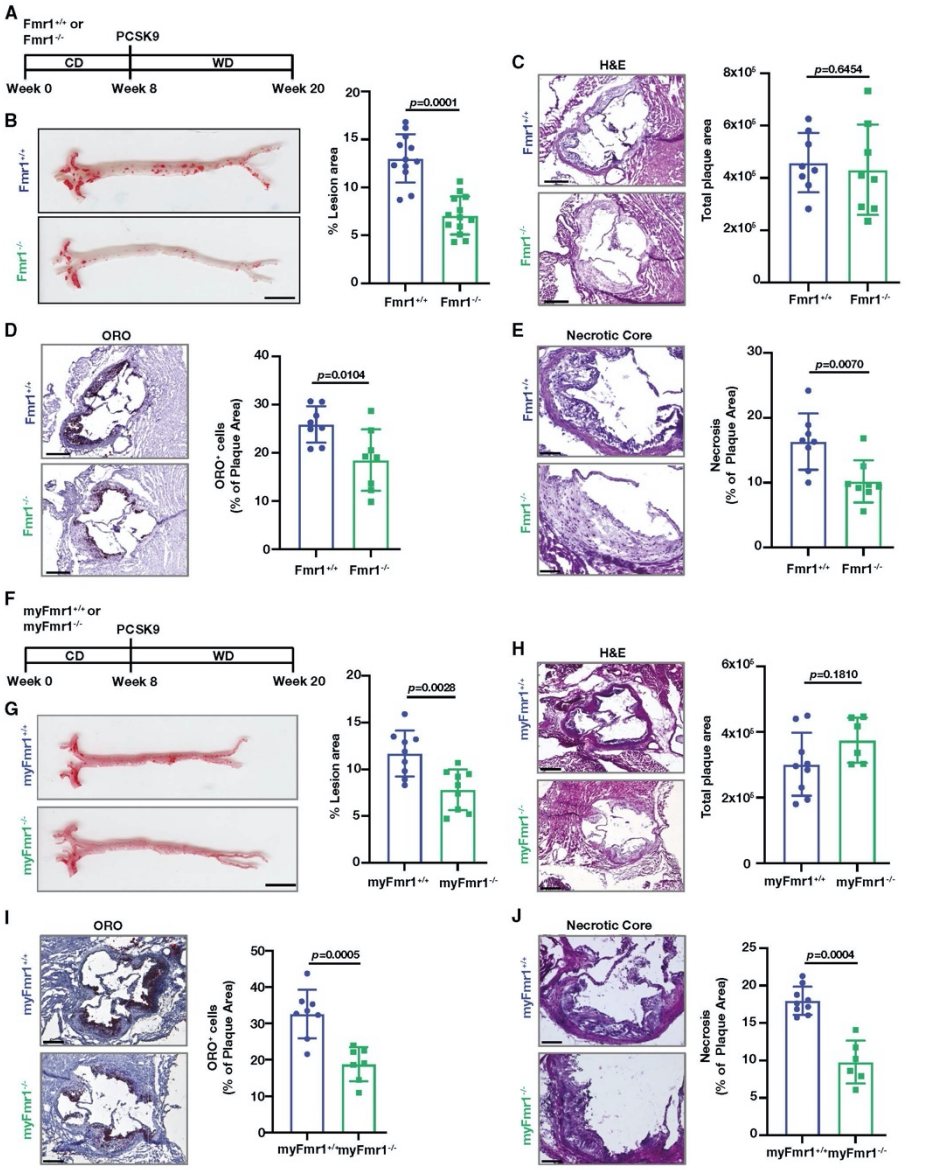

Figure 5.

thus demonstrate that the inhibition of IRE1 kinase activity by a small-molecule inhibitor or genetic ablation of FMRP, its kinase substrate, in macrophages can reduce the progression of hypercholesterolemia-induced atherosclerosis.

Discussion

Chronic lipid accumulation in the ER membranes (e.g., during obesity and in hyperlipidemia) has been shown to impair ER functions and activate UPR signaling (Li *et al*, 2004; Borradaile *et al*, 2006; Fu *et al*, 2011; Volmer *et al*, 2013; Çimen *et al*, 2016b). Numerous studies have shown that ER stress is an important primer for sterile inflammation that drives insulin resistance and atherogenesis (Hotamisligil, 2017). Moreover, alleviating ER stress by inhibiting either PERK or IRE1 signaling prevents atherosclerosis progression (Erbay *et al*, 2009; Tabas, 2010; Tufanli *et al*, 2017; Onat *et al*, 2019). But how does chronic IRE1 kinase activation contribute to the atherosclerotic process? Our work revealed that in ER-stressed macrophages phosphorylation of FMRP, an RBP functioning as a translational suppressor, is enhanced in an IRE1 kinase-dependent manner. This phosphorylation event results in a gain-of-function for FMRP, which leads to enhanced translational suppression of cholesterol transporters and efferocytosis receptors. Although ubiquitously expressed, prior work focused almost exclusively on FMRP's role in neurons in the context of its devastating role in FXS pathology (Sethna *et al*, 2014; Davis & Broadie, 2017; Leboucher *et al*, 2019a). Our work reveals a novel function for FMRP in macrophages. Intriguingly, an earlier publication showed that FMRP protein expression is elevated in the macrophage-enriched area of human atherosclerotic plaques (Tuomisto *et al*, 2003). Moreover, lower cholesterol levels have been measured in a subpopulation of the individuals afflicted with FXS, as well as in Fmr1 $^{/}$ mice (Berry-Kravis *et al*, 2015; Lisik *et al*, 2016; Leboucher *et al*, 2019b). Although these findings foreshadowed a role of FMRP in the regulation of cholesterol homeostasis (Tuomisto *et al*, 2003; Darnell *et al*, 2011; Ascano *et al*, 2012), FMRP's contribution to atherosclerosis was not investigated prior to this study, perhaps because Fmr1 lies on the X chromosome and most genome-wide association studies in humans focus on variants on autosomal chromosomes excluding sex chromosomes. While characterizing the impact of IRE1 kinase activity and it's here proposed kinase substrate, FMRP, on macrophage functions, our current study revealed a role for an "IRE1-FMRP signaling axis" in the regulation of macrophage cholesterol trafficking and efferocytosis, which are among the primary cellular mechanisms that can regress atherosclerosis (Fig 7).

To gain insight into the physiological role of macrophage FMRP, we investigated the consequences of FMRP deficiency on macrophage biology that are relevant to atherosclerosis development and plaque regression, such as foam cell formation, cholesterol efflux, and efferocytosis. Our findings show that FMRP has a prominent role in all three processes. Additionally, our observations are consistent with the finding that several mRNAs encoding cholesterol transporters and efferocytosis receptors interact with FMRP in prior RNA crosslinking immunoprecipitation (CLIP) experiments (Darnell *et al*, 2011; Ascano *et al*, 2012). Our data show that the absence of FMRP in macrophages increases the occupancy of these mRNAs in the polysome fraction, paralleling the increased expression of their corresponding protein products. In agreement with our observations *in cells*, FMRP deficiency in macrophages increased RCT and efferocytosis in mice. Moreover, systemwide and myeloid-specific Fmr1 knock-out mice were protected from hypercholesterolemia-induced atherosclerosis progression. In agreement with this notion, the IRE1 kinase-specific inhibitor, AMG-18, phenocopies the beneficial impact of FMRP deficiency (such as enhanced cholesterol efflux and efferocytosis) in macrophages. While our studies provide strong support for the role of macrophage FMRP in atherosclerosis progression, we did not examine the contribution of FMRP activity in other lesion cell types, such as endothelial or vascular smooth muscle cells, on atherosclerosis. The impairment of RCT and efferocytosis by IRE1-FMRP signaling implies that interventions to ablate FMRP in a macrophage-specific manner and in the adult organism could promote atherosclerotic plaque stabilization and hinder plaque progression, while escaping an adverse impact of FMRP deficiency on neuronal development.

Two recent studies show that FMRP plays a metabolic role in the liver. For example, systemic FMRP deficiency in mice led to enhanced glucose tolerance and insulin sensitivity, while lowering plasma triglyceride and cholesterol content (Leboucher *et al*, 2019b). Another study showed combined deficiency of FMRP and its paralog FXR2 (Fragile X mental retardation autosomal homolog 2) resulted in lower body fat and increased sensitivity to insulin (Lumaban & Nelson, 2015). Intriguingly, the FMRP loss-of-function

Figure 6. IRE1 Kinase inhibition alleviates atherosclerosis.

A Atherosclerosis experiment design in Apoe$^{-/-}$ mice were fed with WD (12 weeks) and injected with vehicle (DMSO) or AMG-18 (30 mg/kg) once a day in the last 4 weeks of WD.
B Lesion area calculated from *en face* aorta, stained with ORO (n – 5 mice per group; Scale bar – 5 mm).
C Total plaque area was calculated from H&E-stained aortic root sections (n – 5 mice per group; Scale bar – 300 μm).
D Foam cell area was calculated from ORO-stained aortic root sections (n – 5 mice per group; Scale bar – 300 μm).
E Necrotic area was calculated from H&E-stained aortic root sections (n – 5 mice per group; Scale bar – 100 μm).
F Atherosclerosis experiment design in Apoe$^{-/-}$ mice were fed with WD (12 weeks) and injected with vehicle (DMSO) or AMG-18 (30 mg/kg) twice a day in the last 4 weeks of WD.
G Lesion area calculated from *en face* aorta, stained with ORO (n – 6 mice per group; Scale bar – 5 mm).
H Total plaque area was calculated from H&E-stained aortic root sections (n – 5 mice per group; Scale bar – 300 μm).
I Foam cell area was calculated from ORO-stained aortic root sections (n – 5 mice per group; Scale bar – 300 μm).
J Necrotic area was calculated from H&E-stained aortic root sections (n – 5 mice per group; Scale bar – 100 μm).

Data information: Data are mean ± SEM; Mann Whitney U test.
Source data are available online for this figure.

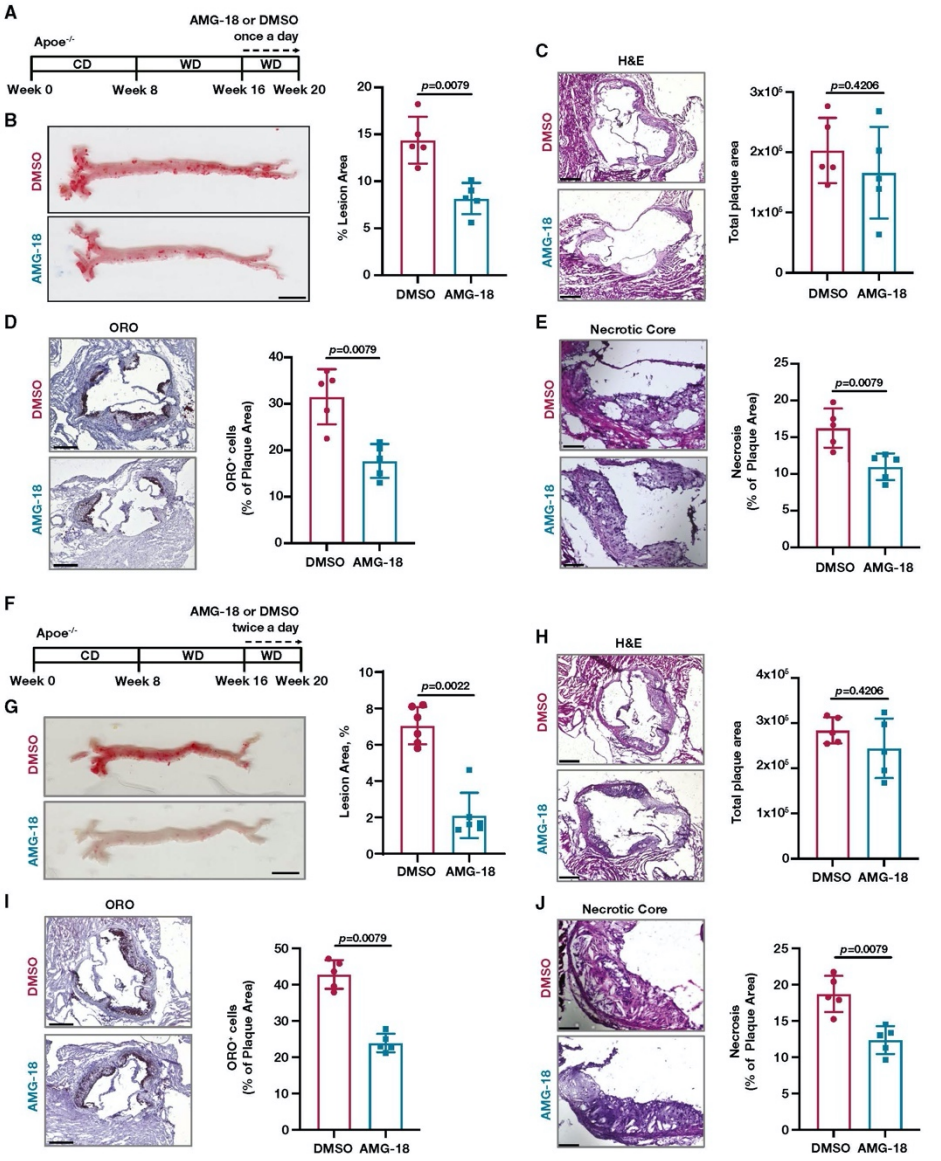

Figure 6.

in liver resulted in increased translation of hepatic mRNA involved in lipid metabolism (Leboucher *et al*, 2019b). In contrast to this previous work, we did not find Fmr1 deficiency-associated changes in plasma cholesterol or lipoprotein levels in our atherosclerosis mouse models, perhaps due to the severe hypercholesterolemia induced by both genetic and dietary interventions.

In an earlier study, we had shown that small-molecule inhibitors that are specific for IRE1's RNase activity prevented lipid-induced inflammasome activation and secretion of mature interleukin-1β (m-IL-1β) and m-IL-18 in both mouse and human macrophages while reducing hyperlipidemia-induced m-IL-1β and m-IL-18 production and atherosclerotic plaque size in mice (Tufanli *et al*, 2017). FMRP suppression also reduces m-IL-1β secreted from macrophages but without altering inflammasome activation (Appendix Fig S6A–F). Knocking out FMRP from macrophages has no effect on IL-1β mRNA levels in the whole cell lysate or in the polysomes, suggesting against transcriptional or translational control over these cytokines' production (Appendix Fig S6G and H). As expected, inhibition of IRE1 kinase also reduces m-IL-1β (Appendix Fig S6I–K). Intriguingly, IL-1β can be secreted through ABCA1 and compete with cholesterol efflux through the same transporter (Tumurkhuu *et al*, 2018). Since the inhibition of IRE1 kinase-FMRP axis leads to a marked upregulation of cholesterol efflux in macrophages (as shown in our study), it is plausible that increased demand for ABCA1 for cholesterol efflux could prevent IL-1β secretion through this route.

Our finding that IRE1 phosphorylates FMRP leads to an important question: Why does the UPR signaling impinge on FMRP-mediated translational suppression? While intensely debated, multiple mechanisms have been proposed for translational suppression by FMRP including polyribosome stalling, miRNA-mediated translational silencing, and impairing translational initiation (Napoli *et al*, 2008; Edbauer *et al*, 2010; Darnell *et al*, 2011; Chen *et al*, 2014). Recently, phosphorylation-dependent FMRP-RNA phase separation

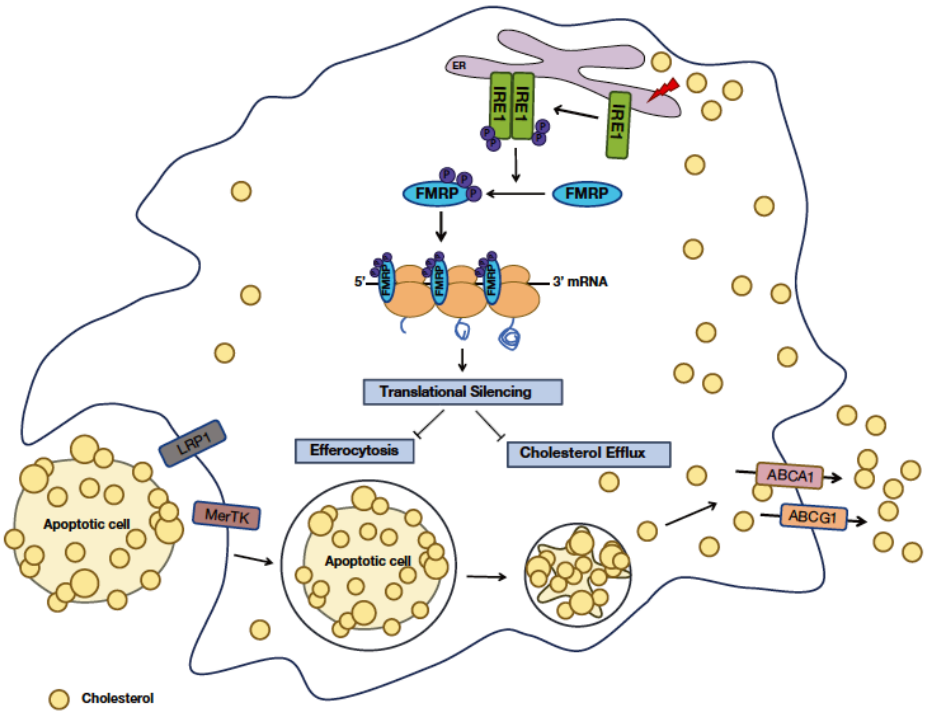

Figure 7. IRE1-FMRP signaling controls cholesterol efflux and efferocytosis pathways in macrophages.

IRE1-mediated FMRP phosphorylation suppresses translation of mRNA for key cholesterol transporters and efferocytosis receptors in macrophages and promotes atherosclerosis.

from Jackson Lab (004781) to obtain myeloid Fmr1-deficient (myFmr1 $^{/}$) mice.

Starting at 8 weeks of age, Fmr1$^{+/+}$, Fmr1 $^{/}$, myFmr1$^{+/+}$, or myFmr1 $^{/}$ mice were injected with 1×10^{10} AAV_PCSK9 (AAV8-D377Y-mPCSK9, Vector BiolabsAAV-268246) via tail vein, then fed with normal chow or high cholesterol/high fat atherosclerotic mouse diet from Envigo (TD.88137) for 6–16 weeks. Apoe $^{/}$ mice were fed with WD (12 weeks) and intraperitoneally injected with vehicle (DMSO) or AMG-18 (30 mg/kg) once or twice a day in the last 4 weeks of WD. C57BL/6 were injected with Tunicamycin (TM, 1 mg/kg) and with AMG-18 (30 mg/kg) or vehicle (DMSO) in 20% vol/vol Cremophor EL saline solution, as described in (Tufanli *et al*, 2017). Eight hours later, peritoneal macrophages were isolated by thioglycolate elicitation for further analysis.

Husbandry conditions and study approval

Mice were kept under specific pathogen-free conditions with food and water *ad libititum*. Both female and male mice were used for experiments. All animal experiments were performed according to protocols approved by the Experimental Animal Ethical Care Committees at Bilkent University, Ankara, Turkey or Cedars Sinai Medical Center, Los Angeles, USA or the University of Ottawa Animal Care Committee, Ottawa, ON K1N 6N5, Canada.

Macrophage isolation

Peritoneal macrophages

3% thioglycolate solution was injected to mice intraperitoneally and peritoneal macrophages were collected 4 days after by washing the peritoneal cavity with ice-cold PBS (10 ml) as described before (Zhang *et al*, 2008; Onat *et al*, 2019). Cells were centrifuged at 500 *g* for 5 min at 4°C and resuspended in RPMI medium in cell culture plates. Macrophages were incubated at 5% carbon dioxide incubator at 37°C for 30 min to attach and non-adherent cells were removed along with media. Cells were rinsed with PBS and used for protein isolation or RNA isolation.

Bone Marrow-Derived Macrophages (BMDM)

Bone marrows were collected form the tibia and femurs of mice into RPMI containing 1% Penicillin/streptomycin (P/S) cocktail as previously described (Tufanli *et al*, 2017). After filtering through a cell strainer (BD, 352350), cells were centrifuged at 500 *g* for 5 min and resuspended in RPMI enriched with 20% L929 cells conditioned medium, 10% heat-inactivated fetal bovine serum (FBS), and 1% P/S cocktail, followed by growth on Petri dishes and differentiation to macrophages for 5–10 days.

Cell lines

Fmr1 $^{/}$ mouse embryonic fibroblasts (MEF) were generated in Dr. David Nelson's laboratory (Baylor College of Medicine, Houston, Texas). HEK293T, Jurkat (human T lymphocytes), and L-929 (mouse fibroblasts) cells were obtained from ATCC. Cells were cultured in RPMI or DMEM supplemented with 10% heat-inactivated FBS and %1 P/S cocktail. Cells were cultured in a humidified CO2 incubator at 37°C. All cells were regularly tested for mycoplasma contamination.

Transfection

60–80% confluent HEK293T, WT or Fmr1 $^{/}$ MEF cells were transfected using Lipofectamine 3000 or Polyethylemine (PEI). BMDM and HEK293T cells were electroporated either with IRE1-, Fmr1-(100 nM), or control-siRNA using Neon electroporator (Thermo Scientific) as per specific conditions provided by the manufacturer and as described earlier (Tufanli *et al*, 2017). 24–36 h after transfection, cells were treated with PA or TG to induce ER stress.

Palmitate (PA)/bovine serum albumin (BSA) complex preparation

PA was dissolved in absolute ethanol to yield a stock concentration of 500 mM and stored at −80°C. Stock PA was diluted to working concentration and suspended with %1 fatty acid-free BSA in serum-free RPMI growth medium by mixing at 55°C for 15 min as described before (Erbay *et al*, 2009).

Western blot analysis

Cells were lysed in lysis buffer (50 mM HEPES pH:7,9, 100 mM NaCl, 10 mM EDTA,10 mM NaF, 4 mM NaPP, 1% Triton, 1 mM phenylmethanesulfonylfluoride (PMSF), 1× phosphatase inhibitor cocktail 3 and 1× (10 μM) protease inhibitor cocktail as described in (Çimen *et al*, 2016b). After centrifugation, clear lysates were mixed with sodium dodecyl sulfate (SDS) loading dye and heated at 95°C for 5 min before loading on SDS–polyacrylamide gel (SDS–PAGE) gels. After separation according to protein molecular weights on these gels, samples were transferred to polyvinylidene difluoride (PVDF) membrane. Blocking and antibody incubation of the membranes were carried out in tris-buffered saline (TBS) buffer prepared with 0.1% Tween-20 (v/v) and 5% (w/v) dry milk or BSA. ECL prime reagent was used to develop the membranes, and images were captured with ChemiDoc (BioRad).

Antibody dilutions

Anti-pIRE1 1:2,000, anti-FMRP 1:2,000, anti-LRP1 1:5,000, anti-IL-1 beta 1:500, Anti-pro Caspase1 + p10 + p12 1:2,000, anti-Thiophosphate ester 1:5,000, anti-pFMRP (phosphor-S499) 1:2,000, anti-IRE1 1:2,000, anti-ABCA1 1:1,000, anti-ABCG1 1:1,000, Anti-MERTK 1:1,000, anti-β-Actin-horse radish peroxidase 1:5,000, Secondary IgG-Goat 1:10,000, Secondary IgG-Rabbit 1:10,000, Secondary-IgG-Mouse 1:10,000.

RNA isolation and quantitative reverse transcription polymerase chain reaction (qRT-PCR)

Total RNA was isolated using TRIsure. RNA extractions were than reverse transcribed by using Revert Aid First strand cDNA synthesis kit to complementary deoxyribonucleic acid (cDNA) according to manufacturer's protocol. Using specific primers, cDNAs were amplified on Rotor Gene (Qiagen). Power-Up-SYBR green (Applied Biosystems, A25742) was used for qRT-PCR reaction. The following PCR primers were used for mRNA expression analysis:

mmu-Fmr1-F 5′ CCGAACAGATAATCGTCCACG 3′
mmu-Fmr1-R 5′ ACGCTGTCTGGCTTTTCCTTC 3′
mmu-Abca1-F 5′ AAAACCGCAGACATCCTTCAG 3′
mmu-Abca1-R 5′ CATACCGAAACTCGTTCACCC 3′

from Jackson Lab (004781) to obtain myeloid Fmr1-deficient (myFmr1 $^{/}$) mice.

Starting at 8 weeks of age, Fmr1$^{+/+}$, Fmr1 $^{/}$, myFmr1$^{+/+}$, or myFmr1 $^{/}$ mice were injected with 1×10^{10} AAV_PCSK9 (AAV8-D377Y-mPCSK9, Vector BiolabsAAV-268246) via tail vein, then fed with normal chow or high cholesterol/high fat atherosclerotic mouse diet from Envigo (TD.88137) for 6–16 weeks. Apoe $^{/}$ mice were fed with WD (12 weeks) and intraperitoneally injected with vehicle (DMSO) or AMG-18 (30 mg/kg) once or twice a day in the last 4 weeks of WD. C57BL/6 were injected with Tunicamycin (TM, 1 mg/kg) and with AMG-18 (30 mg/kg) or vehicle (DMSO) in 20% vol/vol Cremophor EL saline solution, as described in (Tufanli *et al*, 2017). Eight hours later, peritoneal macrophages were isolated by thioglycolate elicitation for further analysis.

Husbandry conditions and study approval

Mice were kept under specific pathogen-free conditions with food and water *ad libititum*. Both female and male mice were used for experiments. All animal experiments were performed according to protocols approved by the Experimental Animal Ethical Care Committees at Bilkent University, Ankara, Turkey or Cedars Sinai Medical Center, Los Angeles, USA or the University of Ottawa Animal Care Committee, Ottawa, ON K1N 6N5, Canada.

Macrophage isolation

Peritoneal macrophages

3% thioglycolate solution was injected to mice intraperitoneally and peritoneal macrophages were collected 4 days after by washing the peritoneal cavity with ice-cold PBS (10 ml) as described before (Zhang *et al*, 2008; Onat *et al*, 2019). Cells were centrifuged at 500 *g* for 5 min at 4°C and resuspended in RPMI medium in cell culture plates. Macrophages were incubated at 5% carbon dioxide incubator at 37°C for 30 min to attach and non-adherent cells were removed along with media. Cells were rinsed with PBS and used for protein isolation or RNA isolation.

Bone Marrow-Derived Macrophages (BMDM)

Bone marrows were collected form the tibia and femurs of mice into RPMI containing 1% Penicillin/streptomycin (P/S) cocktail as previously described (Tufanli *et al*, 2017). After filtering through a cell strainer (BD, 352350), cells were centrifuged at 500 *g* for 5 min and resuspended in RPMI enriched with 20% L929 cells conditioned medium, 10% heat-inactivated fetal bovine serum (FBS), and 1% P/S cocktail, followed by growth on Petri dishes and differentiation to macrophages for 5–10 days.

Cell lines

Fmr1 $^{/}$ mouse embryonic fibroblasts (MEF) were generated in Dr. David Nelson's laboratory (Baylor College of Medicine, Houston, Texas). HEK293T, Jurkat (human T lymphocytes), and L-929 (mouse fibroblasts) cells were obtained from ATCC. Cells were cultured in RPMI or DMEM supplemented with 10% heat-inactivated FBS and %1 P/S cocktail. Cells were cultured in a humidified CO2 incubator at 37°C. All cells were regularly tested for mycoplasma contamination.

Transfection

60–80% confluent HEK293T, WT or Fmr1 $^{/}$ MEF cells were transfected using Lipofectamine 3000 or Polyethylemine (PEI). BMDM and HEK293T cells were electroporated either with IRE1-, Fmr1-(100 nM), or control-siRNA using Neon electroporator (Thermo Scientific) as per specific conditions provided by the manufacturer and as described earlier (Tufanli *et al*, 2017). 24–36 h after transfection, cells were treated with PA or TG to induce ER stress.

Palmitate (PA)/bovine serum albumin (BSA) complex preparation

PA was dissolved in absolute ethanol to yield a stock concentration of 500 mM and stored at −80°C. Stock PA was diluted to working concentration and suspended with %1 fatty acid-free BSA in serum-free RPMI growth medium by mixing at 55°C for 15 min as described before (Erbay *et al*, 2009).

Western blot analysis

Cells were lysed in lysis buffer (50 mM HEPES pH:7,9, 100 mM NaCl, 10 mM EDTA,10 mM NaF, 4 mM NaPP, 1% Triton, 1 mM phenylmethanesulfonylfluoride (PMSF), 1× phosphatase inhibitor cocktail 3 and 1× (10 μM) protease inhibitor cocktail as described in (Çimen *et al*, 2016b). After centrifugation, clear lysates were mixed with sodium dodecyl sulfate (SDS) loading dye and heated at 95°C for 5 min before loading on SDS–polyacrylamide gel (SDS–PAGE) gels. After separation according to protein molecular weights on these gels, samples were transferred to polyvinylidene difluoride (PVDF) membrane. Blocking and antibody incubation of the membranes were carried out in tris-buffered saline (TBS) buffer prepared with 0.1% Tween-20 (v/v) and 5% (w/v) dry milk or BSA. ECL prime reagent was used to develop the membranes, and images were captured with ChemiDoc (BioRad).

Antibody dilutions

Anti-pIRE1 1:2,000, anti-FMRP 1:2,000, anti-LRP1 1:5,000, anti-IL-1 beta 1:500, Anti-pro Caspase1 + p10 + p12 1:2,000, anti-Thiophosphate ester 1:5,000, anti-pFMRP (phosphor-S499) 1:2,000, anti-IRE1 1:2,000, anti-ABCA1 1:1,000, anti-ABCG1 1:1,000, Anti-MERTK 1:1,000, anti-β-Actin-horse radish peroxidase 1:5,000, Secondary IgG-Goat 1:10,000, Secondary IgG-Rabbit 1:10,000, Secondary-IgG-Mouse 1:10,000.

RNA isolation and quantitative reverse transcription polymerase chain reaction (qRT-PCR)

Total RNA was isolated using TRIsure. RNA extractions were than reverse transcribed by using Revert Aid First strand cDNA synthesis kit to complementary deoxyribonucleic acid (cDNA) according to manufacturer's protocol. Using specific primers, cDNAs were amplified on Rotor Gene (Qiagen). Power-Up-SYBR green (Applied Biosystems, A25742) was used for qRT-PCR reaction. The following PCR primers were used for mRNA expression analysis:

mmu-Fmr1-F 5′ CCGAACAGATAATCGTCCACG 3′
mmu-Fmr1-R 5′ ACGCTGTCTGGCTTTTCCTTC 3′
mmu-Abca1-F 5′ AAAACCGCAGACATCCTTCAG 3′
mmu-Abca1-R 5′ CATACCGAAACTCGTTCACCC 3′

mmu-Abcg1-F 5′ GGTCCTGACACATCTGCGAA 3′
mmu-Abcg1-R 5′ CAGGACCTTCTTGGCTTCGT 3′
mmu-Mertk-F 5′ CAGGGCCTTTACCAGGGAGA 3′
mmu-Mertk-R 5′ TGTGTGCTGGATGTGATCTTC 3′
mmu-Lrp1-F 5′ GCCTACACCTGGAGAGATAGC 3′
mmu-Lrp1-R 5′ GGCAACTTACGAGCAGGCT 3′
mmu-Cd36-F 5′ GTGCTCTCCCTTGATTCTGC 3′
mmu-Cd36-R 5′ CTGCACCAATAACAGCTCCA 3′
mmu-Cd47-F 5′ TGGTGGGAAACTACACTTGCG 3′
mmu-Cd47-R 5′ CGTGCGGTTTTTCAGCTCTAT 3′
mmu-Calr-F 5′ GCAGACCCTGCCATCTATTTC 3′
mmu-Calr-R 5′ TCGGACTTATGTTTGGATTCGAC 3′
mmu-Rac1-F 5′ ATGCAGGCCATCAAGTGTG 3′
mmu-Rac1-R 5′ TAGGAGAGGGGACGCAATCT 3′
mmu-IL-1β -F 5′ CAACCAACAAGTGATATTCTCCATG 3′
mmu-IL-1β -R 5′ GATCCACACTCTCCAGCTGCA 3′
mmu-Gapdh-F 5′ ATTCAACGGCACAGTCAAGG 3′
mmu-Gapdh-R 5′ TGGATGCAGGGATGATGTTC 3′

The following primers were used to introduce site-directed mutagenesis on FMRP plasmids:
S500A-F 5′ GCATCAAATGCTGCTGAAGCAGAAGCTGACCACAGAG AC 3′
S500A-R- 5′ GTCTCTGTGGTCAGCTTCTGCTTCAGCAGCATTTGAT GC 3′
S500-T502-S504A-F 5′ GCATCAAATGCTGCTGAAGCAGAAGCTGA CCACAGAGAC 3′S500-T502-S504A-R 5′ GTCTCTGTGGTCAGCTT CTGCTTCAGCAGCATTTGATGC 3′

Identifying phosphorylation sites on hFMRP using Mass spectrometry

Two *in vitro* kinase reactions of hFMRP and ERN1, worth 4.5 µg protein each were methanol-chloroform precipitated (Wessel & Flügge, 1984). Dried pellets were dissolved in either [1] 8 M urea/100 mM triethylammonium bicarbonate (TEAB, Thermo Scientific 90114), pH 8.5, or [2] 100 mM ammonium acetate (Sigma-Aldrich A1542), with or without 8 M urea. Proteins were reduced with 5 mM tris(2-carboxyethyl) phosphine hydrochloride (TCEP-HCl, Thermo Scientific C4709) and alkylated with 10 mM 2-chloroacetamide (Sigma-Aldrich 22790). Proteins dissolved in urea/TEAB were digested at 37°C in 0.8 M urea/100 mM TEAB, pH 8.5, sequentially with 500 ng Trypsin (Promega V5117) for 17 h, followed by 500 ng Endoproteinase GluC (NEB P8100S) for 4.5 h and quenched with formic acid, 5% final concentration, while proteins dissolved in urea/TEAB or urea/ammonium acetate were digested with 200 ng Proteinase K (Sigma-Aldrich P2308) at 37°C for 30 min and heat quenched at 90°C for 15 min (similar reactions in ammonium acetate without urea were performed for 30 min or 15 min followed by 16 h digestion with trypsin) (Baboo *et al*, 2021). The digest was injected directly onto a 20 cm, 100 µm ID column packed with BEH 1.7 µm C18 resin (Waters 186005225). Samples were separated at a flow rate of 400 nl/min on an nLC 1000 (Thermo LC120). Buffer A and B were 0.1% formic acid in 5% acetonitrile and 0.1% formic acid in 80% acetonitrile, respectively. A gradient of 1–25% B over 110 min, an increase to 40% B over next 20 min, an increase to 90% B over another 10 min, and a hold at 90% B for the final 10 min were used for a total run time of 140 min. The column was re-equilibrated with 20 µl of buffer A prior to the injection of sample. Peptides were eluted directly from the tip of the column and nano-sprayed into the mass spectrometer by application of 2.8 kV voltage at back of the column. The Orbitrap Fusion Lumos (Thermo) was operated in data-dependent mode. Full MS1 scans were collected in the Orbitrap at 120K resolution with a mass range of 400–1,500 m/z and an AGC target of 4e5. The cycle time was set to 3 s, and within these 3 s, the most abundant ions per scan were selected for CID MS/MS in the ion trap with an AGC target of 2e4 and minimum intensity of 5,000. Maximum fill times were set to 50 and 35 ms for MS and MS/MS scans, respectively. Quadrupole isolation at 1.6 m/z was used, monoisotopic precursor selection was enabled, charge states of 2–7 were selected, and dynamic exclusion was used with an exclusion duration of 5 s. Samples were also analyzed with HCD fragmentation (35 NCE) and detection at 7,500 resolution.

Protein and peptide identification were done with Integrated Proteomics Pipeline—IP2 (Integrated Proteomics Applications). Tandem mass spectra were extracted from raw files using RawConverter (He *et al*, 2015) and searched with ProLuCID (Xu *et al*, 2015) against a concatenated database comprising of amino acid sequences from vendors for FMRP, hERN1, and Endoproteinase GluC, UniProt reference proteome of *Escherichia coli* K12 (UP000000625) Homo sapiens (UP000005640). The search space included all fully tryptic and half-tryptic peptide candidates (no enzyme specificity for sample treated with Proteinase K). Carbamidomethylation (+57.02146) was considered a static modification on cysteine, and phosphorylation (+79.966331) was considered a differential modification on serine/threonine/tyrosine. Data were searched with 50 ppm precursor ion tolerance and 500 ppm fragment ion tolerance. Identified proteins were filtered to using DTASelect (Tab b *et al*, 2002) and utilizing a target-decoy database search strategy to control the false discovery rate at 1%, at the spectrum level (Peng *et al*, 2003). A minimum of 1 peptide per protein and 1 tryptic end per peptide (no tryptic ends in case of Proteinase K treatment) were required and precursor delta mass cut-off was fixed at 10 ppm. Localization scores were assigned to identified sites of phosphorylation using A-Score (Beausoleil *et al*, 2006).

Co-immunoprecipitation and kinase assay

Co-immunoprecipitation

HEK293T cells were co-transfected with IRE1 and FMRP plasmids for 24 h followed by TG (600 nM) or TM (1 µg/ml) for 2 h. Equal amounts of protein lysates were precipitated with specific antibodies (anti-IRE1 1:250 and anti-FMRP 1:250) at 4°C overnight on a rocker. Protein magnetic beads were added to each sample and incubated at 4°C for overnight. Immunoprecipitates were then analyzed by Western blot.

Kinase assay

HEK293T cells were transfected with either with WT- or KD-IRE1 plasmids for 24 h, followed by TG (600 nM) for 2 h for IRE1 activation. Equal amounts of protein lysates were then precipitated with specific IRE1 antibody-coated magnetic beads at 4°C overnight on a rocker. Immunoprecipitates were incubated at 30°C for 45 min in kinase assay buffer (SignalChem K01-09) with specific ATP analogue (ATP-γ-S, 100 µM) and purified hFMRP protein. p-Nitrobenzyl mesylate (PNBM) and 0.5 M ETDA solution were added

to reaction after 45 min and incubated for additional 2 h at RT to alkylate the kinase substrate. Samples were boiled with SDS–PAGE loading dye at 95°C for 5 min to release the proteins from magnetic beads. Beads were separated using magnetic rack and supernatants were analyzed by Western blot.

Kinase assay for phospho-proteomics

Recombinant active IRE1 (500 ng) and FMRP (500 ng) proteins were incubated in kinase buffer at 30°C for 45 min with ATP-γ-S (100 μM). Samples were then incubated at 24°C for 1 h with PNBM (2.5 mM). Samples were boiled in SDS loading buffer at 95°C and loaded to SDS–PAGE. Anti-thiophosphate ester antibody was used to detect alkylated kinase substrate.

Polysome fractionation

Polysome fractionation protocol was adapted from Stastna *et al* (Stastna *et al*, 2018). Briefly, $Fmr1^{+/+}$ and $Fmr1^{-/-}$ BMDM were treated with PA (500 μM) for 6 h followed by cycloheximide (100 μg/ml) for 10 min prior to lysis with buffer (100 mM KCl, 20 mM Tris pH 7.5, 5 mM $MgCl_2$, 0.4% NP-40, 100 μg/ml cycloheximide, 0.1 U RNase inhibitor and protease inhibitor cocktail). Clear lysates were loaded to 10–50% sucrose gradient (in Beckman Coulter Thinwall, Ultra-Clear tubes, 344059) and centrifuged (in Beckman LE-80K) for 120 min at 28,4061 *g* at 4°C in a swinging bucket rotor (Beckman SW41) with no-brake. Each gradient was collected as 17 fractions in microcentrifuge tubes with continuous monitoring of absorbance at 254 nm (Biologic LP (pump), Biorad 731-8300; BioFrac, Biorad 741-0002) and frozen immediately at −80°C for further analysis.

Cholesterol efflux and foam cell formation assays

Cholesterol efflux assay

Efflux assay were performed according to manufacturer's instructions (ab196985). Briefly, macrophages were pre-loaded with fluorescently labeled cholesterol for 16 h in RPMI media including ACAT inhibitor (5 mg/ml), followed by incubation in efflux medium including cholesterol acceptors apolipoprotein A1 (APOA1; 25 μg/ml) or high-density lipoprotein (HDL; 50 μg/ml) for 6 h. % Efflux was calculated as cholesterol signal in medium/cholesterol signal in medium and cell.

In vitro foam cell formation assay

BMDM were incubated with RPMI containing dil-labeled ac-LDL (25 μg/ml), 10% lipoprotein-deficient serum, and 20% L-Glutamine for 24 h. After cholesterol loading, cells were rinsed with PBS and collected in 2% BSA in PBS. Flow cytometry was performed on a BD Fortessa using FACSDiva software with single stain compensation controls acquired on the same day.

In vivo foam cell formation assay

$Fmr1^{+/+}$ and $Fmr1^{-/-}$ mice were injected with a gain-of-function mutant (D377Y) of proprotein convertase subtilisin kexin 9 (PCSK9)-encoding adeno-associated virus (AAV_mPCSK9) and fed with 16 weeks of WD to induced hypercholesterolemia. $Apoe^{-/-}$ mice were fed with 12 weeks of WD with 4 weeks of AMG-18 (30 mg/kg, once a day) injection during the last 4 weeks of WD. The peritoneal macrophages were collected and assessed for lipid accumulation by Oil-Red O and Hematoxylin staining.

Reverse cholesterol transport (RCT) assay

Preparation of radiolabel cholesterol

Ag-LDL (50 μg/ml, made in house with endotoxin-free LDL isolated from human plasma) and [^{3}H]-cholesterol (5 μCi/ml) were incubated for 1 h at 37°C in a sterile endotoxin free bottle.

RCT assay

$Fmr1^{+/+}$ and $Fmr1^{-/-}$ BMDM were incubated with radiolabeled ag-LDL for 30 h followed by warm HBSS wash and equilibration in 2 mg/ml fatty acid-free BSA overnight. Cells were washed twice in ice cold HBSS and incubated with EDTA (5 mM) for 20 min at 4°C and spun down at 200 *g* for 5 min. Cells were resuspended in ice cold DMEM and injected into C57BL6N mice subcutaneously in the scruff of the neck. Blood was collected at 24 h via the saphenous vein and at 48 h via cardiac puncture of anesthetized mice. Plasma was used for liquid scintillation counting. At 48 h, livers were removed for scintillation counting. Feces were collected over a 48-h period, and total feces radioactivity was measured. All [^{3}H]-tracer measurements are expressed relative to the injected amount.

In vitro and *in vivo* efferocytosis

Induction of apoptosis and labeling of Jurkat cells

Jurkat cells were fluorescently labeled with CellTrace CSFE or Violet (2 μM) in PBS for 20 min. Cells were then washed ones with PBS and seeded in conditioned DMEM medium followed by irradiation under a 254 nm UV lamp for 5 min. Cells were incubated under normal cell culture conditions for 3–4 h. Apoptosis was confirmed by Anexin V^+ staining (minimum 85% Annexin V^+ cells). The apoptotic cells (ACs) were centrifuged at 500 *g* for 5 min and resuspended in conditioned DMEM for experiments.

In vitro efferocytosis

Bone marrow-derived macrophages were plated in six-well dishes at a density of 0.5×10^6 cells per well. CSFE-labeled ACs were incubated with the macrophages for 2–4 min at a 5:1 AC:macrophage ratio followed by washing three times with PBS. Some groups of macrophages were then incubated for another 2 h in normal cell culture media, followed by the addition of Violet-labeled ACs. After 2 h, macrophages were washed three times with PBS to remove unbound ACs, and then the macrophages were fixed with 4% formaldehyde for 20 min, rinsed three times with PBS, blocked by TruStain FcX™ (anti-mouse CD16/32) for 10 min and then stained with PE-F4/80 o/n. The percentage of PE-$F4/80^+$ and $CFSE^+$ double positive cells to total PE-$F4/80^+$ cells was reported as % efferocytosis and PE-$F4/80^+$, $CFSE^+$ and $Violet^+$ triple positive cells to PE-$F4/80^+$ and $CFSE^+$ double positive cells was reported as % continuous efferocytosis.

In vivo efferocytosis

$Fmr1^{+/+}$ or $Fmr1^{-/-}$ mice were fed with WD for 16 weeks and injected with 1×10^6 CFSE-labeled ACs and 1.5 h later subsequently peritoneal lavages were collected and stained for PE-$F4/80^+$ resident macrophages. The percentage of PE-$F4/80^+$ and $CFSE^+$ double

positive cells to total PE-F4/80$^+$ cells was reported as % efferocytosis. Another group of C57BL/6 was injected with AMG-18 (30 mg/kg) or vehicle (DMSO). After 8 h both groups were interperitoneally injected with CFSE-labeled ACs and 1.5 h later peritoneal lavages were collected and cultured for 30 min to allow cells to attach. Macrophages were washed three times with PBS to remove unbound ACs, and then the macrophages were fixed with 4% formaldehyde for 20 min, rinsed three times with PBS, blocked by TruStain FcX™ (anti-mouse CD16/32) for 10 min, and then stained with PE-F4/80 o/n. The percentage of F4/80$^+$ and CFSE$^+$ double positive cells to total F4/80$^+$ cells was reported as % efferocytosis.

En face Oil-Red O staining

Aortas opened longitudinally were rinsed with 60% isopropanol for 1 min, stained with Oil-Red O solution for 20 min, and then distained in 60% isopropanol for 1 min and rinsed in PBS. The lesion area was quantitated as percent of Oil-Red O staining area in total aorta area.

Immunohistochemistry

7-μm-thick aortic root cryosections (from OCT embedded heart tissue) were stained with antibodies for: anti-MOMA-2 (1:500) and anti-α-SMA (1:500) and images were captured with fluorescent microscope. Cryosections were stained with Masson's Trichrome, TUNEL, Hematoxylin and Eosin (H&E) according to manufacturer's instructions. Cryosections were stained with H&E for morphometric lesion analysis. The total lesion area and necrotic area were quantified as previously described from 4 sequential sections (60 μM apart, beginning at the base of the aortic root) as previously described (Çimen *et al*, 2016b). Foam cell area was calculated from Oil-Red O stained 4 sequential sections (60 μM apart, beginning at the base of the aortic root) and collagen content from Masson's Trichrome stained sections using ImageJ as previously described (Çimen *et al*, 2016b).

The fluorescent immunostainings were carried out on cryosections that were fixed in cold acetone for 10 min, blocked in goat serum/BSA/PBS as previously described. All stained sections were mounted with fluoroshield mounting reagent with DAPI. Fluorescent signal calculations: (i) TUNEL staining: the sections were double stained with MOMA-2 to mark the macrophage-enriched area. The Mean Fluorescent Intensity (MFI) corresponding to primary antibody signal was calculated from the MOMA-2-positive area. The background fluorescence of the non-stained area inside the lesion was subtracted from the total MFI corresponding to each signal (ii) α-SMA staining: α-SMA positive area was calculated from the plaque area. The background fluorescence of the non-stained area inside the lesion was subtracted from the total MFI corresponding to each signal. Data were quantified as total MFI signal compared with baseline (Çimen *et al*, 2016b; Tufanli *et al*, 2017).

Apoptosis detection by flow cytometry

Apoptosis was induced after treatments by PA (500 μM) treatment for 12 h. Fc receptors were blocked by pre-incubating cells with 0.25 μg of TruStain FcX™ PLUS (anti-mouse CD16/32) Antibody per 10^6 cells for 5–10 min on ice. Cells were then incubated with PI on ice for 20 min in the dark followed by 2× with 2 ml of cell staining buffer. Cells were resuspended in 500 μl of cell staining buffer and analyzed on a BD Fortessa using FACSDiva software with single stain compensation controls acquired on the same day. Data were analyzed using FlowJo analysis software (FlowJo, LLC).

The paper explained

Problem
A maladaptive immune response to lipid imbalance drives atherosclerosis. Lipid accumulation in plaque-infiltrating macrophages stresses the ER and promotes atherosclerosis progression. Alleviating ER stress by modulating IRE1 reduces atherosclerosis in a murine model. However, whether IRE1 kinase activity contributes to the atherosclerotic process has remained elusive. Targeting chronic ER stress in atherosclerosis is challenging due to the essential cellular homeostatic functions governed by IRE1. A meticulous exploration of IRE1 kinase function in macrophages and mechanistically authenticated IRE1 kinase substrate(s) can develop into novel therapeutic approaches in atherosclerosis.

Results
Here, we identify FMRP as a kinase substrate of IRE1. We show that IRE1 kinase activation leads to FMRP phosphorylation and suppression of macrophage cholesterol efflux and apoptotic cell clearance in a mouse model of atherosclerosis.

Impact
Altogether, our findings provide mechanistic insight into the translational regulation of cholesterol efflux and efferocytosis in ER-stressed macrophages and highlight IRE1 kinase domain and its effector, FMRP, as novel therapeutic targets for atherosclerosis.

Flow cytometric analysis of peripheral blood

100 μl of blood was collected in EDTA-coated tubes and red blood cells were removed by incubation (3×) in Ammonium-Chloride-Potassium (ACK, Thermo Fisher A1049201) solution for 5 min at room temperature. Peripheral blood mononuclear cells were then resuspended in FACS buffers (2% BSA in PBS) and incubated for 20 min on ice with the following antibodies: anti-CD45-Pac. Blue (clone 30-F11), CD3e-PE (Clone 145-2C11), CD11b-APC (Clone M1/70), CD19-BV650 (Clone 6D5), Ly6C-PE/Dazzle (Clone HK1.4), and Ly6G-PerCP Cy5.5 (1A8) in 1:100 dilution ratio. Stained samples were washed once and resuspended in FACS buffer containing DAPI (4 μg/ml). Flow cytometry was performed on a BD Fortessa using FACSDiva software with single stain compensation controls acquired on the same day. Data were analyzed using FlowJo analysis software (FlowJo, LLC). All antibodies were purchased from Biolegend (San Diego, CA) and used at the manufacturer's recommended concentrations.

Plasma lipids and lipoprotein analysis

Plasma was analyzed by FPLC in the Department of Internal Medicine/Lipid Science, Wake Forest University School of Medicine Winston-Salem, NC 27019 as described (Çimen *et al*, 2016b). The total cholesterol and triglyceride measurement were performed using WAKO Cholesterol E kit according to the manufacturer's instructions.

Statistics

Results are reported as mean ± SEM and statistical significance was determined with Unpaired *t*-test with Welch's or Mann–Whitney correction test by GraphPad Software, LLC.

Data availability

All data are available in the main text or the supplementary materials. Research materials used in the article can be requested from authors. The mass spectrometry proteomics data have been deposited to the ProteomeXchange Consortium (Deutsch *et al*, 2020) via the PRIDE (Perez-Riverol *et al*, 2016, 2019) partner repository with the dataset identifier PXD030594 (http://www.ebi.ac.uk/pride/archive/projects/PXD030594).

Expanded View for this article is available online.

Acknowledgements

We express our appreciation to Jennifer C. Darnell (The Rockefeller University, New York) for providing and guiding with Fmr1 plasmid and to Roberta Gottlieb and Juliana Germano (Cedars-Sinai Medical Center) for their guidance with polysome profiling. *This study was funded by the following:* National Institutes of Health grant R01HL152156 (EE), Cedars-Sinai Medical Center Internal Support (EE), National Institutes of Health grant R01GM32384 (PW), Investigator of the Howar Hughes Medical Institute (PW), National Institutes of Health grant P41GM103533 (JRY), Vanier Canada Graduate Scholarship (SR), Canadian Institutes for Health Research PJT-391187 (MO).

Author contributions

Zehra Yildirim: Data curation; Formal analysis; Validation; Investigation; Visualization; Methodology; Writing—original draft; Writing—review & editing. **Sabyasachi Baboo:** Formal analysis; Investigation; Methodology; Writing—review & editing. **Syed Muhammad Hamid:** Formal analysis; Investigation; Methodology. **Asli Ekin Dogan:** Formal analysis; Investigation; Visualization; Methodology. **Ozlem Tufanli:** Formal analysis; Investigation; Methodology. **Sabrina Robichaud:** Formal analysis; Investigation; Methodology. **Christina Emerton:** Formal analysis; Investigation; Methodology. **Jolene K Diedrich:** Formal analysis; Investigation; Methodology. **Hasan Vatandaslar:** Formal analysis; Investigation; Methodology. **Fotis Nikolos:** Formal analysis; Investigation; Methodology. **Yanghong Gu:** Investigation; Methodology. **Takao Iwawaki:** Methodology. **Elizabeth J Tarling:** Formal analysis; Supervision; Funding acquisition; Investigation; Methodology; Writing—review & editing. **Mireille Ouimet:** Formal analysis; Supervision; Investigation; Methodology; Writing—review & editing. **David Nelson:** Formal analysis; Supervision; Investigation; Methodology; Writing—review & editing. **John R Yates III:** Data curation; Formal analysis; Supervision; Investigation; Writing—review & editing. **Peter Walter:** Formal analysis; Investigation; Writing—review & editing. **Ebru Erbay:** Conceptualization; Formal analysis; Supervision; Funding acquisition; Investigation; Writing—original draft; Project administration; Writing—review & editing.

Disclosure and competing interests statement

PW is an inventor on U.S. Patent 9708247 held by the Regents of the University of California that describes ISRIB and its analogs. Rights to the invention have been licensed by UCSF to Calico. EE, SMH, OT, and PW will become employees of Altos Labs. All other authors declare that they have no competing interests.

References

Acosta-Alvear D, Karagöz GE, Fröhlich F, Li H, Walther TC, Walter P (2018) The unfolded protein response and endoplasmic reticulum protein targeting machineries converge on the stress sensor IRE1. *Elife* 7: e43036

Ascano M, Mukherjee N, Bandaru P, Miller JB, Nusbaum JD, Corcoran DL, Langlois C, Munschauer M, Dewell S, Hafner M *et al* (2012) FMRP targets distinct mRNA sequence elements to regulate protein expression. *Nature* 492: 382 – 386

Baboo S, Diedrich JK, Martínez-Bartolomé S, Wang X, Schiffner T, Groschel B, Schief WR, Paulson JC, Yates JR (2021) DeGlyPHER: an ultrasensitive method for the analysis of viral spike N-glycoforms. *Anal Chem* 93: 13651 – 13657

Bagni C, Tassone F, Neri G, Hagerman R (2012) Fragile X syndrome: causes, diagnosis, mechanisms, and therapeutics. *J Clin Invest* 122: 4314 – 4322

Bartley CM, O'Keefe RA, Bordey A (2014) FMRP S499 is phosphorylated independent of mTORC1-S6K1 activity. *PLoS One* 9: e96956

Bartley CM, O'Keefe RA, Blice-Baum A, Mihailescu MR, Gong X, Miyares L, Karaca E, Bordey A (2016) Mammalian FMRP S499 is phosphorylated by CK2 and promotes secondary phosphorylation of FMRP. *eNeuro* 3: ENEURO.0092-16.2016

Beausoleil SA, Villén J, Gerber SA, Rush J, Gygi SP (2006) A probability-based approach for high-throughput protein phosphorylation analysis and site localization. *Nat Biotechnol* 24: 1285 – 1292

Berry-Kravis E, Levin R, Shah H, Mathur S, Darnell JC, Ouyang B (2015) Cholesterol levels in fragile X syndrome. *Am J Med Genet A* 167a: 379 – 384

Borradaile NM, Han X, Harp JD, Gale SE, Ory DS, Schaffer JE (2006) Disruption of endoplasmic reticulum structure and integrity in lipotoxic cell death. *J Lipid Res* 47: 2726 – 2737

Buchan JR, Parker R (2009) Eukaryotic stress granules: the ins and outs of translation. *Mol Cell* 36: 932 – 941

Carotti S, Zingariello M, Francesconi M, D'Andrea L, Latasa MU, Colyn L, Fernandez-Barrena MG, Flammia RS, Falchi M, Righi D *et al* (2021) Fragile X mental retardation protein in intrahepatic cholangiocarcinoma: regulating the cancer cell behavior plasticity at the leading edge. *Oncogene* 40: 4033 – 4049

Ceman S, O'Donnell WT, Reed M, Patton S, Pohl J, Warren ST (2003) Phosphorylation influences the translation state of FMRP-associated polyribosomes. *Hum Mol Genet* 12: 3295 – 3305

Chen E, Sharma MR, Shi X, Agrawal RK, Joseph S (2014) Fragile X mental retardation protein regulates translation by binding directly to the ribosome. *Mol Cell* 54: 407 – 417

Chiu DS, Oram JF, LeBoeuf RC, Alpers CE, O'Brien KD (1997) High-density lipoprotein-binding protein (HBP)/vigilin is expressed in human atherosclerotic lesions and colocalizes with apolipoprotein E. *Arterioscler Thromb Vasc Biol* 17: 2350 – 2358

Çimen I, Kocatürk B, Koyuncu S, Tufanlı Ö, Onat UI, Yıldırım AD, Apaydın O, Demirsoy Ş, Aykut ZG, Nguyen UT *et al* (2016a) Prevention of atherosclerosis by bioactive palmitoleate through suppression of organelle stress and inflammasome activation. *Sci Transl Med* 8: 358ra126

Çimen I, Kocatürk B, Koyuncu S, Tufanlı Ö, Onat UI, Yıldırım AD, Apaydın O, Demirsoy Ş, Aykut ZG, Nguyen UT *et al* (2016b) Prevention of atherosclerosis by bioactive palmitoleate through suppression of organelle stress and inflammasome activation. *Sci Transl Med* 8: 358ra126

Cloots E, Simpson MS, De Nolf C, Lencer WI, Janssens S, Grey MJ (2021) Evolution and function of the epithelial cell-specific ER stress sensor IRE1β. *Mucosal Immunol* 14: 1235 – 1246

Coffee Jr RL, Williamson AJ, Adkins CM, Gray MC, Page TL, Broadie K (2012) *In vivo* neuronal function of the fragile X mental retardation protein is regulated by phosphorylation. *Hum Mol Genet* 21: 900 – 915

Costet P, Luo Y, Wang N, Tall AR (2000) Sterol-dependent transactivation of the ABC1 promoter by the liver X receptor/retinoid X receptor. *J Biol Chem* 275: 28240 – 28245

Darnell J, Van Driesche S, Zhang C, Hung K, Mele A, Fraser C, Stone E, Chen C, Fak J, Chi S *et al* (2011) FMRP stalls ribosomal translocation on mRNAs linked to synaptic function and autism. *Cell* 146: 247 – 261

Davignon J, Cohn JS, Mabile L, Bernier L (1999) Apolipoprotein E and atherosclerosis: insight from animal and human studies. *Clin Chim Acta* 286: 115 – 143

Davis JK, Broadie K (2017) Multifarious functions of the fragile X mental retardation protein. *Trends Genet* 33: 703 – 714

Deutsch EW, Bandeira N, Sharma V, Perez-Riverol Y, Carver JJ, Kundu DJ, García-Seisdedos D, Jarnuczak AF, Hewapathirana S, Pullman BS *et al* (2020) The ProteomeXchange consortium in 2020: enabling 'big data' approaches in proteomics. *Nucleic Acids Res* 48: D1145 – d1152

Edbauer D, Neilson JR, Foster KA, Wang CF, Seeburg DP, Batterton MN, Tada T, Dolan BM, Sharp PA, Sheng M (2010) Regulation of synaptic structure and function by FMRP-associated microRNAs miR-125b and miR-132. *Neuron* 65: 373 – 384

Erbay E, Babaev VR, Mayers JR, Makowski L, Charles KN, Snitow ME, Fazio S, Wiest MM, Watkins SM, Linton MF *et al* (2009) Reducing endoplasmic reticulum stress through a macrophage lipid chaperone alleviates atherosclerosis. *Nat Med* 15: 1383 – 1391

Fu S, Yang L, Li P, Hofmann O, Dicker L, Hide W, Lin X, Watkins SM, Ivanov AR, Hotamisligil GS (2011) Aberrant lipid metabolism disrupts calcium homeostasis causing liver endoplasmic reticulum stress in obesity. *Nature* 473: 528 – 531

Ghosh R, Wang L, Wang E, Perera B, Igbaria A, Morita S, Prado K, Thamsen M, Caswell D, Macias H *et al* (2014) Allosteric inhibition of the IRE1α RNase preserves cell viability and function during endoplasmic reticulum stress. *Cell* 158: 534 – 548

Guo Y, Yuan W, Yu B, Kuai R, Hu W, Morin EE, Garcia-Barrio MT, Zhang J, Moon JJ, Schwendeman A *et al* (2018) Synthetic high-density lipoprotein-mediated targeted delivery of liver X receptors agonist promotes atherosclerosis regression. *EBioMedicine* 28: 225 – 233

Haneklaus M, O'Neil JD, Clark AR, Masters SL, O'Neill LAJ (2017) The RNA-binding protein Tristetraprolin (TTP) is a critical negative regulator of the NLRP3 inflammasome. *J Biol Chem* 292: 6869 – 6881

Hansmeier N, Buttigieg J, Kumar P, Pelle S, Choi KY, Kopriva D, Chao TC (2018) Identification of mature atherosclerotic plaque proteome signatures using data-independent acquisition mass spectrometry. *J Proteome Res* 17: 164 – 176

Harnoss JM, Le Thomas A, Shemorry A, Marsters SA, Lawrence DA, Lu M, Chen Y-C, Qing J, Totpal K, Kan D *et al* (2019) Disruption of IRE1α through its kinase domain attenuates multiple myeloma. *Proc Natl Acad Sci USA* 116: 16420 – 16429

He L, Diedrich J, Chu YY, Yates 3rd JR (2015) Extracting accurate precursor information for tandem mass spectra by RawConverter. *Anal Chem* 87: 11361 – 11367

Hersh JH, Saul RA (2011) Health supervision for children with fragile X syndrome. *Pediatrics* 127: 994 – 1006

Hotamisligil GS (2017) Inflammation, metaflammation and immunometabolic disorders. *Nat Rev* 542: 177 – 185

Hunter J, Rivero-Arias O, Angelov A, Kim E, Fotheringham I, Leal J (2014) Epidemiology of fragile X syndrome: a systematic review and meta-analysis. *Am J Med Genet A* 164a: 1648 – 1658

Iwawaki T, Akai R, Yamanaka S, Kohno K (2009) Function of IRE1 alpha in the placenta is essential for placental development and embryonic viability. *Proc Natl Acad Sci USA* 106: 16657 – 16662

Joyce CW, Amar MJA, Lambert G, Vaisman BL, Paigen B, Najib-Fruchart J, Hoyt RF, Neufeld ED, Remaley AT, Fredrickson DS *et al* (2002) The ATP binding cassette transporter A1 (ABCA1) modulates the development of aortic atherosclerosis in C57BL/6 and apoE-knockout mice. *Proc Natl Acad Sci USA* 99: 407 – 412

Kang JG, Amar MJ, Remaley AT, Kwon J, Blackshear PJ, Wang PY, Hwang PM (2011) Zinc finger protein tristetraprolin interacts with CCL3 mRNA and regulates tissue inflammation. *J Immunol* 187: 2696 – 2701

Khera AV, Cuchel M, de la Llera-Moya M, Rodrigues A, Burke MF, Jafri K, French BC, Phillips JA, Mucksavage ML, Wilensky RL *et al* (2011) Cholesterol efflux capacity, high-density lipoprotein function, and atherosclerosis. *N Engl J Med* 364: 127 – 135

Kim J, Yun EY, Park SW, Goo TW, Seo M (2016) Allomyrina dichotoma larvae regulate food intake and body weight in high fat diet-induced obese mice through mTOR and Mapk signaling pathways. *Nutrients* 8: 100

Klucken J, Buchler C, Orso E, Kaminski WE, Porsch-Ozcurumez M, Liebisch G, Kapinsky M, Diederich W, Drobnik W, Dean M *et al* (2000) ABCG1 (ABC8), the human homolog of the *Drosophila* white gene, is a regulator of macrophage cholesterol and phospholipid transport. *Proc Natl Acad Sci USA* 97: 817 – 822

Kojima Y, Weissman IL, Leeper NJ (2017) The role of efferocytosis in atherosclerosis. *Circulation* 135: 476 – 489

Leboucher A, Bermudez-Martin P, Mouska X, Amri EZ, Pisani DF, Davidovic L (2019a) Fmr1-deficiency impacts body composition, skeleton, and bone microstructure in a mouse model of fragile X syndrome. *Front Endocrinol* 10: 678

Leboucher A, Pisani DF, Martinez-Gili L, Chilloux J, Bermudez-Martin P, Van Dijck A, Ganief T, Macek B, Becker JAJ, Le Merrer J *et al* (2019b) The translational regulator FMRP controls lipid and glucose metabolism in mice and humans. *Mol Metab* 21: 22 – 35

Li J, Tumanut C, Gavigan J-A, Huang W-J, Hampton E, Tumanut R, Suen K, Trauger J, Spraggon G, Lesley S *et al* (2007) Secreted PCSK9 promotes LDL receptor degradation independently of proteolytic activity. *Biochem J* 406: 203 – 207

Li Y, Ge M, Ciani L, Kuriakose G, Westover EJ, Dura M, Covey DF, Freed JH, Maxfield FR, Lytton J *et al* (2004) Enrichment of endoplasmic reticulum with cholesterol inhibits sarcoplasmic-endoplasmic reticulum calcium ATPase-2b activity in parallel with increased order of membrane lipids: implications for depletion of endoplasmic reticulum calcium stores and apoptosis in cholesterol-loaded macrophages. *J Biol Chem* 279: 37030 – 37039

Lisik MZ, Gutmajster E, Sieroń AL (2016) Low levels of HDL in fragile X syndrome patients. *Lipids* 51: 189 – 192

Lumaban JG, Nelson DL (2015) The Fragile X proteins Fmrp and Fxr2p cooperate to regulate glucose metabolism in mice. *Hum Mol Genet* 24: 2175 – 2184

Mobin MB, Gerstberger S, Teupser D, Campana B, Charisse K, Heim MH, Manoharan M, Tuschl T, Stoffel M (2016) The RNA-binding protein vigilin regulates VLDL secretion through modulation of Apob mRNA translation. *Nat Commun* 7: 12848

Moore KJ, Sheedy FJ, Fisher EA (2013) Macrophages in atherosclerosis: a dynamic balance. *Nat Rev Immunol* 13: 709 – 721

Napoli I, Mercaldo V, Boyl PP, Eleuteri B, Zalfa F, De Rubeis S, Di Marino D, Mohr E, Massimi M, Falconi M *et al* (2008) The fragile X syndrome protein represses activity-dependent translation through CYFIP1, a new 4E-BP. *Cell* 134: 1042 – 1054

Narayanan U, Nalavadi V, Nakamoto M, Thomas G, Ceman S, Bassell GJ, Warren ST (2008) S6K1 phosphorylates and regulates fragile X mental retardation protein (FMRP) with the neuronal protein synthesis-dependent mammalian target of rapamycin (mTOR) signaling cascade. *J Biol Chem* 283: 18478 – 18482

Niere F, Wilkerson JR, Huber KM (2012) Evidence for a fragile X mental retardation protein-mediated translational switch in metabotropic glutamate receptor-triggered Arc translation and long-term depression. *J Neurosci* 32: 5924 – 5936

Onat UI, Yildirim AD, Tufanli Ö, Çimen I, Kocatürk B, Veli Z, Hamid SM, Shimada K, Chen S, Sin J *et al* (2019) Intercepting the lipid-induced integrated stress response reduces atherosclerosis. *J Am Coll Cardiol* 73: 1149 – 1169

Oram JF, Lawn RM, Garvin MR, Wade DP (2000) ABCA1 is the cAMP-inducible apolipoprotein receptor that mediates cholesterol secretion from macrophages. *J Biol Chem* 275: 34508 – 34511

Papandreou I, Denko NC, Olson M, Van Melckebeke H, Lust S, Tam A, Solow-Cordero DE, Bouley DM, Offner F, Niwa M *et al* (2011) Identification of an Ire1alpha endonuclease specific inhibitor with cytotoxic activity against human multiple myeloma. *Blood* 117: 1311 – 1314

Peled M, Nishi H, Weinstock A, Barrett TJ, Zhou F, Quezada A, Fisher EA (2017) A wild-type mouse-based model for the regression of inflammation in atherosclerosis. *PLoS One* 12: e0173975

Peng J, Elias JE, Thoreen CC, Licklider LJ, Gygi SP (2003) Evaluation of multidimensional chromatography coupled with tandem mass spectrometry (LC/LC-MS/MS) for large-scale protein analysis: the yeast proteome. *J Proteome Res* 2: 43 – 50

Perez-Riverol Y, Csordas A, Bai J, Bernal-Llinares M, Hewapathirana S, Kundu DJ, Inuganti A, Griss J, Mayer G, Eisenacher M *et al* (2019) The PRIDE database and related tools and resources in 2019: improving support for quantification data. *Nucleic Acids Res* 47: D442 – d450

Perez-Riverol Y, Xu Q-W, Wang R, Uszkoreit J, Griss J, Sanchez A, Reisinger F, Csordas A, Tement T, del-Toro N *et al* (2016) PRIDE inspector toolsuite: moving toward a universal visualization tool for proteomics data standard formats and quality assessment of ProteomeXchange datasets. *Mol Cell Proteomics* 15: 305 – 317

Prieto M, Folci A, Martin S (2020) Post-translational modifications of the Fragile X mental retardation protein in neuronal function and dysfunction. *Mol Psychiatry* 25: 1688 – 1703

Ramírez CM, Lin CS, Abdelmohsen K, Goedeke L, Yoon J-H, Madrigal-Matute J, Martin-Ventura JL, Vo DT, Uren PJ, Penalva LO *et al* (2014) RNA binding protein HuR regulates the expression of ABCA1. *J Lipid Res* 55: 1066 – 1076

Randolph GJ (2014) Mechanisms that regulate macrophage burden in atherosclerosis. *Circ Res* 114: 1757 – 1771

Reynolds CD, Smith GD, Jefferson TS, Lugo JN (2015) Comparison of equivalence between two commercially available S499-phosphorylated FMRP antibodies in mice. *PLoS One* 10: e0143134

Robblee MM, Kim CC, Porter Abate J, Valdearcos M, Sandlund KL, Shenoy MK, Volmer R, Iwawaki T, Koliwad SK (2016) Saturated fatty acids engage an IRE1α-dependent pathway to activate the NLRP3 inflammasome in myeloid cells. *Cell Rep* 14: 2611 – 2623

Rocha VZ, Libby P (2009) Obesity, inflammation, and atherosclerosis. *Nat Rev Cardiol* 6: 399 – 409

Seimon TA, Nadolski MJ, Liao X, Magallon J, Nguyen M, Feric NT, Koschinsky ML, Harkewicz R, Witztum JL, Tsimikas S *et al* (2010) Atherogenic lipids and lipoproteins trigger CD36-TLR2-dependent apoptosis in macrophages undergoing endoplasmic reticulum stress. *Cell Metab* 12: 467 – 482

Sethna F, Moon C, Wang H (2014) From FMRP function to potential therapies for fragile X syndrome. *Neurochem Res* 39: 1016 – 1031

Stastna M, Thomas A, Germano J, Pourpirali S, Van Eyk JE, Gottlieb RA (2018) Dynamic proteomic and miRNA analysis of polysomes from isolated mouse heart after langendorff perfusion. *J vis Exp* 138: 58079

Sukhorukov VN, Khotina VA, Bagheri Ekta M, Ivanova EA, Sobenin IA, Orekhov AN (2020) Endoplasmic reticulum stress in macrophages: the vicious circle of lipid accumulation and pro-inflammatory response. *Biomedicines* 8: 210

Tabas I (2010) The role of endoplasmic reticulum stress in the progression of atherosclerosis. *Circ Res* 107: 839 – 850

Tabb DL, McDonald WH, Yates 3rd JR (2002) DTASelect and contrast: tools for assembling and comparing protein identifications from shotgun proteomics. *J Proteome Res* 1: 21 – 26

Tall AR, Yvan-Charvet L (2015) Cholesterol, inflammation and innate immunity. *Nat Rev Immunol* 15: 104 – 116

Tsang B, Arsenault J, Vernon RM, Lin H, Sonenberg N, Wang LY, Bah A, Forman-Kay JD (2019) Phosphoregulated FMRP phase separation models activity-dependent translation through bidirectional control of mRNA granule formation. *Proc Natl Acad Sci USA* 116: 4218 – 4227

Tsimikas S, Miyanohara A, Hartvigsen K, Merki E, Shaw PX, Chou M-Y, Pattison J, Torzewski M, Sollors J, Friedmann T *et al* (2011) Human oxidation-specific antibodies reduce foam cell formation and atherosclerosis progression. *J Am Coll Cardiol* 58: 1715 – 1727

Tufanli O, Telkoparan Akillilar P, Acosta-Alvear D, Kocaturk B, Onat UI, Hamid SM, Çimen I, Walter P, Weber C, Erbay E (2017) Targeting IRE1 with small molecules counteracts progression of atherosclerosis. *Proc Natl Acad Sci USA* 114: E1395 – e1404

Tumurkhuu G, Dagvadorj J, Porritt RA, Crother TR, Shimada K, Tarling EJ, Erbay E, Arditi M, Chen S (2018) Chlamydia pneumoniae hijacks a host autoregulatory IL-1β loop to drive foam cell formation and accelerate atherosclerosis. *Cell Metab* 28: 432 – 448.e434

Tuomisto TT, Korkeela A, Rutanen J, Viita H, Bräsen JH, Riekkinen MS, Rissanen TT, Karkola K, Kiraly Z, Kölble K *et al* (2003) Gene expression in macrophage-rich inflammatory cell infiltrates in human atherosclerotic lesions as studied by laser microdissection and DNA array: overexpression of HMG-CoA reductase, colony stimulating factor receptors, CD11A/CD18 integrins, and interleukin receptors. *Arterioscler Thromb Vasc Biol* 23: 2235 – 2240

Volmer R, van der Ploeg K, Ron D (2013) Membrane lipid saturation activates endoplasmic reticulum unfolded protein response transducers through their transmembrane domains. *Proc Natl Acad Sci USA* 110: 4628 – 4633

Walter P, Ron D (2011) The unfolded protein response: from stress pathway to homeostatic regulation. *Science* 334: 1081 – 1086

Wang Y, Zhang B, Wang J, Wu H, Xu S, Zhang J, Wang L (2021) Discovery of LAMP-2A as potential biomarkers for glioblastoma development by modulating apoptosis through N-CoR degradation. *Cell Commun Signal* 19: 40

Weber C, Noels H (2011) Atherosclerosis: current pathogenesis and therapeutic options. *Nat Med* 17: 1410 – 1422

Wessel D, Flügge UI (1984) A method for the quantitative recovery of protein in dilute solution in the presence of detergents and lipids. *Anal Biochem* 138: 141 – 143

Westerterp M, Fotakis P, Ouimet M, Bochem AE, Zhang H, Molusky MM, Wang W, Abramowicz S, la Bastide-van Gemert S, Wang N *et al* (2018) Cholesterol efflux pathways suppress inflammasome activation, NETosis, and atherogenesis. *Circulation* 138: 898 – 912

Westerterp M, Murphy AJ, Wang MI, Pagler TA, Vengrenyuk Y, Kappus MS, Gorman DJ, Nagareddy PR, Zhu X, Abramowicz S *et al* (2013) Deficiency of ATP-binding cassette transporters A1 and G1 in macrophages increases

inflammation and accelerates atherosclerosis in mice. *Circ Res* 112: 1456 – 1465

Xu T, Park SK, Venable JD, Wohlschlegel JA, Diedrich JK, Cociorva D, Lu B, Liao L, Hewel J, Han X *et al* (2015) ProLuCID: An improved SEQUEST-like algorithm with enhanced sensitivity and specificity. *J Proteomics* 129: 16 – 24

Yurdagul Jr A, Doran AC, Cai B, Fredman G, Tabas IA (2017) Mechanisms and consequences of defective efferocytosis in atherosclerosis. *Front Cardiovasc Med* 4: 86

Zhang H, Taylor WR, Joseph G, Caracciolo V, Gonzales DM, Sidell N, Seli E, Blackshear PJ, Kallen CB (2013) mRNA-binding protein ZFP36 is expressed in atherosclerotic lesions and reduces inflammation in aortic endothelial cells. *Arterioscler Thromb Vasc Biol* 33: 1212 – 1220

Zhang X, Goncalves R, Mosser DM (2008) The isolation and characterization of murine macrophages. *Curr Protoc Immunol Chapter* 14: Unit 14.11

Zhang Y, O'Connor JP, Siomi MC, Srinivasan S, Dutra A, Nussbaum RL, Dreyfuss G (1995) The fragile X mental retardation syndrome protein interacts with novel homologs FXR1 and FXR2. *Embo J* 14: 5358 – 5366

Zhou AX, Tabas I (2013) The UPR in atherosclerosis. *Semin Immunopathol* 35: 321 – 332

Zimmer S, Grebe A, Bakke SS, Bode N, Halvorsen B, Ulas T, Skjelland M, De Nardo D, Labzin LI, Kerksiek A *et al* (2016) Cyclodextrin promotes atherosclerosis regression via macrophage reprogramming. *Sci Transl Med* 8: 333ra350

Original Article

MOLECULAR METABOLISM

Double bond configuration of palmitoleate is critical for atheroprotection

Ismail Cimen [1], Zehra Yildirim [2,3,4,5], Asli Ekin Dogan [2,3,4,5], Asli Dilber Yildirim [2,3,4,5], Ozlem Tufanli [6], Umut Inci Onat [2,3], UyenThao Nguyen [7], Steven M. Watkins [8], Christian Weber [1,9], Ebru Erbay [2,3,4,5,10,*]

ABSTRACT

Objective: Saturated and trans fat consumption is associated with increased cardiovascular disease (CVD) risk. Current dietary guidelines recommend low fat and significantly reduced trans fat intake. Full fat dairy can worsen dyslipidemia, but recent epidemiological studies show full-fat dairy consumption may reduce diabetes and CVD risk. This dairy paradox prompted a reassessment of the dietary guidelines. The beneficial metabolic effects in dairy have been claimed for a ruminant-derived, trans fatty acid, trans-C16:1n-7 or trans-palmitoleate (trans-PAO). A close relative, cis-PAO, is produced by *de novo* lipogenesis and mediates inter-organ crosstalk, improving insulin-sensitivity and alleviating atherosclerosis in mice. These findings suggest trans-PAO may be a useful substitute for full fat dairy, but a metabolic function for trans-PAO has not been shown to date.

Methods: Using lipidomics, we directly investigated trans-PAO's impact on plasma and tissue lipid profiles in a hypercholesterolemic atherosclerosis mouse model. Furthermore, we investigated trans-PAO's impact on hyperlipidemia-induced inflammation and atherosclerosis progression in these mice.

Results: Oral trans-PAO supplementation led to significant incorporation of trans-PAO into major lipid species in plasma and tissues. Unlike cis-PAO, however, trans-PAO did not prevent organelle stress and inflammation in macrophages or atherosclerosis progression in mice.

Conclusions: A significant, inverse correlation between circulating trans-PAO levels and diabetes incidence and cardiovascular mortality has been reported. Our findings show that trans-PAO can incorporate efficiently into the same pools that its cis counterpart is known to incorporate into. However, we found trans-PAO's anti-inflammatory and anti-atherosclerotic effects are muted due to its different structure from cis-PAO.

Keywords Lipid-induced inflammation; Lipokines; Palmitoleate; Ruminant trans-fatty acids; Organelle stress; Inflammasome; Atherosclerosis

1. INTRODUCTION

Diet is a significant modifier of cardiovascular (CVD) and diabetes risk. The health effects of dietary fats are researched extensively and findings from these studies have been shaping the dietary guidelines. Compelling evidence suggests that a significant reduction in CVD risk can be achieved by replacing saturated fatty acids (SFA) with mono- or poly-unsaturated fatty acids (MUFA or PUFA, respectively) [1]. Moreover, studies consistently associate industrial trans fatty acids (TFA), fatty acid isoforms bearing a trans configuration at the double bond, with a higher CVD risk [2–4]. Industrial TFA has also been linked to other complex diseases like diabetes, fatty liver disease, stroke, Alzheimer's disease, and cancer [3,5–9]. These negative associations have led to the assumption that TFA intake, regardless of its source and type, increases disease risk. However, different TFA subtypes or isomers can be obtained from a variety of dietary sources and they could have divergent metabolic effects [10]. One example is *trans*-palmitoleate (*trans*-16:1n-7 or trans-PAO), a naturally-occurring TFA in full fat dairy, which has been associated with beneficial metabolic effects [11–13]. Increased circulating ruminant-derived trans-PAO levels mostly reflect dairy fat consumption, which has been associated with lower blood glucose levels, increased insulin sensitivity and overall a lower risk of type II diabetes [13,14]. More recently, trans-PAO was associated with improved lipid profiles and lower CVD mortality and sudden cardiac death risk [4]. However, the notion that trans-PAO represents a beneficial type of trans-fat remains highly controversial and requires direct experimental evidence [11–13,15–17]. While trans-PAO's role in CVD is debated, its cis isoform has been associated with beneficial metabolic changes in humans and these metabolic benefits have been experimentally demonstrated in mice

[1]Institute for Cardiovascular Prevention, LMU Munich, German Cardiovascular Research Centre (DZHK), Partner Site Munich Heart Alliance Munich, 80336, Germany [2]Department of Molecular Biology and Genetics, Bilkent University, Ankara, 06800, Turkey [3]National Nanotechnology Center, Bilkent University, Ankara, 06800, Turkey [4]Department of Biomedical Sciences, Cedars-Sinai Medical Center, Los Angeles, CA, 90048, USA [5]Smidt Heart Institute, Cedars-Sinai Medical Center, Los Angeles, CA, 90048, USA [6]New York University, Lagone Medical Center, New York, NY 10016, USA [7]Metabolon, Morrisville, NC, 27560, USA [8]Verso Biosciences, San Francisco, CA, 94124, USA [9]Department of Biochemistry, Cardiovascular Research Institute Maastricht (CARIM), Maastricht University, Maastricht, the Netherlands [10]David Geffen School of Medicine, University of California, Los Angeles, CA, 90095, USA

*Corresponding author. Cedars Sinai Medical Center, Department of Medicine, Heart Institute & Department of Biomedical Sciences, 127 S. San Vincente Boulevard, Advanced Health Sciences Pavillion, A9104, Los Angeles, CA, 90048, USA. E-mail: ebru.erbay@cshs.org (E. Erbay).

Received June 14, 2019 • Revision received July 26, 2019 • Accepted August 2, 2019 • Available online 7 August 2019

https://doi.org/10.1016/j.molmet.2019.08.004

[18–24]. Circulating cis-PAO produced by *de novo* lipogenesis (DNL) from the adipose has been shown to mediate inter-organ communication [25]. The beneficial metabolic effects of cis-PAO in high fat-fed mice include increased insulin sensitivity, suppressed hepatic gluconeogenesis, reduced vascular inflammation and atherosclerosis [12,19,20,22,23,25]. It remains to be demonstrated that the two isomers of PAO impact immune-metabolic homeostasis and atherosclerosis in the same way.

The primary impact of cis-PAO on atherosclerosis appears to be mediated by its anti-inflammatory actions and especially through preventing inflammasome activation [23]. Driven by hyperlipidemia, atherosclerosis is a chronic inflammatory disease impacting the blood vessel walls [26,27]. Activation of the Nod-like receptor family, pyrin domain-containing 3 (NLRP3) inflammasome complex in macrophages by cholesterol crystals or saturated fatty acids (SFA), which can be found in these lesions, plays a crucial role in driving a chronic inflammatory response and atherogenesis [28–30]. The inflammasome complex consists of NACHT, LRR, and PYD domains–containing protein (NALP), apoptosis-associated speck-like protein containing a caspase-1 recruitment domain (ASC), and caspase-1. Their assembly results in proteolytic cleavage of dormant pro-caspase-1 into active caspase-1, which transforms the precursors forms of IL-1β and IL-18 into mature and bioactive cytokines [23,29,31]. These cytokines can recruit innate immune cells to the site of infection and modulate adaptive immune cells to drive atherogenesis [31]. Cis-PAO can effectively reduce IL-1β and IL-18 in hyperlipidemic mice [23].

Inflammasome activation can occur in response to organelle stress such as endoplasmic reticulum (ER) and mitochondrial stress. ER stress can be triggered by disruption of ER functions (such as protein folding and calcium homeostasis), but also by excessive lipid flux (such as cholesterol or saturated fatty acids) into cells [32–35]. ER stress activates the inflammasome through various mechanisms including mobilization of intracellular calcium and the release of reactive oxygen species [23,36]. Moreover, ER stress propagates mitochondrial oxidative stress and induces mitochondrial ROS (mtROS) production. In most metabolic stress conditions, ER and mitochondrial oxidative stress are intertwined and propagate each other [32,37]. Just like inflammasome activation, stress in these two organelles plays a causal role in atherosclerosis [23,29,30,36,38,39].

In response to ER stress, an elaborate, adaptive signaling is initiated from ER membranes, known as the Unfolded Protein Response (UPR), to re-establish homeostasis in the ER. Three UPR signaling branches are initiated by the ER stress sensors known as inositol-requiring enzyme-1 (IRE1), protein kinase RNA-like endoplasmic reticulum kinase (PERK) and activating transcription factor-6 (ATF6). UPR initiates a gene expression program that up-regulates the expression of chaperones and components of the ER-associated degradation pathway to promote protein folding or to remove misfolded proteins, respectively. Moreover, general protein translation is attenuated to reduce the protein load in the ER lumen [40,41]. In addition to proteotoxic stress, high fat diets and hyperlipidemia can induce ER stress and activate of UPR pathways *in vivo* in mice and humans, playing a role in the pathogenesis of many complex, inflammatory and metabolic diseases [42–44]. Whereas in proteotoxic conditions, unfolded proteins activate IRE1 and PERK by recruiting away the glucose-regulated protein 78 (GRP78) from binding these UPR stress sensor's luminal domain, in lipotoxic conditions, the increased lipid levels are instead sensed by their transmembrane domains, inducing IRE1 and PERK oligomerization and activation through auto-phosphorylation [44–48]. Studies show that inhibition of UPR signaling arms initiated by either IRE1 or PERK prevents inflammasome activation and atherosclerosis in mice [36,49,50]. IRE1 and PERK arms have been shown to contribute to inflammasome activation by propagating mitochondrial oxidative stress and mtROS release [36,49]. Oral supplementation with cis-PAO inhibits both hyperlipidemia-induced UPR signaling and NLRP3 inflammasome activation in macrophages in plaques, resulting in reduced atherosclerosis in mice. Mechanistically, cis-PAO supplementation leads to dynamic integration of this bioactive fatty acid into ER membranes in macrophages and tissues in mice, and prevents high fat-induced adverse remodeling of organelle membranes and subsequent UPR activation [23].

These findings have resulted in a great excitement that dietary supplementation with cis-PAO could prevent CVD. Moreover, recent human epidemiological studies suggest trans-PAO could mediate the beneficial metabolic effects that are associated with high fat dairy consumption. To date, there is no information about trans-PAO's impact on organelles or inflammation [11–13]. Here, we directly investigated trans-PAO's impact on lipid-induced inflammation and atherosclerosis in a hypercholesterolemic mouse model. Oral supplementation with trans-PAO in mice resulted in its dynamic integration into the major lipid species found in plasma and tissues. Trans-PAO supplementation did not prevent nor augment lipid-induced ER stress, inflammasome activation and atherosclerosis. These findings demonstrate that the cis double bond configuration is crucial for PAO's ability to remodel ER membranes and prevent organelle stress and inflammation, which underlies cis-PAO's atheroprotective action. Therefore, our findings on the two PAO isoforms provide critical guidance for future clinical trials that will continue to address PAO's potential for CVD prevention in humans.

2. MATERIALS AND METHODS

2.1. General study design

All cell culture experiments were performed as three independent biological replicates. Quantitative reverse transcript polymerase chain reaction (qRT-PCR) analysis was performed from four biological replicates. All the mouse experiments were performed as independent cohorts. The analysis of the *in vivo* experiments (such as atherosclerotic lesion analysis, or immunoflurescent and immunohistochemical staining quantifications) were preformed blind to sample identity. The only elimination criteria for the *in vivo* experiments was based on visible health changes mice and determined by the veterinarian.

2.2. Reagents and plasmid

Tissue culture reagents: L-glutamine, DMEM, PBS, HBSS, RPMI, penicillin/streptomycin (P/S), fetal bovine serum (FBS) and RPMI were obtained from Thermo Scientific HyClone. Trypsin-EDTA and HEPES were obtained from GIBCO. Ultrapure LPS, fatty acid-free BSA, palmitate, cis-palmitoleate, NaCl, EDTA, NaF, Triton, sodium orthovanadate (Na_3VO_4), phenylmethanesulfonylfluoride (PMSF), and phosphatase inhibitor cocktail-3 were obtained from Sigma Aldrich. Trans palmitoleate was obtained from NuCheck Prep. Primary antibodies used: P-PERK Thr980 (3179), PERK (3192), p-AMPK (2535), total AMPK (2532) from Cell Signaling Technologies; p-eIF2α (144-28G) from Invitrogen; p-IRE1 and IL-1β (ab9722) from Abcam; β-Actin (sc-47778), Caspase-1(sc-514) from Santa Cruz Biotechnology. ECL Prime Western Blot Detection Kit was purchased Amersham Pharmacia and Trisure reagent was purchased from Bioline. The pCMV-Myc-GFP-KDEL plasmid and pcDNA5- IRE1-3F6HGFP-FRT plasmid were obtained from Peter Walter (UCSF) [51].

2.3. Cell cultures and treatmentMouse BMDM isolation

BMDM were isolated from the tibiae and femurs of mice and differentiated for five to seven days in RPMI-1640 growth medium enriched with %15 L929 cells (ATCC) conditioned medium. The differentiated BMDM cells were primed with 200 ng ultrapure LPS for 3 h, Then, cells were stimulated with ethanol-BSA (negative control), palmitate-BSA (500 μM, cis-palmitoleate-BSA (500 μM) or trans-palmitoleate-BSA (500 μM) for the indicated amounts of time. Proteins (from cells or conditioned medium) and RNA were isolated from the cells as described earlier [23].Fatty acid-Bovine albumin serum complex
Palmitate (500 mM in ethanol) was prepared as previously described and added to the cell media at indicated dose [49].

2.4. Protein analysis

Protein lysates were prepared as described before [23,36]. All lysates were run on SDS-PAGE gels, transferred to PVDF membranes, before blocking (in TBS with 0.1% Tween-20 (v/v) and 5% (w/v) dry milk or BSA). For cleaved caspase-1 and IL-1β detection: the conditioned medium was collected and mixed with 5X SDS loading dye, followed by heating at 95 °C for 5 min before loading on SDS-PAGE gels. After secondary-HRP conjugated antibody incubation, all blots were developed using ECL prime reagent (GE Healthcare) and visualized by BioRAD MP imager.

2.5. RNA isolation and qRT-PCR

Total RNA was extracted with Trisure reagent (Bioline) and converted to cDNA with Revert Aid First Strand cDNA Synthesis Kit (Thermo Scientific). Using specific primers, cDNAs were amplified on Light Cycler 480II (Roche) or Rotor Gene (Qiagen). The formula that was used for calculating expression changes is as follows: (primer efficiency)$^{-\Delta\Delta Ct}$ where ΔΔCt means ΔCt (target gene) - ΔCt (reference gene) and Ct means (threshold cycle). Results are representative from three or more independent experiments that were quantified and analyzed by Student's t-test.
The following primers were used
mTNFα-Frw:5′-CATCTTCTCAAAATTCGAGTGACAA-3′;
mTNFα-Rev:5′-TGGGAGTAGACAAGGTACAACCC-3′;
mCCL2-Frw: 5′- CTTCTGGGCCTGCTGTTCA-3′
mCCL2-Rev: 5′-CCAGCCTACTCATTGGGATCA-3′
mGAPDH-Frw:5′-GTGAAGGTCGGTGTGAACG-3′;
mGAPDH-Rev: 5′- GGTCGTTGATGGCAACAATCTC -3′.

2.7. mtROS staining and quantification

For staining of mtROS production, MitoSOX™ Red mitochondrial superoxide indicator (Life Technologies) was used as previously described [36]. Mitochondrial stainings were done with Mitotracker GreenFM (Life Technologies) according to the manufacturer's instructions. The images were analyzed with ImageJ program. The images were taken with Leica DMI 4000B equipped with Andor DSD2 spinning disk confocal microscope (Cagdas Son Lab, METU).

2.8. IRE1 oligomerization

IRE1-3F6HGFP expressing HEK-293 stable cell lines were used as published [23]. 1×10^6 cells HEK-293 stable cells on cover slips were treated with BSA (control), palmitate-BSA (500 μM), cis-palmitoleate-BSA (500 μM) or trans-palmitoleate-BSA (500 μM) alone or in combination for 6 h. Images of the cells were acquired on Leica DMI 4000B equipped with Andor DSD2 spinning disk confocal microscope (Cagdas Son Lab, Middle East Technical University, Ankara, Turkey). Oligomerization analysis was performed according to previously published protocols by counting IRE1 foci in >100 cells from multiple replicates for each treatment [23].

2.9. Cytokine measurements

To quantify IL-1β amount in plasma, samples were diluted 1:1 using assay diluent A and ninety-six-well colorimetric "sandwich" ELISA plates (Abcam, mouse IL-1β ELISA kit) was used: Recombinant mouse IL-1β standard (100 μl of 2000—2.74 pg/ml) and 100 μl of diluted plasma samples were run in duplicate according to manufacturer's instructions. The absorbance was detected at 450 nm using plate readers. Results were calculated by Prism 8.1.2 (GraphPad Software Inc.).

2.10. Mouse models, dietary treatments, and experimental procedures

Animal care and experimental procedures were performed according to the local animal care and ethical review committee guidelines accepted at İhsan Dogramaci Bilkent University. For our studies, Apoe$^{-/-}$ mice (Charles River) were used. Male mice were fed with Western diet from the age of week 8 for 12 weeks. Then, the mice were treated by oral gavage with vehicle (1% BSA in PBS) or 1400 mg/kg/day cis or trans-PAO dissolved in vehicle for 4 weeks while continuing on Western diet. The mice weights were measured weekly and blood glucose measurements were done at the beginning and at the end of injections before sacrifice. The mouse sacrifice and tissue collection was described in detail in our previous publications [23,36].

2.11. En face aorta lesion analysis

Aortas were pinned on a black wax surface, and atherosclerotic lesions were analyzed in all aorta after Sudan IV staining as described earlier [23]. Lesion area was quantified using ImageJ and expressed as the percentage of SUDAN IV stained plaque area over the aortic area.

2.12. Plasma lipids and lipoprotein analysis

Mouse blood was obtained via heart puncture during sacrifice, centrifuged and plasma collected. Then, the plasma was analyzed by FPLC in the Mouse Metabolic Phenotyping Center at the University of Cincinnati. For the resolution of major lipoprotein classes from plasma, the columns were equilibrated in 50 mM PBS. Using a microtiter plate enzyme-based assay, the major lipoprotein classes were measured in cholesterol or triglyceride assays from collected fractions.

2.13. Lipidomic analysis

Lipidomic analysis of plasma and tissues including muscle, liver, and adipose tissue (control; n = 5, trans-PAO; n = 5, and cis-PAO; n = 6) were done by Metabolon. The analysis was performed as previously described [18,23]. Individual lipid species were quantified by taking the peak area ratios of target compounds and their assigned internal standards, then multiplying by the concentration of internal standard added to the sample. Lipid class concentrations were calculated from the sum of all molecular species within a class, and fatty acid compositions were determined by calculating the proportion of each class comprised of individual fatty acids.
Quantitative analysis were for the following: (A) lipid classes: FFA: free fatty acid, CE: cholesteryl ester, DAG: diacylglycerol, TAG: triacylglycerol, CL: cardiolipin, LYPC: lysophosphatidylcholine, PC: phosphatidylcholine, PE: phosphatidylethanolamine, PS: phosphatidylserine. (B) fatty acids: 14:0, 15:0, 16:0, 18:0, 20:0, 22:0, 24:0, 14:1n5, 16:1n7, 18:1n7, 18:1n9, 20:1n9, 20:3n9, 22:1n9, 24:1n9, 18:2n6, 18:3n6, 20:2n6, 20:3n6, 20:4n6, 22:2n6, 22:4n6, 22:5n6,

18:3n3, 18:4n3, 20:3n3, 20:4n3, 20:5n3, 22:5n3, 22:6n3, 24:6n3, plasmalogen derivatives of 16:0, 18:0, 18:1n7, 18:1n9, t16:1n7, t18:1n9, and t18:2n6.

2.14. Immunohistochemistry

7-μm thick cryosections were obtained using a cryostat (Leica CM 1850) from the aortic roots. Immunofluorescent stainings were performed using the following antibodies: anti—MOMA-2 (monocyte/macrophage marker) (abcam ab33451), anti—CD3-Alexa488 (Biolegend 100—210), anti—α-SMA (abcam ab5694), anti-P-eIF2α (Invitrogen 144-28G), anti-ATF3 (sc-188; Santa Cruz Biotechnology), IL-1β antibody (abcam ab9722) and DAPI (abcam ab104140). Cryosections were stained with Masson's Trichrome (Bio-Optica), OilRedO (Sigma), FAM/FLICA caspase1 detection kit (Immunochemistry Tech FAM-YVAD-FMK(655) # 97), TUNEL (In situ Cell Death detection Kit, Fluorescenin; Roche 11684795910) and hematoxylin and eosin (H&E). Representative images were taken with a Zeiss fluorescent microscope.

Cryosections were stained with H&E stain for morphometric lesion analysis. The total lesion area and necrotic area were quantified using ImageJ software as previously described from 4 sequential sections (60 μM apart, beginning at the base of the aortic root) [23,52—54]. Foam cell area was calculated from OilRedO stained 4 sequential sections and collagen content from Masson's Trichrome stained sections using ImageJ as previously described [23].

The fluorescent immunostainings were carried out on cryosections that were fixed in cold acetone for 10 min, blocked in %4—6 BSA/PBS with %10—20 species specific serum (compatible with the primary antibody) as previously described [49]. All stained sections were mounted with Fluorosave mounting reagent containing DAPI. Florescent signal calculations: (a) ATF3, P-eIF2α, and FAM/FLICA stainings: the sections were double stained with MOMA-2 to mark the macrophage-enriched area. The Mean Fluorescent Intensity (MFI) corresponding to primary antibody signal was calculated from this MOMA-2 positive area. The background fluorescence of the non-stained area inside the lesion was subtracted from the total MFI corresponding to each signal. Data were quantified as total MFI signal compared with baseline [22,55,56]. (b) CD3: The total T cell number (cells/mm2) to the lesion area was quantified from CD3 as previously described [23] (c) other fluorescent stainings was calculated as percentage of MOMA-2, IL-1 β, and α-SMA positive-stained area over total lesion area [23,36].

2.15. Statistical analysis

Results are reported as mean ± SEM. Statistical significance of the results was determined using the Student's t test, one-way ANOVA (for more than two groups) or the Mann—Whitney test (for *in vivo* analysis). $P < 0.05$ was considered as significant.

3. RESULTS

3.1. The impact of trans-PAO on lipid-induced ER stress and inflammation in macrophages

Cholesterol, phospholipids, and the fatty acid content in these lipids determine the biophysical properties of membrane systems, including the ER. The lipid composition of the ER membranes is sensed through the transmembrane domains of the ER stress sensors and determines their activation status [23,48]. Previously, we showed that SFA can alter macrophage ER membrane lipid composition and initiate UPR signaling such as by inducing IRE1 oligomerization on the ER membranes [23]. SFA-induced UPR signaling can be counteracted by cis-PAO, which enters and remodels ER membranes [23]. Here, we assessed the impact of trans-PAO on IRE1 oligomerization on the ER membranes and compared to cis-PAO. As expected, cis-PAO treatment significantly reduced IRE1 oligomer formation (as assessed by visualizing green fluorescent protein (GFP)—tagged IRE1 foci formation on ER membranes). However, trans-PAO treatment did not alter PA-induced IRE1 oligomerization on ER membranes ($P < 0.05$, Figure 1A). While cis-PAO prevented SFA-induced IRE1 activation (as assessed by IRE1 auto-phosphorylation) as expected, trans-PAO treatment did not inhibit lipid-induced IRE1 activation in mouse and human macrophages (Figure 1B, S. Fig. 1A). Similarly, cis-PAO, but not trans-PAO, prevented SFA-induced PERK activation (as assessed by PERK auto-phosphorylation) in mouse macrophages (Figure 1B), demonstrating trans-PAO does not have an impact on lipid-induced ER stress.

Next, we assessed the two PAO isomers' impact on SFA-induced mitochondrial oxidative stress in macrophages side by side. We observed cis-PAO treatment significantly suppressed lipid-induced mtROS generation, but trans-PAO treatment did not ($P < 0.001$, Figure 1C, S. Fig. 1B). Taken together, our results show trans-PAO can't prevent SFA-induced organelle stress. These findings thus suggest that trans-PAO and cis-PAO may differ in their biological activities such as inflammation and in their role in atheroprotection.

SFA specifically leads to the induction of NLRP3 inflammasome and IL-1β and IL-18 secretion in UPR-dependent manner in both mouse and human macrophages, and this can be blocked by cis-PAO treatment [23,30,36,57,58]. Therefore, we next investigated whether trans-PAO has an impact on SFA-induced inflammasome activation. We observed that trans-PAO treatment does not abolish PA-induced caspase-1 and IL-1β secretion, which was significantly blocked by cis-PAO in the same experimental set up (Figure 1D). Moreover, trans-PAO co-treatment did not prevent PA from inducing inflammatory cytokines such as tumor necrosis factor-alpha (TNFα) and monocyte chemotactic protein-1 (MCP1)/chemokine (C—C) motif ligand-2 (CCL2) in mouse macrophages, but appeared to augment it ($P < 0.001$; Figure 1E, F). A previous study suggested that cis-PAO increases oxidative respiration and reduces inflammation in macrophages through activation of AMPK. However, both trans-PAO and cis-PAO treatment increased AMPK phosphorylation in macrophages suggesting this is not the mechanism by which these two PAO isoforms differentially impact lipid-induced inflammation in macrophages (S. Fig. 1C) [59]. These findings demonstrate that unlike cis-PAO, trans-PAO treatment of macrophages does not appear prevent SFA-induced inflammation and it may not impact atherosclerosis in a beneficial way.

3.2. *The impact of trans-PAO on lipid composition* in vivo

In contrast to the epidemiological data linking trans-PAO with beneficial outcomes in CVD, our findings in macrophages suggest that trans-PAO does not prevent organelle stress and inflammation in macrophages stimulated with PA *in vitro* and therefore trans-PAO may be devoid of the atheroprotective qualities that are attribute to cis-PAO. We next conducted an *in vivo* study to observe the impact of trans-PAO supplementation on hyperlipidemia-induced inflammation and atherogenesis. For this purpose, 8 week-old male apolipoprotein E-deficient ($Apoe^{-/-}$) mice were fed with Western diet (WD) for 16 weeks to induce hyperlipidemia and atherosclerosis development. Starting at 12 weeks of this diet regimen, we administered 1400 mg/kg/day cis or trans-PAO (based on the atheroprotective cis-PAO dosage determined by our earlier experiments [23]) or vehicle (control group) by oral gavage (Figure 2A; experimental design). Although incorporation efficiency into various lipid classes in tissues varies for different TFA species, dietary TFA can incorporate into serum lipoproteins and adipose tissue in the form of triglyceride, phospholipids, and cholesterol esters [60]. The

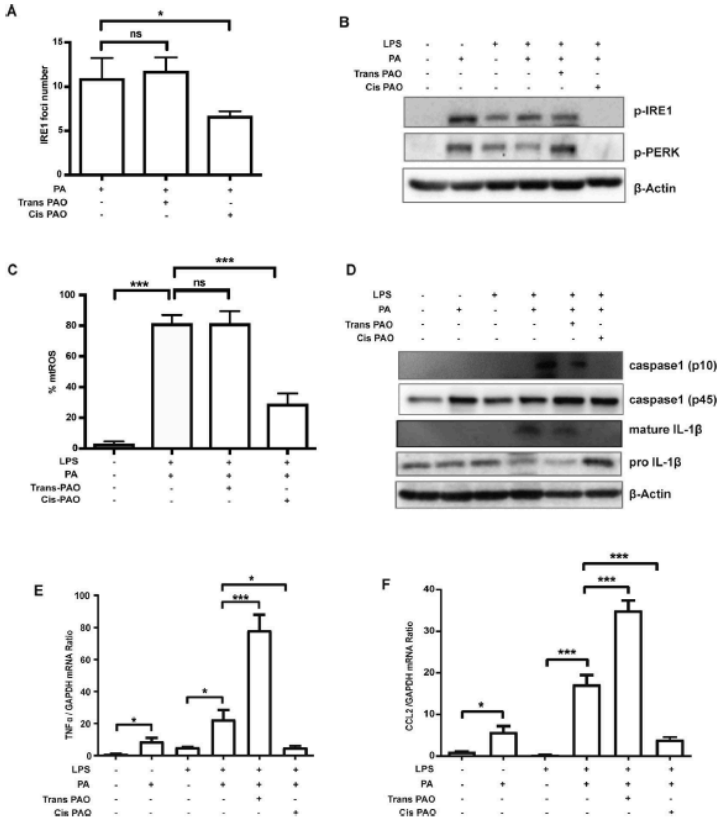

Figure 1: Trans-PAO treatment does not prevent lipid-induced organelle stress or inflammation in mouse macrophages. (A) Cells co-transfected with a green fluorescent protein (GFP)-tagged IRE1 plasmid and Cherry-KDEL amino acid sequence expressing construct were treated with 500 μMPA or co-treated with 500 μMPA and 500 μM trans-PAO/cis-PAO for six hours. IRE1 oligomer/foci formation (green) on ER membranes (red) was analyzed by confocal microscopy. The graph displays quantification of IRE1 oligomerization (distinct IRE1 foci per cell). Data represents mean ± SEM; $^{**}P < 0.01$, $n \geq 100$ from four experiments. **(B)** LPS-primed and PA-stressed BMDM were co-treated with trans-PAO or cis-PAO and protein lysates were analyzed by western blotting using specific antibodies against: p-PERK, p-IRE1 and β-actin. **(C)** LPS-primed and PA-stressed BMDM were treated with cis- or trans-PAO and mtROS production was measured with MitoSOX™ (red mitochondrial superoxide indicator kit) ($n \geq 3$). **(D)** LPS-primed and PA-stimulated BMDM were co-treated with cis- or trans-PAO and the conditioned medium was analyzed by western blotting using specific antibodies against IL-1β, caspase-1 and β-actin ($n \geq 3$). **(E-F)** qRT-PCR analysis **(E)** TNFα and **(F)** CCL2 mRNA in LPS-primed, PA-stressed BMDMs co-treated with cis- or trans-PAO ($n \geq 3$). Data are shown as means ± SEM. $^{*}P < 0.05$,$^{**}P < 0.01$,$^{***}P < 0.001$. One way ANOVA was used for statistical analysis.

effect of dietary trans-PAO on plasma and tissue lipid composition has not been studied before. We investigated the efficiency of trans-PAO incorporation into various lipid classes such as free fatty acids (FFA), cholesterol esters (CE), diacylglycerol (DAG), triacylglycerol (TG) and phospholipid (PL) in plasma and multiple tissues by way of quantitative lipidomics analysis. We observed 4 weeks of trans-PAO treatment increased trans-PAO levels in the plasma of Apoe$^{-/-}$ mice ($P < 0.01$; Figure 2B). Trans-PAO treatment did not cause a change in the plasma MUFA/SFA ratio (Figure 2C). While trans-PAO concentration in FFA, CE, DAG, TG and PL was higher compared to control ($P < 0.05$; Figure 2D, E), the concentration of these lipid classes was unaltered in the plasma (Figure 2F). Trans-PAO concentration was also increased in many of the PL species without expanding the PL compartment in plasma ($P < 0.05$; Figure 2D–F). Additionally, trans-PAO treatment did not impact cis-PAO total concentration (Figure 2G) or cis-PAO amount within any major lipid class in plasma (Figure 2H). These findings

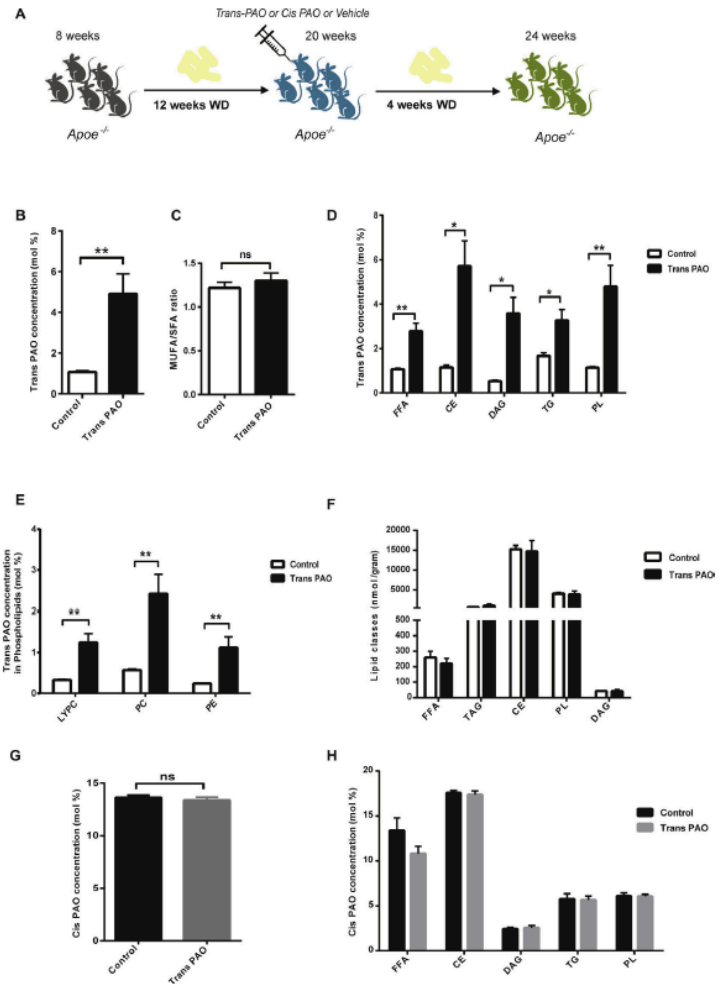

Figure 2: The impact of trans-PAO treatment on plasma lipid composition in the Apoe$^{-/-}$ mice. **(A)** Experimental design for the analysis of atherosclerosis in Apoe$^{-/-}$ mice on a Western diet (WD). Quantitative lipidomic analysis was performed with plasma isolated from trans-PAO- and vehicle-treated Apoe$^{-/-}$ mice on WD: **(B)** The mean concentration of trans-16:1n-7 (mole %; the ratio of moles of fatty acids to total moles of fatty acids) in plasma. **(C)** MUFA/SFA ratio. **(D)** The mean concentration of trans-C16:1n-7 (mole %) in various lipid classes. **(E)** The mean concentration of trans-C16:1n-7 (mole %) in the various phospholipid classes. **(F)** The mean concentration (mole %) of various lipid classes. **(G)** The mean concentration of cis-C16:1n7 (mole %). **(H)** The mean concentration of cis-C16:1n7 (mole %) in various lipid metabolites. Data represents means ± SEM; *P < 0.05, **P < 0.01, ns = not significant, (n = 5 per group). Unpaired two-tailed Student's t test was used for statistical analysis. (FFA: free fatty acid, CE: cholesteryl ester, DAG: diacylglycerol, TAG: triacylglycerol, CL: cardiolipin, LYPC: lysophosphatidylcholine, PC: phosphatidylcholine, PE: phosphatidylethanolamine, PS: phosphatidylserine).

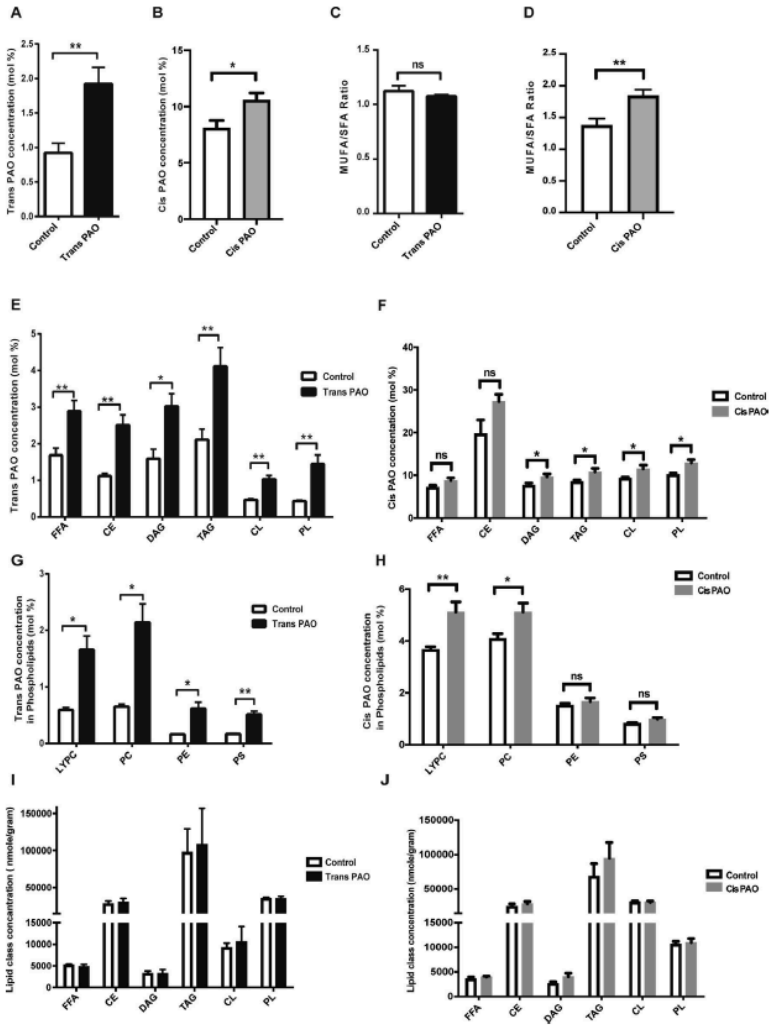

Figure 3: The effect of trans- or cis-PAO treatments on liver lipid composition in Apoe$^{-/-}$ mice. Quantitative lipidomic analysis was performed with livers from trans-PAO- or cis-PAO-treated and control Apoe$^{-/-}$ mice on WD: **(A,B)** The mean concentration of trans- or cis-C16:1n-7 (mole %), **(C,D)** MUFA/SFA ratio after trans- or cis-PAO treatment. **(E, F)** The mean concentration (mole %) of trans- or cis-C16:1n-7 in various lipid classes are shown. **(G,H)** The mean concentration (mole %) of trans- or cis-C16:1n-7 in the various phospholipid classes. **(I,J)** The mean concentration (mole/gram) of various lipid classes in trans- or cis-PAO treated and control mice. Data represents mean ± SEM; *P < 0.05, **P < 0.01, ns = not significant, (n = 5 for trans-PAO and n = 6 for cis-PAO). Unpaired two-tailed Student's t test was used for statistical analysis.

indicate that oral trans-PAO supplementation effectively increases plasma trans-PAO concentration and trans-PAO incorporation into various lipid compartments in plasma.

Next, we assessed the lipid profiles from liver, skeletal muscle tissue and adipose tissue of trans-PAO, cis-PAO and vehicle-treated Apoe$^{-/-}$ mice. The concentration of trans-PAO or cis-PAO significantly increased in the liver and muscle from the trans-PAO-treated mice or cis-PAO-treated when compared to control ($P < 0.05$; Figure 3A,B, S. Fig. 2A, B). Similar to plasma, trans-PAO treatment did not alter the MUFA/SFA ratio in liver or muscle (Figure 3C, S. Fig. 2C), whereas cis-PAO treatment significantly increased MUFA/SFA ratio in liver or muscle (Figure 3D, S. Fig. 2D). Trans-PAO amount in the major lipid class (FFA, EC, DAG, TAG, CL, PL) or cis-PAO amount in the major lipid class (DAG, TG, CL, PL) was increased in liver and muscle but without causing an expansion of these lipid classes analyzed in the samples ($P < 0.05$; Figure 3E—J and S. Fig. 2E—J). The concentration of trans-PAO significantly increased in the adipose tissue, while concentration of cis-PAO did not ($P < 0.05$; S. Fig. 3A, B). Trans-PAO or cis-PAO treatment did not alter MUFA/SFA ratio in adipose tissue (S. Fig. 3C, D). Trans-PAO amount in the major lipid class (FFA, DAG, TAG, PL) significantly increased in adipose tissue (S. Fig. 3E) but the amount of cis-PAO in these lipid classes was similar (S. Fig. 3F). Furthermore, trans-PAO or cis-PAO treatment did not cause the expansion of these lipid classes in adipose tissue (S. Fig. 3G, H). In conclusion, chronic trans-PAO treatment significantly increased the incorporation of trans-PAO into the major lipid classes (FFA, EC, DAG, TAG, CL, PL) in the tissues but these lipids' levels or the overall fatty acid desaturation index (MUFA: SFA ratio) remained unchanged. Cis-PAO treatment significantly increased the incorporation of cis-PAO into major lipid classes in the liver (DAG, TAG, CL, PL) and in the muscle (CE, CL, PL), but not in adipose tissue cis-PAO treatment significantly changed the fatty acid desaturation index in liver and muscle but not adipose tissue.

3.3. *The impact of trans-PAO on macrophage ER stress and inflammasome activation* in vivo

Macrophages form the vast majority of inflammatory cells in atherosclerotic plaques, and they play an important role in the development and progression of atherosclerosis through modulation of cholesterol homeostasis, the immune-inflammatory response, and plaque cellularity [61—63]. Increased ER stress in lipid-laden macrophages has been connected to plaque progression, vulnerability, and rupture and to CAD in humans, whereas suppression of ER stress alleviates atherosclerosis in mouse models [64]. In addition, decreasing ER stress suppresses inflammasome activation in lesion macrophages [23,36]. Even though cis-PAO suppressed lipid-induced ER stress and subsequent NLRP3 inflammasome activation [23], trans-PAO could not block SFA-induced IL-1β secretion in macrophages (Figure 1D). Hence, we sought to understand the impact of trans-PAO on ER stress and subsequent inflammasome activation in atherosclerotic plaque macrophages *in vivo*. For this purpose, we stained the macrophage-enriched areas of aortic root and performed immunofluorescence signal intensity analysis for two surrogate markers of UPR, namely phosphorylation of eukaryotic initiation factor 2α (eIF2α) and downstream of eif2α signaling, the induction of the expression of cyclic adenosine monophosphate—dependent transcription factor 3 (ATF3). The data confirmed that trans-PAO treatment does not suppress P-eIF2α or ATF3 expression in macrophage-filled (MOMA2-positive) plaque area when compared to the control mice (Figure 4A,B). To investigate the trans-PAO's impact on inflammasome activation *in vivo*, we performed immunofluorescence staining for IL-1β and active caspase-1 in plaque macrophages. We did not find any differences in immunofluorescence staining for IL-1β and active caspase-1 in the macrophage-enriched (MOMA2 positive) plaque regions (Figure 4C,D). ELISA analysis of the serum from mice treated with trans-PAO showed no significant differences in systemic IL-1β levels between trans-PAO and control treatment mice, whereas cis-PAO significantly reduces systemic IL-1β levels (Figure 4E). These findings show that trans-PAO unlike cis-PAO, does not prevent hyperlipidemia-induced macrophage ER stress and inflammasome activity in plaque areas *in vivo*.

3.4. The impact of trans-PAO on atherosclerosis

We next investigated trans-PAO's role in atherosclerotic plaque development. Our previous studies showed cis-PAO can prevent hyperlipidemia-induced organelle stress, inflammasome activation, and inflammation and reduce atherosclerosis progression. However, in this study we observed that trans-PAO did not prevent PA-stimulated and inflammasome-produced IL-1β or other inflammatory cytokine production from macrophages *in vitro*. In fact, we observed some induction of cytokines with trans-PAO and PA co-stimulation of the macrophages (Figure 1D—E). Moreover, trans-PAO could not prevent SFA-induced ER or mitochondrial oxidative stress as cis-PAO does (Figure 1A—C). Therefore, our findings suggest that trans-PAO may be pro-inflammatory and pro-atherogenic, in contrast to the published epidemiological studies that imply a beneficial role for trans-PAO in cardiometabolic disease [4,11—13]. While we observed effective trans-PAO enrichment in plasma and tissues of our mice (Figures 2 and 3), this was not accompanied with significant changes in body weight or blood glucose levels (S. Fig. 4A). Similarly, cis-PAO treatment in mice did not alter body weight or blood glucose levels (S. Fig. 4A). We then evaluated the impact of trans-PAO on atherosclerosis development in *en face* aorta preparations and aortic root sections. To our surprise, we found that trans-PAO treatment did not impact (neither preventing nor promoting) the development of atherosclerotic lesions in lesions in en face aorta preparations, whereas cis-PAO significantly reduces atherosclerosis (Figure 5A). Oil RedO staining analysis of the aortic root cryosections also did not show any significant changes in foamy macrophage accumulation in the aortic sinus area whereas cis-PAO significantly reduced foamy macrophages in lesions (Figure 5B). There were no significant differences in lesion area or the necrotic core area assessed from the hematoxylin and eosin (H&E)-stained lesions from trans-PAO-treated mice while cis-PAO significantly reduced necrotic core area (Figure 5C,D). Macrophage numbers in lesions were not reduced by trans-PAO whereas cis-PAO treatment resulted in significant drop in lesion macrophages (Figure 5E). Also, we noted no significant changes in the plasma total cholesterol or total triglycerides or the cholesterol content of lipoproteins between trans-PAO-treated and control mice, but we noted a small but significant increase in the TG amount found in plasma high density lipoprotein (S. Fig. 4B—F).

Vascular smooth muscle cells (SMC), endothelial cells, and immune cells, including lymphocytes, neutrophils, dendritic cells, and macrophages play important roles in the development of atherosclerotic plaques in the arterial wall [64]. Next, we performed immunohistochemical analysis of the aortic root sections from these mice in order to determine the impact of trans-PAO on plaque cellular composition. We observed that total T lymphocyte content did not differ between trans-PAO and control groups (Figure 6A). In addition, SMC content (assessed by α-smooth muscle actin staining) and collagen content (determined by Masson Trichrome staining) did not reflect significant differences between the lesions obtained from trans-PAO-treated mice

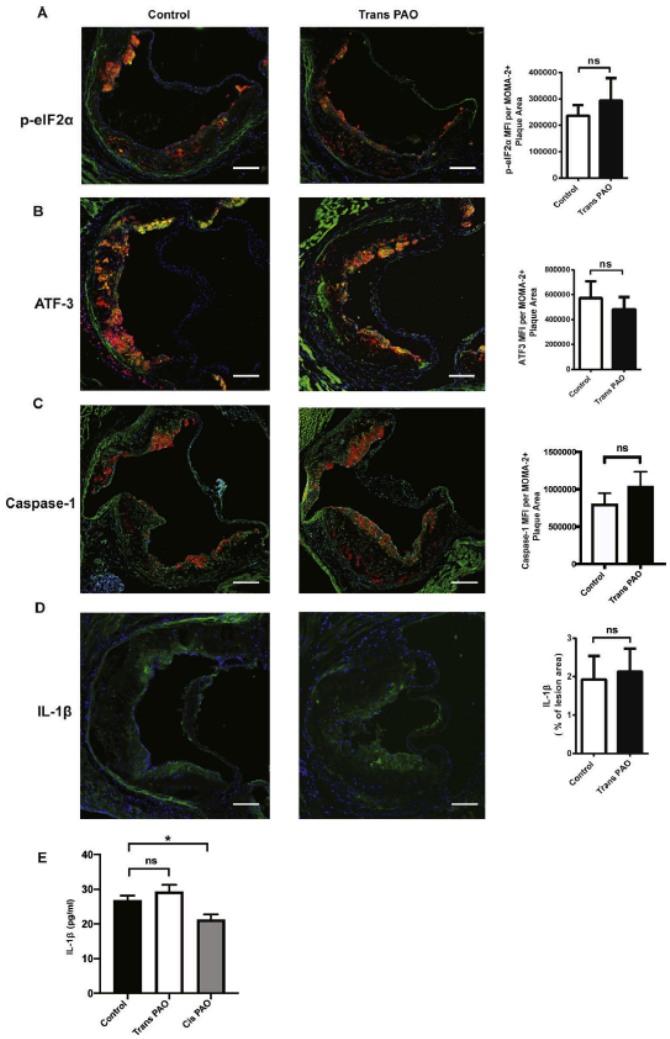

Figure 4: Trans-PAO does not prevent ER stress or inflammasome activation *in vivo*. Aortic root sections from trans-PAO or vehicle treated mice were analyzed by immunofluorescent (IF) staining using specific antibodies for: **(A)** p-eIF2α (green), **(B)** ATF3 (green), **(C)** FLICA (green), and **(D)** IL-1β (green). For each staining, a representative image is shown in left and center, and the quantification of the data appears on the right. Relative IF intensities (green) for P-eIF2α, ATF3 and FLICA were quantified from the macrophage positive area (red) ($n = 5$ per group). **(E)** Plasma IL-1β levels were measured from the Apoe$^{-/-}$ mice treated with trans- or cis-PAO or vehicle for 4 weeks ($n = 6$ per group). All data represent mean ± SEM; $^{*}P < 0.05$, $^{**}P < 0.01$. Control versus trans-PAO (A,B,C,D) or Cis-PAO (E); Mann Whitney U test was used for statistical analysis. Scale bars: 150 μm.

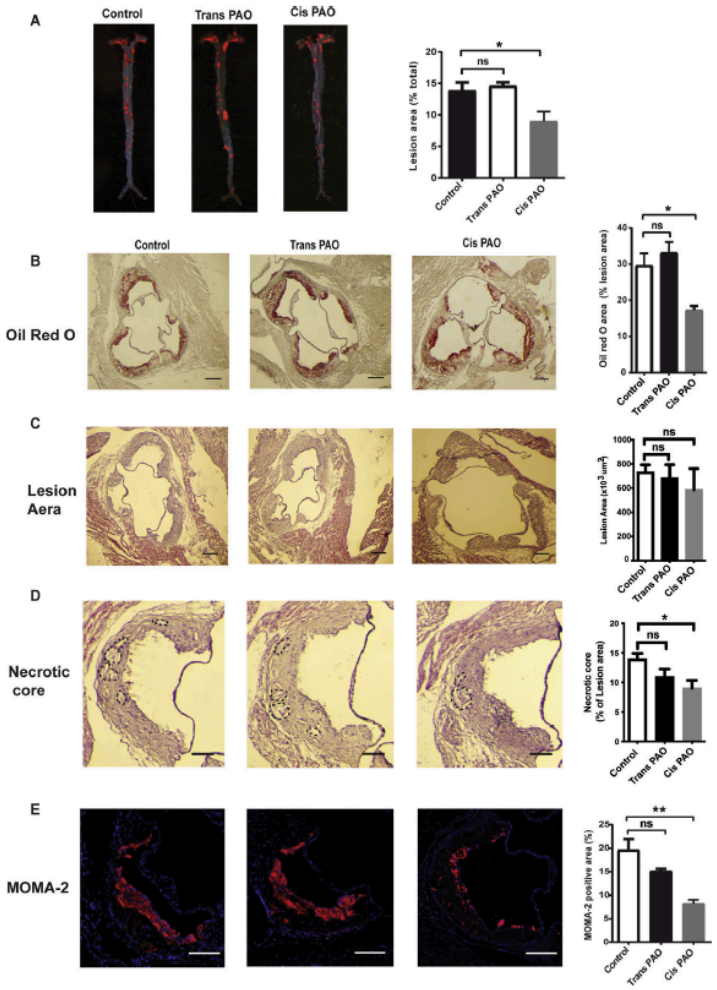

Figure 5: Trans-PAO does not prevent atherosclerosis in Apoe$^{-/-}$ mice. (**A**) Lesion area was calculated from en face aorta preparations stained with Sudan IV (Control; n = 12; Trans-PAO; n = 9; Cis-PAO; n = 6). (**B**) Foam cell area was calculated from Oil RedO stained aortic root sections (control; n = 9; Trans-PAO; n = 9, Cis-PAO; n = 5 scale bar: 300 µm). (**C**) Total plaque area and (**D**) necrotic area were calculated from hematoxylin and eosin (H&E)-stained aortic root lesions (control; n = 9; Trans-PAO; n = 9,Cis-PAO; n = 5 scale bar: 300 µm). (**E**) Macrophage content in aortic root lesions, as quantified after staining for MOMA-2 (green). (n = 5 per group, scale bar: 150 µm). In each case, a representative image is shown in left and center, and the quantification of the data appears on the right. Control versus trans-PAO or cis-PAO; Mann Whitney U test (in A B,C,D) Student's t test was used for statistical analysis.

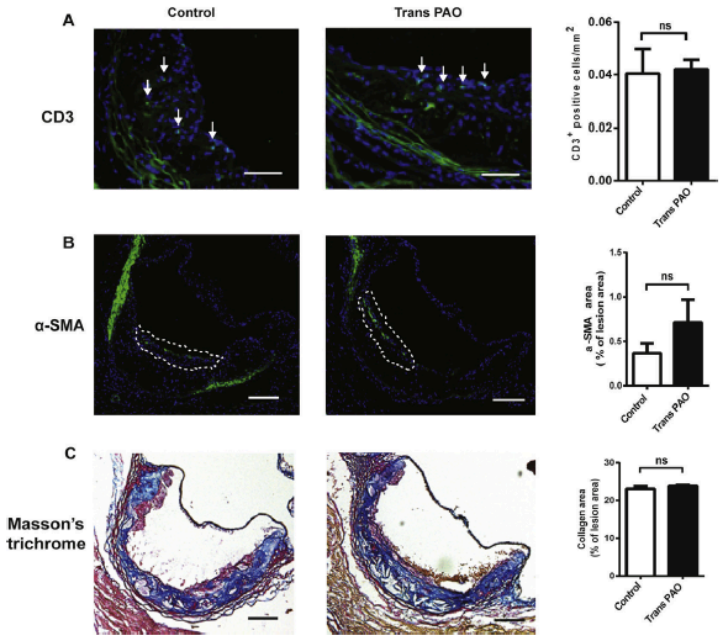

Figure 6: Trans-PAO does not alter plaque composition of atherosclerotic lesions. Immunohistochemical analysis of aortic root cryosections from Apoe$^{-/-}$ mice from treated with trans-PAO or vehicle (1% BSA in PBS). The representative images and quantification are shown for: **(A)** CD3 (green), **(B)** α-SMA (green) **(C)** Masson's Trichrome staining (blue: collagen; red: cytoplasm and muscle fibers) (n = 5 per group). In each case, a representative image is shown in left and center, and the quantification of the data appears on the right. Data represents mean ± SEM; NS = not significant. Control versus trans-PAO; Mann Whitney U test was used for statistical analysis. Scale bars: 150 μm.

and controls (Figure 6B and Figure 6C). Collectively, these findings demonstrate that trans-PAO treatment does not impact atherosclerosis development in mice.

4. DISCUSSION

Owing to their effects on the plasma lipids, lipoprotein metabolism and inflammation, the quantity and type of dietary fatty acids have a considerable impact on the development of CVD [65]. Whereas MUFA with cis double bond configuration has been consistently associated with beneficial metabolic effects (such as anti-inflammatory, anti-diabetic and cardio protective actions) [63], MUFA with trans double bond configuration are often generated as by-products of industrially processed foods and have been associated with harmful effects on metabolism (such as inflammation and increased diabetes and CVD risk) [66,67]. An exception to this appears to be ruminant-derived TFA such as vaccenic acid and trans-PAO, which have been associated with beneficial cardiometabolic outcomes [67]. Circulating trans-PAO represents less than one percent of total fatty acids (and significantly lower than cis-PAO levels) in humans. However, studies have shown a significant increase in this minor plasma trans-fatty acid mirrors full fatty dairy consumption and associates with lower TG, atherogenic dyslipidemia, and diabetes incidence [4,12]. These beneficial attributes of trans-PAO are reminiscent of its isomer's (cis-PAO's) role in preventing insulin resistance, hepatic lipogenesis, and atherosclerosis [13,23]. Despite having been implied by epidemiological studies as a beneficial TFA, a causal relationship between trans-PAO and metabolic health has not been experimentally demonstrated. In this study, we demonstrated trans-PAO, despite two to three folds enrichment in various tissues, has no direct impact on hyperlipidemia-induced inflammation and atherosclerosis progression in the Apoe$^{-/-}$ mouse model of hypercholesterolemia-driven atherosclerosis.

SFA or cholesterol loading of macrophages is known to induce robust ER stress and mitochondrial oxidative stress, upstream of NLRP3 inflammasome activation and IL-1β and IL-18 secretion, resulting in an inflammatory response that drives atherosclerosis progression [23,36,59]. Genetic or pharmacological suppression of ER stress, mitochondrial oxidative stress and inflammasome activity reduces atherosclerosis [28,36,49,68–70]. The results of the recent CANTOS trial showed neutralizing IL-1β with a human monoclonal antibody leads to dose-dependently reduction in C-reactive protein (CRP) and IL-6 levels (43% reduction from the baseline) in patients with previous myocardial infarction, providing support for the inflammatory basis of athero-thrombosis in humans [71]. Previous studies in humans also showed chronic cis-PAO administration reduced CRP and inflammation

in humans. Further characterization of cis-PAO in mice demonstrated that this bioactive lipid prevents hyperlipidemia-induced ER stress, inflammasome activation, and inflammation, thereby reducing the progression of atherosclerosis. While trans-PAO has been associated with healthy cardiometabolic indicators in humans, we were surprised to discover that trans-PAO, unlike cis-PAO, could not antagonize SFA-induced organelle stress (as evidenced by unaltered UPR signaling and mtROS production) and inflammasome-induced IL-1β secretion in macrophages. Intriguingly, in cultured macrophages trans-PAO appeared to induce the production of TNFα and MCP1. Our findings are therefore in contrast to the epidemiological studies that have associated trans-PAO with reduced inflammation [12,72]. Moreover, both of these cytokines were shown to be significantly inhibited by cis-PAO treatment in lipid-stressed mouse and human macrophages [23]. Therefore, in order to evaluate trans-PAO's impact on hyperlipidemia-induced organelle stress and inflammation in an *in vivo* setting, we administered trans-PAO orally to $Apoe^{-/-}$ mouse model of atherosclerosis. Despite being partially pro-inflammatory in cultured macrophages, chronic trans-PAO treatment *in vivo* did not enhance nor reduce hyperlipidemia-induced atherosclerosis development in mice. Moreover, orally active trans-PAO did not reduce or induce hyperlipidemia-induced IL-1β levels in the plaques or in the serum of $Apoe^{-/-}$ mice, which was consistent with our observations on trans-PAO's impact on IL-1β secretion in macrophages. In addition, trans-PAO did not alter macrophage accumulation or formation of foamy macrophages or necrotic core in lesions obtained from the aortic roots of $Apoe^{-/-}$ mice. These *in vivo* findings therefore suggest ruminant-derived trans-PAO may not be the beneficial factor found in full fat dairy that appears to reduce the risk for CVD in humans [66]. Similar to our findings, others have shown that another ruminant TFA, trans-vaccenic acid (trans-18:1n−7), does not alter atherosclerosis development in rabbits and monkeys [73,74]. In summary, results of this study support the findings from epidemiological studies that show trans-PAO does not increase the risk of CVD in humans, but it also shows that it doesn't possess the anti-inflammatory and atheroprotective properties attributed to its cis isomer. Whether trans-PAO has an impact on increasing insulin sensitivity requires further investigation in a diet-induced obesity mouse model as the $Apoe^{-/-}$ mice do not represent a good model to study insulin resistance.

The cis isomer of PAO shows a protective effect against atherosclerosis through a major remodeling of intracellular organelle membranes. Both unsaturated and saturated fatty acids are potent regulators of membrane fluidity in part by their incorporation into phospholipids alters cholesterol affinity and incorporation into membranes [75]. This phenomenon can impact the activities of membrane proteins such as G-protein coupled receptors on the plasma membrane as much as the stress sensor/effector protein on the ER membrane (such as IRE1) [23,75].

We previously showed that cis-PAO actively incorporates into major lipid classes in mice as well as isolated macrophages [23]. In this study, we observed that orally administered trans-PAO also incorporates into major lipids in plasma and membranes in tissues. Trans-PAO concentration is usually less than 1% of total lipids in humans [12,13]. Our current lipidomics findings represent the first in depth analysis of trans-PAO in mice, revealing ~1% of trans-PAO is found among lipid species in plasma and tissues of $Apoe^{-/-}$ mice (fed with WD), whereas cis-PAO concentration is ~10–15 folds more than its trans isomer. These results confirm that trans-PAO levels are significantly lower than cis-PAO isomer in mice. Although trans fatty acids are unsaturated, their pi bonds are not kinked (degree of acyl chain bending) compared to cis pi bonds. Thus, when incorporated into membranes, it is expected that they pack like saturated fatty acids and a smaller pool of trans fatty acids will be incorporated into the membranes [76]. Our data show that oral trans-PAO supplementation in hyperlipidemic mice leads to 2–3 folds trans-PAO enrichment in various tissues and plasma. Oral supplementation with cis-PAO in the hyperlipidemic mice leads to about 1.5 fold enrichment in various tissues. Albeit total trans-PAO levels remain much lower than normal cis-PAO levels, the fold enrichment of the trans isomer (2–3 fold) is bigger than the cis-isoform (about 1.5 fold). While cis-PAO enrichment is merely ~1.5 fold in the examined tissues, its impact on inflammation and atheroprotection is profound [23]. The differential action of the two PAO isomers may involve their differential impact on the membrane desaturation index. A noticeable consequence of cis-PAO supplementation is the increase in systemic desaturation ratio in tissues, but trans-PAO treatment doesn't impact the systemic desaturation ratio in plasma or tissues in mice. Differential impact of cis-PAO and trans-PAO on the desaturation index can have important consequences for membranes. It is known that as a result of increased desaturation of membranes cis-PAO prevents SFA-induced IRE1 oligomerization on ER membranes [23]. Consistent with a lack of impact on the desaturation index, trans-PAO does not alter SFA-induced IRE oligomerization on ER membranes [23]. Because this trans fatty acid does not create the degree of acyl chain bending that cis does, the effect of the double bond on membrane physical properties could be greatly diminished [76]. Although our data show that trans-PAO can incorporate into the lipid pools leading to 2–3 fold enrichment of this trans-fatty acid, trans-PAO's effects on membrane desaturation, organelle stress and inflammation are muted due to its structure.

Plasma trans-PAO levels are regarded as a circulating fatty acid biomarker of full fat dairy consumption, which is associated with higher HDL-cholesterol and lower triglycerides concentrations [13,77,78]. In the present work, we found that chronic trans-PAO treatment did not influence LDL or HDL-cholesterol and triglycerides in plasma. Interestingly, trans-PAO treatment significantly increased HDL-triglyceride in plasma of $Apoe^{-/-}$ mice, but this doesn't appear to promote atherosclerosis progression in mice. Our findings show that double bond configuration is critical for PAO's incorporation into lipids and beneficial metabolic properties such as reduction of organelle stress and anti-inflammatory actions that help prevent atherosclerosis. Of the two isoforms that we tested in our studies, only orally active cis-PAO reduced organelle stress, inflammation, and atherosclerosis [23]. Trans-PAO neither prevented nor promoted atherogenesis in mice. Therefore, our findings support previous epidemiological studies that found elevated trans-PAO levels, despite being a TFA, does not increase risk for CVD [79].

5. CONCLUSION

Our findings demonstrate the importance of comprehensive and direct investigation of lipids, which have been associated with metabolic benefits in epidemiological studies, in appropriate disease models. The results of our two studies on cis-PAO and trans-PAO will provide useful guidance for future dietary intervention strategies in humans that are based on PAO supplementation. Our findings show trans-PAO is not atheroprotective like cis-PAO but also confirm epidemiological studies that showed trans-PAO does not promote CVD.

ACKNOWLEDGEMENTS

We express our appreciation to Alexander Bartelt (Ludwig Maximillians University) for critical reading of the manuscript, Peter Walter (University of California, San Francisco) for providing the GFP-IRE1 and KDEL plasmids, and Metabolon for lipidomic analysis. This work was supported by a Marie Curie Reintegration Grant (Lipokines — 276922) to EE and European Research Council AdG °692511 to CW.

CONFLICT OF INTEREST

None declared.

APPENDIX A. SUPPLEMENTARY DATA

Supplementary data to this article can be found online at https://doi.org/10.1016/j.molmet.2019.08.004.

REFERENCES

[1] Wang, D.D., Hu, F.B., 2017. Dietary fat and risk of cardiovascular disease: recent controversies and advances. In: Stover, P.J., Balling, R. (Eds.), Annual review of nutrition, vol. 37. Palo Alto: Annual Reviews. p. 423—46.

[2] Brouwer, I.A., Wanders, A.J., Katan, M.B., 2013. Trans fatty acids and cardiovascular health: research completed? European Journal of Clinical Nutrition 67(5):541—547 https://doi.org/10.1038/ejcn.2013.43.

[3] Mozaffarian, D., Katan, M.B., Ascherio, A., Stampfer, M.J., Willett, W.C., 2006. Medical progress - trans fatty acids and cardiovascular disease. New England Journal of Medicine 354(15):1601—1613. https://doi.org/10.1056/NEJMra054035.

[4] Kleber, M.E., Delgado, G.E., Lorkowski, S., Marz, W., von Schacky, C., 2016. Trans-fatty acids andmortality in patients referred for coronary angiography: the Ludwigshafen Risk and Cardiovascular Health Study. European Heart Journal 37(13):1072—1078. https://doi.org/10.1093/eurheartj/ehv446.

[5] Willett, W.C., Stampfer, M.J., Manson, J.E., Colditz, G.A., Speizer, F.E., Rosner, B.A., et al., 1993. Intake of trans-fatty-acids and risk of coronary heart-disease among women. Lancet 341(8845):581—585. https://doi.org/10.1016/0140-6736(93)90350-p.

[6] Sun, Q., Ma, J., Campos, H., Hankinson, S.E., Manson, J.E., Stampfer, M.J., et al., 2007. A prospective study of Trans fatty acids in erythrocytes and risk of coronary heart disease. Circulation 115(14):1858—1865. https://doi.org/10.1161/circulationaha.106.679985.

[7] Chien, K.L., Lin, H.J., Hsu, H.C., Chen, P.C., Su, T.C., Chen, M.F., et al., 2013. Comparison of predictive performance of various fatty acids for the risk of cardiovascular disease events and all-cause deaths in a community-based cohort. Atherosclerosis 230(1):140—147. https://doi.org/10.1016/j.atherosclerosis.2013.06.015.

[8] Laake, I., Pedersen, J.I., Selmer, R., Kirkhus, B., Lindman, A.S., Tverdal, A., et al., 2012. A prospective study of intake of trans-fatty acids from ruminant fat, partially hydrogenated vegetable oils, and marine oils and mortality from CVD. British Journal of Nutrition 108(4):743—754. https://doi.org/10.1017/s0007114511005897.

[9] Dyer, O., 2012. Bans and labelling helped to reduce Americans' trans fat levels by 58%. British Medical Journal 344 https://doi.org/10.1136/bmj.e1084.

[10] Kuhnt, K., Degen, C., Jahreis, G., 2016. Evaluation of the impact of ruminant trans fatty acids on human health: important aspects to consider. Critical Reviews in Food Science and Nutrition 56(12):1964—1980. https://doi.org/10.1080/10408398.2013.808605.

[11] Kratz, M., Marcovina, S., Nelson, J.E., Yeh, M.M., Kowdley, K.V., Callahan, H.S., et al., 2014. Dairy fat intake is associated with glucose tolerance, hepatic and systemic insulin sensitivity, and liver fat but not beta-cell function in humans. American Journal of Clinical Nutrition 99(6):1385—1396. https://doi.org/10.3945/ajcn.113.075457.

[12] Mozaffarian, D., Cao, H.M., King, I.B., Lemaitre, R.N., Song, X.L., Siscovick, D.S., et al., 2010. Trans-Palmitoleic acid, metabolic risk factors, and new-onset diabetes in U.S. Adults a cohort study. Annals of Internal Medicine 153(12):790. https://doi.org/10.7326/0003-4819-153-12-201012210-00005.

[13] Mozaffarian, D., Otto, M.C.D., Lemaitre, R.N., Fretts, A.M., Hotamisligil, G., Tsai, M.Y., et al., 2013. trans-Palmitoleic acid, other dairy fat biomarkers, and incident diabetes: the Multi-Ethnic Study of Atherosclerosis (MESA). American Journal of Clinical Nutrition 97(4):854—861. https://doi.org/10.3945/ajcn.112.045468.

[14] Santaren, I.D., Watkins, S.M., Liese, A.D., Wagenknecht, L.E., Rewers, M.J., Haffner, S.M., et al., 2014. Serum pentadecanoic acid (15:0), a short-term marker of dairy food intake, is inversely associated with incident type 2 diabetes and its underlying disorders. American Journal of Clinical Nutrition 100(6):1532—1540. https://doi.org/10.3945/ajcn.114.092544.

[15] Kroger, J., Zietemann, V., Enzenbach, C., Weikert, C., Jansen, E., Doring, F., et al., 2011. Erythrocyte membrane phospholipid fatty acids, desaturase activity, and dietary fatty acids in relation to risk of type 2 diabetes in the European Prospective Investigation into Cancer and Nutrition (EPIC)-Potsdam Study. American Journal of Clinical Nutrition 93(1):127—142. https://doi.org/10.3945/ajcn.110.005447.

[16] Patel, P.S., Sharp, S.J., Jansen, E., Luben, R.N., Khaw, K.T., Wareham, N.J., et al., 2010. Fatty acids measured in plasma and erythrocyte-membrane phospholipids and derived by food-frequency questionnaire and the risk of new-onset type 2 diabetes a pilot study in the European Prospective Investigation into Cancer and Nutrition (EPIC)-Norfolk co. American Journal of Clinical Nutrition 92(5):1214—1222. https://doi.org/10.3945/ajcn.2010.29182.

[17] Castro-Webb, N., Ruiz-Narvaez, E.A., Campos, H., 2012. Cross-sectional study of conjugated linoleic acid in adipose tissue and risk of diabetes. American Journal of Clinical Nutrition 96(1):175—181. https://doi.org/10.3945/ajcn.111.011858.

[18] Cao, H., Gerhold, K., Mayers, J.R., Wiest, M.M., Watkins, S.M., Hotamisligil, G.S., 2008. Identification of a lipokine, a lipid hormone linking adipose tissue to systemic metabolism. Cell 134(6):933—944. https://doi.org/10.1016/j.cell.2008.07.048. S0092-8674(08)01014-3 [pii].

[19] Dimopoulos, N., Watson, M., Sakamoto, K., Hundal, H.S., 2006. Differential effects of palmitate and palmitoleate on insulin action and glucose utilization in rat L6 skeletal muscle cells. Biochemical Journal 399:473—481. https://doi.org/10.1042/bj20060244.

[20] Sauma, L., Stenkula, K.G., Kjolhede, P., Stralfors, P., Soderstrom, M., Nystrom, F.H., 2006. PPAR-gamma response element activity in intact primary human adipocytes: effects of fatty acids. Nutrition 22(1):60—68. https://doi.org/10.1016/j.nut.2005.04.011.

[21] Maedler, K., Oberholzer, J., Bucher, P., Spinas, G.A., Donath, M.Y., 2003. Monounsaturated fatty acids prevent the deleterious effects of palmitate and high glucose on human pancreatic beta-cell turnover and function. Diabetes 52(3):726—733. https://doi.org/10.2337/diabetes.52.3.726.

[22] Erbay, E., Babaev, V.R., Mayers, J.R., Makowski, L., Charles, K.N., Snitow, M.E., et al., 2009. Reducing endoplasmic reticulum stress through a macrophage lipid chaperone alleviates atherosclerosis. Nature Medicine 15(12):1383—1391. https://doi.org/10.1038/nm.2067 nm.2067 [pii].

[23] Cimen, I., Kocaturk, B., Koyuncu, S., Tufanl, O., Onat, U.I., Y ld r m, A.D., et al., 2016. Prevention of atherosclerosis by bioactive palmitoleate through suppression of organelle stress and inflammasome activation. Science Translational Medicine 8(358). https://doi.org/10.1126/scitranslmed.aaf9087, 358ra126-358ra126.

[24] Bernstein, A.M., Roizen, M.F., Martinez, L., 2014. Purified palmitoleic acid for the reduction of high-sensitivity C-reactive protein and serum Lipids: a double-blinded, randomized, placebo controlled study. Journal of Clinical Lipidology 8(6):612—617. https://doi.org/10.1016/j.jacl.2014.08.001.

[25] Yilmaz, M., Claiborn, K.C., Hotamisligil, G.S., 2016. De novo lipogenesis products and endogenous lipokines. Diabetes 65(7):1800–1807. https://doi.org/10.2337/db16-0251.

[26] Tabas, I., 2017. 2016 russell ross memorial lecture in vascular biology molecular-cellular mechanisms in the progression of atherosclerosis. Arteriosclerosis, Thrombosis, and Vascular Biology 37(2):183–189. https://doi.org/10.1161/atvbaha.116.308036.

[27] Tabas, I., Bornfeldt, K.E., 2016. Macrophage phenotype and function in different stages of atherosclerosis. Circulation Research 118(4):653–667. https://doi.org/10.1161/circresaha.115.306256.

[28] Duewell, P., Kono, H., Rayner, K.J., Sirois, C.M., Vladimer, G., Bauernfeind, F.G., et al., 2010. NLRP3 inflammasomes are required for atherogenesis and activated by cholesterol crystals. Nature 464(7293):1357–1361.. http://www.nature.com/nature/journal/v464/n7293/suppinfo/nature08938_S1.html.

[29] Libby, P., Lichtman, A.H., Hansson, G.K., 2013. Immune effector mechanisms implicated in atherosclerosis: from mice to humans. Immunity 38(6):1092–1104. https://doi.org/10.1016/j.immuni.2013.06.009.

[30] Wen, H.T., Gris, D., Lei, Y., Jha, S., Zhang, L., Huang, M.T.H., et al., 2011. Fatty acid-induced NLRP3-ASC inflammasome activation interferes with insulin signaling. Nature Immunology 12(5):408. https://doi.org/10.1038/ni.2022. U61.

[31] He, Y., Hara, H., Nunez, G., 2016. Mechanism and regulation of NLRP3 inflammasome activation. Trends in Biochemical Sciences 41(12):1012–1021. https://doi.org/10.1016/j.tibs.2016.09.002.

[32] Hotamisligil, G.S., Erbay, E., 2008. Nutrient sensing and inflammation in metabolic diseases. Nature Reviews Immunology 8(12):923–934. https://doi.org/10.1038/nri2449 nri2449 [pii].

[33] Feng, B., Yao, P.M., Li, Y., Devlin, C.M., Zhang, D., Harding, H.P., et al., 2003. The endoplasmic reticulum is the site of cholesterol-induced cytotoxicity in macrophages. Nature Cell Biology 5(9):781–792.

[34] Gora, S., Maouche, S., Atout, R., Wanherdrick, K., Lambeau, G., Cambien, F., et al., 2010. Phospholipolyzed LDL induces an inflammatory response in endothelial cells through endoplasmic reticulum stress signaling. The FASEB Journal 24(9):3284–3297. https://doi.org/10.1096/fj.09-146852.

[35] Xu, C.Y., Bailly-Maitre, B., Reed, J.C., 2005. Endoplasmic reticulum stress: cell life and death decisions. Journal of Clinical Investigation 115(10):2656–2664. https://doi.org/10.1172/jci26373.

[36] Tufanli, O., Telkoparan Akillilar, P., Acosta-Alvear, D., Kocaturk, B., Onat, U.I., Hamid, S.M., et al., 2017. Targeting IRE1 with small molecules counteracts progression of atherosclerosis. Proceedings of the National Academy of Sciences 114(8):E1395–E1404. https://doi.org/10.1073/pnas.1621188114.

[37] Verfaillie, T., Rubio, N., Garg, A.D., Bultynck, G., Rizzuto, R., Decuypere, J.P., et al., 2012. PERK is required at the ER-mitochondrial contact sites to convey apoptosis after ROS-based ER stress. Cell Death & Differentiation 19(11):1880–1891. https://doi.org/10.1038/cdd.2012.74.

[38] Gregor, M.F., Hotamisligil, G.S., 2011. Inflammatory mechanisms in obesity. Annual Review of Immunology 29:415–445. https://doi.org/10.1146/annurev-immunol-031210-101322.

[39] Horng, T., 2014. Calcium signaling and mitochondrial destabilization in the triggering of the NLRP3 inflammasome. Trends in Immunology 35(6):253–261.. https://doi.org/10.1016/j.it.2014.02.007.

[40] Walter, P., Ron, D., 2011. The unfolded protein response: from stress pathway to homeostatic regulation. Science 334(6059):1081–1086. https://doi.org/10.1126/science.1209038, 334/6059/1081 [pii].

[41] Park, S.W., Ozcan, U., 2013. Potential for therapeutic manipulation of the UPR in disease. Seminars in Immunopathology 35(3):351–373. https://doi.org/10.1007/s00281-013-0370-z.

[42] Ozcan, U., Yilmaz, E., Ozcan, L., Furuhashi, M., Vaillancourt, E., Smith, R.O., et al., 2006. Chemical chaperones reduce ER stress and restore glucose homeostasis in a mouse model of type 2 diabetes. Science 313(5790):1137–1140.

[43] Ozcan, U., Ozcan, L., Yilmaz, E., Duvel, K., Sahin, M., Manning, B.D., et al., 2008. Loss of the tuberous sclerosis complex tumor suppressors triggers the unfolded protein response to regulate insulin signaling and apoptosis. Molecular Cell 29(5):541–551. https://doi.org/10.1016/j.molcel.2007.12.023. S1097-2765(08)00066-X [pii].

[44] Ron, D., Walter, P., 2007. Signal integration in the endoplasmic reticulum unfolded protein response. Nature Reviews Molecular Cell Biology 8(7):519–529.

[45] Harding, H.P., Zhang, Y.H., Ron, D., 1999. Protein translation and folding are coupled by an endoplasmic-reticulum-resident kinase (vol 397, pg 271, 1999). Nature 398(6722):90. https://doi.org/10.1038/18057.

[46] Schroder, M., Kaufman, R.J., 2005. The mammalian unfolded protein response. Annual Review of Biochemistry 74:739–789. https://doi.org/10.1146/annurev.biochem.73.011303.074134.

[47] Halbleib, K., Pesek, K., Covino, R., Hofbauer, H.F., Wunnicke, D., Hanelt, I., et al., 2017. Activation of the unfolded protein response by lipid bilayer stress. Molecular Cell 67(4):673. https://doi.org/10.1016/j.molcel.2017.06.012.

[48] Volmer, R., van der Ploeg, K., Ron, D., 2013. Membrane lipid saturation activates endoplasmic reticulum unfolded protein response transducers through their transmembrane domains. Proceedings of the National Academy of Sciences of the United States of America 110(12):4628–4633. https://doi.org/10.1073/pnas.1217611110.

[49] Onat, U.I., Yildirim, A.D., Tufanli, Ö., Çimen, I., Kocatürk, B., Veli, Z., et al., 2019. Intercepting the lipid-induced integrated stress response reduces atherosclerosis. Journal of the American College of Cardiology 73(10):1149–1169. https://doi.org/10.1016/j.jacc.2018.12.055.

[50] Robblee, M.M., Kim, C.C., Abate, J.P., Valdearcos, M., Sandlund, K.L.M., Shenoy, M.K., et al., 2016. Saturated fatty acids engage an IRE1 alpha-dependent pathway to activate the NLRP3 inflammasome in myeloid cells. Cell Reports 14(11):2611–2623. https://doi.org/10.1016/j.celrep.2016.02.053.

[51] Li, H., Korennykh, A.V., Behrman, S.L., Walter, P., 2010. Mammalian endoplasmic reticulum stress sensor IRE1 signals by dynamic clustering. Proceedings of the National Academy of Sciences of the United States of America 107(37):16113–16118. https://doi.org/10.1073/pnas.1010580107.

[52] Han, S., Liang, C.P., DeVries-Seimon, T., Ranalletta, M., Welch, C.L., Collins-Fletcher, K., et al., 2006. Macrophage insulin receptor deficiency increases ER stress-induced apoptosis and necrotic core formation in advanced atherosclerotic lesions. Cell Metabolism 3(4):257–266.

[53] Seimon, T.A., Wang, Y., Han, S., Senokuchi, T., Schrijvers, D.M., Kuriakose, G., et al., 2009. Macrophage deficiency of p38alpha MAPK promotes apoptosis and plaque necrosis in advanced atherosclerotic lesions in mice. Journal of Clinical Investigation 119(4):886–898. https://doi.org/10.1172/JCI37262, 37262 [pii].

[54] Döring, Y., Noels, H., van der Vorst, E.P.C., Neideck, C., Egea, V., Drechsler, M., et al., 2017. Vascular CXCR4 limits atherosclerosis by maintaining arterial integrity. Circulation 136(4):388–403. https://doi.org/10.1161/CIRCULATIONAHA.117.027646.

[55] Rinne, P., Rami, M., Nuutinen, S., Santovito, D., van der Vorst, E.P.C., Guillamat-Prats, R., et al., 2017. Melanocortin 1 receptor signaling regulates cholesterol transport in macrophages. Circulation 136(1):83–+. https://doi.org/10.1161/circulationaha.116.025889.

[56] Doran, A.C., Ozcan, L., Cai, B.S., Zheng, Z., Fredman, G., Rymond, C.C., et al., 2017. CAMKII gamma suppresses an efferocytosis pathway in macrophages and promotes atherosclerotic plaque necrosis. Journal of Clinical Investigation 127(11):4075–4089. https://doi.org/10.1172/jci94735.

[57] Diakogiannaki, E., Morgan, N.G., 2008. Differential regulation of the ER stress response by long-chain fatty acids in the pancreatic beta-cell. Biochemical Society Transactions 36(Pt 5):959–962. https://doi.org/10.1042/bst0360959.

[58] Guo, H.T., Callaway, J.B., Ting, J.P.Y., 2015. Inflammasomes: mechanism of action, role in disease, and therapeutics. Nature Medicine 21(7):677—687. https://doi.org/10.1038/nm.3893.

[59] Chan, K.L., Pillon, N.J., Sivaloganathan, D.M., Costford, S.R., Liu, Z., Theret, M., et al., 2015. Palmitoleate reverses high fat-induced proinflammatory macrophage polarization via AMP-activated protein kinase (AMPK). Journal of Biological Chemistry 290(27):16979—16988. https://doi.org/10.1074/jbc.M115.646992.

[60] Niu, S.L., Mitchell, D.C., Litman, B.J., 2005. Trans fatty acid derived phospholipids show increased membrane cholesterol and reduced receptor activation as compared to their cis analogs. Biochemistry 44(11):4458—4465. https://doi.org/10.1021/bi048319+.

[61] Libby, P., 2012. Inflammation in atherosclerosis. Arteriosclerosis, Thrombosis, and Vascular Biology 32(9):2045—2051. https://doi.org/10.1161/atvbaha.108.179705.

[62] Babaev, V.R., Yeung, M., Erbay, E., Ding, L., Zhang, Y.M., May, J.M., et al., 2016. Jnk1 deficiency in hematopoietic cells suppresses macrophage apoptosis and increases atherosclerosis in low-density lipoprotein receptor null mice. Arteriosclerosis, Thrombosis, and Vascular Biology 36(6):1122. https://doi.org/10.1161/atvbaha.116.307580.

[63] Hirata, Y., Takahashi, M., Kudoh, Y., Kano, K., Kawana, H., Makide, K., et al., 2017. trans-Fatty acids promote proinflammatory signaling and cell death by stimulating the apoptosis signal-regulating kinase 1 (ASK1)-p38 pathway. Journal of Biological Chemistry 292(20):8174—8185. https://doi.org/10.1074/jbc.M116.771519.

[64] Tabas, I., 2010. The role of endoplasmic reticulum stress in the progression of atherosclerosis. Circulation Research 107(7):839—850. https://doi.org/10.1161/circresaha.110.224766.

[65] Machado, R.M., Nakandakare, E.R., Quintao, E.C., Cazita, P.M., Koike, M.K., Nunes, V.S., et al., 2013. Omega-6 polyunsaturated fatty acids prevent atherosclerosis development in LDLr-KO mice, in spite of displaying a pro-inflammatory profile similar to trans fatty acids (vol 224, pg 66, 2012). Atherosclerosis 226(1):301—302. https://doi.org/10.1016/j.atherosclerosis.2012.10.030.

[66] Estadella, D., do Nascimento, C., Oyama, L.M., Ribeiro, E.B., Damaso, A.R., de Piano, A., 2013. Lipotoxicity: effects of dietary saturated and transfatty acids. Mediators of Inflammation. https://doi.org/10.1155/2013/137579.

[67] Nettleton, J.A., Lovegrove, J.A., Mensink, R.P., Schwab, U., 2016. Dietary fatty acids: is it time to change the recommendations? Annals of Nutrition and Metabolism 68(4):249—257 https://doi.org/10.1159/000446865.

[68] Abderrazak, A., Couchie, D., Mahmood, D.F.D., Elhage, R., Vindis, C., Laffargue, M., et al., 2015. Anti-inflammatory and antiatherogenic effects of the NLRP3 inflammasome inhibitor arglabin in ApoE(2).Ki mice fed a high-fat diet. Circulation 131(12):1061—1070. https://doi.org/10.1161/circulationaha.114.013730.

[69] Sheedy, F.J., Grebe, A., Rayner, K.J., Kalantari, P., Ramkhelawon, B., Carpenter, S.B., et al., 2013. CD36 coordinates NLRP3 inflammasome activation by facilitating intracellular nucleation of soluble ligands into particulate ligands in sterile inflammation. Nature Immunology 14(8):812—+. https://doi.org/10.1038/ni.2639.

[70] Wang, Y., Wang, G.Z., Rabinovitch, P.S., Tabas, I., 2014. Macrophage mitochondrial oxidative stress promotes atherosclerosis and nuclear factor-kappa B-mediated inflammation in macrophages. Circulation Research 114(3):421—433. https://doi.org/10.1161/circresaha.114.302153.

[71] Ridker, P.M., Everett, B.M., Thuren, T., MacFadyen, J.G., Chang, W.H., Ballantyne, C., et al., 2017. Antiinflammatory therapy with canakinumab for atherosclerotic disease. New England Journal of Medicine 377(12):1119—1131. https://doi.org/10.1056/NEJMoa1707914.

[72] Yakoob, M.Y., Shi, P.L., Willett, W.C., Rexrode, K.M., Campos, H., Orav, E.J., et al., 2016. Circulating biomarkers of dairy fat and risk of incident diabetes mellitus among men and women in the United States in two large prospective cohorts. Circulation 133(17):1645—1654. https://doi.org/10.1161/circulationaha.115.018410.

[73] Ruttenberg, H., Davidson, L.M., Little, N.A., Klurfeld, D.M., Kritchevsky, D., 1983. Influence of trans unsaturated fats on experimental atherosclerosis in rabbits. Journal of Nutrition 113(4):835—844.

[74] Kritchevsky, D., Davidson, L.M., Weight, M., Kriek, N.P.J., Duplessis, J.P., 1984. Effect of trans-unsaturated fats on experimental atherosclerosis in vervet monkeys. Atherosclerosis 51(1):123—133. https://doi.org/10.1016/0021-9150(84)90148-5.

[75] Ganguly, R., Pierce, G.N., 2012. Trans fat involvement in cardiovascular disease. Molecular Nutrition & Food Research 56(7):1090—1096. https://doi.org/10.1002/mnfr.201100700.

[76] Roach, C., Feller, S.E., Ward, J.A., Shaikh, S.R., Zerouga, M., Stillwell, W., 2004. Comparison of Cis and Trans fatty acid containing phosphatidylcholines on membrane properties. Biochemistry 43(20):6344—6351. https://doi.org/10.1021/bi049917r.

[77] Sun, Q., Ma, J., Campos, H., Hu, F.B., 2007. Plasma and erythrocyte biomarkers of dairy fat intake and risk of ischemic heart diseased. American Journal of Clinical Nutrition 86(4):929—937.

[78] Jaudszus, A., Kramer, R., Pfeuffer, M., Roth, A., Jahreis, G., Kuhnt, K., 2014. Trans Palmitoleic acid arises endogenously from dietary vaccenic acid. American Journal of Clinical Nutrition 99(3):431—435. https://doi.org/10.3945/ajcn.113.076117.

[79] Liang, J.J., Zhou, Q., Amakye, W.K., Su, Y.X., Zhang, Z.Q., 2018. Biomarkers of dairy fat intake and risk of cardiovascular disease: a systematic review and meta analysis of prospective studies. Critical Reviews in Food Science and Nutrition 58(7):1122—1130. https://doi.org/10.1080/10408398.2016.1242114.

